A Measurement of the Michel Parameters ρ and η in Leptonic Tau Decays

Thesis by

Mandeepa Chadha

In Partial Fulfillment of the Requirements
for the Degree of
Doctor of Philosophy

California Institute of Technology
Pasadena, California

1998

(Submitted September 23, 1997)

This is my letter to the world,
That never wrote to me, -
The simple news that nature told,
With simple majesty.
-Emily Dickinson

Acknowledgements

A work many years in the making, I dedicate this thesis to Tarun who's held my hand through the last four!

I cannot thank enough the many people who helped in many ways along the way. First of all, I would like to thank Barry Barish and Ryszard Stroynowski for providing the motivation for this analysis. Next, I'd like to thank Alan Weinstein for picking up where they left off, and for his patience and guidance, without which this thesis would not have been possible. I'd also like to thank Jon Urheim and Mauritius Schmidtler for many discussions and arguments; Doug Cowen for teaching me to like Ithaca; and Bill Ross for providing all those laughs. I would also like to thank my undergraduate professors, R. C. Verma and M. P. Gupta, for introducing me to the wonderful world of High Energy Physics.

Last but not the least, I'd like to thank my parents who provided the strength and encouragement long-distance over the airwaves, and Michael Rogers for playing the parent whenever I needed one nearby. I might not be great at expressing my feelings, but I do appreciate all that you all have done for me!

Abstract

This thesis describes a precise measurement of the Michel parameters ρ and η using the leptonic tau decays recorded by the CLEO II detector. These measurements can be used to provide limits on the non-$(V-A)$ contributions to the Lorentz structure of the charged weak interactions in tau decays.

The electronic decay of the tau lepton, $\tau \rightarrow e\nu\bar{\nu}$, is used to measure the spectral shape Michel parameter:

$$\rho_e = 0.732 \pm 0.014 \pm 0.009 \ ,$$

where the first error is statistical and the second systematic. This measurement is extracted from the electron energy spectrum; the energy spectrum is insensitive to the low energy spectral shape Michel parameter η_e, and thus insensitive to the presence of scalar couplings.

The muonic decay mode of the tau lepton, $\tau \rightarrow \mu\nu\bar{\nu}$, is used to measure both the spectral shape Michel parameters:

$$\begin{aligned} \rho_\mu &= 0.747 \pm 0.048 \pm 0.044 \\ \text{and} \quad \eta_\mu &= 0.010 \pm 0.149 \pm 0.171 \end{aligned}$$

simultaneously. Once again, the first errors are statistical and the second systematic. The two parameters are strongly correlated; the correlation coefficient $C_{\rho\eta}$ is 0.949.

Assuming lepton universality of the vector-like couplings, the two leptonic decay modes are simultaneously analyzed to improve the measurement of the η parameter. Since the electron mode is insensitive to the η parameter, we can measure ρ very precisely using the electron mode. This measurement can now be used to constrain

the ρ measurement in the muon analysis, and thus obtain:

$$\begin{aligned} \rho_{e\mu} &= 0.735 \pm 0.013 \pm 0.008 \\ \text{and} \quad \eta_{e\mu} &= -0.015 \pm 0.061 \pm 0.062 \ , \end{aligned}$$

where the first errors are statistical and the second systematic. The correlation coefficient is now reduced to 0.615.

These measurements are all more precise than previous measurements; some are more precise than previous world average measurements. No indications for any deviations from the Minimal Standard Model have been found.

This measurement of the η parameter provides a lower limit on the charged Higgs mass in the Minimal Supersymmetric Standard Model: $m_{H^\pm} > (0.97 \times \tan\beta)$ GeV at the 90% confidence level. This limit is not very interesting unless $\tan\beta$ is very large.

Contents

List of Figures

List of Tables

Chapter 1 Introduction and Overview

Elementary particle physics * is the science that studies the fundamental building blocks of matter and their interactions. The Standard Model describes the interactions between these particles, and has been extremely successful [1]. It is the starting point for any investigation of modern particle physics, and provides the fundamental hypotheses which form the framework on which many extended theories are based.

Over the last twenty-five years, many tests of the Standard Model have been carried out with increasing precision, but no lasting significant discrepancy has been established. Despite the many successes, which started with the observations of neutral currents [2, 3] in 1973, and including both the observations of the W and Z^0 bosons [4, 5] in 1983, and the recent discovery of the top quark [6, 7] in 1995, there remain several basic unanswered questions:

- Are the quarks, leptons, and gauge bosons truly elementary?
- Why are there so many "elementary particles"?
- Why do they have their observed pattern of masses?
- What is the origin of mass? Is it the Higgs mechanism?
- What is the origin of CP violation?
- What is the "true" theory of everything?

The Standard Model requires numerous input parameters obtained from experiment, and does not satisfactorily connect electroweak interactions with quantum chromodynamics or gravity. Further, the Standard Model contains known flaws, revealed at very high energy, making it an unsatisfying final theory. In spite of the fact that

---

*The term physics is derived from the Greek word 'physis', which means the endevour of seeing the essential nature of all things.

the Standard Model accounts for a vast array of experimental data, it is far from the "final" theory. While the ultimate goal of high energy physics is to understand the underlying principles that govern our physical universe, the immediate goals are to test the Standard Model and to probe for new phenomena beyond. The analysis described in this thesis addresses both these immediate goals.

We present a high precision measurement of the Michel parameters ρ and η measured in leptonic decays of the tau. These parameters have been precisely measured in muon decay, and have been found to be consistent with Standard Model W-boson exchange, *i.e.*, with the $V-A$ structure hypothesis. The tau lepton, with its two leptonic decays $\tau^- \rightarrow \mu^-\overline{\nu}_\mu\nu_\tau$ and $\tau^- \rightarrow e^-\overline{\nu}_e\nu_\tau$, gives us a unique opportunity to study the universality of the charged leptonic weak interaction. Are these two decay modes just duplicates of the muon decay mode $\mu^- \rightarrow e^-\overline{\nu}_e\nu_\tau$, governed by the same type of weak interaction, *i.e.*, $V-A$? The current precision of experimental measurements of the Michel parameters in the tau sector are an order of magnitude weaker than corresponding measurements in the muon sector, where, in spite of the good experimental precision reached, an overall analysis with all possible weak couplings leaves much room for decay contributions in addition to those from the standard W-boson. The higher tau mass makes leptonic tau decays (compared to muon decay) more sensitive to physics beyond the Standard Model. Scalar couplings, induced by charged Higgs bosons, for example, would be proportional to the mass of the charged lepton, and thus this effect would show up in the muonic decay of the tau lepton with a factor $\approx 10^7$ larger than in the electronic decay of the muon! The much higher mass of the tau lepton is therefore a strong motivation to search for deviations of the Michel parameters from their $V-A$ predictions in tau decays.

The thesis is organized in chapters and appendices as follows:

We begin in Chapter 2 with a brief overview of the current understanding of the Standard Model of particle physics. This chapter concentrates on the physics of tau leptons at electron-positron colliders in general, and on their weak decays in particular. The Michel parameters, the focus of this thesis, are discussed here in detail.

Chapter 3 describes the measurement device and experimental setup, i.e., the CLEO II detector at the CESR e^+e^- collider. This chapter also contains a brief overview of the Monte Carlo simulations consisting of the event generation and the detector simulation processes. CESR is constantly upgraded to achieve higher luminosities, and the detector is periodically upgraded both to handle this increased luminosity, and to improve its detection capabilities. The collaboration installed a silicon vertex microstrip detector in the fall of 1995. The author has worked on the mechanical support system for this device, as well as the new data acquisition system required for it. Details of this work are outlined in Appendix D.

Chapter 4 describes the event reconstruction procedure. We list the selection criteria used to obtain the event samples used in the analysis, and then proceed to describe in some detail some of the more interesting/unusual requirements.

Chapter 5 describes in some detail all the potential sources of backgrounds. Each of the significant background sources is minimized using several special cuts and the surviving backgrounds are well understood.

The two event samples used to measure the Michel parameters can also be used to measure the two leptonic branching ratios of the tau lepton. Chapter 6 describes the results obtained for $\mathcal{B}(\tau^- \to e^-\overline{\nu}_e\nu_\tau)$ and $\mathcal{B}(\tau^- \to \mu^-\overline{\nu}_\mu\nu_\tau)$. No attempt is made to minimize the systematic errors since these branching ratios have already been well measured at CLEO [8].

Chapter 7 describes the special reference frame utilized in this thesis to achieve maximum sensitivity to the Michel parameters studied. This "pseudo" rest frame technique, first pioneered by the ARGUS Collaboration [9] is essential in the η measurements.

Chapter 8 discusses the fit procedure employed to obtain the measurements of the Michel parameters. It also includes all the results obtained using this fit procedure.

Chapter 9 describes in great detail the work done to ensure that all the systematic errors were minimized and well understood. This work was important to achieve the level of precision desired in this analysis.

Chapter 10 summarizes the work presented in this document, and discusses its significance. Future improvements on the results presented here are briefly described.

Four appendices to this thesis are attached. Some of the mathematical integrals used in Chapter 2 are detailed in Appendix A.1.

Appendix B describes in detail the determination of muon fake rates in the muon chambers in the CLEO II detector. This study is performed using the data, and its results are used to calibrate the fake rates in the Monte Carlo generator. A precise knowledge of these fake rates is essential to obtain the level of precision achieved in this thesis.

Appendix C defines the spin sensitive variable ω, used to test the Monte Carlo simulation of the spin-spin correlations that exist between the two τ leptons in $e^+e^- \longrightarrow \tau^+\tau^-$.

Appendix D describes the author's involvement in hardware projects which primarily revolved around the new silicon vertex detector. The analysis presented here does not include any data collected after the installation of this new detector component.

Chapter 2 The Standard Model of Particle Physics

The Standard Model of particle physics describes our knowledge of what composes the material universe, and what interactions occur among these constituents. This chapter first gives a brief overview of the elementary particles and their interactions, followed by a brief description of the formalism of the Standard Model. It then concentrates on the τ lepton and its interactions and defines the Michel parameters, the focus of this thesis.

2.1 Elementary Particles

In our current understanding, matter everywhere is composed of only a few fundamental building blocks: six kinds of leptons and six kinds of quarks. These spin 1/2 fermions are considered fundamental for two reasons. They and their antiparticles make up all matter, and each of these fermions is not decomposable. At the current experimental level of 10^{-16} m, no compositeness has been observed. Both leptons and quarks are smaller than this level, and are many orders of magnitude smaller than the atom (approximately 10^{-10} m).

The best known lepton is the electron (e^-), the negatively charged particle found in the outermost portion of all atoms. There also exist two heavier versions of the electron: the muon (μ^-) and the tau (τ^-). Aside from their larger masses (so that they can decay into lighter particles), these two leptons are identical in many respects to the electron. Each of the three leptons is associated with a massless neutral particle (three more leptons) called the neutrino (ν_e, ν_μ, ν_τ). The tau-neutrino ν_τ is the only lepton which has not yet been directly observed experimentally. The six leptons are grouped into three doublets, or generations, as shown in Table 2.1, where we list some of the properties of the various leptons.

Lepton	Charge (e)	Mass (MeV/c^2)	Lifetime (sec)
e	-1	0.511	stable ($> 4.3 \times 10^{23}$ years)
ν_e	0	$< 15 \times 10^{-6}$	stable
μ	-1	105.7	2.197×10^{-6}
ν_μ	0	< 0.17	stable
τ	-1	1777.0 ± 0.3	$(291.0 \pm 1.5) \times 10^{-15}$
ν_τ	0	< 24	stable

Table 2.1: Properties of the six leptons. For the neutrino masses, the current 90% confidence level upper limits from experiment are listed. The different generations are enclosed by the double lines.

The six quarks can also be grouped into three generations with progressively larger mass as shown in Table 2.2, where we list some of the quark properties. The u and d quarks are the constituents of the proton and neutron in the nuclei of atoms.

Quark	Charge (e)	Mass (GeV/c^2)	I_3	S	C	B	T
d	$-1/3$	~ 0.004	$-1/2$	0	0	0	0
u	$2/3$	~ 0.007	$+1/2$	0	0	0	0
s	$-1/3$	~ 0.3	0	-1	0	0	0
c	$2/3$	~ 1.3	0	0	$+1$	0	0
b	$-1/3$	~ 4.8	0	0	0	-1	0
t	$2/3$	~ 174	0	0	0	0	$+1$

Table 2.2: Properties of the six quarks. The symbol I_3 denotes the third component of isospin; S, C, B, and T denote strangeness, charm, bottom (or beauty), and top (or truth) respectively. The quark masses are all model dependent. The double lines enclose the different generations.

2.2 Fundamental Forces

The interactions between all matter are governed by four fundamental forces: the strong, electromagnetic, weak and gravitational forces. These forces are all mediated by the gauge bosons. The different kinds of interactions, their mediators, and some of their properties are listed in Table 2.3.

Force	Relative Strength	Range (m)	Boson	Charge (e)	Spin	Mass (GeV/c^2)
Strong	1	$< 10^{-15}$	gluon (g)	0	1	0
Electromagnetic	10^{-2}	∞	photon (γ)	0	1	0
Weak	10^{-13}	$< 10^{-18}$	$W^{\pm}$	± 1	1	80.2
			Z^0	0	1	91.2
Gravitational	10^{-38}	∞	graviton (G)	0	2	0

Table 2.3: The four fundamental forces and their mediators.

The forces are listed in order of decreasing strengths; the listed strengths are evaluated at a distance scale of 10^{-15} m and serve only as a rough comparison. Gluons mediate the strong interactions between any two quarks, photons carry the electromagnetic force between any two quarks or charged leptons, the $W^{\pm}$ and Z^0 bosons mediate the weak interactions within one and between two families of fermions, and finally the graviton carries the gravitational force between any two particles with mass. The gravitational force is far too weak to be detected at the level of particle mass scales.

The photons and the $W^{\pm}$, Z^0 bosons have been experimentally observed. Jet structure in certain hadronic events ($e^+e^- \rightarrow q\bar{q}g$) [10] provides indirect evidence for the existence of gluons. The photons and gluons are stable, and the massive W and Z bosons decay into lighter particles in approximately 10^{-27} s. Gravitons are not observable at experimentally achievable energies.

2.3 Weak Interactions and the $(V - A)$ Theory

Although all hadrons and leptons participate in weak interactions, these interactions can only be observed in circumstances where the much faster strong or electromagnetic decays are forbidden by conservation laws. The lifetimes for weak decays with energy $\ll m_W, m_Z$ depend on the phase-space factors, as well as the weak coupling constant G_F, but are long compared with typical lifetimes for the electromagnetic decays ($\simeq 10^{-19}$ s) or strong decays ($\simeq 10^{-23}$ s). The weak cross sections are correspondingly small.

Weak forces are produced by the "weak charge"; electric charge produces the electromagnetic forces and color produces the strong forces. All quarks and leptons are carriers of this weak charge. Leptons have no color and thus cannot participate in strong interactions. The electrically neutral neutrinos cannot participate in electromagnetic decays either, thus making them unique.

There are two kinds of weak interactions: electrically charged (mediated by the $W^{\pm}$ bosons) and electrically neutral (mediated by the Z^0 boson). Both the leptonic decays of the tau lepton studied in this thesis $\tau^- \to \ell^- \overline{\nu}_\ell \nu_\tau$, where ℓ is either the muon or the electron, are examples of the charged weak interaction.

Weak interactions were first observed in the slow process of nuclear β-decay,

$$n \to p + e^- + \bar{\nu}_e \ ,$$

or, in terms of quark constituents,

$$d \to u + e^- + \bar{\nu}_e \ .$$

This example of the charged weak interaction is mediated by the exchange of a virtual $W^{\pm}$ boson, but since the momentum transfer involved is small, *i.e.*, $q^2 \ll m_W^2$, the interaction is effectively point-like and can be described by the four-fermion coupling $G = g^2/m_W^2$, the Fermi constant [*]. Fermi first postulated this contact interaction in

---

[*] g characterizes the coupling strength of the fermionic current to the W boson.

1935, and developed his theory of β-decay in analogy with the theory of electromagnetic decays. He suggested the matrix element:

$$\begin{aligned} \mathcal{M} &= G\, J^{weak}_{baryon}\, J^{weak}_{lepton} = G\left[\bar{\psi}_p\gamma_\mu\psi_n\right]\left[\bar{\psi}_e\gamma^\mu\psi_\nu\right] , \\ \text{in analogy with} \quad \mathcal{M} &\propto \frac{e^2}{q^2}\, J_{baryon}\, J_{lepton} . \end{aligned} \tag{2.1}$$

The coupling constant G replaces e^2/q^2. Since weak currents are assumed to interact at a point, the propagator of the exchanged photon in electromagnetic interactions, $1/q^2$ is replaced by $1/(m_W^2 - q^2)$, and since $q^2 \ll m_W^2$ at low energies characteristic of tau decays, it plays no role. Fermi's choice of a vector-vector form of the weak amplitude $\mathcal{M}$ was satisfactory (prior to the discovery of parity violation in 1956) in describing nuclear β-decay, but *a priori*, there is no reason to use only vectors. The Lorentz invariant amplitude $\mathcal{M}$ can be constructed using all other possible bilinear covariants listed in Table 2.4. The matrix element can now be written as:

$$\mathcal{M} = G \sum_{i=S,V,T,P,A} C_i \left[\bar{\psi}_p O_i \psi_n\right]\left[\bar{\psi}_e O_i \psi_\nu\right] , \tag{2.2}$$

where C_i are the appropriate coefficients. The different forms for the operator O_i are named according to the transformation properties of the weak currents under rotations and space inversions: scalar (S), vector (V), tensor (T), pseudoscalar (P), and axial vector (A).

O_i		No. of components	Parity
Scalar	$\bar{\psi}\psi$	1	+
Vector	$\bar{\psi}\gamma_\mu\psi$	4	− (Space)
Tensor	$\bar{\psi}\sigma_{\mu\nu}\psi$	6	
Axial vector	$\bar{\psi}\gamma_5\gamma_\mu\psi$	4	− (Space)
Pseudoscalar	$\bar{\psi}\gamma_5\psi$	1	−

Table 2.4: Exhaustive list of possible bilinear quantities with definite properties under Lorentz transformations.

After a careful analysis of nuclear β decay, μ decay, and parity violation, Fermi arrived at the conclusion that the decay was dominated by $(V-A)$ interactions. Using lepton universality, τ decays must be dominated by $(V-A)$ also. In this thesis, we search for small deviations from this $(V-A)$ theory.

2.4 The Tau Lepton

The tau is the third heavy lepton. Today, many of the properties of the tau lepton are precisely known [11, 12]. In this section, we present a brief account of the discovery of this particle, followed by an account of its production mechanism, with an emphasis on its production in e^+e^- annihilation. Finally, a brief summary of the theory of leptonic tau decays is presented.

2.4.1 The Discovery of the Tau Lepton

The possibility of a third, heavier, sequential lepton was investigated in detail by Y. S. Tsai [13] in 1971. He predicted decay correlations and branching fractions dependent on the lepton's mass. The first experimental confirmation of its existence took place in 1975 in annihilations of e^+e^- into tau pairs. These observations were made by M. L. Perl et al. [14] using the Mark I detector at the SPEAR storage ring at the Stanford Linear Accelerator Center (SLAC). They observed 24 events containing an electron and a muon, and no other visible charged or neutral particles. The acoplanar tracks did not fulfill energy and momentum conservation requirements, implying the presence of undetected particles in the event. The list of possible candidates for the undetected particles is comprised of charged particles or photons that escaped the 2.6 π steradian acceptance, and particles not easily detectable like neutrinos, K_L^0 mesons and neutrons. The Dalitz distributions for these events did not exhibit any significant structure at a particular missing mass value, implying that there were at least two missing particles in each event. This suggested that the particles were **not** the charged particles or photons that escaped detection.

To interpret this observation, MARK I had to collect more data. The next analysis [15] included 105 such events. The almost collinear angle between the two tracks suggested that the origin must be from the production of a pair of new particles, and the inclusive momentum spectrum indicated that each of these new particles decayed into at least three bodies. Systematic elimination of other possibilities suggested that the undetected particles were neutrinos. Finally, the observed production cross section suggested that the mass of the heavy particle was in the range 1.6 to 2.0 GeV/c^2. All these observations were consistent with the creation of a pair of heavy leptons (later named the τ), each of which decayed into a charged lepton and two neutrinos: $\tau \longrightarrow \ell\nu\bar{\nu}$, where ℓ was either an electron or a muon.

A following experiment [16] confirmed that the production occurred below the threshold for open charm meson production, thus eliminating any possibility that these new observations were associated with purely leptonic decays of the charm quark.

Today, many of the properties of the tau lepton are precisely known, and are summarized in the following sections. They are consistent with the Standard Model ($V - A$) interaction theory, but permit small departures, which are the subject of this thesis.

2.4.2 Tau Production

This subsection describes the different ways tau leptons can be created. The leptonic tau decays, analyzed in this thesis, utilize tau pairs produced in e^+e^- annihilations observed by the CLEO II detector. Tau leptons can also be produced in photoproduction and electroproduction reactions, in $p\bar{p}$ collisions, in the decay of heavy quarks, and in interactions such as $\nu_\tau + N \rightarrow \tau + N'$.

e^+e^- Annihilation

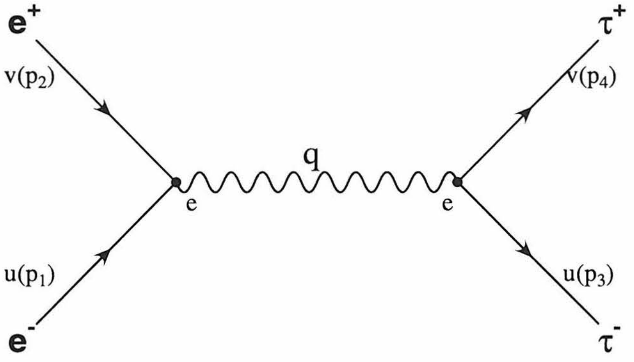

The squared matrix element for the process $e^+e^- \rightarrow \tau^+\tau^-$ is given by:

$$|\mathcal{M}|^2 = \frac{e^4}{q^4} L_e^{\mu\nu} L^\tau_{\mu\nu} ,$$

where the two leptonic tensors are given by:

$$L_e^{\mu\nu} = \frac{1}{2}\sum_{s,s'} [\bar{v}_{s'}(p_2)\gamma^\mu u_s(p_1)]\ [\bar{v}_{s'}(p_2)\gamma^\nu u_s(p_1)]^*$$

$$\text{and } L^\tau_{\mu\nu} = \frac{1}{2}\sum_{s,s'} [\bar{v}_{s'}(p_4)\gamma_\mu u_s(p_3)]\ [\bar{v}_{s'}(p_4)\gamma_\nu u_s(p_3)]^* , \quad (2.3)$$

where p_1, p_2, p_3 and p_4 represent the four-vectors of the e^-, e^+, τ^- and τ^+ respectively. Now, averaging over the initial electron and positron spins, and summing over the final tau spins, we get:

$$\begin{aligned} L_\epsilon^{\mu\nu} &= \frac{1}{2}\,\mathrm{Tr}\left[(\not{p}_2 - m)\,\gamma^\mu\,(\not{p}_1 + m)\,\gamma^\nu\right] \\ \text{and } L^\tau_{\mu\nu} &= \frac{1}{2}\,\mathrm{Tr}\left[(\not{p}_4 - M)\,\gamma_\mu\,(\not{p}_3 + M)\,\gamma_\nu\right] \ , \end{aligned} \tag{2.4}$$

where m is the mass of the electron and positron, and M is the mass of the tau leptons. Neglecting the masses of the electron and positron, and using the trace relation:

$$\mathrm{Tr}\left(\gamma^\mu\gamma^\nu\gamma^\lambda\gamma^\delta\right) = 4\ \left(g^{\mu\nu}g^{\lambda\delta} - g^{\mu\lambda}g^{\nu\delta} + g^{\mu\delta}g^{\nu\lambda}\right) \ , \tag{2.5}$$

the leptonic tensor $L_\epsilon^{\mu\nu}$ simplifies to:

$$L_\epsilon^{\mu\nu} = 4\left[p_2^\mu p_1^\nu + p_2^\nu p_1^\mu - p_2 p_1 g^{\mu\nu}\right] \ . \tag{2.6}$$

Next, using the fact that the trace of an odd number of gamma matrices vanishes, and that $\mathrm{Tr}\,(\gamma_\mu\gamma_\nu) = 4\,g_{\mu\nu}$, in addition to the above trace relation, the other leptonic tensor $L^\tau_{\mu\nu}$ simplifies to:

$$L^\tau_{\mu\nu} = 2\left[p_{4\mu}p_{3\nu} + p_{4\nu}p_{3\mu} - \left(p_4 p_3 + M^2\right)g^{\mu\nu}\right] \ . \tag{2.7}$$

Thus,

$$\langle|\mathcal{M}|^2\rangle = 8\,\frac{e^4}{q^4}\left[(p_2\cdot p_4)(p_1\cdot p_3) + (p_2\cdot p_3)(p_1\cdot p_4) + (p_2\cdot p_1)M^2\right] \ . \tag{2.8}$$

Now, assuming that the electron and the positron have energy E, and that their momenta are parallel to the $+z$ and $-z$ axis respectively, the four-vectors for the electron and positron are:

$$p_1 = (E, 0, 0, \vec{p}) \qquad\qquad p_2 = (E, 0, 0, -\vec{p}) \ , \tag{2.9}$$

and the four-vectors for the produced taus are:

$$p_3 = (E, p_x, p_y, p_z) \qquad\qquad p_4 = (E, -p_x, -p_y, -p_z) \ . \tag{2.10}$$

In terms of the polar angle θ and azimuth angle ϕ,

$$\begin{aligned} p_x &= |p| \sin\theta \cos\phi \ , \\ p_y &= |p| \sin\theta \sin\phi \ , \\ \text{and } p_z &= |p| \cos\theta \ . \end{aligned} \tag{2.11}$$

Now, defining $\beta = |\vec{p}\,|/E$, and using $s = q^2 = (p_1 + p_2)^2 = 4E^2$, we get:

$$\begin{aligned} (p_2 \cdot p_4) &= (p_1 \cdot p_3) = \frac{s}{4}(1 - \beta\cos\theta) \ , \\ (p_2 \cdot p_3) &= (p_1 \cdot p_4) = \frac{s}{4}(1 + \beta\cos\theta) \ , \\ \text{and } (p_1 \cdot p_2) &= \frac{s}{2} \ . \end{aligned} \tag{2.12}$$

Substituting the results obtained in Equation 2.12 into Equation 2.8, we get:

$$\langle|\mathcal{M}|^2\rangle = 8\,\frac{e^4}{q^4}\left[\frac{s^2}{8}\left(1 + \beta^2\cos^2\theta\right) + \frac{s^2}{8}\left(1 - \beta^2\right)\right] = e^4\left[2 - \beta^2 + \beta^2\cos^2\theta\right] \ . \tag{2.13}$$

The differential cross section is given by:

$$\frac{d\sigma}{d\Omega} = \frac{1}{F}\langle|\mathcal{M}|^2\rangle dLips \ , \tag{2.14}$$

where the flux, $F = 4p_1\sqrt{s} = 4p_2\sqrt{s}$, and the two body phase space,

$$dLips = \frac{1}{4\pi^2}\frac{p_3}{4\sqrt{s}}d\Omega \ . \tag{2.15}$$

Thus, in e^+e^- annihilation, tau pairs are produced with a differential cross section,

$$\frac{d\sigma}{d\Omega} = \frac{\alpha^2}{4s}\cdot\beta\cdot(2 - \beta^2\sin^2\theta) \ , \tag{2.16}$$

where θ is the angle between the τ^+ and e^+, $p_3/p_1 = \beta = v/c$ is the tau velocity, and $\alpha = e^2/2\pi$ is the fine structure constant. The integrated cross section can now be expressed as:

$$\sigma_0(e^+e^- \to \tau^+\tau^-) = \frac{4\pi\alpha^2}{3s} \cdot \beta \cdot \frac{3-\beta^2}{2} \, . \tag{2.17}$$

At high center of mass energies, where $\beta = 1$, the integrated cross section simplifies to:

$$\sigma_0(e^+e^- \to \tau^+\tau^-) = \frac{4\pi\alpha^2}{3s} = \frac{86.86 \text{ nb GeV}^2}{s} \tag{2.18}$$

with $\alpha = 1/137.036$ and $(\hbar c)^2 = 389386$ nb GeV ^{2}.

Photoproduction and Electroproduction

Tau pairs can be produced in the following photoproduction [17] and electroproduction reactions:

$$\begin{aligned} \gamma + N &\to \tau^+ + \tau^- + N' \, , \\ \text{and } e^- + N &\to e^- + \tau^+ + \tau^- + N' \, , \end{aligned} \tag{2.19}$$

where N is the target proton or nucleus, and N' represents the final hadronic state.

Particle Decays to τ and ν_τ

These particle decay modes include the decays of the heavy W and Z bosons, as well as the semi-leptonic decays of the heavy b and c quarks.

W decays: the decay modes, $W^+ \to \tau^+ + \nu_\tau$ and $W^- \to \tau^- + \bar{\nu}_\tau$, have been observed by the UA1 [18], UA2 [19], and CDF [20] experiments. Aside from being used to identify the W bosons [21], these decays are used to study the $W\tau\nu_\tau$ vertex at $\sqrt{s} = m_W$. Using the ratio of the branching fractions of the leptonic decays,

$$\frac{\mathcal{B}(W^- \to \tau^- \bar{\nu}_\tau)}{\mathcal{B}(W^- \to e^- \bar{\nu}_e)} , \tag{2.20}$$

the ratio of the charged current couplings g_τ / g_e can be deduced, and used as a test of universality. The average of the three measurements mentioned above is:

$$\sqrt{g_\tau / g_e} = 1.00 \pm 0.04 \ ,$$

in agreement with Standard Model expectations.

The width for Z^0 **decay into lepton pairs** is given by:

$$\Gamma(Z^0 \to \ell\bar{\ell}) = \frac{1}{3} m_Z \alpha(m_Z)(v_\ell^2 + a_\ell^2) \ , \tag{2.21}$$

where $\alpha(m_Z) \simeq 1/127$ is the QED fine structure constant evaluated at the Z^0 mass,

$$v_\ell = \frac{-1 + 4\sin^2\theta_W}{4\sin\theta_W \cos\theta_W} \ , \qquad a_\ell = \frac{-1}{4\sin\theta_W \cos\theta_W} \ ,$$

and

$$\sin^2\theta_W = 1 - \left(\frac{m_W}{m_Z}\right)^2 = 0.233 \pm 0.001 \ ,$$

where m_W and m_Z are the masses of the $W^\pm$ and Z^0 bosons respectively.

The universality of the lepton coupling implies equality of the partial widths for the decay of the Z^0 to e^+e^-, $\mu^+\mu^-$ and $\tau^+\tau^-$ pairs. Further, the Standard Model predicts that the τ's from the decay of the $Z^0 \to \tau^+\tau^-$ are polarized as a direct consequence of parity violations in the weak neutral current.

Pure leptonic decays of the $D^\pm$ and $D_s^\pm$,

$$\begin{aligned} D^+ &\to \ell^+ + \nu_\ell \\ D_s^+ &\to \ell^+ + \nu_\ell \end{aligned} \tag{2.22}$$

where ℓ is the τ lepton, have not been observed. These modes have a decay width given by:

$$\Gamma(D^+, D_s^+ \rightarrow \ell^+ \nu_\ell) = \frac{G_F^2}{8\pi} f_{D,D_s}^2 m_{D,D_s} m_\ell^2 |V_{cd,cs}|^2 \left[1 - \frac{m_\ell^2}{m_{D,D_s}^2}\right] , \qquad (2.23)$$

where f_{D,D_s} are the weak decay constants of the D and D_s, and take into account the strong interaction dynamics of cd and cs annihilation inside the meson. Theory estimates their size to be 150 to 250 MeV, but they must be measured through these decay processes. The m_ℓ^2 term leads to the tau mode having larger rate than the electron and muon modes, and thus the decay to the tau mode provides the best way to measure the weak decay constants.

The theory of **leptonic decays of the B mesons**,

$$\begin{aligned} B^+ &\rightarrow \tau^+ + \nu_\tau \\ B_c^+ &\rightarrow \tau^+ + \nu_\tau \end{aligned} \qquad (2.24)$$

is analogous to that for D decays (see Equation 2.23), but the smaller values of V_{ub} and V_{cb} suppress the decay widths.

Tau Production in Hadron Collisions

Taus can be **produced in $p + N$ Collisions**, the largest contribution to the rate is expected to be from the decay mode $D_s \rightarrow \tau + \bar{\nu}_\tau$, where the D_s is created in the reaction:

$$p + N \rightarrow D_s + \ldots , \qquad (2.25)$$

and N is a nucleon or a nucleus. These collisions can be from an external proton beam on a fixed target or from a circulating proton beam on a gas jet target. Tau leptons can also be produced in a proton-proton collider ($p\bar{p} \rightarrow W^- X$), where the produced W boson subsequently decays into the tau lepton.

Heavy ion collisions [22, 23] can also result in the production of tau pairs:

$$\text{Ion} + \text{Ion} \rightarrow \tau^+ + \tau^- + \ldots \; ; \tag{2.26}$$

the virtual photons emitted in the collision of a pair of heavy ions can produce a $\tau^+\tau^-$ pair when the ions are at energies much greater than the tau mass.

Neutrino production

Tau leptons can be produced in a new generation of accelerator experiments searching for neutrino oscillations, first suggested [24] many years back in analogy with the oscillations of neutral K^0 mesons. The CHORUS and NOMAD experiments were conceived to detect the appearance of the tau neutrino in a rather pure CERN muon neutrino beam following the hypothetical flavor oscillation phenomenon. The charged current interaction,

$$\nu_\tau + N \rightarrow \tau^- + X \; , \tag{2.27}$$

results in the production of the tau lepton when the neutrino energy is sufficiently above the tau production threshold.

Other experiments, such as the short baseline E-803 and the MINOS long baseline neutrino oscillation experiments at FNAL, also hope to observe neutrino oscillations by observing the tau lepton produced when the tau neutrino interacts.

The reaction shown in Equation 2.27 (and related reactions) can help determine the overall Lorentz structure; see Section 2.6 for details.

2.4.3 Theory of Tau Decays

The decay of the charged tau lepton probes the weak charged current sector at a mass scale characterized by the mass of the tau m_τ, while the production of $\tau^+\tau^-$ pairs at e^+e^- colliders probes the neutral current sector at the higher energy scale characterized by m_Z.

The leptonic decays of the charged tau lepton to a lighter charged lepton ℓ ($\ell = e, \mu$) are purely weak in nature, and the Standard Model $(V-A)$ four fermion coupling scheme, described in Section 2.3, can be used for the calculation of the leptonic tau decay,

$$\tau^-(p_\tau, s_\tau) \rightarrow \ell^-(p_\ell, s_\ell) + \bar{\nu}_\ell\,(p_1, s_1) + \nu_\tau\,(p_2, s_2)\,,$$

where p_τ, p_ℓ, p_1, p_2 are the four-momentum of the tau, daughter charged lepton, $\bar{\nu}_\ell$ and ν_τ respectively, and s_τ, s_ℓ, s_1, and s_2 are their polarization four-vectors.

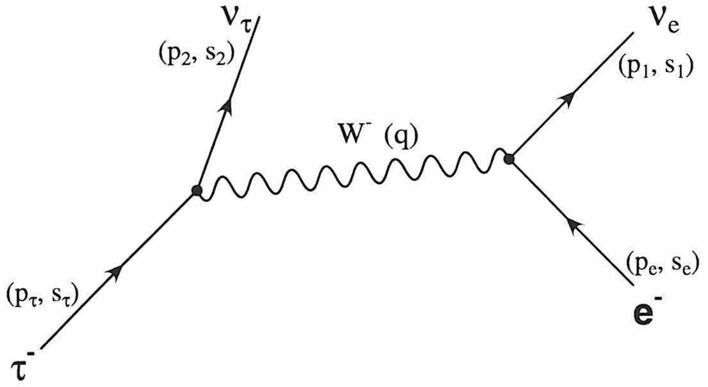

$p_\tau = p_{\bar{\nu}} + p_\nu + p_\ell$ and

$q = p_\tau - p_{\bar{\nu}} = p_\ell + p_\nu$

Using the Feynman rules in the $(V-A)$ theory, the matrix element is given by:

$$-i\mathcal{M} \;=\; \bar{u}_2 \frac{-ig}{\sqrt{2}} \frac{\gamma^\mu(1-\gamma^5)}{2} u_\tau \left[\frac{i}{q^2 - m_W^2}(-g^{\mu\nu} + \frac{q^\mu q^\nu}{m_W^2})\right] \bar{u}_\ell \frac{-ig}{\sqrt{2}} \frac{\gamma^\nu(1-\gamma^5)}{2} v_1\,. \tag{2.28}$$

Since, $\max q^2 = m_\tau^2 = 4.8 \times 10^{-4} m_W^2 \ll m_W^2$, the W boson propagator can be taken to the $q^2 \to 0$ limit, $ig^{\mu\nu}/m_W^2$, leading to:

$$\mathcal{M} \;=\; \frac{g^2}{8m_W^2}\left[\bar{u}_2\gamma^\mu(1-\gamma^5)u_\tau\right]\left[\bar{u}_\ell\gamma_\mu(1-\gamma^5)v_1\right] \; . \tag{2.29}$$

$$\begin{aligned}
\text{Now,} \qquad |\mathcal{M}|^2 &= \frac{g^4}{64m_W^4}L^{\mu\nu}M_{\mu\nu} \; , \\
\text{where} \;\; L^{\mu\nu} &= \left[\bar{u}_2\gamma^\mu(1-\gamma^5)u_\tau\right]\left[\bar{u}_\tau\gamma^\nu(1-\gamma^5)u_2\right] \\
&= -\mathrm{Tr}\left[\not{p}_2\gamma^\mu(\not{p}_\tau - m_\tau \not{s}_\tau)\gamma^\nu(1-\gamma^5)\right] \\
&= -p_{2\alpha}(p_\tau - m_\tau s_\tau)_\beta \mathrm{Tr}\left[\gamma^\alpha\gamma^\mu\gamma^\beta\gamma^\nu(1-\gamma^5)\right] \; , \\
\text{and} \;\; M_{\mu\nu} &= \left[\bar{u}_\ell\gamma_\mu(1-\gamma^5)v_1\right]\left[\bar{v}_1\gamma_\nu(1-\gamma^5)u_\ell\right] \\
&= -\mathrm{Tr}\left[(\not{p}_\ell - m_\ell \not{s}_\ell)\gamma_\mu \not{p}_1\gamma_\nu(1-\gamma^5)\right] \\
&= -(p_\ell - m_\ell s_\ell)^\sigma p_1^\theta \mathrm{Tr}\left[\gamma_\sigma\gamma_\mu\gamma_\theta\gamma_\nu(1-\gamma^5)\right] \; .
\end{aligned} \tag{2.30}$$

Thus, substituting for the leptonic tensors $L^{\mu\nu}$ and $M_{\mu\nu}$, and using the trace relations:

$$\begin{aligned}
\mathrm{Tr}\left[\gamma_\sigma\gamma_\mu\gamma_\theta\gamma_\nu\right] &= 4g_{\sigma\mu}g_{\theta\nu} - 4g_{\sigma\theta}g_{\mu\nu} + 4g_{\sigma\nu}g_{\mu\theta} \\
\text{and} \;\; \mathrm{Tr}\left[\gamma_\sigma\gamma_\mu\gamma_\theta\gamma_\nu\gamma^5\right] &= 4i\varepsilon_{\sigma\mu\theta\nu} \; ,
\end{aligned} \tag{2.31}$$

Equation 2.30 can be written as:

$$\begin{aligned}
|\mathcal{M}|^2 &= \frac{g^4}{m_W^4}p_2\cdot(p_\ell - m_\ell s_\ell)\; p_1\cdot(p_\tau - m_\tau s_\tau) \\
&= 32\; G_F^2\; p_2\cdot(p_\ell - m_\ell s_\ell)\; p_1\cdot(p_\tau - m_\tau s_\tau) \; ,
\end{aligned} \tag{2.32}$$

where $G_F^2 = g^4/(32m_W^4)$ is used.

The differential transition probability is given by:

$$\begin{aligned}
d\Gamma &= \frac{1}{2m_\tau}\cdot|\mathcal{M}|^2 dPS \\
&= \frac{1}{2m_\tau}\; 32\; G_F^2\; p_2\cdot(p_\ell - m_\ell s_\ell)\; p_1\cdot(p_\tau - m_\tau s_\tau) \\
&\quad \frac{d^3\mathbf{p}_1}{(2\pi)^3 2E_1}\;\frac{d^3\mathbf{p}_2}{(2\pi)^3 2E_2}\;\frac{d^3\mathbf{p}_\ell}{(2\pi)^3 2E_\ell}\;(2\pi)^4\delta^4(-p_\tau + p_1 + p_2 + p_\ell) \; .
\end{aligned} \tag{2.33}$$

Integrating over the neutrinos,

$$d\Gamma = \frac{2\,G_F^2}{(2\pi)^5}\,\frac{1}{m_\tau E_\ell}\,(p_\ell - m_\ell s_\ell)^\alpha (p_\tau - m_\tau s_\tau)^\beta d^3\mathbf{p}_\ell\; I_{\alpha\beta}\;, \tag{2.34}$$

with the covariant integral:

$$I_{\alpha\beta} = \int p_{2\alpha}\;p_{1\beta}\frac{d^3\mathbf{p}_1}{E_1}\frac{d^3\mathbf{p}_2}{E_2}\delta^4(p_1 + p_2 - \overline{p_\tau - p_\ell})\;. \tag{2.35}$$

Using the result obtained in Appendix A.1, the differential transition probability can be written as:

$$\begin{aligned} d\Gamma &= \frac{2\,G_F^2}{(2\pi)^5}\,\frac{1}{m_\tau E_\ell}\,(p_\ell - m_\ell s_\ell)^\alpha (p_\tau - m_\tau s_\tau)^\beta d^3\mathbf{p}_\ell\;\frac{\pi}{6}\left[q^2 g_{\alpha\beta} + 2q_\alpha q_\beta\right] \\ &= \frac{\pi}{3}\frac{G_F^2}{(2\pi)^5}\,\frac{d^3\mathbf{p}_\ell}{m_\tau E_\ell}\left[q^2(p_\ell - m_\ell s_\ell)\cdot(p_\tau - m_\tau s_\tau) + 2(p_\tau - m_\tau s_\tau)\cdot q(p_\ell - m_\ell s_\ell)\cdot q\right]\;. \end{aligned} \tag{2.36}$$

In the rest frame of the parent tau lepton, the four-momentum vectors $p_\tau = (m_\tau, 0)$, $p_\ell = (E_\ell,\, \mathbf{p}_\ell)$, $q = (m_\tau - E_\ell, -\mathbf{p}_\ell)$, and the four-spin vector $s_\tau = (0, \hat{\mathbf{s}}_\tau\,)$, where $\hat{\mathbf{s}}$ is a unit vector denoting the three-spin in the tau rest frame. The daughter charged lepton's four-spin can be calculated using a Lorentz transformation to a new frame in which the lepton has a three-momentum $\mathbf{p}_\ell$, and

$$\begin{aligned} s_{\ell 0} &= \frac{\mathbf{p}_\ell\;\cdot\hat{\mathbf{s}}_\ell}{m_\ell} \\ \mathbf{s}_\ell &= \hat{\mathbf{s}}_\ell + \frac{\mathbf{p}_\ell\;\cdot\hat{\mathbf{s}}_\ell}{m_\ell(E_\ell + m_\ell)}\mathbf{p}_\ell\;. \end{aligned} \tag{2.37}$$

Making appropriate substitutions in Equation 2.36, the differential decay width:

$$\begin{aligned} d\Gamma &= \frac{\pi}{3}\frac{G_F^2}{(2\pi)^5}\,\frac{d^3\mathbf{p}_\ell}{m_\tau E_\ell}\Big\{(m_\tau^2 + E_\ell^2 - 2m_\tau E_\ell - \mathbf{p}_\ell{}^2) \\ &\quad[(E_\ell - \mathbf{p}_\ell\;\cdot\hat{\mathbf{s}}_\ell\;)m_\tau + m_\tau(\mathbf{p}_\ell\; - m_\ell\hat{\mathbf{s}}_\ell\; - frac\mathbf{p}_\ell\;\cdot\hat{\mathbf{s}}_\ell\,E_\ell + m_\ell\mathbf{p}_\ell\;)\cdot\hat{\mathbf{s}}_\tau\,] \\ &\quad+2(m_\tau^2 - m_\tau E_\ell - m_\tau\hat{\mathbf{s}}_\tau\;\cdot\mathbf{p}_\ell\;) \\ &\quad[(E_\ell - \mathbf{p}_\ell\;\cdot\hat{\mathbf{s}}_\ell\;)(m_\tau - E_\ell) + (\mathbf{p}_\ell\; - m_\ell\hat{\mathbf{s}}_\ell\; - \frac{\mathbf{p}_\ell\;\cdot\hat{\mathbf{s}}_\ell}{E_\ell + m_\ell}\mathbf{p}_\ell\;)\cdot\hat{\mathbf{s}}_\tau\,]\Big\}\;. \end{aligned} \tag{2.38}$$

Neglecting the daughter lepton's mass m_ℓ in the first approximation, $\mathbf{p}_\ell = E_\ell \, \hat{\mathbf{n}}$, where $\hat{\mathbf{n}}$ is a unit vector in the direction of the charged daughter lepton's motion in the tau rest frame. Now,

$$\begin{aligned} d\Gamma &= \frac{\pi}{3} \frac{G_F^2}{(2\pi)^5} \frac{d^3\mathbf{p}_\ell}{m_\tau E_\ell} \Big\{ (m_\tau^2 - 2m_\tau E_\ell) \left[E_\ell m_\tau (1 - \hat{\mathbf{n}} \cdot \hat{\mathbf{s}}_\ell) + m_\tau E_\ell \, \hat{\mathbf{n}} \cdot \hat{\mathbf{s}}_\tau (1 - \hat{\mathbf{n}} \cdot \hat{\mathbf{s}}_\ell) \right] \\ & +2(m_\tau^2 - m_\tau E_\ell - m_\tau \hat{\mathbf{n}} \cdot \hat{\mathbf{s}}_\tau) \Big[E_\ell (1 - \hat{\mathbf{n}} \cdot \hat{\mathbf{s}}_\ell)(m_\tau - E_\ell) + E_\ell^2 (1 - \hat{\mathbf{n}} \cdot \hat{\mathbf{s}}_\ell) \Big] \\ &= \frac{\pi}{3} \frac{G_F^2}{(2\pi)^5} \frac{d^3\mathbf{p}_\ell}{m_\tau E_\ell} \, m_\tau^2 E_\ell (1 - \hat{\mathbf{n}} \cdot \hat{\mathbf{s}}_\ell) \left[(3m_\tau - 4E_\ell) + (m_\tau - 4E_\ell) \hat{\mathbf{n}} \cdot \hat{\mathbf{s}}_\tau \right] \\ &= \frac{\pi G_F^2}{3(2\pi)^5 m_\tau} d\Omega_\ell \mathbf{p}_\ell \, dE_\ell \; E_\ell m_\tau^2 (1 - \hat{\mathbf{n}} \cdot \hat{\mathbf{s}}_\ell) \left[(3m_\tau - 4E_\ell) + (m_\tau - 4E_\ell) \hat{\mathbf{n}} \cdot \hat{\mathbf{s}}_\tau \right] . \end{aligned} \tag{2.39}$$

The maximum values for the charged daughter lepton's energy and momentum are obtained when the two neutrinos are emitted in one direction, and the lepton ℓ is emitted in the opposite direction:

$$E_{\ell,max} = \frac{m_\tau^2 + m_\ell^2}{2m_\tau} \qquad \text{and} \qquad |\mathbf{p}_{\ell,max}| = \frac{m_\tau^2 - m_\ell^2}{2m_\tau} . \tag{2.40}$$

For $m_\ell = 0$, the maximum lepton energy $E_{\ell,max} = m_\tau/2$, and defining $\varepsilon = E_\ell / E_{\ell,max}$, the entire lepton's energy range is spanned by the interval $0 < \varepsilon < 1$. Now, $E_\ell = \varepsilon \, m_\tau/2$, and choosing the tau spin axis along the $+z$ direction in polar coordinates, $\hat{\mathbf{n}} \cdot \hat{\mathbf{s}}_\tau = \cos\theta$. The differential decay rate can now be written as:

$$\Gamma = \frac{G_F^2 m_\tau^5}{192\pi^3} \left[2\varepsilon^2 (3 - 2\varepsilon) \right] \left[1 + \frac{1 - 2\varepsilon}{3 - 2\varepsilon} \cos\theta \right] \left[\frac{1 - \hat{\mathbf{n}} \cdot \hat{\mathbf{s}}_\ell}{2} \right] d\varepsilon \, \frac{\sin\theta d\theta d\phi}{4\pi} , \tag{2.41}$$

where $n(\varepsilon) = 2\varepsilon^2(3 - 2\varepsilon)$ is the normalized lepton energy spectrum with an energy dependence corresponding to a Michel parameter [25] $\rho = 3/4$. Since we do not measure any spins in this analysis, and since the net tau polarization at CLEO is zero, we can sum over the daughter lepton spin and average over the tau spin, to obtain:

$$d\Gamma = \frac{G_F^2 m_\tau^5}{192\pi^3} \left[2\varepsilon^2 (3 - 2\varepsilon) \right] d\varepsilon . \tag{2.42}$$

The final integration over the charged lepton momentum yields:

$$\Gamma(\tau^- \to e^-\bar{\nu}_e\nu_\tau\,) = \frac{G_F^2 m_\tau^5}{192\pi^3}\,. \tag{2.43}$$

For $\tau^- \to \mu^-\bar{\nu}_\mu\nu_\tau$, the lepton mass m_μ cannot be neglected and

$$\begin{aligned} \Gamma(\tau^- \to \mu^-\bar{\nu}_\mu\nu_\tau\,) &= \frac{G_F^2 m_\tau^5}{192\pi^3} \cdot F(m_\mu/m_\tau)\,, \\ \text{with} \quad F(x) &= 1 - 8x^2 + 8x^6 - x^8 - 24x^4 \ln x^2\,. \end{aligned} \tag{2.44}$$

The phase space factor [13], $F(x) = 0.9726$ for muons. Another factor $F(m_{\nu_\tau}/m_\tau)$, of the same functional form as $F(x)$, would apply in case of a heavy tau neutrino in $\tau \to \nu e\bar{\nu}$; for $\tau \to \nu\mu\bar{\nu}$ the factor is more complicated if both ν_τ and ν_μ are considered heavy. Since $m(\nu_e\,) \ll m(\nu_\tau\,)$, the present limit on the tau neutrino mass, $m(\nu_\tau\,) < 24$ MeV , implies that $1 - F(m_{\nu_\tau}/m_\tau) < 1.5 \times 10^{-3}$.

The non-local structure of the W propagator results in an additional multiplicative correction factor [26] given by:

$$F_W = \left(1 + \frac{3}{5}\frac{m_\tau^2}{m_W^2}\right) \approx 1.0003\ . \tag{2.45}$$

The QED radiative corrections to first order to this decay width are given by the multiplicative factor:

$$F_{rad} = 1 - \frac{\alpha(m_\tau)}{2\pi}\left(\pi^2 - \frac{25}{4}\right)\,, \tag{2.46}$$

and are calculated [27, 28] assuming the $(V - A)$ theory as a starting point. The diagrams which contribute to order α are shown in Figure 2.1. Radiative decays or bremsstrahlung (d, e) is very important for the low energy part of the spectrum, while the virtual photon diagrams (a, b, c) are relatively more important at higher energies.

The numerical values above are calculated using world average results [29] for all particle masses. The running coupling constant of QED [28] at the τ mass is $\alpha(m_\tau) = 1/133.29$ incorporating virtual photon corrections as well as the emission of

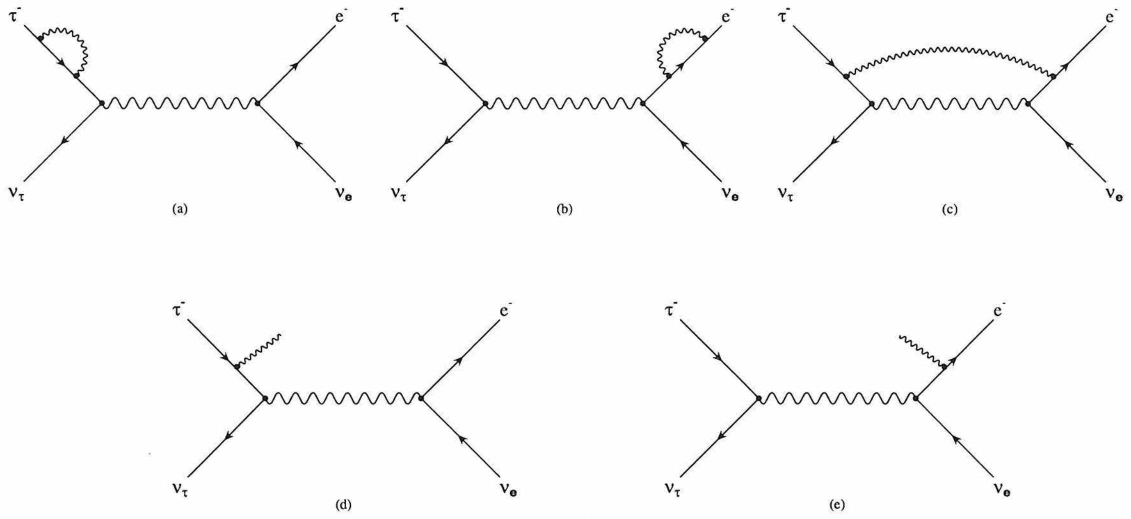

Figure 2.1: Lowest order radiative corrections.

real photons and light fermion pairs.

The differential transition probability can also be written in terms of the Dalitz [30] plot variables E_ℓ and $E_1 = E_{\bar{\nu}_\ell}$ as:

$$\begin{aligned} d\Gamma &= \frac{1}{m_\tau}|\mathcal{M}|^2 dPS_3 \ , \\ \text{where} \qquad dPS_3 &= \frac{1}{32\pi^3} dE_\ell dE_1 \ , \ \text{ and } \ |\mathcal{M}|^2 = 64\ G_F^2 (p_\tau \cdot p_1)(p_2 \cdot p_\ell) \ . \end{aligned} \tag{2.47}$$

In the tau rest frame,

$$\begin{aligned} p_\tau \cdot p_1 &= m_\tau E_1 \ , \\ p_2 \cdot p_\ell &= \frac{1}{2}(m_\tau^2 + m_1^2 - m_2^2 - m_\ell^2 - 2m_\tau E_1) \ , \end{aligned}$$

and assuming $m_1 = m_2 = m_\ell = 0$,

$$d\Gamma = \frac{G_F^2}{2\pi^3} m_\tau E_1 (m_\tau - 2E_1) dE_\ell dE_1 \ , \tag{2.48}$$

a parabola in E_1 with zeros at $E_1 = 0$ and $E_1 = E_1^{max} = m_\tau/2$.

Defining $\varepsilon = E/E_{max}$, where $E_\ell^{max} = E_1^{max} = m_\tau/2$, the differential decay rate:

$$d\Gamma = \frac{G_F^2 m_\tau^5}{16\pi^3}\varepsilon_1(1-\varepsilon_1)d\varepsilon_1 d\varepsilon_\ell \ , \tag{2.49}$$

and the decay rate:

$$\Gamma = \frac{G_F^2 m_\tau^5}{16\pi^3}\int_0^1 d\varepsilon_\ell \int_{1-\varepsilon_\ell}^1 d\varepsilon_1 \varepsilon_1(1-\varepsilon_1) \ , \tag{2.50}$$

where the limits of integration are calculated in Appendix A.2. Now, performing the integration over the anti-neutrino scaled energy ε_1, we get:

$$d\,\Gamma = \frac{G_F^2 m_\tau^5}{16\pi^3}\, d\varepsilon_\ell\, \frac{1}{6}\, \varepsilon_\ell^2(3-2\varepsilon_\ell) \ , \tag{2.51}$$

which is the famous $\rho = 3/4$ Michel spectrum for the Standard Model $(V-A)$ coupling. If the coupling were $(V+A)$ instead of $(V-A)$, the matrix element in Equation 2.47 would be replaced by:

$$|\mathcal{M}|^2 \ = \ 64\, G_F^2(p_\tau \cdot p_\ell)\,(p_1 \cdot p_2) \ = \ 32\, G_F^2 m_\tau^2 E_\ell[m_\tau - 2E_\ell] \ , \tag{2.52}$$

which results in a parabola in E_ℓ instead on E_1, as found before. The corresponding differential decay rate can be written as:

$$d\Gamma = \frac{G_F^2 m_\tau^5}{16\pi^3}\varepsilon_\ell(1-\varepsilon_\ell)d\varepsilon_1 d\varepsilon_\ell \ , \tag{2.53}$$

and the integration over ε_1 results in:

$$d\,\Gamma = \frac{G_F^2 m_\tau^5}{16\pi^3} d\varepsilon_\ell \varepsilon_\ell(1-\varepsilon_\ell)\int_{1-\varepsilon_\ell}^1 d\varepsilon_1 = \frac{G_F^2 m_\tau^5}{16\pi^3} d\varepsilon_\ell\, \varepsilon_\ell^2(1-\varepsilon_\ell) \ , \tag{2.54}$$

which corresponds to the $\rho = 0$, $(V+A)$ spectrum.

Figure 2.2 shows plots in the $E_\ell E_{\bar{\nu}_\ell}$ plane for both the $(V-A)$ (left) and the

$(V+A)$ couplings. The non-uniformity in the plot is directly proportional to $|\mathcal{M}|^2$.

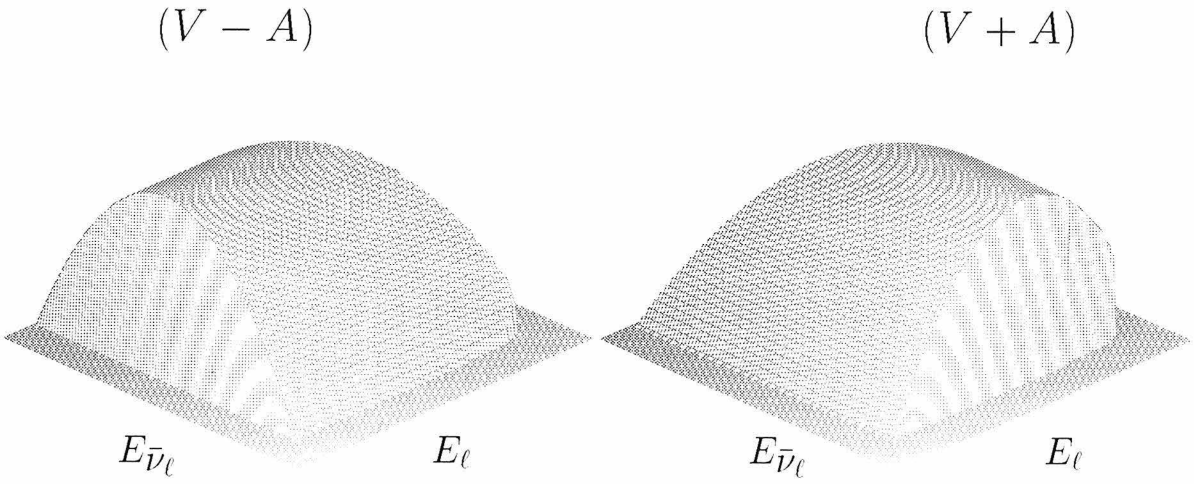

Figure 2.2: Dalitz plots for the three body final state $\tau^- \to \ell^- \overline{\nu}_\ell \nu_\tau$ assuming the $(V-A)$ (left) and the $(V+A)$ (right) interaction.

The final integration over the lepton ℓ scaled energy in both Equation 2.51 $(V-A)$ and Equation 2.54 $(V+A)$ results in the same decay rate obtained earlier in this section (Equation 2.43) independent of the type of coupling considered:

$$\Gamma = \frac{G_F^2 m_\tau^5}{192\pi^3} \ . \tag{2.55}$$

2.5 Michel Parameters

Instead of the Standard Model matrix element in Equation 2.29, one can use a more general matrix element for the decay $\tau^- \to \ell^- \bar{\nu}_\ell \nu_\tau$:

$$\mathcal{M} \ = \ \frac{G_F}{\sqrt{2}} \sum_{i=S,P,V,A,T} \bar{u}_\ell (C_i + C_i' \gamma^5) O_i v_1 \bar{u}_2 O_i u_\tau \tag{2.56}$$

where the O_i are the usual Dirac matrices shown in Table 2.4, and the index i runs through S, V, T, A and P. The 10 complex coupling constants (20 real parameters) C_i

and C_i' must be determined by experiment. However, the overall phase is arbitrary, and so 19 real parameters remain to be determined.

The matrix element in Equation 2.56 can now be written in the helicity projection form as:

$$\mathcal{M} = 4\frac{G_F}{\sqrt{2}} \sum_{\substack{i=S,V,T \\ \lambda_\ell,\lambda_\tau=R,L}} g^i_{\lambda_\ell\lambda_\tau} \bar{u}_\ell O_i v_1 \bar{u}_2 O_i u_\tau \tag{2.57}$$

where i labels the type of interaction: scalar, vector, tensor, and λ_ℓ, $\lambda_\tau = R, L$ indicate a right- or left- handed chirality of the daughter lepton and the parent tau respectively. The corresponding 10 complex parameters † $g^i_{\lambda_\ell\lambda_\tau}$ are linearly related to the C_i and C_i' parameters in Equation 2.56, and are to be determined by experiments.

The differential transition probability summed over the final charged lepton ℓ spin for the decay of the tau is now found to be:

$$\begin{aligned} d\Gamma = & \frac{G_F^2 m_\tau^5}{192\pi^3}\Bigg[\frac{1+h(x)}{1+4\eta(m_\ell/m_\tau)}\left(12(x-1)+\frac{4}{3}\rho(8x-6)+24\eta\frac{m_\ell}{m_\tau}\frac{(1-x)}{x}\right) \\ & +\xi\cos\theta\left(4(1-x)+\frac{4}{3}\delta(8x-6)+\frac{\alpha}{2\pi}\frac{g(x)}{x^2}\right)\Bigg]\frac{\sin\theta\, d\theta\, d\phi}{4\pi}x^2 dx \end{aligned} \tag{2.58}$$

where $x = E_\ell/E_{max}$ is the scaled lepton energy in the τ rest frame. The maximum kinematically allowed energy in the τ rest frame is given by $E_{max} = (m_\tau^2 + m_\ell^2)/2m_\tau$. The angle between the tau spin direction and the charged daughter lepton is denoted by θ, and $h(x)$ and $g(x)$ are radiative corrections to $\mathcal{O}(\alpha/\pi)$. The Michel parameters [25, 31] denoted by ρ, η, ξ and δ are combinations of the complex coupling constants $g^i_{\lambda_\ell\lambda_\tau}$ (or C_i and C_i') as shown later.

The terms in ρ and δ give zero when integrated over the whole spectrum and these quantities characterize the shape of the isotropic and anisotropic spectra at the high-energy end. The η parameter characterizes the low-end of the isotropic spectrum. The terms in ξ average out for unpolarized taus.

---

†The g^T_{RR} and g^T_{LL} couplings are not linearly independent of the other coupling constants and are excluded.

The Michel parameters can be written as:

$$
\begin{aligned}
\rho &= \frac{3}{4} - \frac{12}{A}\left[\left|g^V_{LR}\right|^2 + \left|g^V_{RL}\right|^2 + 2\left|g^T_{LR}\right|^2 + 2\left|g^T_{RL}\right|^2 + \Re\left(g^S_{LR}g^{T*}_{LR} + g^S_{RL}g^{T*}_{RL}\right)\right] \\
&= \frac{3}{4B}\Big[2|C_A|^2 + 2|C'_A|^2 + 2|C_V|^2 + 2|C'_V|^2 + 4\Re(C^*_A C_V + C'^*_A C'_V) \\
&\qquad\qquad + |C_P|^2 + |C'_P|^2 + |C_S|^2 + |C'_S|^2\Big] ,
\end{aligned}
$$

$$
\begin{aligned}
\eta &= \frac{8}{A}\Re\left(6g^V_{LR}g^{T*}_{LR} + 6g^V_{RL}g^{T*}_{RL} + g^S_{RR}g^{V*}_{LL} + g^S_{RL}g^{V*}_{LR} + g^S_{LR}g^{V*}_{RL} + g^S_{LL}g^{V*}_{RR}\right) \\
&= \frac{2}{B}\Re(C^*_P C_A - C'^*_P C'_A + C^*_S C_V - C'^*_S C'_V) ,
\end{aligned}
$$

$$
\begin{aligned}
\xi &= \frac{4}{A}\Big[\left|g^S_{RR}\right|^2 - \left|g^S_{LL}\right|^2 + \left|g^S_{LR}\right|^2 - \left|g^S_{RL}\right|^2 + 4\left(\left|g^V_{RR}\right|^2 - \left|g^V_{LL}\right|^2 + 3\left|g^V_{RL}\right|^2 - 3\left|g^V_{LR}\right|^2\right) \\
&\qquad -20\left(\left|g^T_{LR}\right|^2 - \left|g^T_{RL}\right|^2\right) + 16\,\Re\left(g^S_{RL}g^{*T}_{RL} - g_{LR}Sg^{*T}_{LR}\right)\Big] \\
&= \frac{2}{B}\Big[\Re(C^*_P C'_P + C^*_S C'_S) - 4\Re(C^*_A C'_A + C^*_V C'_V) + 8\Re(C^*_A C'_V + C^*_V C'_A)\Big] ,
\end{aligned}
$$

$$
\begin{aligned}
\xi\delta &= \frac{3}{A}\Big[\left(\left|g^S_{RR}\right|^2 - \left|g^S_{LL}\right|^2 + \left|g^S_{LR}\right|^2 - \left|g^S_{RL}\right|^2\right) + 4\left(\left|g^V_{RR}\right|^2 - \left|g^V_{LL}\right|^2\right) \\
&\quad -4\left(\left|g^T_{RL}\right|^2 - \left|g^T_{LR}\right|^2\right) + 4\,\Re\left(g^S_{RL}g^{*T}_{RL} - g_{LR}Sg^{*T}_{LR}\right)\Big] \\
&= \frac{3}{2B}\Big[\Re(C^*_P C'_P + C^*_S C'_S) + 2\Re(C^*_A C'_A + C^*_V C'_V) + 2\Re(C^*_A C'_V + C^*_V C'_A)\Big] ,
\end{aligned}
$$

with

$$
\begin{aligned}
A &= 4\left(\left|g^S_{RR}\right|^2 + \left|g^S_{LR}\right|^2 + \left|g^S_{RL}\right|^2 + \left|g^S_{LL}\right|^2\right) + 16\left(\left|g^V_{RR}\right|^2 + \left|g^V_{LR}\right|^2 + \left|g^V_{RL}\right|^2 + \left|g^V_{LL}\right|^2\right) \\
&\qquad +48\left(\left|g^T_{RL}\right|^2 + \left|g^T_{LR}\right|^2\right)
\end{aligned}
$$

and

$$
\begin{aligned}
B &= |C_S|^2 + |C'_S|^2 + |C_P|^2 + |C'_P|^2 + 4|C_V|^2 + 4|C'_V|^2 + 4|C_A|^2 + 4|C'_A|^2 \\
&\qquad +6|C_T|^2 + 6|C'_T|^2 .
\end{aligned}
\tag{2.59}
$$

Redefining the coupling constant G_F allows one to choose the normalization parameter: $A \equiv B \equiv 16$. The Fermi Coupling constant is now given by [32]:

$$G_F^2 = \frac{1}{\tau_\ell} \frac{192\pi^3}{m_\ell^5} \frac{1}{1 + 4\eta \, m_{\ell'}/m_\ell} , \tag{2.60}$$

where τ_ℓ is the lifetime of the mother lepton ℓ, m_ℓ, its mass and $m_{\ell'}$, the mass of the charged daughter lepton. η is the low energy spectrum parameter and is important in the muonic decay of the τ. Higher order corrections have been neglected here.

In the Standard Model, the weak interaction proceeds via the $(V-A)$ coupling, so that the only non-zero coupling constant is $g_{LL}^V = 1$ (or $C_A = C_V = 1, C'_A = C'_V = -1$ and all others zero). Thus, substituting in Equation 2.59, we find the Standard Model Michel parameters are:

$$\rho = \frac{3}{4} , \quad \eta = 0 , \quad \xi = -1 , \quad \xi\delta = -\frac{3}{4} , \quad \text{and} \quad A = B = 16 .$$

Now, substituting these values for the Michel parameters in Equation 2.58, we find that this equation reduces to the original transition probability expression in Equation 2.41.

Integrating Equation 2.58, and including the leading order corrections, the width can be written as:

$$\begin{aligned} \Gamma_\ell &= \frac{G_F^2 m_\tau^5}{192\pi^3} \left[1 - 8\frac{m_\ell^2}{m_\tau^2} - 8\frac{m_{\nu_\tau}^2}{m_\tau^2} + 4\eta\frac{m_\ell}{m_\tau} + 4\lambda\frac{m_{\nu_\tau}}{m_\tau} + 8\sigma\frac{m_\ell m_{\nu_\tau}}{m_\tau^2} + \frac{3}{5}\frac{m_\tau^2}{m_W^2} \right. \\ &\qquad \left. - \frac{\alpha(m_\tau)}{2\pi}\left(\pi^2 - \frac{25}{4}\right) \right] \end{aligned} \tag{2.61}$$

where η is one of the Michel parameters defined above, and

$$\begin{aligned} \lambda &= \frac{1}{2}\Re\left[g_{RR}^S g_{LR}^{S*} + g_{RR}^S g_{RL}^{S*} - 2 g_{LL}^V g_{LR}^{V*} - 2 g_{RR}^V g_{RL}^{V*} \right] \\ \sigma &= \frac{1}{2}\Re\left[-6 g_{LL}^V g_{RL}^{T*} - 6 g_{LL}^V g_{LR}^{T*} + g_{RR}^S g_{LR}^{V*} + g_{RL}^S g_{LL}^{V*} + g_{LR}^S g_{RR}^{V*} + g_{LL}^S g_{RL}^{V*} \right] . \end{aligned} \tag{2.62}$$

Neglecting neutrino masses and higher order terms in Equation 2.61, we find that the ratio of leptonic branching ratios:

$$\frac{\mathcal{B}_\mu}{\mathcal{B}_e} = \frac{f(x_\mu)}{[1+4\eta(m_\mu/m_\tau)]}\left(\frac{g_\mu}{g_e}\right)^2, \tag{2.63}$$

where $f(x_\mu) = 0.9726$, and $g_\mu/g_e = 1.0012 \pm 0.0016$, can also be used to measure the η parameter.

Table 2.5 lists other possible values of the Michel parameters. We note that the parameter value depends on the product of the couplings at the two vertices in the interaction. In this thesis, we can use the available experimental information about the daughter ℓ vertex to infer information about the τ vertex. The coupling at the ℓ vertex is known to be $(V-A)$ to a precision that is more than an order of magnitude better than the corresponding precision on the τ vertex couplings (see Table 2.6).

Coupling		Parameters			
$\tau \times \ell$		ρ	η	ξ	$\xi\delta$
$(V-A)\times(V-A)$	LL	$3/4$	0	-1	$-3/4$
$(V+A)\times(V+A)$	RR	$3/4$	0	$+1$	$+3/4$
$V\times V$		$3/8$	0	0	0
$A\times A$		$3/8$	0	0	0
$(V-A)\times(V+A)$	LR	0	0	-3	0
$(V+A)\times(V-A)$	RL	0	0	$+3$	0
$V\times(V-A)$		$3/8$	0	-2	$-3/8$
$A\times(V-A)$		$3/8$	0	$+2$	$+3/8$
$(V-rA)\times(V-rA)$		$\frac{3}{8}\left[1+\left(\frac{2r}{1+r^2}\right)^2\right]$	0	$-\frac{2r}{1+r^2}$	$3\xi/4$
$(V-A)\times(V-A)\ldots$					
$\ldots+\varepsilon^2\ (V+A)\times(V+A)$		$3/4$	0	$2\varepsilon^2$-1	$3\xi/4$
$\ldots+\varepsilon^2\ (S-P)\times(S-P)$	LL	$3/4$	0	-1	$+3/4$
$\ldots+\varepsilon^2\ (S+P)\times(S+P)$		$3/4$	$\Re\varepsilon/2$	$\varepsilon^2/2-1$	$3\xi/4$
$\ldots+\varepsilon^2\ S\times S$		$3/4$	$\Re\varepsilon/8$	$\varepsilon^2/16-1$	$3\xi/4$
$\ldots+\varepsilon^2\ T\times T$		$\frac{3}{4}(1-2\varepsilon^2)$	0	$-1+f\varepsilon^2$	$-\frac{3}{4}(1-2\varepsilon^2)$

Table 2.5: Michel parameter predictions for different couplings. For entries with admixtures we assume $\varepsilon \ll 1$. The f in the $T\times T$ admixture term is $f = +8, +3, -2$ for $LR, (LR+RL), RL$.

If $\rho = 3/4$ (see Equation 2.59), we can exclude the mixing of right-handed and left-handed currents (g^V_{RL} and g^V_{LR}) if there are no simultaneous scalar and tensor couplings. However, $V + A$ cannot be excluded, and the pure right-handed coupling, g^V_{RR}, is always possible. Such interactions are expected to be mediated by a heavy right-handed W_R boson which exists in some simple extensions of the Standard Model and are briefly described in Section 2.7.

A non-zero η measurement shows there are at least two different couplings with opposite chiralities for the charged leptons which would result in parity violation. If we now assume $(V - A)$ (g^V_{LL}) to be dominant, then the second coupling would be a Higgs type coupling g^S_{RR} with the right-handed tau and daughter lepton (see Equation 2.59). The presence of this scalar coupling would result in an interference between the amplitude mediated by the Standard Model W boson and the new scalar boson. The effects of this interference would be seen in the differential decay rate of the leptonic tau decay and the low energy part of the momentum spectrum of the charged daughter lepton. The change in the low energy spectrum is parameterized by a non-zero measurement of the η parameter.

Table 2.6 lists the current status of measurements of the Michel parameters in both the muon and tau sectors. All the tau sector measurements shown here assume lepton universality in the vector-like couplings.

Experiment	Parameter	Value	Standard Model
		τ Decays	
ARGUS [33]	ρ	$0.732 \pm 0.034 \pm 0.020$	0.75
ALEPH [34]		$0.751 \pm 0.039 \pm 0.027$	
L3 [35]		$0.794 \pm 0.039 \pm 0.031$	
SLD [36]		$0.71 \pm 0.09 \pm 0.05$	
average [37]		0.742 ± 0.027	
ARGUS [9]	η	$0.03 \pm 0.18 \pm 0.12$	0
ALEPH [34]		$-0.04 \pm 0.15 \pm 0.10$	
L3 [35]		$0.25 \pm 0.17 \pm 0.11$	
average [37]		-0.01 ± 0.14	
ARGUS [33]	ξ	$0.98 \pm 0.11 \pm 0.05$	1
ALEPH [34]		$1.18 \pm 0.15 \pm 0.08$	
L3 [35]		$0.94 \pm 0.21 \pm 0.07$	
SLD [36]		$1.03 \pm 0.36 \pm 0.05$	
average [37]		1.03 ± 0.12	
ARGUS [33]	$\xi\delta$	$0.65 \pm 0.10 \pm 0.05$	0.75
ALEPH [34]		$0.88 \pm 0.11 \pm 0.07$	
L3 [35]		$0.81 \pm 0.14 \pm 0.06$	
SLD [36]		$0.84 \pm 0.27 \pm 0.05$	
average [37]		0.76 ± 0.11	
		μ Decays	
average [38]	ρ	0.7518 ± 0.0026	0.75
average [38]	η	-0.007 ± 0.013	0
average [38]	ξ	1.003 ± 0.008	1
average [38]	δ	0.749 ± 0.004	0.75

Table 2.6: Current status of measurements of the Michel parameters.

2.6 Helicity Basis Probabilities

In order to determine the coupling constants $g^i_{\lambda_\ell \lambda_\tau}$ uniquely from experimental measurements, it is convenient to introduce [39] the probabilities $Q_{\lambda_\ell \lambda_\tau}$ ($\lambda_\ell, \lambda_\tau = R, L$) for the decay of a λ_τ-handed tau into an λ_ℓ-handed daughter lepton ℓ [‡]. These probabilities are given in terms of the coupling constants by:

$$Q_{\lambda_\ell \lambda_\tau} = \frac{1}{4}|g^S_{\lambda_\ell \lambda_\tau}|^2 + |g^V_{\lambda_\ell \lambda_\tau}|^2 + 3(1-\delta_{\lambda_\ell \lambda_\tau})|g^T_{\lambda_\ell \lambda_\tau}|^2 , \qquad (2.64)$$

where $\delta_{\lambda_\ell \lambda_\tau} = 1$ for $\lambda_\ell = \lambda_\tau$ and $\delta_{\lambda_\ell \lambda_\tau} = 0$ for $\lambda_\ell \neq \lambda_\tau$. These probabilities are related to the Michel parameters ρ, η, ξ, and δ as shown below:

$$\begin{aligned}
Q_{LL} &= \frac{1}{4}\left(-3 + \frac{16}{3}\rho - \frac{1}{3}\xi + \frac{16}{9}\xi\delta + \xi' + \xi''\right) \\
Q_{RR} &= \frac{1}{4}\left(-3 + \frac{16}{3}\rho + \frac{1}{3}\xi - \frac{16}{9}\xi\delta - \xi' + \xi''\right) \\
Q_{LR} &= \frac{1}{4}\left(5 - \frac{16}{3}\rho + \frac{1}{3}\xi - \frac{16}{9}\xi\delta + \xi' - \xi''\right) \\
Q_{RL} &= \frac{1}{4}\left(5 - \frac{16}{3}\rho - \frac{1}{3}\xi + \frac{16}{9}\xi\delta - \xi' - \xi''\right) \qquad (2.65)
\end{aligned}$$

where the parameters ξ' (longitudinal polarization of the daughter lepton), and ξ'' (angular dependence of the longitudinal polarization) have not been measured in τ decays. In the Standard Model $\xi' = \xi'' = 1$. Now, defining P^τ_R as the probability that a right-handed tau lepton decays into a daughter charged lepton ℓ, and P^ℓ_R as the probability that the tau lepton decays into a right-handed daughter charged lepton ℓ, we get:

$$\begin{aligned}
P^\tau_R &= Q_{RR} + Q_{LR} = \frac{1}{4}|g^S_{RR}|^2 + \frac{1}{4}|g^S_{LR}|^2 + |g^V_{RR}|^2 + |g^V_{LR}|^2 + 3|g^T_{LR}|^2 \\
&= \frac{1}{2}\left[1 + \frac{1}{9}(3\xi - 16\xi\delta)\right] \quad \text{and} \\
P^\ell_R &= Q_{RR} + Q_{RL} = \frac{1}{4}|g^S_{RR}|^2 + \frac{1}{4}|g^S_{RL}|^2 + |g^V_{RR}|^2 + |g^V_{RL}|^2 + 3|g^T_{RL}|^2
\end{aligned}$$

[‡] The corresponding parameters in muon decay can be obtained by replacing the τ by the μ, and by replacing the daughter lepton ℓ by the e in this entire section.

$$= \frac{1}{2}(1 - \xi') \ . \qquad (2.66)$$

For μ decay, where precise measurements of the polarizations of both the daughter and the parent lepton have been performed, there exist upper bounds on Q_{RR}, Q_{LR} and Q_{RL}, and a lower bound on Q_{LL}. These bounds imply corresponding bounds on the 8 couplings, $|g^n_{RR}|$, $|g^n_{RL}|$ and $|g^n_{LR}|$, where n includes S, V, and T[§] couplings. It is not possible to deduce an upper limit for $|g^V_{LL}|$ from normal muon decay without detecting the neutrinos. One cannot tell if

$$g^S_{LL} = 0, \ \ g^V_{LL} = 1 \quad \text{or} \quad g^S_{LL} = 2, \ \ g^V_{LL} = 0 \ . \qquad (2.67)$$

A measurement of the cross section of the inverse muon decay $\nu_\mu e^- \to \mu^- \nu_e$ [40, 39] normalized to the $(V - A)$ prediction can be used to resolve this ambiguity. This normalized cross section S can be written as:

$$\begin{aligned} S \ &= \ \frac{1}{2}(1-h)\left(|g^V_{LL}|^2 + \frac{3}{8}|g^V_{RL}|^2 + \frac{3}{32}|g^S_{LR} - \frac{10}{3}g^T_{LR}|^2 + \frac{3}{32}|g^S_{RR}|^2 + \frac{4}{3}|g^T_{LR}|^2\right) \\ &+ \ \frac{1}{2}(1+h)\left(|g^V_{RR}|^2 + \frac{3}{8}|g^V_{LR}|^2 + \frac{3}{32}|g^S_{RL} - \frac{10}{3}g^T_{RL}|^2 + \frac{3}{32}|g^S_{LL}|^2 + \frac{4}{3}|g^T_{RL}|^2\right) \ , \end{aligned} \qquad (2.68)$$

where h is the helicity of the ν_μ, and is known very precisely from pion decay experiments: $h = -1$ [41]. Thus S gives information about five coupling constants (g^V_{LL}, g^V_{RL}, g^S_{LR}, g^T_{LR}, and g^S_{RR}), all of which couple to the left-handed ν_μ. The influence of four of these constants on S is found to be negligible with the upper limits derived from normal muon decay. One now obtains

$$S = |g^V_{LL}|^2 \ , \qquad (2.69)$$

[§] $|g^T_{RR}|$ is excluded since it is not linearly independent.

which yields a lower limit for g^V_{LL}, and through the normalization requirement, one gets an upper limit for the remaining g^S_{LL}:

$$|g^S_{LL}|^2 \leq 4(1-S)\ . \tag{2.70}$$

Thus the weak interaction can be completely determined in muon decay using the normal and inverse decay.

The present 90% confidence level bounds on the couplings in the muon sector are shown in Figure 2.3. The outer circles display the mathematical limits for the $g^i_{\lambda_e \lambda_\mu}$ in the complex plane, the inner circles show the areas still allowed by experiments. For g^V_{LL}, which has been chosen to be real, one gets the small line close to $g^V_{LL} = 1$. These limits confirm that the bulk of the μ decay transition amplitudes are consistent with the Standard Model $(V-A)$ type.

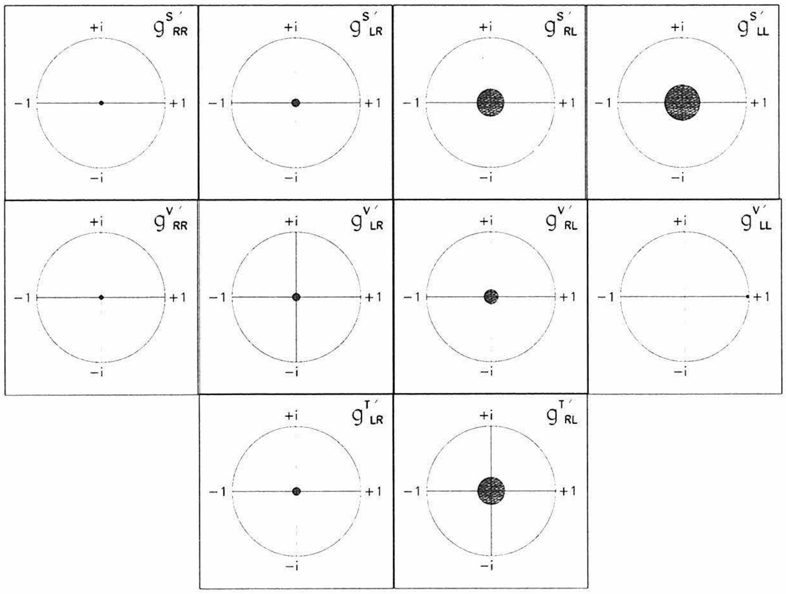

Figure 2.3: 90% confidence level experimental limits for the normalized μ-decay couplings $g^{n'}_{\lambda_e \lambda_\mu} \equiv g^n_{\lambda_e \lambda_\mu}/N^n$, where $N^n \equiv \max(|g^n_{\lambda_e \lambda_\mu}|) = 2,\ 1,\ 1/\sqrt{3}$ for $n = S,\ V,\ T$.

The experimental analysis in the tau lepton sector is necessarily different from the one applied to the muon sector, because of the much shorter tau lifetime. Effects of a finite tau neutrino mass m_{ν_τ} on the couplings $g^i_{\lambda_\ell \lambda_\tau}$ are $m^2_{\nu_\tau}/m^2_\tau$ [42]. With the present experimental limit of 24 MeV$/c^2$, any possible effect is $\leq 0.2 \times 10^{-3}$.

The polarization dependent Michel parameters ξ and δ in muon decays are measured using measurements of the decay asymmetry of the positrons from muon decay. This asymmetry is measured by stopping polarized muons and detecting the decay positrons as a function of the emission angle relative to the muon polarization. In tau decays at CESR energies (far below the Z^0), it is not possible, at present, to prepare polarized tau leptons, thus rendering the above mentioned analysis impossible. One can, however, get information about the tau spin polarization by making use of the spin correlation of the two tau leptons [13]. These spin correlations have now been exploited by several experiments (ARGUS [33], L3 [35], and CLEO [44]) to measure the polarization dependent Michel parameters in tau decays. Another possibility is to use the polarization in production (and decay) at the Z^0 resonance (LEP), enhanced when the electron beam is polarized (SLC).

The Michel parameters ξ' and ξ'' require a measurement of the polarization of the charged daughter lepton emitted in the tau decay. This polarization has never been measured. In principle, this could be done for the $\tau^- \rightarrow \mu^- \overline{\nu}_\mu \nu_\tau$ decay by stopping the muons and detecting their decay products [43].

As explained earlier, one requires either the measurement of the inverse decay $\nu_\tau \ell^- \rightarrow \tau^- \bar{\nu}_e$, or the measurement of the correlations between one of the neutrinos and the μ^- or τ^- for the muonic decay to distinguish between the g^S_{LL} and the g^V_{LL} couplings. Neither of these measurements exist to-date, and thus the limits on the relevant couplings in the tau sector are much weaker than the corresponding limits in the muon sector.

The present 90% confidence level bounds on the couplings in the tau sector are shown in Figure 2.4. The outer circles display the mathematical limits for the $g^{i}_{\lambda_\ell \lambda_\tau}$ in the complex plane, and the inner circles show the areas still allowed by experiments. We note that these limits are much weaker, but consistent with the corresponding limits obtained in the muon sector.

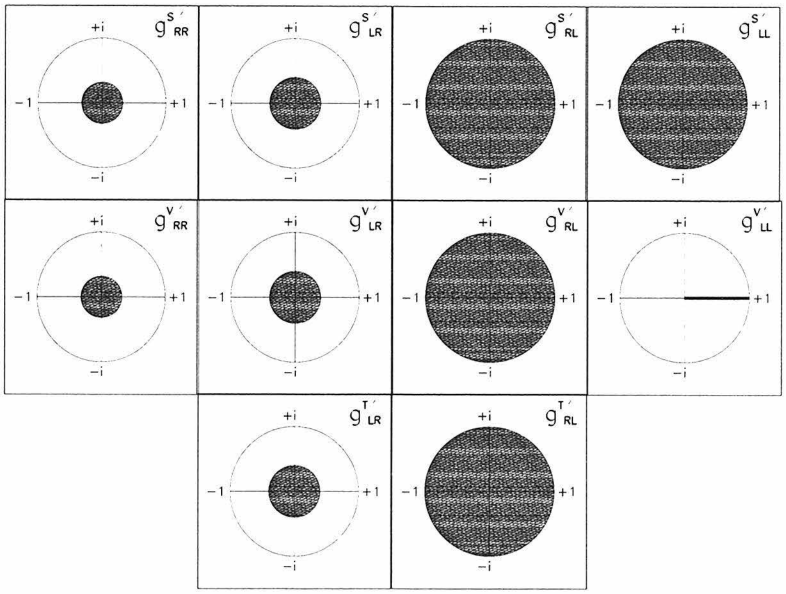

Figure 2.4: 90% confidence level experimental limits for the normalized τ-decay couplings $g^{n'}_{\lambda_\ell \lambda_\tau} \equiv g^{n}_{\lambda_\ell \lambda_\tau}/N^n$, where $N^n \equiv \max(|g^{n}_{\lambda_\ell \lambda_\tau}|) = 2, 1, 1/\sqrt{3}$ for $n = S, V, T$. The Particle Data Group [37] world average results for the Michel parameters are used to calculate these limits.

In this thesis, we do not exploit the afore-mentioned spin correlations. Since the beams are unpolarized, and left- and right-handed tau leptons are produced in equal amounts at CLEO beam energies, there is no net polarization (in contrast to LEP, where there is net polarization at the Z^0 pole). The $\cos\theta$ term in Equation 2.58 averages to zero, and one is sensitive only to the spectral shape Michel parameters, ρ and η. The allowed range for the parameters ρ and η is shown in Figure 2.5. The solid lines enclose the allowed region in parameter space; the dotted lines enclose the allowed region when we assume that there are no tensor couplings. We note that a measurement of $\rho > 3/4$ indicates the presence of tensor couplings.

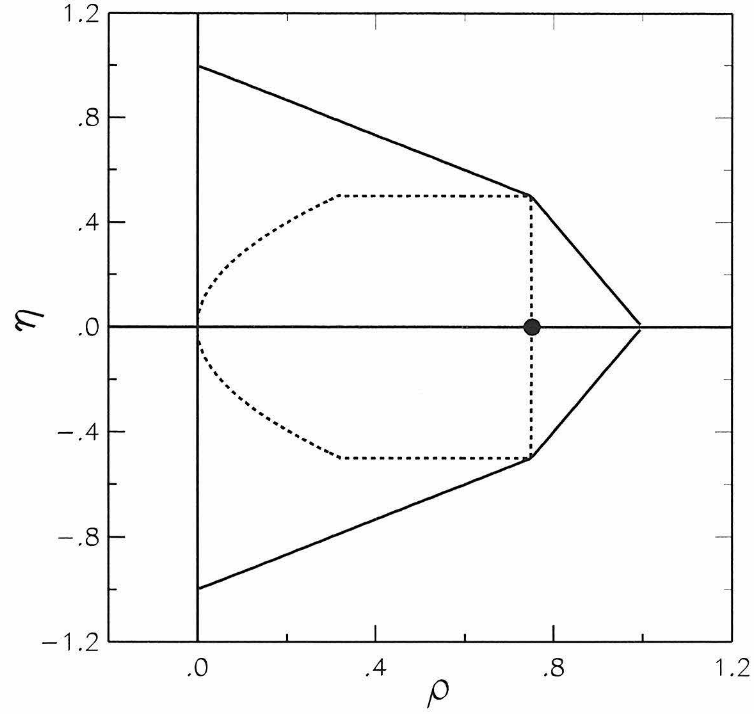

Figure 2.5: Limits for the Michel parameters ρ and η are defined by the solid lines. The dotted line encloses the allowed region in the absence of tensor couplings. The Standard Model prediction is denoted by the dot.

The asymmetry parameters ξ and δ are not measured in this thesis. These parameters can be measured at CLEO by exploiting the correlations between the spins of the two tau leptons. The decay of one tau in the event is used as a spin analyzer, from which one can infer information on the spin direction of the other tau. The details of this CLEO analysis to measure the asymmetry parameters are discussed in reference [44].

2.7 Beyond the Standard Model

The study of the tau lepton provides a particularly clean laboratory in the hunt for new physics beyond the Standard Model. Strong interaction effects are absent in the leptonic tau decays studied in this thesis. In this section, we briefly describe some of the physics beyond the Standard Model, and a precise measurement of the Michel parameters can be used to constrain this new physics.

2.7.1 Charged Higgs

Comparing Figures 2.3 and 2.4, we find that the limits on non-standard couplings obtained from the tau Michel parameters leave large holes in which new physics might hide. Tau results become much more interesting if specific models are considered. Examples of such models are those which predict the presence of charged Higgs bosons leading to mass dependent scalar couplings [45].

One possible scalar candidate is the scalar charged Higgs of the Two Higgs Doublet Model [46]. In this model, the Michel parameter η is related to the mass of the charged Higgs:

$$\eta = -\frac{m_\tau m_\mu tan^2\beta}{2m_H^2}, \tag{2.71}$$

where β is the ratio of the vacuum expectation value of the neutral components of the two Higgs doublets and m_H denotes the mass of the charged Higgs which mediates the decay. Since the charged Higgs is a scalar particle, this effect corresponds to the spin flip of the daughter charged lepton; the effect scales with the mass of the daughter lepton and is strongly suppressed in the electron spectrum.

2.7.2 Right-Handed W' Bosons

The presence of a W' boson [47] which couples to right-handed fermions would result in the mixing of mass eigen states

$$\begin{aligned} W_1 &= W_L \cos\zeta - W'_R \sin\zeta \\ W_2 &= W_L \sin\zeta - W'_R \cos\zeta \end{aligned}$$

thus distorting the daughter lepton spectrum, resulting in the Michel parameters:

$$\begin{aligned} \rho &= \frac{3}{8}\frac{(m_1^2+m_2^2)^2+(m_1^2-m_2^2)^2\cos^2 2\zeta}{m_1^4+m_2^4} \\ \xi &= \frac{m_1^4-m_2^4}{m_1^4+m_2^4}\cos 2\zeta \end{aligned} \tag{2.72}$$

where m_1 and m_2 are the masses of the W_1 and W_2 bosons respectively, and ζ is the mixing angle between the W_L and W_R states.

2.7.3 Anomalous Electric and Magnetic Couplings

Constraints on the universality of the charged and neutral current interactions, as well as the shape of the daughter electron and muon energy spectrum, provide the strongest bounds on anomalous, CP conserving, $\tau\nu W$ dipole moment type couplings. The presence of non-zero anomalous couplings produces a distortion in the final state charged lepton spectrum which in general cannot be expressed as shifts in the Michel parameters. The Michel spectrum assumes the absence of derivative couplings which arise as a result of anomalous moments.

To lowest order, the normalized lepton energy spectrum in the tau rest frame can be written as [48]:

$$\frac{1}{\Gamma}\frac{d\Gamma}{dx} = x^2[6-4x+\kappa(4x-3)]\ , \tag{2.73}$$

where κ corresponds to the anomalous dipole complex form factor, and $x = E_\ell/E_{max}$

with $E_{max} = (m_\tau^2 + m_\ell^2)/2m_\tau$. Comparing with the conventional Michel spectrum (ignore polarization terms in Equation 2.58), we see that the effect of κ on the normalized spectrum to this order is the same as $8\delta\rho/3$. Using the current world average value $\delta\rho = \rho - 0.750 = -0.021 \pm 0.027$ [37], we obtain $\kappa = -0.021 \pm 0.072$. A more precise measurement of the ρ parameter in this analysis should improve this constraint on κ.

2.7.4 Massive Neutrinos

The presence of a massive Dirac neutrino would permit right-handed couplings and would thus result in changes to the Michel parameters. The ρ parameter would be slightly less than 3/4 [49]. Mixing between this new massive neutrino and the tau neutrino would also distort the spectrum in a manner not characterized by the Michel parameters.

Chapter 3 The CLEO Experiment at CESR

In this chapter, we provide a description of the apparatus that was used to generate (CESR) and collect (CLEO) the sample of leptonic tau decays used to determine the Michel parameters measured in this thesis. We also provide details about the Monte Carlo simulation packages used to simulate the processes studied.

3.1 CESR

The Cornell electron storage ring CESR serves both the CLEO experiment and the Cornell high energy synchrotron source CHESS. The former studies the electron positron collisions while the latter focuses the synchrotron radiation emitted by the beams to study a variety of topics. CESR is located inside a 768 m circumference tunnel approximately 10 meters underground. The tunnel, on the Cornell University campus in Ithaca, New York, collides electrons against positrons with center of mass energies in the range of 9 to 12 GeV , the region of the Υ resonances.

The main components of CESR are shown schematically in Figure 3.1. Electrons are stripped from a metal cathode plate and accelerated by high voltage fields inside an electron "gun" producing a high intensity electron beam. The positrons are produced by directing 50 MeV energy electrons on to a thin tungsten target. This leads to the QED pair production reaction: $(e^- + \text{nucleus}) \rightarrow (e^+e^-\ e^-\text{nucleus})$.

These particles are injected into the linear accelerator (LINAC), which boosts their energy to approximately 150 MeV . Next, the particles are transferred to the 768 m circumference synchrotron, located along the inner tunnel wall. Magnets separate the electrons and positrons, and the electrons (positrons) travel in counterclockwise (clockwise) circular orbits in a vacuum chamber. A periodic arrangement of dipole, quadrupole, and sextapole magnets keep them in orbit, confined within small well defined bunches in the x and y dimensions. In less than 8 ms (corresponding to less

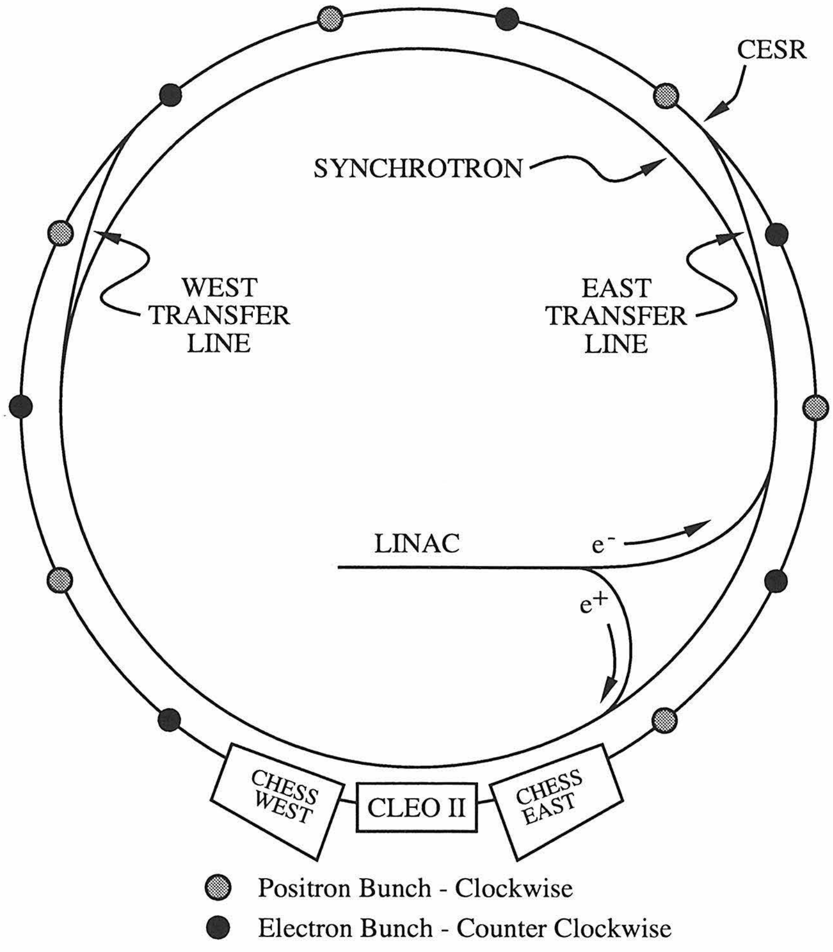

Figure 3.1: A schematic view of the Cornell Electron Storage Ring, CESR.

than 3200 revolutions), the particles reach an energy of 5.3 GeV . The acceleration is achieved by four 2 m long radio frequency (RF) cavities.

Electrons (positrons) are then transferred into the storage ring through the east (west) transfer lines into one of seven different bunches *, evenly spaced about in the ring. The counter rotating bunches of electrons and positrons are kept apart by a series of electrostatic separators to prevent collisions at all but one point in the ring. This is achieved by deflecting the beams horizontally in a novel beam orbit known as the pretzel orbit. Thus parasitic collisions are prevented, to ensure a long beam life

---

*The present configuration utilizes 9×2 bunches.

time.

The particles lose about 1 MeV energy per orbit due to synchrotron radiation. This lost energy is replaced by 500 MHz RF cavities putting out 500 KW. The extremely good vacuum (10^{-8} Torr) in the storage ring, along with the optics configuration, allow stored beams to be maintained for several hours.

The electron and positron beams are focused at the interaction point by a series of strong quadrupole magnets. The final set of quadrupole focusing magnets are permanent sumerium cobalt magnets that surround the beam pipe part of the way inside the CLEO II detector. The beams are focused to a small cross section: $\sigma_x \sim 10\ \mu\text{m}$ (vertical), $\sigma_y \sim 100\ \mu\text{m}$ (horizontally), and $\sigma_z \sim 1$ cm (length). The small cross section is essential for increasing the particle flux at the interaction point, thus increasing the rate of e^+e^- collisions.

The rate at which the electrons and positrons collide is the product of the instantaneous luminosity of the machine times the cross section. The instantaneous luminosity of the collider is given by

$$\mathcal{L} = \frac{N_1 N_2 f n}{A}, \tag{3.1}$$

where N_1 and N_2 are the number of particles per bunch, n is the number of bunches, f is the revolution frequency per bunch, and A is the cross sectional area of the region where the bunches cross. Each bunch is comprised of $N_1 \simeq N_2 \simeq 10^{11}$ particles and there are $n = 7$ bunches. The revolution frequency, $f \sim 400$ kHz and $A = 4\pi\sigma_x\sigma_y = 1.25 \times 10^{-4}\ \text{cm}^2$, resulting in a typical luminosity of $2.25 \times 10^{32}\ \text{cm}^{-2}\ \text{sec}^{-1}$ (now higher). CESR is currently the world's highest luminosity collider.

3.2 The CLEO Detector

CLEO II is a general purpose solenoidal magnet spectrometer and calorimeter with excellent particle and shower energy detection capabilities. The original CLEO detector was completed in 1979 and started recording data that year. A series of upgrades including improved time of flight detectors, muon detectors, and vastly improved electromagnetic calorimetry over the next 10 years resulted in the CLEO II detector which began operating in 1989. The upgraded detector, designed for optimum performance near the $\Upsilon(4S)$ resonance (center of mass energy of 10.58 GeV) is shown in Figures 3.2 and 3.3 and is described in detail in [50].

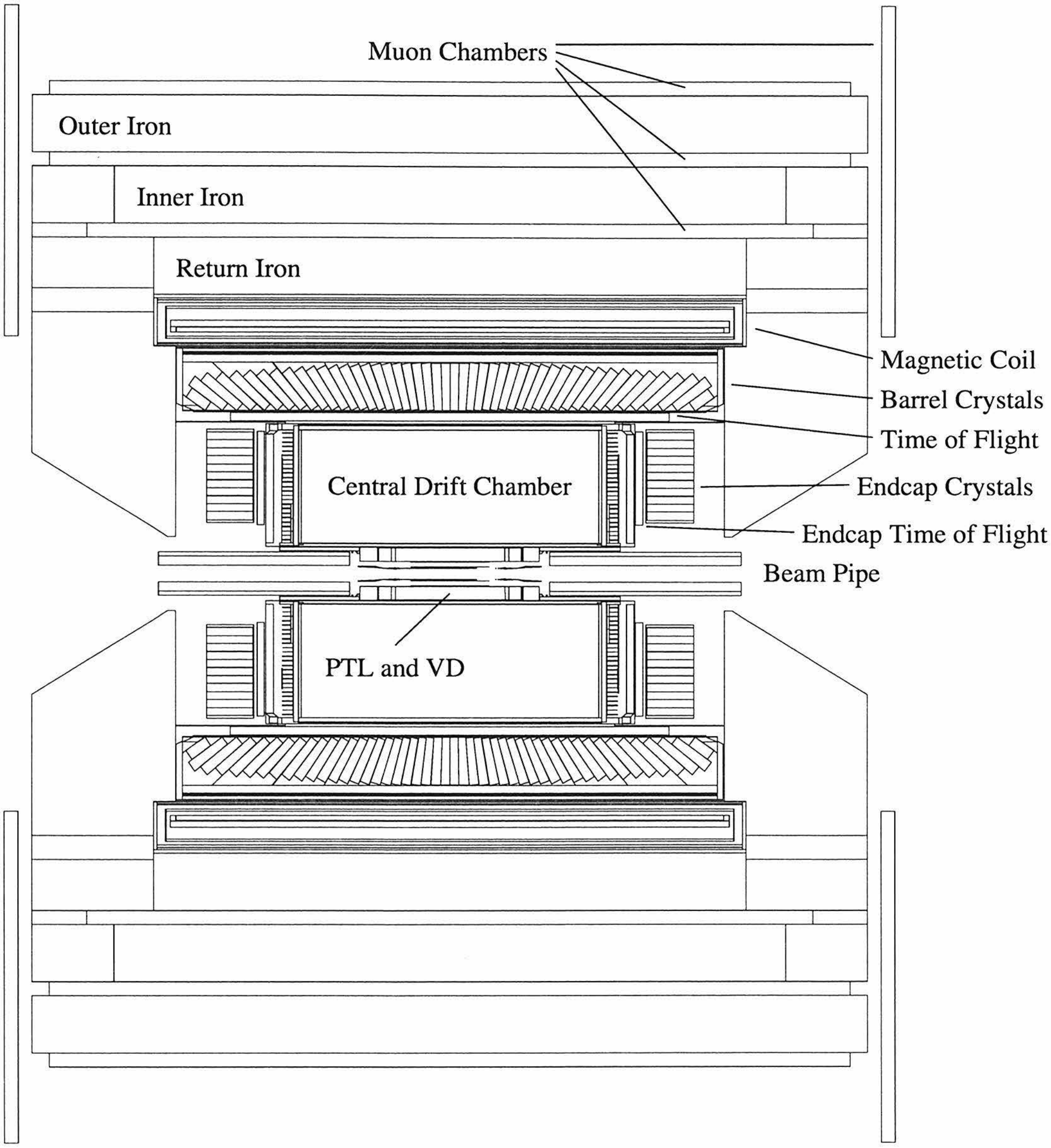

Figure 3.2: A schematic view of the side view of the CLEO II detector.

In the CLEO coordinate system, the direction of the positron beam through the detector defines the z axis, the y axis points vertically up, and the x axis is selected such that it defines a right-handed coordinate system (southward and away from the center of the ring). In polar coordinates the xy plane defines the $r\phi$ plane and the third coordinate, θ, is the angle made by a given vector with respect to the z axis.

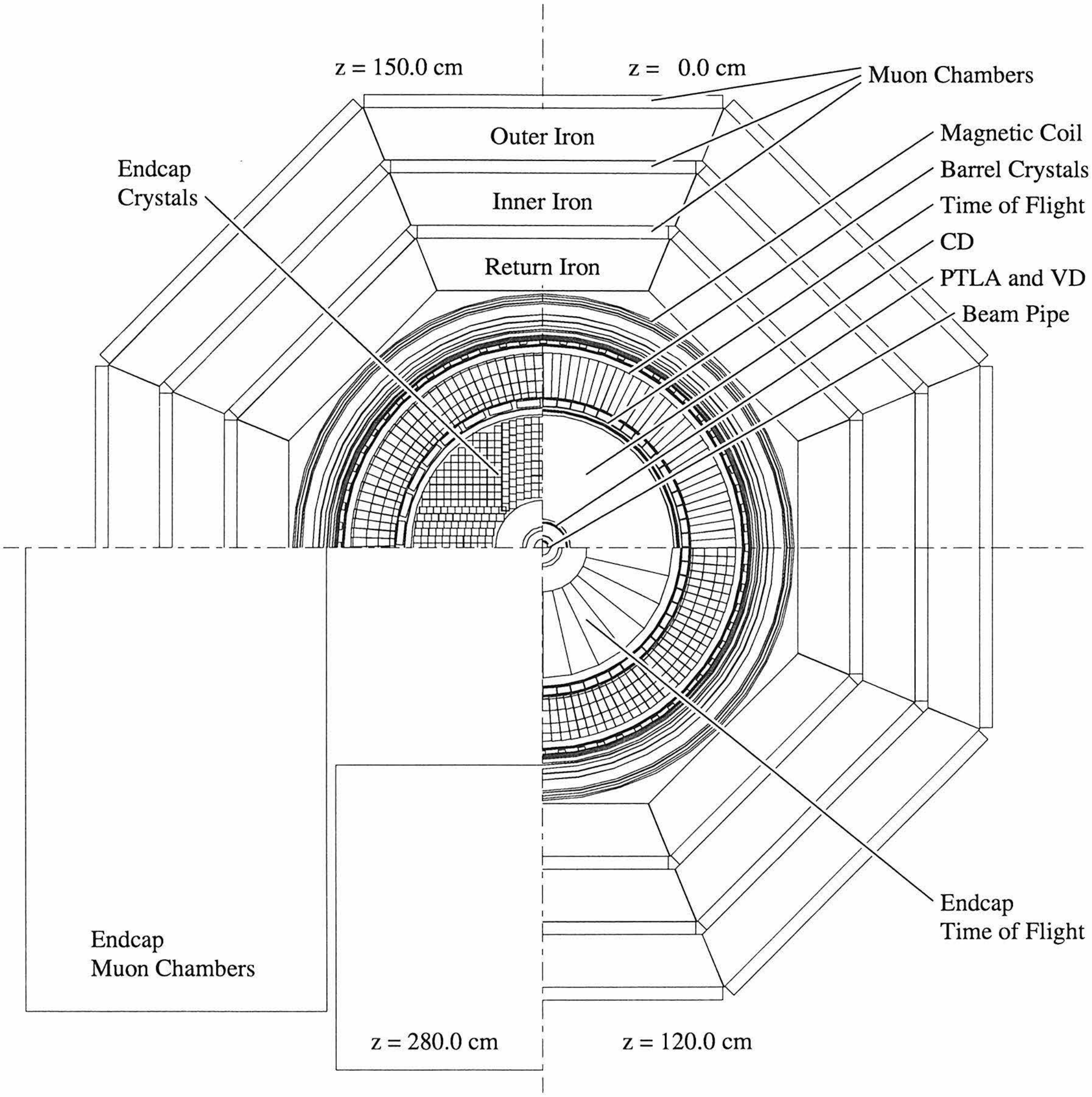

Figure 3.3: A schematic end-view of the CLEO II detector.

In the fall of 1995, the detector was upgraded to CLEO II.5. Since the measurements described in this thesis do not use any of the data collected with the upgraded detector, the details of the upgrade are not described here. In the subsections that follow, we briefly describe the detector components of the CLEO II detector, in order of their radial distance from the interaction point.

3.2.1 Beam Pipe

The 33 cm long beryllium beam pipe with a 3.5 cm inner radius separates the vacuum of the storage ring from the other detector components. The walls of the pipe are designed to be as thin as possible to reduce both scattering and energy loss by particles passing through it, while still providing mechanical stability against the stresses introduced by 1 atmosphere of pressure. The 0.5 mm thick pipe is lined with a 1 μm layer of nickel and a 20 μm layer of silver, corresponding to 0.44% of a radiation length. The coating is designed to absorb synchrotron radiation photons.

3.2.2 Central Tracking System

The three innermost devices are proportional wire chambers. They measure the trajectory of charged particles and perform measurements of specific ionization loss as the charged particles traverse the third chamber.

All three chambers share the same gas mixture [†] of 50% argon and 50% ethane. When particles travel through the gas volume, they ionize the gas atoms, thus leaving a trail of electrons and ions. All three chambers collect and amplify this ionization on anode wires. The cathodes and the anodes establish an electric field causing the electrons to drift toward the closest anode. There, they gain energy in the electric field of the anode wire resulting in secondary ionization. An avalanche is created, resulting in an electronic pulse which is registered as a "hit" if it is passes a threshold in the readout electronics.

The particle trajectories through these devices are helical because of the 1.5T solenoidal magnetic field. The field along the z axis bends the charged particles in

---

[†] The gas in the PTL was switched to DME (di methyl ether) in April 1992, resulting in an improvement in the spatial resolution on the position measurements from 100 μm to 50 μm. The main drift chamber gas was also switched to helium isobutane in 1995.

the $r\phi$ plane by the Lorentz force. The clockwise or counterclockwise bending of the track depends on the charge of the particle. The radius of curvature is a measure of its momentum p_t transverse to the beam axis; $p_t = 0.03BR$, where B is the magnetic field strength in Tesla and R is the radius of curvature in meters. The tracking devices measure the curvature, $\kappa = 1/(2R)$, and thus p_t. There is no bending in the rz plane; the polar angle θ combined with the p_t measurement provides a measurement of the magnitude of the momentum.

The drift chambers have an acceptance that is homogeneous over azimuth, and covers the polar angle range $|\cos\theta| < 0.98$. However, track reconstruction efficiency and resolutions are poorer for $|\cos\theta| > 0.71$ (angles below 45° and above 135°) because the track exits in z resulting in a reduction in the number of layers.

A brief description of each of the three drift chambers is given below.

Precision Tracking Layers

The Precision Tracking Layers or the PTL is the innermost drift chamber lying closest to the beam pipe and extending from a radius of 4.5 cm to 7.5 cm. The chamber's relatively small cell size and proximity to the interaction point allows us to separate primary from secondary vertices. It is 0.5 m long and consists of 384 polycarbonate tubes arranged in 6 concentric layers with 64 cells/layer. Each of the tubes is held at ground providing a field cage for a single axially aligned sense wire which runs through its center. The anode wires are 15 μm gold plated tungsten. The walls of the tubes are made of conductive aluminized mylar and serve as the cathode. The cells in two consecutive layers are staggered by 1/2 cell to help in resolving the ambiguity induced by the fact that the distance between the ionizing particle and wire does not determine on which side of the wire the particle passed.

No longitudinal (z coordinate) direction measurements are made with this chamber, since the sense wires all run parallel to the chamber. No attempt is made to instrument charge division read out.

Vertex Detector

The oldest component of the CLEO II detector, the vertex detector (VD), started being used as the second (intermediate) drift chamber when the PLT was installed. It extends from a radius of 8.1 cm to 16.4 cm and is 0.9 m long (see Figure 3.4). A total of 800 sense wires and 2272 field wires are arranged to form 10 layers of small hexagonal cells, with 3 field wires for each sense wire. All wires are axial, the inner five layers have 64 cells per layer, and the outer five layers have 96 cells per layer. The cells are staggered from layer to layer as shown in Figure 3.5, to resolve the ambiguity in the sign of the drift distance (left or right of the wire).

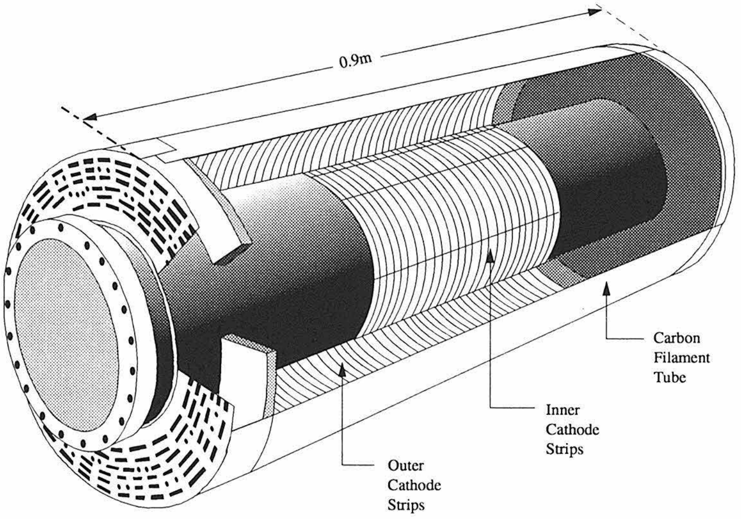

Figure 3.4: The vertex detector (VD).

On the inside of the first layer and the outside of the tenth layer, segmented cathode strips complete the remaining field shaping. The signals induced on these cathode strips are also read out to provide z measurements. The segmentation, shown in Figure 3.4, is 5.85 (6.85) mm along the beam direction on the inner (outer) cathode surface. The image charge of avalanche at the wire is spread over approximately three pads of the cathode. Both inner and outer cathode surfaces are divided into eight azimuthal sections to reduce confusion of cathode signals correlated to different sense wires.

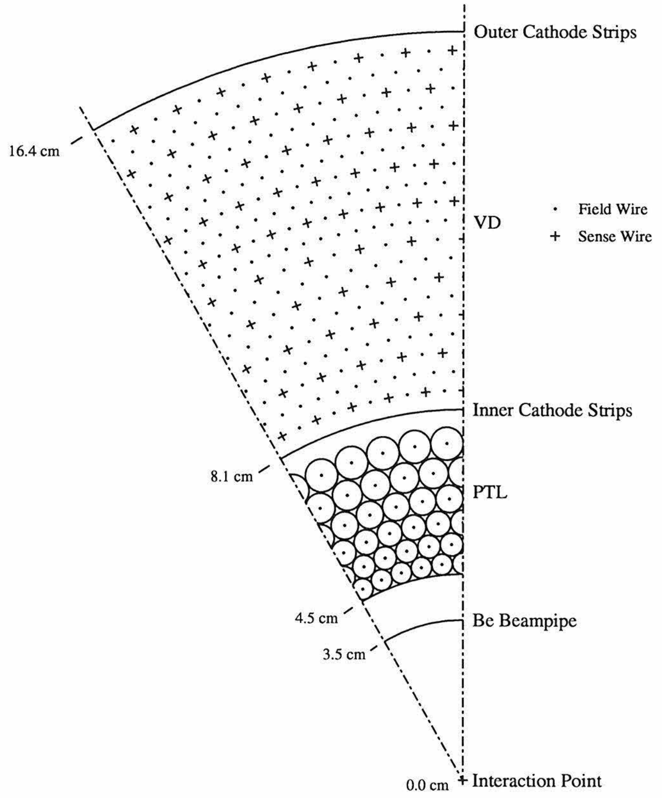

Figure 3.5: Cross section of the precision tracking layers and the vertex detector.

To provide further measurements in the axial direction, the sense wires are made of a nickel-chromium alloy with about three times the resistivity of gold plated tungsten and are instrumented for charge division measurements. Comparing the relative amplitude of signals observed at opposite ends of each sense wire provides z coordinate track information, and the z coordinate where the track passes nearest each sense wire is measured with a resolution of 1.7 cm. The field wires are made of aluminium.

The gas in the vertex detector is maintained at 20 psi absolute pressure to provide higher gain and shorter drift times.

Central Drift chamber

The outer drift chamber (DR) is the primary tracking chamber of the CLEO II detector. It covers the region from a radius of 17.8 cm to 94.7 cm, with an active length of 189 cm. It is used primarily to measure charged particle momentum vectors at the vertex, and for particle identification. The momentum transverse to the beam axis, the radial distance of closest approach of the track extrapolation to the beam line, the p_t, and the azimuthal direction ϕ, are measured with 40 axial (parallel to the beam axis) wire layers. Longitudinal measurements, polar angle and the longitudinal distance from the center of the interaction region to the extrapolation of the track to the beam axis (z coordinate), are measured with 11 small angle stereo wire layers and 2 layers of segmented cathode readouts. The pitched stereo wires are spaced every fourth layer.

A total of 12240 sense wires and 36240 field wires are arranged in 51 layers of cells, with three field wires for each sense wire as illustrated in Figure 3.6.

The 20 μm diameter gold plated tungsten sense wires are arranged in square cells, staggered by 1/2 cell from layer to layer. The number of sense wires per layer increases with radius so as to keep the cell sizes uniform; there are 96 wires in the innermost layer and 384 wires in the outermost layer. The sense wires are readout at only one end and thus has no instrumentation for charge division.

As in the VD, the inner and outer surfaces of the chamber have segmented cathode surfaces which shape the field cage. They also provide z measurements from the induced signals. The segmentation of the cathode surfaces is about 1 cm along the beam direction. The cathode is divided into 16 (8) azimuthal sections in the inner (outer) cathode, each covering 6 (48) wires, to reduce confusion of cathode signals correlated to different sense wires.

The drift chamber runs at atmospheric pressure.

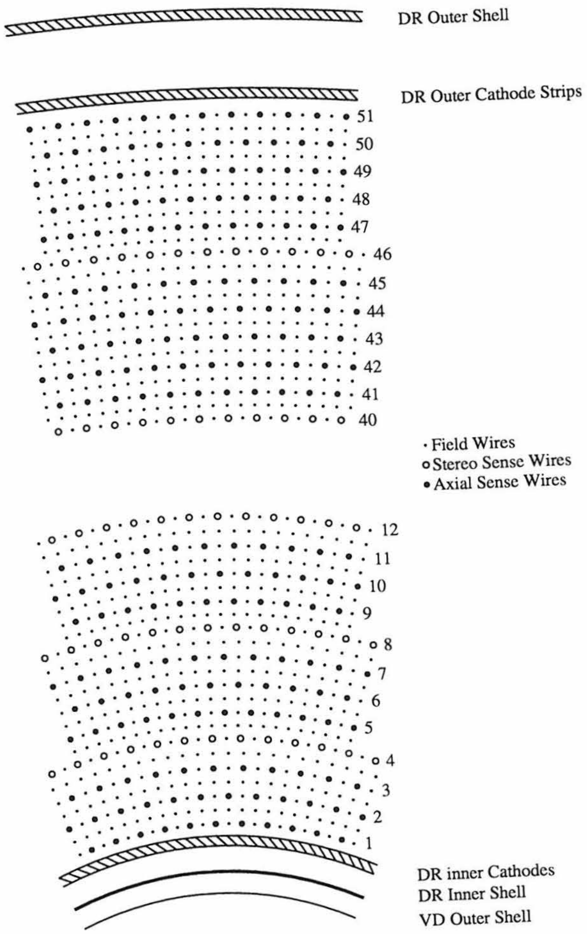

Figure 3.6: Main drift chamber cell structure.

Momentum and Angular Resolution

The resolution of the tracking system can be parameterized as:

$$(\delta p_t/p_t)^2 = \left(\frac{53\sigma p_t}{BL^2\sqrt{n}}\right)^2 + \left(\frac{0.054\sqrt{t}}{BL}\right)^2 \qquad (3.2)$$

where the first term is a result of individual measurement errors in drift distances, and the second term arises due to the distortion of the track from a true helix by multiple scattering. B is the magnetic field strength in tesla, σ is the accuracy of the individual position measurements in the drift chambers in meters, p_t is the transverse momentum in GeV/c, L is the length over which the measurements are made in meters, n is the number of position measurements, and t is the thickness of the obstructing material in the chambers in radiation lengths. For the CLEO II tracking chambers, $B = 1.5$T, $L = 0.85$ m, $n = 49$, $s = 150$ μm, and $t = 0.025$ radiation lengths. Equation 3.2 now becomes

$$(\delta p_t/p_t)^2 = (0.0011p_t)^2 + (0.0067)^2 \qquad (3.3)$$

and leads to $\delta p_t = 47$ MeV/c at a $p_t = 5.28$ GeV/c. This is lower than the resolution of 64 MeV/c measured by a sample of $e^+e^- \to \mu^+\mu^-$ at 5.28 GeV/c beam energy. The angular resolution is measured to be

$$\delta\phi = 1\text{mrad}\ , \quad \delta\theta = 4\text{mrad}\ .$$

This difference between the azimuthal and polar angle resolution is expected because there are only 15 measurements in the polar direction: 11 from stereo wire layers in the drift chamber and 4 from the cathode readout layers in the drift chamber and the vertex detector.

Charged particles coming from the interaction point with a momentum lower than 65 MeV/c are not detected due to the material in the particle path. With a 1.5 Tesla magnetic field, only particles with p_t >220 MeV/c exit the main drift chamber; a lower transverse momentum and $p_z < 45$ MeV/c results in a track which executes a full turn within the active volume (curlers). The particles with lower p_z result in tracks with several turns.

Charged Particle Identification

Pulse height measurements in the main 51 layer drift chamber provide energy loss measurements (dE/dx) on charged tracks with a resolution of 6.5% determined for Bhabhas and 7.1% for minimum ionizing pions. The energy loss per unit distance is a function of the particle mass, as is illustrated in Figure 3.7.

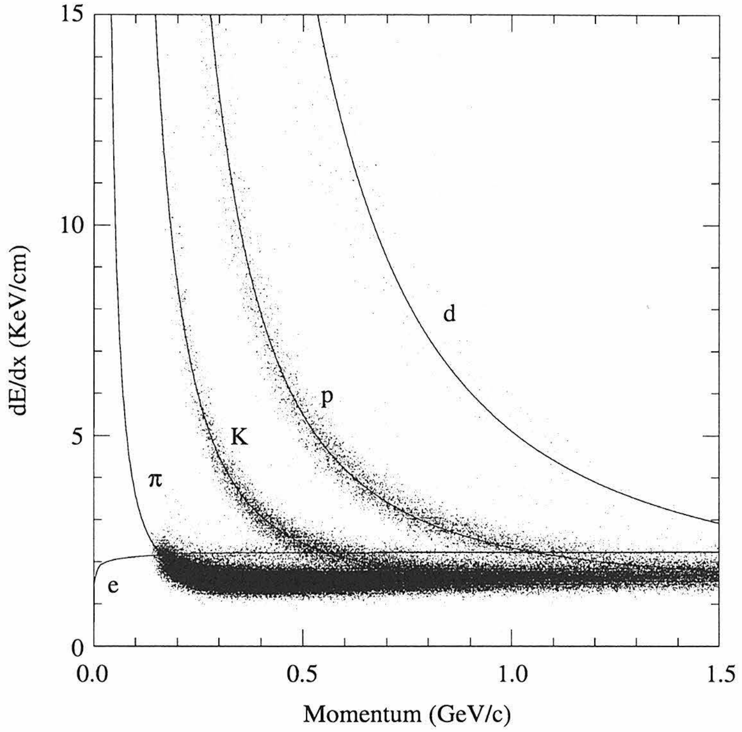

Figure 3.7: dE/dx in the drift chamber versus the track momentum.

The resolution on the measured dE/dx depends on the energy loss distribution in a cell and the number of cells that a particle passes through in the drift chamber. Because of the large Landau tail of the ionization distribution, we take the 50% truncated mean [51] of all the measurements along a track trajectory as the best estimator of dE/dx.

We note that dE/dx measurements yield good separation of pions and kaons up to roughly 700 MeV/c, and good separation of pions and protons up to 1.1 GeV/c. We define SGxxDI as the difference between the measured dE/dx and the dE/dx one would expect for a particle species xx, divided by the resolution where xx is either EL (e), MU (μ), PI (π), KA (K) or PR (p).

No π/K particle identification is employed in this thesis; particle identification is used only to help identify electrons.

3.2.3 Time of Flight

This detector component, comprising of particle scintillation counters, is located just outside the central tracking chambers at a radius of 95 cm from the interaction point. These counters measure the time interval between a beam crossing and when the particle strikes the counters. The time of flight counters are used as a fast element in the trigger system and can be used for particle identification as well [‡].

This system is comprised of 64 Bicron BC-408 plastic scintillator slabs (10 cm wide, 279 cm long and 5 cm thick) arranged parallel to the beam pipe. Both ends of the scintillator are connected to lucite pipes which transfer the scintillation photons to photomultiplier tubes. The light guides are necessary to keep the photomultiplier tubes operating safely away from the magnetic field of the detector.

In addition to the 64 barrel time of flight counters, each end of CLEO is covered with 28 wedge-shaped scintillators. The endcap counters are read out with a single photomultiplier tube at the small end. These Hamamatsu proximity mesh type tubes are designed to operate inside high magnetic fields.

The solid angle subtended by the barrel counters is 81% of 4π and that by the endcap counters is 16%. The barrel counters have a resolution of 154 ps as measured using hadrons. In Figure 3.8, we show a scatter plot of the time of flight measurements (barrel) versus the track momentum for tracks in hadronic events.

[‡] They are now used as a bunch-finder for the multi-bunch operation.

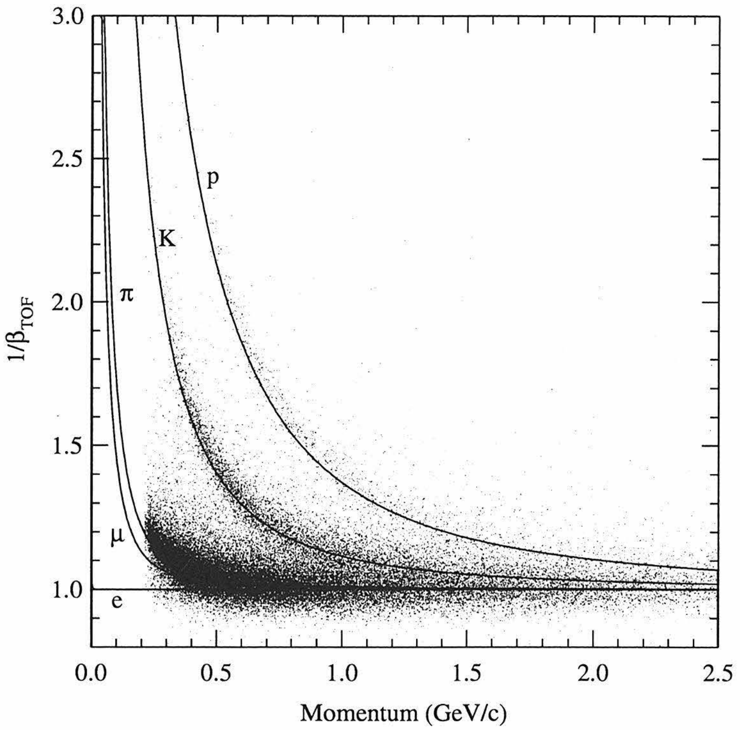

Figure 3.8: $1/\beta$ versus track momentum in the barrel time of flight counters.

For this plot, the time of flight information is expressed in terms of $1/\beta$ with $\beta = v/c$. The velocity v is inferred from the measured time of flight information and the path length of the charged tracks in the central detector. The superimposed curves are

$$\frac{1}{\beta} = \frac{E}{p} = \sqrt{1 + \left(\frac{M}{p}\right)^2} \tag{3.4}$$

for tracks of momentum p and particle species of mass M.

The time of flight measurements extend the separation of the three particle species to higher momenta than dE/dx, producing good pion/kaon separation up to 1.2 GeV/c and kaon/proton separation up to more than 2 GeV/c.

3.2.4 Electromagnetic Calorimeter

The calorimeter records the passage of charged particles, and measures the energy of photons and electrons in the CLEO II detector. A photon incident on a block of material interacts in one of three possible ways depending on its energy:

- low energy photons ($E_\gamma \leq 100$ KeV) result in the production of photoelectrons from the atoms of the material;
- in intermediate energy photons, Compton scattering of the photons with the atomic electrons is dominant;
- photons with energy above the threshold of $2m_e \approx 1.02$ MeV result in the creation of a e^+e^- pair from the interaction of the photon with the material nuclei.

At the CLEO energy scale, typical photon energies are in the 10 MeV to 5 GeV range, and the photons primarily produce e^+e^- pairs. The electrons and positrons, in turn, undergo bremsstrahlung, leading to a cascading shower of e^+, e^- particles and photons. This process continues until the energy is totally dissipated in the material. Some fraction of this energy is converted into scintillation light, enhanced by the doping.

The calorimeter is a 27,000 Kg array of 7800 thallium doped cesium iodide crystals, each with an inner face of about 5 cm (2.7 radiation lengths) $\times$ 5 cm and a length of 30 cm (16 radiation lengths and 1 nuclear interaction length). The length of the crystal almost fully contains the electromagnetic shower. A 6 mm thick UVT lucite window separates the back end of the crystals from 4 photodiodes, which detect the scintillation light from the crystals. The four-fold redundancy insures that isolated failures of photodiodes do not compromise the calorimeter performance, since all 7800 crystals in the CLEO II detector have at least two working photodiodes. The four preamplifier signals from a single crystal are summed and shaped before being sent to an ADC.

Thallium doped cesium iodide has a high light output with an emission spectrum that is well matched to the photodiodes. In addition, both the radiation length (1.83 cm) and the Moliere radius [§] (3.8 cm) are short. The dimensions of the crystals used in CLEO are a compromise. Longer crystals would give a superior resolution for the high energy showers by reducing the leakage at the back of the crystal, but because of transmission losses, a longer crystal would have a lower resolution for the low energy showers. Smaller lateral dimensions for each crystal, and hence a larger number of crystals, would improve the angular resolution. However, the increased number of crystals that would need to be summed to find shower energies would increase the electronic noise. The cost of machining and instrumenting the device would also increase.

The system is located just outside the time of flight detectors and is divided into the barrel and endcap region as illustrated in Figures 3.2 and 3.3. The barrel portion of the calorimeter contains 6144 trapezoidal crystals arranged in 48 z rows of 128 azimuthal segments each. These crystals all point towards the interaction region and photons originating at the interaction point strike the barrel crystal surface at nearly normal incidence. The remaining 1656 crystals are rectangular and are arranged in concentric rings at both ends of the detector. These cells are all arranged to have their axes parallel to the z axis of the detector, and thus lack the projective geometry found in the barrel crystals. The barrel crystals cover the angular region between 32 and 90 degrees; the endcap pieces cover 15 to 36 degrees. The total coverage is 95% of the solid angle resulting in a nearly hermetic calorimeter.

The resolution on the energy depends on the amount of material between the interaction point and the crystals. The presence of material degrades the resolution through photon conversions and the subsequent ionization loss of the resulting charged particles. Further, energy from conversions far from the crystals spread laterally and will not be associated with the proper shower. The energy resolution in the CLEO II

[§] The Moliere radius characterizes the lateral spread of showers.

calorimeter is excellent, and for the barrel region, it can be parametrized as

$$\frac{\sigma_E}{E}(\%) = \frac{0.35}{E^{3/4}} + 0.19 - 0.1E \tag{3.5}$$

where E is the photon energy in GeV. The angular resolution in the barrel region can be parametrized as

$$\sigma_\phi(mr) = \frac{2.8}{\sqrt{E}} + 1.9\ , \quad \sigma_\theta(mr) = 0.8\sigma_\phi \sin\theta \tag{3.6}$$

where, once again, E is the photon energy in GeV. The energy and angular resolution parameterizations come from the Monte Carlo simulation of showering in the CLEO II detector, including electronic noise. The barrel region has 16 radiation lengths material while the endcaps have about 1 radiation length material at normal incidence. The energy resolution in the barrel is about 1.5% at 5 GeV and 3.8% at 100 MeV. The endcap resolution is worse due to the drift chamber endplate in front of the crystals. The angular resolution at 5 GeV is 3 mrad in the barrel and 9 mrad in the endcaps.

The fine granularity of the calorimeter permits very good position resolution, critical in the reconstruction of π^0 decays to $\gamma\gamma$ ($\mathcal{B}(\pi^0 \rightarrow \gamma\gamma) = 98.8\%$). The photons from π^0's with $E_{\pi^0} < 3$ GeV are well separated in the calorimeter and are identified as separate showers. The lineshape of E_γ is asymmetric due to leakage and preconversions, and is calibrated such that $E_\gamma = E_{\text{peak}}$. Thus $m_{\gamma\gamma}$ peaks below m_{π^0}, and has a lower mass tail (Figure 4.1). The rms width of the π^0 invariant mass peak varies from 10 MeV for the low energy π^0's to 5 MeV for the high energy π^0's.

The electromagnetic calorimeter is used extensively in the analysis presented in this thesis. In addition to the π^0 reconstruction, it is used to help identify electrons, and to veto potential background events as explained in Chapter 5. Electron identification utilizes the ratio E/p of the energy measured in the calorimeter to the momentum measured in the tracking chamber. E/p close to 1 is consistent with an e hypothesis, since all the electron's energy should be deposited in the calorimeter.

Hadrons and muons both have smaller E/p.

3.2.5 Superconducting Solenoidal Magnet

This solenoid was designed to provide a uniform 1.5 Tesla magnetic field parallel to the beam line. It had to be large enough to contain the electromagnetic calorimeter inside the coil; the 3.5 m long solenoid has a 3.1 m diameter with a 2.9 m clear bore resulting in a 26 m^3 cylindrical volume. The magnetic field is uniform to $\pm 0.2\%$ in the drift chamber volume over 95% of the total solid angle.

There are two layers of 5 mm × 16 mm aluminium rectangular tubing containing a flat ribbon of Cu-Nb-Ti superconducting cable, wound on the inside surface of the aluminium cylinder. The inner layer of tubing contains an 11 strand ribbon, while the outer layer contains a ribbon of 9 strands, all carrying 3300 A current.

The entire system is cooled to a temperature of 4K by a liquid helium circulation system. The flux return is provided by four layers of iron outside the magnet, each 36 cm thick. These iron layers serve as absorbers for the muon detection system as well.

3.2.6 Muon Chambers

The muon system was designed to be highly efficient with low fake rates, and to cover the maximum possible solid angle. There are three superlayers of muon detectors between the iron layers for the magnetic flux return. The barrel chambers are arranged in an octagonal geometry as illustrated in Figure 3.3 and cover 86% of 4π steradians. These chambers are imbedded at depths of 36, 72 and 108 cm of iron. Additional chambers cover the two ends of the detector. The total equivalent thickness of iron absorber varies from 7.2 to 10 nuclear absorption lengths, depending on the direction of the track.

Each superlayer consists of three sublayers of plastic Iarocci streamer tubes, operated in the proportional mode at 2500V with a 50-50 argon ethane mixture. The counters are about 5 m long and 8.3 cm wide. The cross section of a counter is shown in Figure 3.9.

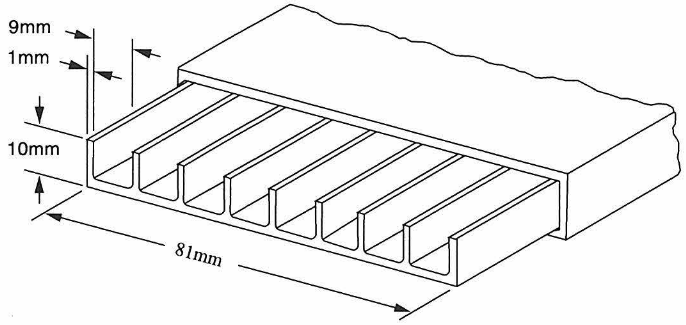

Figure 3.9: Cross section of the muon chamber proportional tubes.

A 50 μm silver plated Cu - Be anode wire runs down the center of each of the eight channels of the proportional tube shown in the figure. Three sides of the comb-like plastic profile are coated with a layer of graphite which acts as a conductive cathode. The anode signals provide one hit coordinate; the orthogonal coordinate (along the counter) is measured with external copper pick up strips, of the same width as the counters (see Figure 3.10). The anode wires from each counter are ganged together, and the readouts from a number of neighboring counters and neighboring strips are ganged together at both ends through 100Ω resistors. Charge division on the anode wires is used to determine the coordinate of the hit, eliminating the need for a large number of readout channels. The spatial resolution obtained is 2.4 cm for the counters. This resolution is adequate, since it is smaller than the uncertainty in the projected track position in the muon chamber due to multiple scattering in the iron absorber.

Each reconstructed track in the central detector is extrapolated into the muon detector taking into account the energy lost by dE/dx. The path length to each muon layer is calculated in nuclear absorption lengths. Then a search is made for hits in the muon counters that are likely to be transversed by the track and a 2-D χ^2 of the distance between the measured and the projected hit positions is calculated. If the $\chi^2 < 16$, we consider that layer to be hit. The track is considered as definitely

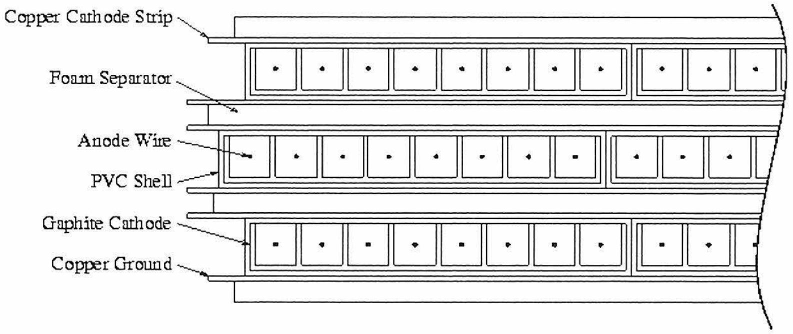

Figure 3.10: Cross section of one muon chamber superlayer.

detected in a unit if at least two out of the three layers in that unit are hit. The track is assigned the depth of the outermost unit in which it is detected. If the track's depth is less than the depth predicted by track extrapolation, the track is considered as a non-muon.

3.2.7 Trigger and Data Acquisition

The CLEO II trigger is designed to be very loose in accepting events, and at the same time to have a small dead time. The crossing rate for electron and positron bunches in CESR is 2.8 MHz, while the rate of interesting physics events is only about 10 Hz.

A hierarchy of hardware triggers, and a final software trigger, select events to be written to tape. At each level, either a set of criteria are passed and the trigger proceeds to the next level, or the criteria are failed, the event is not read out, and the trigger directs the experiment to re-arm itself.

The Level 0 (L0) trigger is fast, 405 ns, *i.e.*, the decision is made before the next beam crossing. It receives inputs from the time of flight counters, the vertex detector, and the electromagnetic calorimeter. The L0 trigger is passed every 300-400 crossings on average (depending on the beam current, level of background, and so on) and the rate of events passed by L0 is $\sim$ 10kHz. After a L0 trigger, all detector gating is disabled, and a search is made for the Level 1 (L1) requirement. L1 takes inputs from the time of flight counters, the vertex detector, the drift chamber and the calorimeter. Approximately 1.5 μs is required for all the information to be ready for the L1 decision, thus introducing a 2% dead time. The L1 trigger reduces the rate to about 50Hz. The surviving events are then subject to the Level 2 (L2) trigger, which takes inputs from the vertex detector and the drift chamber and forms detailed pattern recognition to reject backgrounds from cosmic ray events, and interactions of the beam with the beam pipe or the residual gas molecules. L2 decreases the event rate by a factor of between 2 to 4. As with L1, if the requirement of L2 are not met, gating resumes.

Starting at the L1 level, the trigger is specified in terms of several parallel "lines" or "streams" tailored to specific physics processes of interest. There is an intentional redundancy in these lines, so that many processes such as $e^+e^- \to e^+e^-$ satisfy many of the L2 lines. This redundancy allows for inefficiencies in detector elements, and also allows one to determine these inefficiencies.

Once an event passes the L2 trigger, the signals from all detector components are digitized, and read out into a data acquisition (DAQ) computer.

The final level of event filtering is Level 3 (L3) and occurs in software after the entire event has been read out by the detector, but before it is written to tape. It uses detailed information from reconstructed events and further reduces the number of events by a factor of 2. Every one out of eight events failing L3 is flagged as such and is saved for diagnostic purposes.

3.3 Simulation of Physics Processes and Detector Response

An essential tool for making the measurements presented in this thesis is the simulated data set produced by a computerized Monte Carlo simulation of the physics processes involved and of the CLEO II detector. Computer simulations are very valuable in the analysis of the data to extract the parameters and to perform precision measurements with small systematic errors. Given the complexity of the detector geometry and its response to particle passage, as well as the complexity of the kinematics of final state particles, the Monte Carlo simulation of the physics reaction and the detector response provides a convenient and effective way of studying the data. The simulation accounts for all the complicated correlations present in the data. These simulations are carried out in two logically different steps. First, "events" corresponding to the initial physics process are generated. Then the detector response to the stable particles in the final state is simulated.

3.3.1 Event Generation

Event generators simulate the high energy collisions produced in the accelerator. They produce events which contain the type, energy-momentum and space-time four-vectors for all the final state particles. The event generator for τ pairs is a combined package of KORALB(v2.2), TAUOLA(v2.4) and PHOTOS(v2.0) [52, 53, 54, 55, 56]. KORALB simulates the process $e^+e^- \rightarrow \tau^+\tau^-(\gamma)$. The simulation includes in its treatment $\mathcal{O}(\alpha^3)$ QED radiative corrections; up to one photon can be radiated from the initial and final state leptons. It also includes effects associated with a finite τ mass, interference of the photon exchange process with the lowest order annihilation through the Z^0 resonance, spin polarization in any direction for the initial electron and positron, and spin correlations of the produced tau pair.

TAUOLA simulates the decays of polarized tau leptons into all major expected final states including $\mu\nu\nu$, $e\nu\nu$, $\pi\nu$, $K\nu$, $\rho\nu$, $K^*\nu$ and $a_1\nu$. Table 3.1 lists all τ decay modes simulated in TAUOLA. Further, the decay of the vector resonances ρ and a_1 to two and three pions respectively, and the decay of the K^* to $K\pi$ is modeled according to the full matrix element calculation. Order α radiative corrections, which permit one radiated γ are included for the leptonic decays. PHOTOS is used to generate up to one radiated photon in semi-hadronic decays.

The non-Standard Model $V + A$ ($\rho = 0, \eta = 0$) and $\eta = 1$ ($\rho = 3/4, \eta = 1$) Monte Carlo event samples are generated with a modified version of the TAUOLA package [57].

Tau Decay Modes Simulated in TAUOLA			
Decay Mode of τ	Branching Fraction [%]	Matrix element including Spin	Decay Radiation
$\tau^- \longrightarrow e^- \overline{\nu}_e \nu_\tau$	18.00	yes	$\mathcal{O}(\alpha)$ m.e.
$\tau^- \longrightarrow \mu^- \overline{\nu}_\mu \nu_\tau$	17.51	yes	$\mathcal{O}(\alpha)$ m.e.
$\tau^- \longrightarrow \pi^- \nu_\tau$	11.10	yes	PHOTOS
$\tau^- \longrightarrow \rho^- \nu_\tau$	25.15	yes	PHOTOS
$\tau^- \longrightarrow a_1^- \nu_\tau$	17.90	yes	PHOTOS
$\tau^- \longrightarrow K^- \nu_\tau$	0.71	yes	PHOTOS
$\tau^- \longrightarrow K^{*-} \nu_\tau$	1.34	yes	PHOTOS
$\tau^- \longrightarrow K^- \pi^- K^+ \nu_\tau$	0.15	yes*	PHOTOS
$\tau^- \longrightarrow K^0 \pi^- \bar{K}^0 \nu_\tau$	0.15	yes*	PHOTOS
$\tau^- \longrightarrow K^- K^0 \pi^0 \nu_\tau$	0.15	yes*	PHOTOS
$\tau^- \longrightarrow \pi^0 \pi^0 K^- \nu_\tau$	0.05	yes*	PHOTOS
$\tau^- \longrightarrow K^- \pi^- \pi^+ \nu_\tau$	0.50	yes*	PHOTOS
$\tau^- \longrightarrow \pi^- \bar{K}^0 \pi^0 \nu_\tau$	0.55	yes*	PHOTOS
$\tau^- \longrightarrow \eta \pi^- \pi^0 \nu_\tau$	0.17	yes*	PHOTOS
$\tau^- \longrightarrow \pi^- \pi^0 \gamma \nu_\tau$	0.13	yes*	PHOTOS
$\tau^- \longrightarrow \pi^- \pi^- \pi^+ \pi^0 \nu_\tau$	4.50	no	PHOTOS
$\tau^- \longrightarrow \pi^- \pi^0 \pi^0 \pi^0 \nu_\tau$	1.00	no	PHOTOS
$\tau^- \longrightarrow \pi^- \pi^- \pi^- \pi^+ \pi^+ \nu_\tau$	0.08	no	PHOTOS
$\tau^- \longrightarrow \pi^- \pi^- \pi^+ \pi^0 \pi^0 \nu_\tau$	0.09	no	PHOTOS
$\tau^- \longrightarrow \pi^- \pi^0 \pi^0 \pi^0 \pi^0 \nu_\tau$	0.10	no	PHOTOS
$\tau^- \longrightarrow \pi^- \pi^- \pi^- \pi^+ \pi^+ \pi^0 \nu_\tau$	0.03	no	PHOTOS
$\tau^- \longrightarrow \pi^- \pi^- \pi^+ \pi^0 \pi^0 \pi^0 \nu_\tau$	0.05	no	PHOTOS
$\tau^- \longrightarrow \pi^- \omega \pi^0 \nu_\tau$	0.39	no	PHOTOS
$\tau^- \longrightarrow K^- K^0 \nu_\tau$	0.10	no	PHOTOS
$\tau^- \longrightarrow K^- \omega \nu_\tau$	0.10	no	PHOTOS
All Modes	100.00		

Table 3.1: Tau decay modes simulated in TAUOLA. The first seven decay modes take into account the full matrix element including helicity. The modes marked with the "yes*" in column 3 indicate that only approximate form factors are used in their calculation.

3.3.2 Detector Simulation

The modeling of the response of the measurement device CLEO II is carried out by the CLEOG [58] simulation program which contains a nearly complete description of the detector's material and geometry. CLEOG uses GEANT [59] routines to track particles through the detector as they travel through the magnetic field, recording their trajectories and those of their decay daughters. The package also contains a parametrization of hadronic interactions between the particle and nuclear matter of the detector components (NUCRIN/FLUKA), an electromagnetic shower algorithm based on the EGS package and facilities for managing decay in flight, multiple scattering, Compton scattering, pair production, ionization, δ ray production and bremsstrahlung.

For precision measurements, the time dependence of the detector status and performance also must be taken into account. Each Monte Carlo event is assigned a time and date such that all events are distributed over a certain data-taking period with the correct luminosity weighting. The actual detector status at that very moment is taken into account; the status of the trigger and each component of the detector is recorded for each data-taking period.

The CLEOG output files are in identical format to that of the raw data from the CLEO II data acquisition system. Further, characteristic electronics noise in all devices is added to the simulated signals to ensure that the simulated output resembles real physics data as closely as possible. The characteristic noise is obtained from random triggers of the detector in the presence of colliding beams. We run the same event reconstruction on both the data and the Monte Carlo output for further analysis.

3.4 Future Upgrades to CESR and CLEO

The first phase of both the CESR and CLEO upgrades are complete. CESR has converted to a 9 bunch operation with a small crossing angle. A new digital feedback system and improved vacuum pumping have made possible the handling of multi-bunch trains (9 trains of three bunches each). CESR delivers a peak luminosity which increases every other month, and is expected to reach a peak luminosity of $\mathcal{L} = 6 \times 10^{32}$ cm^{-2}s^{-1} in 1997. The next phase of the upgrade is aimed to achieve a peak luminosity of $\mathcal{L} = 10 \times 10^{32}$cm^{-2}s^{-1}. It requires the use of superconducting RF cavities to handle the 9×5 bunch trains, new vacuum pipe and pumps to handle the synchrotron radiation load and a more complex interaction region focusing element and masking configuration.

The first phase of the detector upgrade is now also complete. CLEO II.5 has a new 3 layer silicon microstrip vertex detector (SVD) which replaced the precision tracking layers (PTL) in CLEO II. It surrounds a new 2.0 cm radius Beryllium beam pipe and masking system. The author has worked on the development of this detector device and its mechanical support. Most of the work involved the SVD data acquisition system and is described in detail in Appendix D.

The next phase of the detector upgrade involves a new silicon vertex detector with four layers, a new drift chamber, a fast Ring Imaging Čerenkov Counter (Fast RICH) for particle identification, and a new data acquisition system and trigger. The combination of the upgraded collider and detector to be commissioned in 1998-99 is expected to yield data samples comparable to the ones expected at the B-factories, and will be able to probe the physics of B and τ decays with an order of magnitude greater sensitivity.

Chapter 4 Data Analysis

In this chapter, we describe all the cuts applied to select the $e - vs. - h\pi^0$ and $\mu - vs. - h\pi^0$ samples studied. Three different types of criteria are applied: criteria based on the reconstruction of $\tau\tau$ events, those based on the reconstruction of the tag tau decay $\tau^+ \rightarrow h^+\pi^0\,\bar{\nu}_\tau$, and those based on the reconstruction of the leptonic tau decay $\tau^- \rightarrow \ell^-\bar{\nu}_\ell\nu_\tau$.

Tagging one tau decay helps ensure that we select a $\tau\tau$ event. The $\tau^+ \rightarrow h^+\pi^0\,\bar{\nu}_\tau$ decay mode, where h^+ refers to the charged hadron (π^+ or K^+), is utilized to tag the $\tau\tau$ events in this analysis. It is dominated by $\rho^+\bar{\nu}_\tau$, but also receives contributions from $K^{*+}\bar{\nu}_\tau$, $\rho'^+\bar{\nu}_\tau$ and other non-resonant modes. No attempt is made to distinguish pions from kaons in this analysis. Using this particular decay mode of the τ lepton has several advantages. It has a large branching ratio ($\simeq 25\%$), and there is negligible uncertainty associated with particle identification. This would not be true if leptonic modes were used to tag $\tau\tau$ events. The reconstruction of the entire event helps suppress backgrounds from hadronic events, two-photon physics, $q\bar{q}$, and cosmic ray events. The tag decay mode is also utilized to estimate the flight direction of its parent tau, necessary to reconstruct the pseudo rest frame spectra described in Chapter 7.

In the following section, we present details about the event reconstruction procedure including tracking, track-cluster matching, lepton identification and the π^0 reconstruction. The last section in this chapter includes the cuts applied to select the events in this analysis.

4.1 Event Reconstruction

After the data are copied to tape, there begins a process of "offline" software analysis, and the event reconstruction is done with several software routines. Standard routines apply calibration constants to convert raw signals to measure energy, time, etc.;

tracking algorithms convert wire hit patterns to particle tracks; clustering algorithms associate crystal hits with one electromagnetic shower; and so forth.

4.1.1 Tracking

The Michel parameters are extracted from a fit to the momentum spectrum of the charged lepton in the event, and to measure the momentum we rely on the tracking chambers described in Section 3.2.2. These chambers provide the input for a tracking program DUET [60], based on a tree algorithm. DUET creates 'links' of hits in close proximity, forms these into elementary 'trees' based on the fiducial volume from which they appear to originate, and then combines the trees into 'chains' and finally 'tracks'. These tracks are fit to a helix. DUET operates with an efficiency of roughly 99% for particles from hadronic tracks within the region of primary acceptance of the tracking chambers (approximately $\cos\theta < 0.9$).

DUET was designed to find as many tracks as possible, and thus it provides a list of tracks which often contains spurious entries. The situation is further complicated by the 1.5 Tesla magnetic field. Only particles with more than 220 MeV/c of p_t actually exit the outer surface of the drift chamber; others execute a full turn within the active volume and are called 'curlers'. Tracks with very small p_z execute several turns.

To pare down the list of tracks, we use a program called TRKMAN [61] which addresses three problems revealed in visual scanning of events: "ghost" tracks arise when DUET fits two tracks to a set of hits created by the passage of a single particle; undesirable curlers result in tracks formed from the second half of a particle's arc, or the first half of an arc from a particle's second (or third) trip through the chamber; tracks formed when DUET fits a track through a set of unrelated hits, or simply does a bad job on hits that do come from a single particle. TRKMAN algorithms kill more than 90% of the ghost tracks, eliminate more than 80% of undesirable curler tracks, and eliminate 86% of the third type of undesirable tracks.

4.1.2 Crystal Calorimeter Clustering

For photon measurement (π^0 reconstruction) and electron identification, we rely on the Cesium Iodide calorimeter described in Section 3.2.4. An algorithm in the data acquisition hardware searches for all crystals (out of 7800 crystals) with more than $\simeq 6$ MeV deposited, defines them as seeds and writes them out. Then, any crystal that is one of the 24 nearest and next-to-nearest neighbors of a seed crystal and has more than $\simeq 0.5$ MeV deposited is also written out.

The crystal clustering program CCFC takes the crystals written out, and creates connected regions. In these regions, every crystal is the nearest neighbor of at least one other crystal in the region. These regions are then divided if a secondary nucleus is found. The secondary nucleus is defined as a local maximum, separated from the absolute maximum by at least one crystal. Next the region is divided, with the maxima receiving their nearest neighbors and the next-nearest neighbors. CCFC then attempts to divide the energy of the shared nearest neighbors between the nuclei. This helps to resolve the two photons from a π^0 which have produced overlapping showers. Finally, all remaining hits are assigned to a cluster if they are the nearest neighbor of a crystal in that cluster. This allows some hits to remain unconnected with any cluster at all [62].

The position vector of a cluster is calculated in two steps. The first step is the determination of a centroid from the energy-weighted sum of the coordinates of the geometric centers of the crystals. Due to biases in the centroid method, the position of the cluster center must be laterally adjusted. The lateral adjustment depends on the energy and on the proximity of the uncorrected centroid to the geometrical center of the crystal in which it lies. Since there is no longitudinal segmentation of the calorimeter, the correct depth is determined analytically as a function of cluster energy. For both the lateral adjustment and the correct depth, a photon is assumed to have created the cluster [63].

The cluster energy E_{clus}, the direction of the cluster from the beam position θ_{clus}

and ϕ_{clus}, and the measure of the lateral shape of the cluster $\frac{E9}{E25}$ defined as:

$$\frac{E9}{E25} = \frac{\text{summed energy of the 9 central crystals}}{\text{summed energy of the 25 central crystals}}, \tag{4.1}$$

where the most central crystal contains the cluster center, are all useful parameters. Photon clusters tend to have higher values of $\frac{E9}{E25}$ than splinters from hadronic showers (split-offs). To enhance the utility of $\frac{E9}{E25}$, a quantity $P^{1\%}_{9/25}$ is computed from E_{clus} and θ_{clus}. It is designed such that for any given energy and angle, 99% of all photon clusters will have $\frac{E9}{E25}$ greater than $P^{1\%}_{9/25}$.

4.1.3 Track-Cluster Matching

With the tracking chambers for charged particles, and the calorimeter for photons, we are poised to reconstruct the entire event. This full reconstruction of the event is essential for the reconstruction of the pseudo rest frame lepton spectrum. This special frame of reference improves the sensitivity to the parameters and is described at length in Section 7.1. Accurate measurement of cluster energy is necessary, but not sufficient, for determining photon momenta. Charged particles can also create substantial clusters, depositing energy through hadronic and electromagnetic interactions, and specific ionization losses. To discriminate between the clusters caused by photons, and those from charged particles, we associate the tracks with clusters.

If a track left by a charged particle projects directly into a cluster, the chances that the cluster was caused by a photon are very slim indeed. Unfortunately, a simple projection of the track to the calorimeter with a cut on cluster proximity turns out to be completely inadequate. Very often, the centres of hadronic showers are quite far from the track projection, while at least one crystal in a cluster is usually near the projection. Further, the depth to which a track is projected is critical. Tracks with appropriate values of p_t will often graze the calorimeter, hitting crystals along their entire tangential approach, never reaching an otherwise reasonable projection depth. Finally, some hadronic reactions give rise to secondary photons (or even charged particles) which travel back into the central detector and reenter the calorimeter, creating a disconnected region that would ideally be associated with a track.

To address these difficulties we use the CDCC [64] program which matches each track to multiple clusters and *vice versa*. It tries every track-cluster combination. If a track passes within 8 cm of the cluster center (TYPE = 1), or within 8 cm of a crystal within the cluster (TYPE = 2), the cluster is matched to the track (and *vice versa*). All TYPE = 1 or 2 matched clusters are considered to belong to the track. The subtlety of the method comes in the calculation of the distance of approach. The matched energy E_{match} for a track is defined as the cluster energies summed over all clusters with TYPE = 1 or 2 matches to that track. For identifying electrons E_{match}/p_{track} is a very useful quantity.

4.1.4 Muon Identification

Muon identification is done with a set of dedicated detectors: the muon chambers described in Section 3.2.6. The muon identification package MUTR [65, 66] extrapolates DUET tracks and its error matrix with a muon hypothesis, taking into account specific ionization energy loss (dE/dx), multiple scattering, and curvature from magnetic fields. Muons in this analysis are identified using the SMID [67] software package which improves on the MUTR performance in the Monte Carlo simulation. In the data, SMID requires that DPTHMU ≥ 5 for tracks above 2.0 GeV/c in momentum and DPTHMU ≥ 3 for tracks with a momentum in the 1.5 - 2.0 GeV/c range, where DPTHMU denotes the maximum number of absorption lengths that the particle penetrates in the muon counters. Tracks with a momentum down to 1.0 GeV/c can penetrate the first set of counters in the muon chambers located at approximately 3 absorption lengths. However, these tracks are not utilized in this analysis because the muon identification efficiencies measured in the data are not well known [*] below a momentum of 1.5 GeV /c. SMID further requires that the penetrated depth be con-

---

[*] The 1.0 - 1.5 GeV/c momentum muons increase the sample size considerably. The smaller statistical errors obtained as a result of the increased statistics, and the inclusion of a more sensitive momentum region is offset by the fact that the errors on the Michel parameters are now dominated by systematic errors resulting from the poor knowledge of the muon identification efficiencies measured in the data using $\mu\mu$ and $\mu\mu\gamma$ events.

sistent with the expected depth determined from the track's momentum measured in the tracking chambers (MUQUAL = 0), that the total shower energy deposited in the calorimeter and matched to the track under consideration be less than 600 MeV , and that the track lie in the good barrel region of the detector defined by $\cos\theta \leq 0.71$, where θ is the polar angle of the track with respect to the beam axis.

In the Monte Carlo simulation, the SMID software package reads look-up tables with muon identification efficiencies and fake muon rates measured in the data. A real weight between 0 and 1 is set expressing the probability that the track is a muon. Finally, a logical flag is set if a random number is less than this weight.

4.1.5 Electron Identification

To identify electrons, we utilize the SEID [68] software package which relies upon two independent and powerful pieces of information: dE/dx measurements from the tracking chambers and the ratio of the energy measured in the calorimeter to the momentum of the track E/p. In the data, SEID requires that SGELDI > -2.0, where SGELDI is the difference between the measured dE/dx and the dE/dx expected for an electron divided by the resolution, and $E/p > 0.85$. The momentum of the track under consideration is also required to be greater than 500 MeV $/c$, since electron identification efficiencies (measured in the data using ee and $ee\gamma$ events) are both high and well understood above this minimum momentum requirement. The track is also required to lie in the good barrel region of the detector. In the Monte Carlo simulation, SEID reads look-up tables with run dependent electron identification efficiencies and fake electron rates measured in the data. A logical flag is set to identify the electrons in an manner identical to the one in the SMID software package described above.

4.1.6 Reconstruction of $\pi^0 \rightarrow \gamma\gamma$ Decays

Energy clusters are analyzed with the CCFC package. Unmatched barrel showers above 100 MeV in energy and lying in the good barrel region of the detector ($|\cos\theta| \leq 0.71$, where θ is the polar angle of the shower with respect to the beam axis) are used in the reconstruction of the π^0's. No requirement is made on either the quality or shape of the shower. This results in a high π^0 finding efficiency which is relatively insensitive to uncertainties in the modeling of photon showers in the CsI calorimeter and split-offs from hadronic showers by the GEANT-based Monte Carlo program.

Reconstruction of π^0 decays is well simulated by the Monte Carlo program, as seen in Figure 4.1. The distribution of the difference between the invariant mass, $m_{\gamma\gamma}$ and the π^0 mass, normalized to the mass resolution, $\sigma_{\gamma\gamma}$, is shown here. The mass resolution varies from 5 to 10 MeV depending on the photon energies and angles. The peak position, width, low mass tail, and background level are all well reproduced.

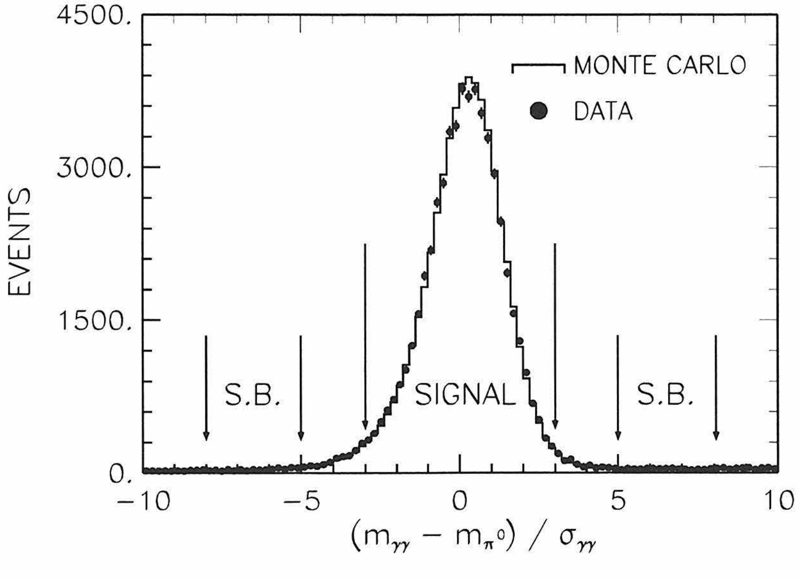

Figure 4.1: The difference between the $\gamma\gamma$ effective mass and the π^0 mass, normalized by the measurement error. This distribution includes both electron and muon mode events, and has been shifted by 0.5 σ to allow for symmetrical signal and sideband regions shown.

4.2 Event Selection

We use the 4S2-4SA data sample which comprises $\simeq 3.5$ pb^{-1} of data. The different data sets considered and their luminosities are listed in Table 4.1. From the luminosity-weighted cross section, the total sample corresponds to 3.2×10^6 produced tau-pairs.

Data Set	Collection Dates	Luminosity
4S2	Nov 1990 - Jun 1991	642 pb^{-1}
4S3	Sep 1991 - Feb 1992	620 pb^{-1}
4S4	Apr 1992 - May 1992	315 pb^{-1}
4S5	Jul 1992 - Oct 1992	322 pb^{-1}
4S6	Nov 1992 - Jan 1993	318 pb^{-1}
4S7	Mar 1993 - Jul 1993	463 pb^{-1}
4S8	Aug 1993 - Sep 1993	282 pb^{-1}
4S9	Nov 1993 - Jan 1994	347 pb^{-1}
4SA	Jan 1994 - Feb 1994	193 pb^{-1}

Table 4.1: Luminosity break-down for the different data sets considered in this analysis.

4.2.1 TAUSKM

The analysis begins with the tau skim cuts listed below. A skim is a set of loose preliminary event selection criteria performed to reduce the large initial data sample to a more manageable size. This skim is designed to provide an enriched sample of tau events without losing a significant number of these events. Since it is rarely possible that the skim requirements have no effect on the signal, skim cuts whose effects are well modeled by the Monte Carlo simulation are selected.

1. We require between two and six "good" charged tracks. A good track is defined as one with KINCD = 0 and $|\text{DBCD}| \leq 0.01$, where KINCD = 0 is the track classification for a good primary track, and DBCD is the signed impact parameter with respect to the run-averaged beam spot.

2. The total charge in the event $|\sum Q| \leq 1$, where Q is the charge of the tracks seen.

3. We require no more than one charged track with momentum greater than 85% of the beam energy, to reject Bhabha scattering $e^+e^- \rightarrow e^+e^-(\gamma)$ and mu-pair events $\mu^+\mu^- \rightarrow \mu^+\mu^-(\gamma)$.

4. The total visible energy in the electromagnetic calorimeter must be less than 85% of the center-of-mass energy, to reject Bhabha events.

5. We require the visible energy in the charged tracks (assumed to be pions) and neutral showers to be greater than 20% of the center-of-mass energy, to reject two-photon physics, cosmic rays, beam-gas events, and spurious triggers.

6. If the number of good tracks is five or six, we require KLASGL $\neq$ 10,11 to reject events identified as hadronic events, where KLASGL is a global event classification variable. Events satisfying this selection criteria are written into a separate data stream for offline analysis.

All other cuts applied are listed below and are specific to this analysis. The first set of cuts described are designed to select the event topology with a high efficiency. Additional cuts identify the lepton and tag side of the event. Finally, we list the cuts applied to minimize background contamination from a myriad of potential sources. Chapter 5 discusses these in detail.

4.2.2 Event Topology

Events with exactly two "good" tracks are selected. A track is defined to be a "good" track when in addition to KINCD ≥ 0, and $|\text{DBCD}| \leq 0.01$ as defined earlier, $|\text{PQCD}| \geq 0.1$, where PQCD is the signed track momentum. Events with three such defined good tracks are retained if TRKMAN [†] discards any one of the three tracks.

[†] TRKMAN attempts to clean up events by imposing careful track quality cuts and setting a flag when it decides a track is spurious. A track can be spurious for many reasons, as described earlier in this chapter.

The two good tracks are required to lie in opposite hemispheres, *i.e.*, separated by at least 90° in angle to ensure that they are produced from the two distinct tau leptons in the event. Further, we require charge conservation: $\sum Q = 0$.

Events with one and only one π^0 with an invariant mass, $m_{\gamma\gamma}$ lying within 3 σ of the π^0 peak (SIGNAL) are selected as shown in Figure 4.1. We note that the peak was shifted by 0.5 σ to make this a symmetric requirement. To estimate the combinatoric background, the sideband regions (S.B.): $5 < |(m_{\gamma\gamma} - m_{\pi^0})/\sigma_{\gamma\gamma}| < 8$ are used. The sideband subtraction also suppresses "feed-up" from $\tau \to \pi\nu_\tau$ events, where the random combination of showers result in a fake π^0. Events with more than two photons may result in multiple combinations. The combination with the lowest energy unused photon-like cluster in the barrel is selected. Photon-like clusters are unmatched clusters with $E_{clus} > 50\mathrm{MeV}$, E9/E25 greater than $P^{1\%}_{9/25}$, and lie more than 30 cm from the track. This choice does not force the combinatoric background to peak under the signal region. Hence, the sideband subtraction procedure is bias free.

The track that lies closer in angle to the reconstructed π^0 is assigned to be the hadron from the decay of the tag tau lepton. Using a Monte Carlo simulation of the decay topology, we find that the upper limit on the probability of this track assignment being wrong is 1.2×10^{-4} at 90% C.L. for events where the other tau lepton decays into a muon, and 3.0×10^{-5} at 90% C.L. for events where the other tau lepton decays into an electron. Since this wrong assignment probability is very small, it is neglected. No particle identification requirements are made on this track, but we do require that its momentum be larger than 300 MeV/c, and that it lies in the good barrel region of the detector (as defined earlier) to ensure good tracking and trigger efficiencies.

The track that lies further away in angle to the reconstructed π^0 is subject to lepton identification criteria and must be identified as either an electron or a muon. The SEID and SMID software packages are used to identify electrons and muons respectively. Both these packages treat the data and the Monte Carlo simulation events differently as described earlier in this chapter.

The event should trigger at least one of the seven non-prescaled trigger lines. All events are also required to pass the Level 3 trigger selection criteria.

4.2.3 Cuts to Minimize Backgrounds

Stringent requirements are made to exclude any events with unused showers in the electromagnetic calorimeter. These requirements are designed to minimize the feed-down of multi-π^0 tau decay modes into the tag mode. The tag mode is used to reconstruct the pseudo rest frame spectrum, and the presence of feed-down modes would bias this spectrum. The highest energy unused shower in the good barrel region must satisfy $E_{clus} < 75$ MeV, and the highest energy unused shower in the endcaps ($0.71 < |\cos\theta| < 0.95$) must satisfy $E_{clus} < 125$ MeV. This veto on the event is applied only if the unused shower is isolated (more than 30 cm from closest track) and if its E9/E25 is greater than $P^{1\%}_{9/25}$. Clusters which lie within 30 cm of each track are ignored as they are often due to final state or decay radiation, bremsstrahlung and/or hadronic split-offs. Events with high energy unused showers which do not pass the photon-like selection criteria are discarded if the energy is greater than 125 MeV in the barrel or greater than 250 MeV in the endcaps. In the "hot" region ($|\cos\theta| > 0.95$), an event is discarded if there are any showers with energies greater than 500 MeV. These veto requirements are further discussed in Section 5.1.2.

Cosmic ray events in the muon analysis are reduced by requiring that the two tracks are not back-to-back: $|\vec{p_1} + \vec{p_2}|/(|\vec{p_1}| + |\vec{p_2}|) > 0.05$, where $\vec{p_1}$ and $\vec{p_2}$ are the momentum vectors of the hadron and the lepton track respectively. Radiative Bhabha contamination in the electron analysis is minimized by requiring that the track assigned as the hadron in the event be inconsistent with being an electron, *i.e.*, the SEID software package should **not** identify it as an electron. The average of the z-positions for the two tracks, ZVPTX at the point of intersection of the two tracks in the xy plane, is required to be less than 0.05.

The momentum spectrum for all events that survive all the above listed criteria is utilized to measure the Michel parameters as described in Chapter 7.

Chapter 5 Backgrounds

Figure 5.1 shows the classification of backgrounds due to all possible sources. Fake leptons are the single most dominant source of backgrounds and are described in detail in Section 5.1.1. Fake muons are significant and a background subtraction is performed to remove their contribution. Feed-down from other tau decays mimicking $\tau^- \rightarrow h^- \pi^0 \nu_\tau$ decays is minimized and discussed in Section 5.1.2. All other backgrounds are heavily suppressed by selection criteria. All non-τ background sources (including the two-photon production of tau-pairs) are estimated to total less than 1% for each mode.

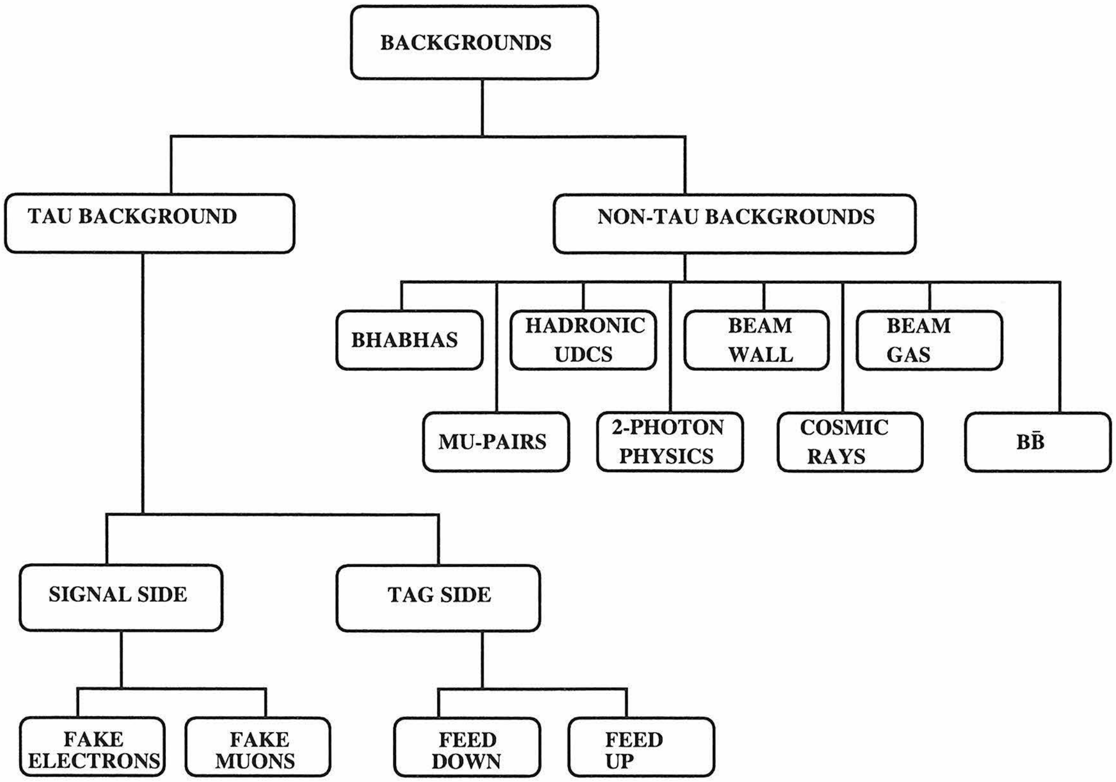

Figure 5.1: All potential background sources.

5.1 τ Background

Feed-across from tau-pair decays is the dominant background source. Fake leptons feed into the signal side of the event and tau decays into modes with multi-π^0's feed into the tag side of the event.

5.1.1 Fake Leptons

The data events in this analysis ($\ell - h\pi^0$), and closely related data events, are utilized to estimate the fake lepton background spectrum. First, we calculate the probability that a hadron fakes a lepton signal, and then we estimate the number of hadrons in the sample that could potentially fake the lepton signal. The product of the momentum dependent fake rates and the potential hadronic spectrum results in a good estimate of the fake lepton spectrum. The momentum dependence and normalization of this background spectrum are estimated entirely from the data. Knowledge of the background spectrum's momentum dependence is crucial to this analysis, since the Michel parameters are measured from the shape of the lepton momentum spectrum.

The leptons in this analysis are identified as e or μ and the hadron is "tagged" by requiring a nearby reconstructed π^0. The probabilities that hadrons fake leptons $P(h \rightarrow e)$ and $P(h \rightarrow \mu)$ are obtained by applying the lepton identification criteria to the hadronic track (tag decay mode) in the event. Events with two leptons and a fake π^0 in this sample could potentially bias the fake probabilities. Such events arise from radiative lepton-pairs and are heavily suppressed by the selection criteria. Further, the small remaining fake-π^0 backgrounds ($\simeq 2\%$ of the sample) are explicitly removed with a π^0-sideband subtraction of the probabilities. The e-tag and μ-tag samples have consistent fake rates after this subtraction, yielding no indication of any residual lepton contamination in the hadron sample.

The parent hadron distribution is obtained by examining the track recoiling against the $h\pi^0$ system in the data. Here, by discarding all identified electrons and muons, we obtain a hadron distribution normalized to the data sample. This parent hadron sample contains hadrons from all possible sources, including the decays of intermediate resonances such as the $\rho^{\pm}$ or the $a_1^{\pm}$, where the photons from π^0 decay are not found, or do not satisfy our criteria for vetoing the event. It also contains real electrons and muons which do not satisfy the lepton identification criteria, but, since the lepton identification efficiencies are close to 100% in the region of interest (above 0.5 GeV/c in the electron mode and above 1.5 GeV/c in the muon mode), this lepton contamination in the hadron sample is small. Hadrons which fake leptons are depleted in this hadronic sample, since they were identified as leptons and thus removed. Again, this is a small effect since the fake probabilities are small as shown below.

Electron Fakes

Electrons are identified using E/p and dE/dx. Since the two identification criteria are independent, the probability for a hadron to pass each requirement separately is measured, and the two resulting probabilities are multiplied together for each momentum bin. The resulting fake probabilities are shown in Figure 5.2 as a function of the hadron charge and the momentum. At low momentum, the probability that a positive hadron showers in the cesium iodide is higher, thereby satisfying the E/p criterion. Thus, positive hadrons have higher fake rates below 2.5 GeV/c.

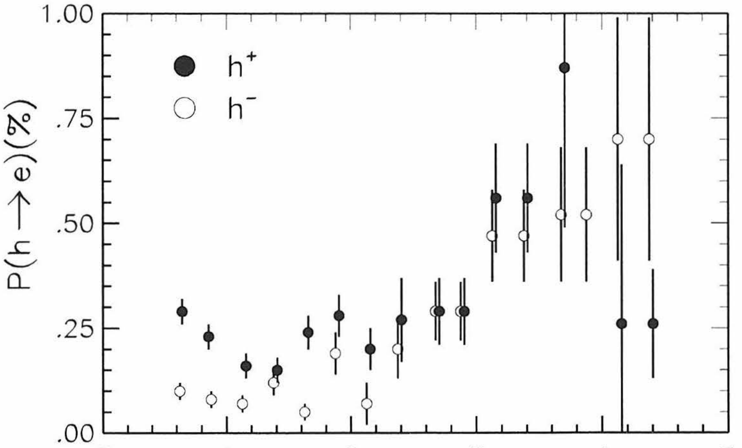

Figure 5.2: Probability for a hadron to be identified as an electron as a function of the momentum and charge of the hadron. The errors are both statistical and systematic.

Backgrounds, variations of rate with angle, and the π/K content relative to that of fake electrons in the signal sample can lead to systematic effects and increase the errors on the measured fake rates from ± 5% to ± 15% (integrated over momentum).

The fake electron rate ranges from 0.1-0.5%, depending on the momentum and the charge of the hadron considered. Since this rate is small, fake electrons are neglected in the nominal calculations and a systematic error is evaluated to cover the resulting bias.

Muon Fakes

Muons are identified using DPTHMU ≥ 3 for $1.5\ \mathrm{GeV}/c \leq p_\mu < 2.0\ \mathrm{GeV}/c$ and DPTHMU ≥ 5 for $p_\mu \geq 2.0\ \mathrm{GeV}/c$, MUQUAL $= 0$, and $\sum_S E_S \leq 600$ MeV, where DPTHMU denotes the maximum number of absorption lengths that the particle penetrates in the muon counters, MUQUAL $=0$ denotes that this depth is comparable with the expected range determined from the track's momentum in the drift chambers, and $\sum_S E_S$ denotes the total shower energy matched to the track. Approximately one-third of all hadrons deposit more than 600 MeV in the electromagnetic calorimeter as shown in Figure 5.3. The few muons that deposit more than 600 MeV in this figure are probably hadrons that have been misidentified as muons.

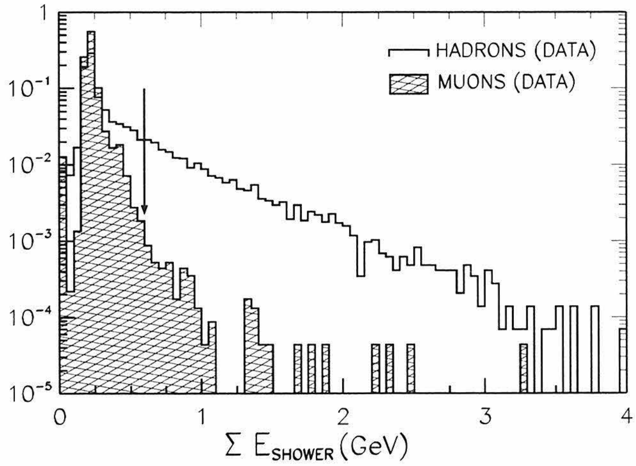

Figure 5.3: The total shower energy associated with the hadronic (histogram) and muonic (hatched region) tracks in the data sample. Both energy spectra have been normalized to unity.

The determination of the fake muon probabilities and their momentum dependence are described in detail in Appendix B. The probability that a hadron would fake a DPTHMU = 3, 5, 7 signal in the muon counters, shown in Figure B.2, were obtained after the addition of the total shower energy cut described above. Above 2.0 GeV/c momentum, the fake muon rate ranges from 1.5 - 3.0% depending on the momentum, and below 2.0 GeV/c the fake muon rate is as high as 8%. We further note that the Monte Carlo simulation of these fake probabilities does not identically reproduce the data [69, 70] *.

To obtain an estimate of the fake muon spectrum, we now need a good estimate of the parent hadron distribution normalized to this data sample. Following the procedure described earlier in the section, we obtain using the data, the distributions shown in Figure 5.4(b) before and after the application of the total shower energy cut. These distributions are normalized to the muon momentum distributions shown in Figure 5.4(a) and include hadrons from all possible sources. The maximum shower energy requirement clearly reduces the hadronic sample, but leaves the muon sample approximately unchanged.

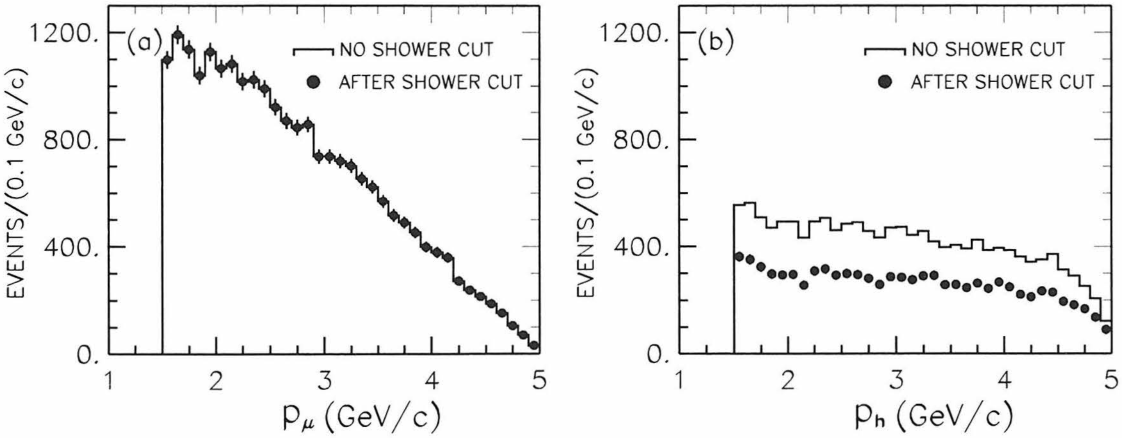

Figure 5.4: The figure on the left (right) shows the muon (hadron) momentum spectrum before and after the application of the maximum shower energy requirement. All distributions have been obtained in the data and are absolutely normalized with respect to each other.

---

[*] This exercise to measure the fake rates using the data was redone by other members at CLEO [71] with a larger data set, and the Monte Carlo simulation has now been tuned to read in the fake rates as measured in the data.

The bin by bin product of the momentum dependent fake rates and the parent hadron distribution leads to a momentum dependent estimate of the fake muon spectrum normalized to the muon sample. This estimate is obtained entirely from the data and is approximately 1% integrated over the momentum range studied in this analysis. In Figure 5.5 we show the momentum dependence of this fake muon spectrum in the laboratory frame (a) and the pseudo rest frame (b). The hatched histograms indicate the shape of the corresponding muon signal.

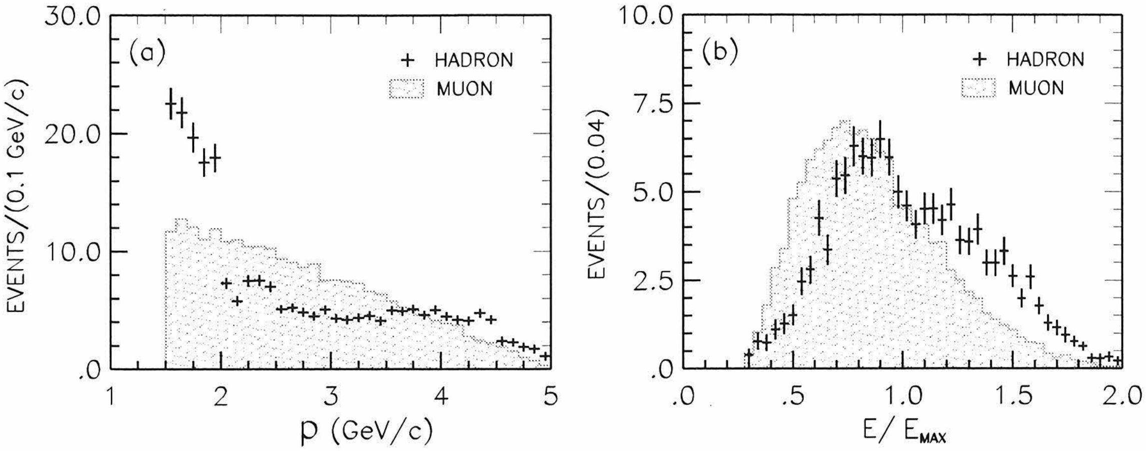

Figure 5.5: The fake muon momentum spectrum used in the subtraction in the laboratory frame (pseudo rest frame) analysis is shown in the figure on the left (right). The hatched spectra illustrate the shape of the muon spectra. The number of events in the muon spectrum has been normalized to the number of events in the fake muon spectrum to compare the shapes.

Although the background contamination from fake muons is small ($\approx 1\%$), it is important since this background clearly alters the shape of the spectrum. The fake muon spectrum is subtracted from the signal momentum spectrum before the fit is performed to obtain the Michel parameters. Both the normalization and the shape of the subtracted background spectrum are varied to obtain a systematic error arising from the imperfect estimation of the fake spectrum used in the subtraction procedure.

5.1.2 Feed Across Into Tag $\tau \rightarrow h\pi^0\,\nu_\tau$ Mode

In Table 5.1, we list all significant tau decay modes that can feed across into the tag $\tau^+ \rightarrow h^+\pi^0\,\bar{\nu}_\tau$ mode. Both the branching ratio (Particle Data Group 1996 [72]), and the detection efficiency, as determined using the generic tau Monte Carlo simulation of these events, are shown in this table. The ratio of the product of these two variables for each feed-across mode to the sum of the products for all possible modes indicates the amount of contamination from each mode.

Tag	$\mathcal{B}$ (%)	ϵ (%)		$\mathcal{B} \times \epsilon \times 10^{-4}$	
		e	μ	e	μ
$h^+\bar{\nu}_\tau$	12.03 ± 0.14	< 0.001	< 0.001	< 0.01	< 0.01
$h^+\pi^0\,\bar{\nu}_\tau$	25.76 ± 0.15	10.54 ± 0.03	7.46 ± 0.03	271.51 ± 1.76	192.17 ± 1.36
$h^+2\pi^0\,\bar{\nu}_\tau$	9.50 ± 0.14	0.39 ± 0.01	0.33 ± 0.01	3.71 ± 0.11	3.14 ± 0.11
$h^+3\pi^0\,\bar{\nu}_\tau$	1.28 ± 0.10	< 0.001	< 0.001	< 0.001	< 0.01
$h^+4\pi^0\,\bar{\nu}_\tau$	$(1.8 \pm 0.6) \times 10^{-3}$	< 0.001	< 0.01	< 0.001	0.01 ± 0.01
$K^0\pi^+\pi^0\,\bar{\nu}_\tau$	$(4.1 \pm 0.6) \times 10^{-3}$	2.64 ± 0.10	1.72 ± 0.08	0.01 ± 0.01	< 0.01
$K^0K^+\pi^0\,\bar{\nu}_\tau$	$(1.38 \pm 0.32) \times 10^{-3}$	2.36 ± 0.21	1.41 ± 0.16	< 0.01	< 0.01
$K^+K^0\bar{\nu}_\tau$	$(1.55 \pm 0.28) \times 10^{-3}$	0.05 ± 0.03	0.08 ± 0.04	< 0.01	< 0.01
$\pi^+\eta\pi^0\,\bar{\nu}_\tau$	$(1.71 \pm 0.28) \times 10^{-3}$	0.01 ± 0.01	0.01 ± 0.01	< 0.01	< 0.01
$\pi^+\omega\bar{\nu}_\tau$	1.91 ± 0.09	0.35 ± 0.07	0.61 ± 0.10	0.67 ± 0.14	1.17 ± 0.20
$\pi^+\omega\pi^0\,\bar{\nu}_\tau$	$(4.1 \pm 0.6) \times 10^{-3}$	0.01 ± 0.01	0.01 ± 0.01	< 0.01	<0.01
All modes				275.90 ± 1.77	196.49 ± 1.38

Table 5.1: Feed-down and feed-up modes for both the muon and electron sample. $\mathcal{B}$ denotes the input Particle Data Group (1996) branching ratios and ϵ denotes detection efficiency as determined by the generic tau Monte Carlo simulation. All errors are statistical only. The ω particle in the last two entries in the table decays via the decay mode $\omega \rightarrow \pi^0\gamma$. The sum over the products of the branching ratio and the efficiency for each of these modes is used in the branching ratio calculation shown in Chapter 6.

We note that multi-π^0 modes feed-down into the tag mode when one or more of the π^0's in the decay are not reconstructed. The largest background contamination results from the feed-down of the $\tau^+ \rightarrow \pi^+2\pi^0\,\bar{\nu}_\tau$ decay mode. This feed-down is minimized by the application of cuts on the highest energy, isolated unused [†] showers in both the barrel and endcap regions of the CLEO II detector. After these cuts, we find that the background from this mode is $(1.34 \pm 0.04)\%$ in the electron sample and $(1.60 \pm 0.05)\%$ in the muon sample. Removing the extra energy veto requirements, these background levels are as much as ten times these levels.

In Figure 5.6 we show on a logarithmic scale, the energy distribution of the highest energy unused shower in the barrel region defined by $|\cos\theta| \leq 0.71$, where θ is the polar angle of the photon with respect to the beam axis. The photons in the distribution on the top of this figure survive "good" photon selection defined by the 1% E9/E25 cut and lie more than 30 cm from the closest track. The photons in the second distribution all fail these two criteria. The nominal cuts applied on these distributions are indicated by the arrows. We require that the event not have any isolated unused shower passing the photon quality requirement above 75 MeV in energy. For showers which fail the photon quality and distance requirements, this maximum energy allowed is raised to 100 MeV.

We note that the agreement between the data and the generic τ Monte Carlo simulation which includes the feed-down modes is reasonably good, even out to large energies. The difference between the signal Monte Carlo distribution and the generic τ Monte Carlo distribution indicates the size of the feed-down. These veto requirements remove signal events with radiative photons, hadronic split-offs and/or beam related showers. These photons are all modeled in the Monte Carlo simulation. The systematic error associated with their imperfect modeling are addressed in Section 9.

In Figure 5.7 the distributions for the highest energy unused isolated showers in the endcap region of the detector are shown. Once again the figure on the top plots photons that survive the photon quality requirement, while the figure shown on the bottom plots showers that fail this requirement. The veto cuts applied in the endcap region of the detector are looser than the corresponding cuts in the barrel region on the detector, since photons in the endcaps are not as well simulated as the ones in the barrel. Further, the beam related noise is more in the endcap region, and the

---

[†] An unused shower is one that is not used to reconstruct the π^0.

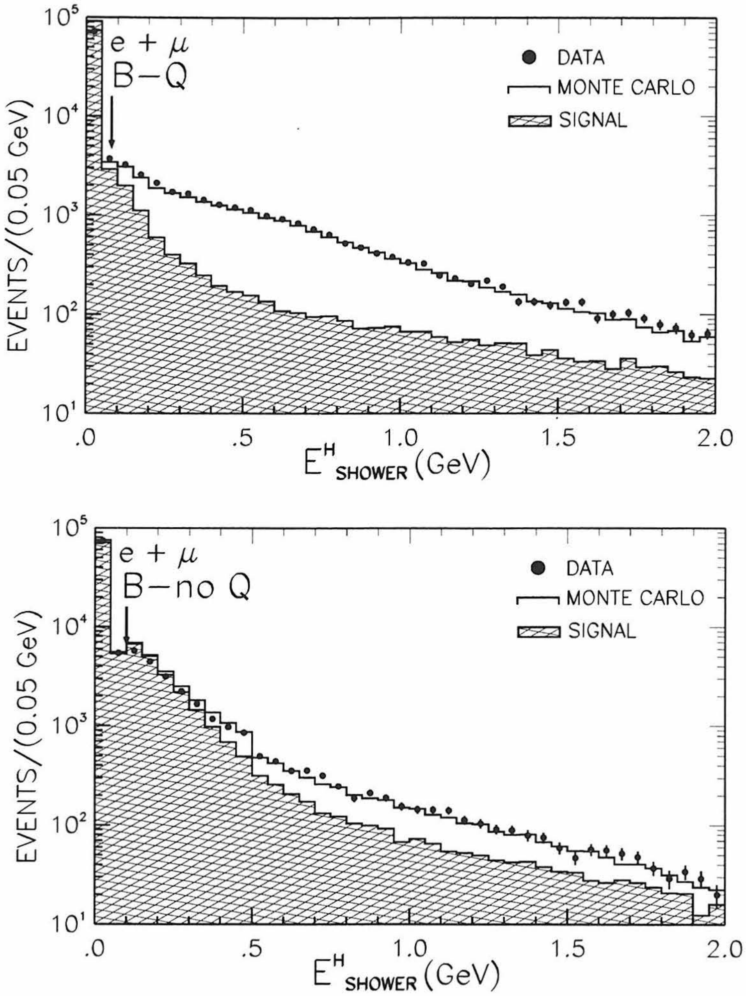

Figure 5.6: The distributions for the single highest energy unused shower in the BARREL region of the detector. The distribution on the top includes all the highest energy showers which survive some photon quality requirements, while the distribution shown at the bottom plots the highest energy shower which fails the photon requirements.

simulation of the drift chamber end plate material lying in front of the endcap crystals is not perfect. We require that the maximum shower energy for showers that survive (fail) photon quality cuts is 125 MeV (150 MeV).

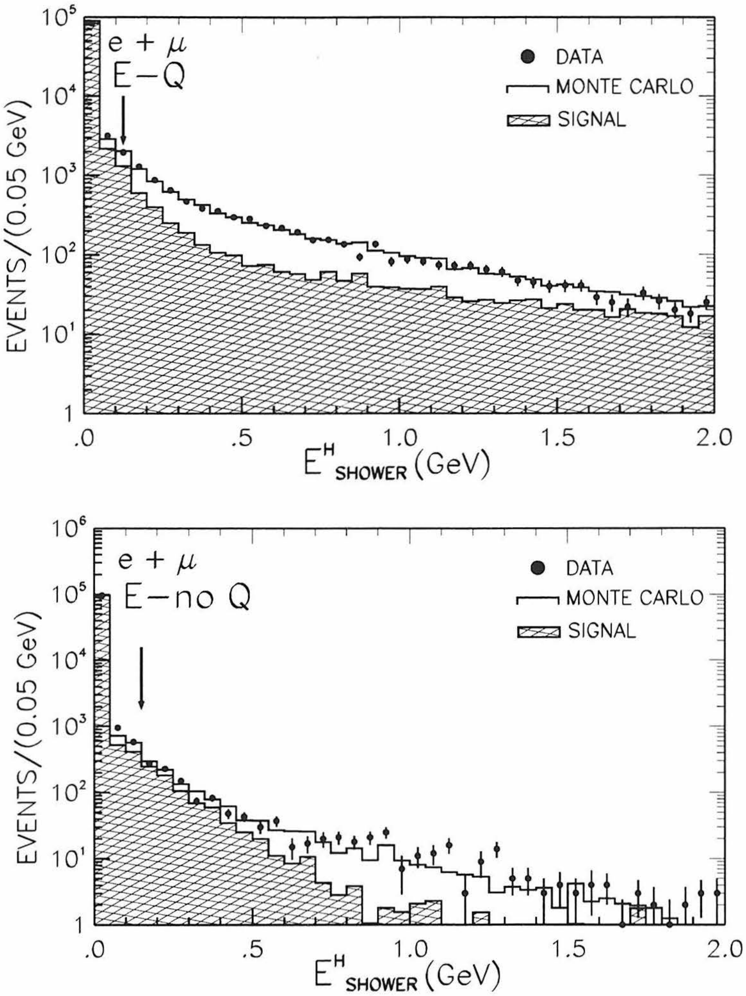

Figure 5.7: The distributions for the single highest energy unused shower in the ENDCAP region of the detector. The distribution on the top includes all the highest energy showers which survive some photon quality requirements, while the distribution shown at the bottom plots the highest energy shower which fails the photon requirements.

All the efficiencies listed in Table 5.1 have been calculated after the application of these veto requirements as well as all other selection cuts with the exception of the $\cos\alpha$ requirement used to select events for the pseudo rest frame analysis. Events that survive either the electron mode or the muon mode selection criteria are included in each of these figures.

The 1-3% feed-down is relatively unimportant for the laboratory frame analysis, since the lepton side of the event is in principle independent of the tag side. Global cuts and the trigger do correlate the two sides of the event to a small degree, but this effect is negligible. On the other hand, this feed-down becomes increasingly important for the pseudo rest frame analysis, where the tag mode is directly utilized to reconstruct the pseudo rest frame of the lepton. After the application of the $\cos\alpha$ requirement, the background from feed-down modes is reduced to the 1.5-2.0% level; the $\cos\alpha$ distribution peaks at lower $\cos\alpha$ for feed-down events as shown in Figure 5.8. The remaining background is well modeled in the Monte Carlo simulation, and any uncertainties associated with the imperfect modeling of the remaining background is evaluated in Section 9.6.3.

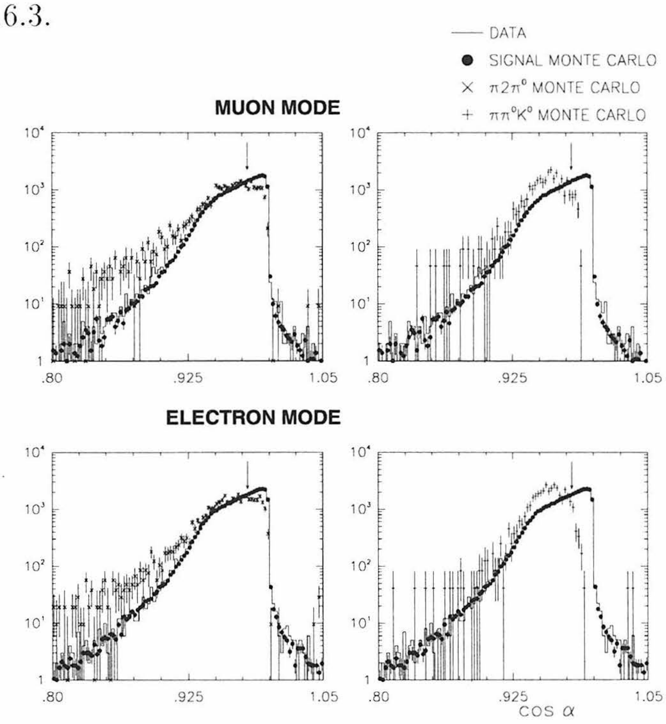

Figure 5.8: $\cos\alpha$ plots for the data (solid histogram), the signal Monte Carlo (dots), as well as the two most significant feed-down modes. The background has been normalized to the data.

5.2 Non-τ Backgrounds

In this section, we consider all the non-tau background sources listed in Figure 5.1. First, cosmic-rays, mu-pairs, beam wall and beam gas events can enter the sample. Second, two photon events $e^+e^- \rightarrow e^+e^-\tau^+\tau^-$, in which the two electrons escape detection by the CLEO II detector at low polar angles can survive the selection criteria. Third, radiative Bhabha events can fake the π^0 in the event and enter the electron sample. Finally, we consider the hadronic *udsc* [‡] and $B\overline{B}$ backgrounds. Data is used wherever possible to confirm that each of these background sources can be neglected.

5.2.1 Cosmic Rays, Beam Gas and Beam Wall Events

These background events typically have uniformly distributed vertex Z-positions, as opposed to collision related events, which have a roughly triangular distribution centered at zero and extending out to ±4 cm. These sources tend to produce tracks in one hemisphere and not from the beam spot.

The two tracks in the event are used to reconstruct the event vertex. At the point where the two tracks intersect in the xy plane, we calculate the average of the z-positions for the two tracks at their respective points of closest approach to the beam center in $r - \phi$, ZVPTX. In Figure 5.9, we show on a logarithmic scale the distribution of ZVPTX for the data and the Monte Carlo simulation for all events that survive either the electron or the muon sample selection criteria. We note that the two distributions agree well in the peak region with slightly larger tails observed in the data. In the electron (muon) Monte Carlo sample, 0.0008% (0.0011%) of all events fall outside the $|\text{ZVPTX}| \leq 0.05$ requirement indicated by the arrows in the figure. These events are probably a result of poorly reconstructed track z measurements. In the electron (muon) data sample, 0.0013% (0.0016%) of all events fall outside the allowed ZVPTX region. This excess of events in the data samples is used to estimate the background contamination from these sources. Assuming a flat

---

[‡] $e^+e^- \rightarrow q\bar{q}$ $(q = u, d, s, c)$

distribution for the background sources, we estimate that there is a 0.05% (0.06%) background contamination in the electron (muon) sample.

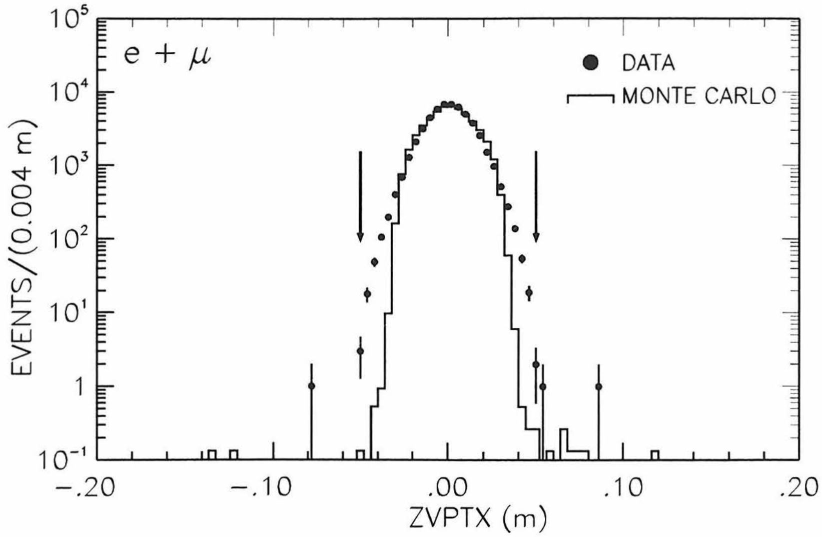

Figure 5.9: Distribution of the ZVPTX variable in the data and the Monte Carlo samples. These distributions include events that survive either the electron or the muon selectrion criteria.

The background contamination is negligible; several different requirements help contain the contamination. The TAUSKM requirement that the total visible energy of the event be at least 20% of the center of mass energy rejects cosmic rays and two-photon physics events. Another TAUSKM requirement: there be at most one track with momentum greater than 85% of the beam energy rejects mu-pair events. The full reconstruction of the π^0 in the event further reduces the contamination from all these sources and the $|\vec{p_1} + \vec{p_2}|/(|\vec{p_1}| + |\vec{p_2}|) > 0.05$ requirement contains the contamination from any remnant cosmic ray events. This constraint also helps minimize any contamination from $\mu\mu$ events.

5.2.2 Two Photon Physics

Two-photon events are usually low in visible energy and in visible p_t with respect to the beam. Both these quantities are calculated using only the charged pion, the charged lepton, and the π^0 in the event. The tracks are corrected for dE/dx energy losses before they are used to reconstruct these variables. The figure on the left in Figure 5.10 shows the p_t distribution, and the figure on the right shows the distribution for the visible energy scaled to the beam energy. All events that survive either the electron or muon selection criteria are included in these figures. We note that the data and the Monte Carlo simulation agree extremely well, especially in the region close to the cuts indicated by the arrows. There is no excess above the nominal cut requirement and thus we conclude that there is no evidence for any contamination from this source.

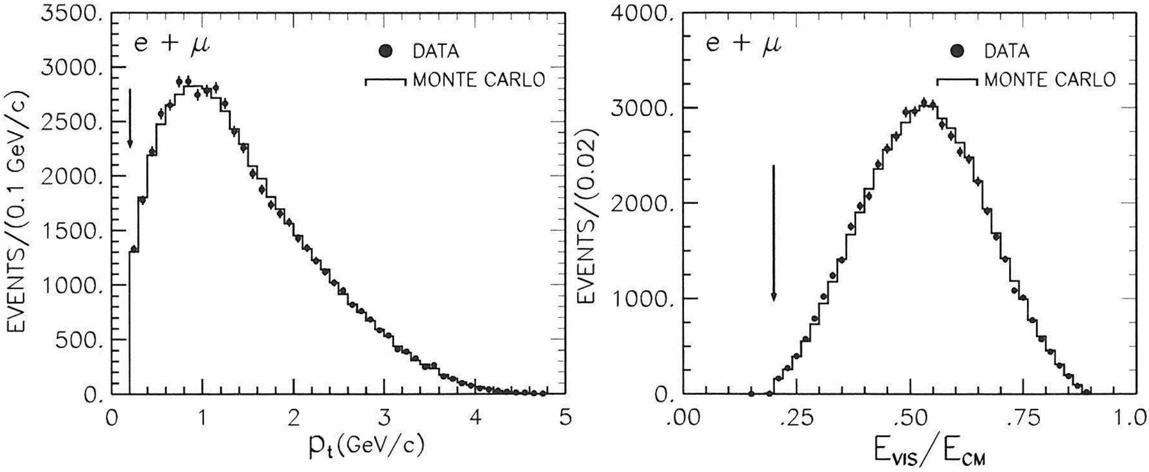

Figure 5.10: Distributions of the visible p_t and the visible energy scaled to the beam energy. Both these plots have been made after the application of all selection criteria.

To confirm that no two-photon events survive the above requirements we use the variable Θ_{min} [73], which is the minimum polar angle that at least one unseen particles must have for the event to conserve both energy and momentum. The angle is defined by:

$$\Theta_{\mathrm{min}} = \sin^{-1}\left(\frac{p_t}{2E_{\mathrm{beam}} - p_1 - p_2}\right) , \qquad (5.1)$$

where p_t is the net transverse momentum, E_{beam} is the beam energy, and x_1, x_2 are the momenta of the two charged tracks in the event. For any unseen particles (other than neutrinos) to escape detection, Θ_{min} must be below the minimum angle covered by the electromagnetic calorimeter, about 11°. Hence all two-photon events that pass the nominal requirements imposed to suppress them must populate only the region with $\Theta_{\mathrm{min}} < 11°$ (the case where both beam electrons travel down the beam pipe), while tau decays can populate all angles, because the invisible neutrinos can carry off momentum in any direction.

In Figure 5.11, data and tau-pair Monte Carlo events are overlaid in the variable Θ_{min}. We do not observe any excess of data over Monte Carlo events in the region below 11°, indicated by the arrow in the figure. We conclude that the background from two-photon physics is less than 0.1% and is neglected.

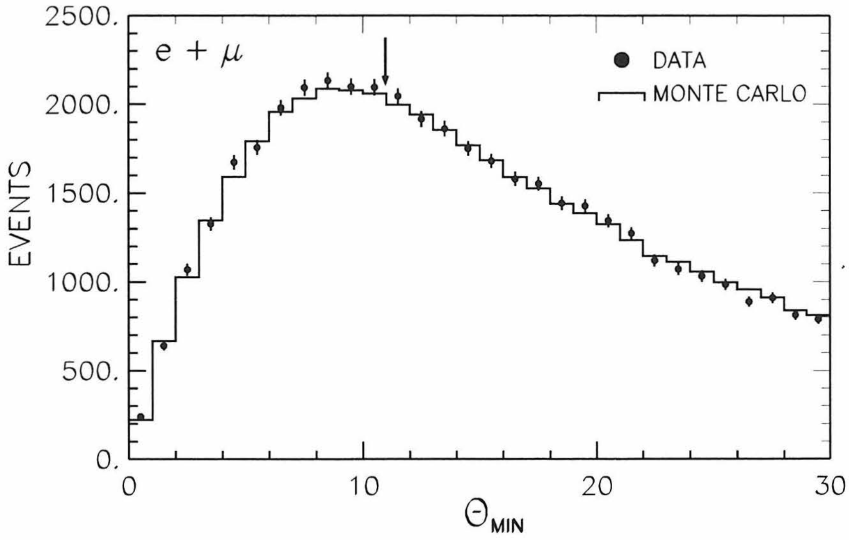

Figure 5.11: Distribution of the Θ_{min} variable in the data and the tau-pair Monte Carlo samples. These distributions include events that survive either the electron or the muon selectrion criteria.

5.2.3 Bhabha Events

The cross section for $e^+e^- \rightarrow e^+e^-$ is quite large compared to the final states used in this analysis. Thus, the selection criteria must suppress this process by a factor of roughly 10^6 to attain less than 1% contamination. In the muon mode analysis, the muon identification renders this background source negligible since electrons rarely fake muons. In the electron mode analysis, the TAUSKM cuts #3 and #4 (see Section 4.2.1) reduce the contamination from these events. The full reconstruction of the π^0 in the event helps reduce contaminations from Bhabha events among many other sources.

Radiative Bhabha events, however, can fake the $e - h\pi^0$ signal when random combinations of photon-like showers form a fake π^0. The π^0 sideband subtraction should eliminate these events. In addition, we require that the hadronic track in the event not be identified as an electron by requiring that its $E/p \leq 0.9$, where $p = |PQCD|$ is the momentum of the track closer in angle to the reconstructed π^0, and E is the sum over all CCFC shower energies matched to the track under consideration. In Figure 5.12, we plot the E/p distributions for the hadronic tracks in the electron and muon samples in the data. Both histograms shown here are prior to the sideband subtraction procedure. The excess of events in the electron sample over the muon sample above $E/p = 0.9$, indicated by the arrow, shows the radiative Bhabha events that survive the selection criteria. After the sideband subtraction, this excess disappears. The net effect of this requirement is to reduce the size of the π^0 sideband subtraction.

Another test of the negligible radiative Bhabha background is the Θ_{min} variable shown in Figure 5.11. The presence of these events in the data would result in an excess of events in the $\Theta_{\text{min}} < 11^\circ$ region. We do not observe any such excess after all cuts, including the E/p cut on the hadronic track and the π^0 sideband subtraction.

One can utilize the charge-weighted polar angle distribution in Figure 5.13 to check that Bhabhas do not contaminate the sample. Both tracks from each event are entered with their respective $\cos\theta$ multiplied by charge in this figure. Bhabha

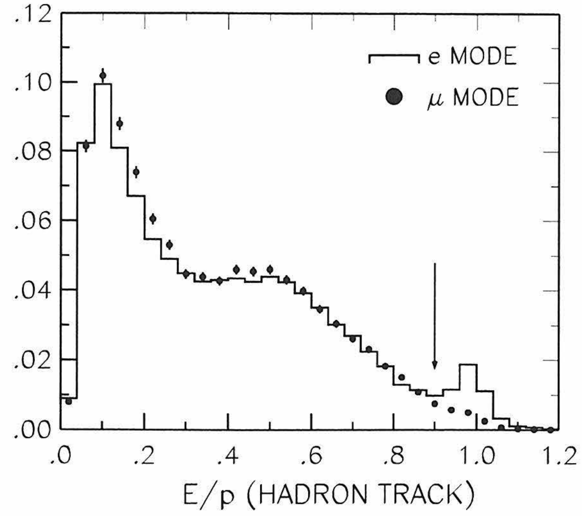

Figure 5.12: E/p distributions of the hadron track in the data before the sideband subtraction and E/p cuts are applied. The excess of events in the electron sample over the corresponding muon sample, above the $E/p \leq 0.9$ cut-off indicates the presence of the Bhabha background removed by the sideband subtraction procedure.

events are heavily asymmetric due to the t channel diagrams and would result in large asymmetries in the extreme $\cos\theta$ bins. The mean of the data histogram is 0.0080, consistent with zero and with the tau-pair Monte Carlo simulations. There is no evidence for any Bhabha background in this distribution. This background is estimated to be less than 0.2% and is neglected.

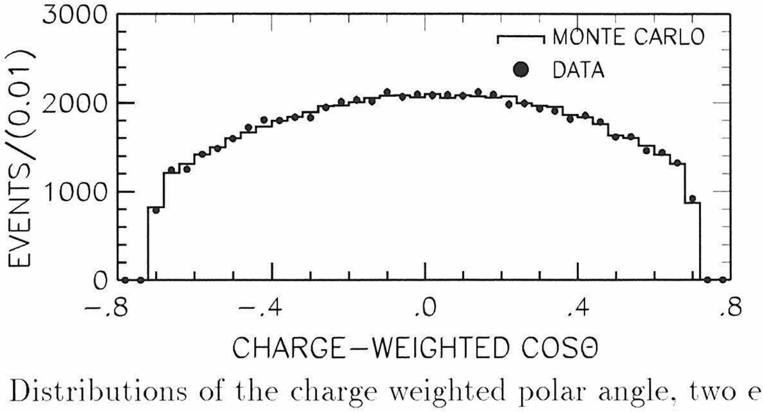

Figure 5.13: Distributions of the charge weighted polar angle, two entries per event, for the data (dots) and the Monte Carlo simulation (solid histogram).

5.2.4 Hadronic Backgrounds

Hadronic events can be produced from e^+e^- annihilations and from two-photon collisions. The former have high charged particle multiplicities and little missing energy, whereas the latter typically result in events with low visible energy and visible p_t. Cuts on all these quantities help minimize this background source.

The entire event selection was run on 1.5×10^6 fully-simulated *udsc* events; two events survived the selection criteria. Taking the ratio of the *udsc* cross section to the radiatively-corrected tau-pair cross section to be 3.6, one would expect eight such events in this sample. Since this corresponds to only 0.05% of the total events, this background source can be neglected.

One expects that running on fully simulated $B\overline{B}$ events, with the $B\overline{B}$ cross section of 1.07 nb, would lead to approximately zero events surviving the selection criteria. Thus this background source is neglected.

Chapter 6 Yields and Branching Ratios

While it is not an intent of this analysis to measure the electronic and muonic branching ratios of the tau lepton, this chapter presents the results obtained in a simple analysis to measure these branching ratios. No attempt has been made to minimize the systematic errors listed here. The latest CLEO II measurements for these branching ratios can be found in reference [8].

The leptonic branching ratio is computed using:

$$\mathcal{B}(\tau^- \to \ell^- \overline{\nu}_\ell \nu_\tau \ ) = \frac{N_S(1 - f_B)}{2\ N_{\tau\tau}\ \sum_i(\mathcal{B}_i \times \epsilon_i)}, \tag{6.1}$$

where N_S is the number of events surviving all cuts [*] including the π^0 sideband subtraction, f_B is the fraction of the leptons that are truly backgrounds (*e.g.*, hadrons faking leptons), $N_{\tau\tau}$ is the total number of produced $\tau\tau$ events, ϵ, the tag dependent efficiency, and $\mathcal{B}$ is the tag mode branching ratio. The sum i includes the tag decay mode $\tau^+ \to h^+\pi^0\overline{\nu}_\tau$, along with all other tau decay modes that feed across into the tag mode (see Table 5.1). The overall reconstruction efficiencies for all contributing modes is obtained from the generic tau Monte Carlo simulation, and the 1996 PDG [72] branching ratio values are used for all contributing modes. The Monte Carlo sample used in these calculations is approximately a factor of five larger than the data sample [†].

The total number of produced $\tau\tau$ events is given by:

$$N_{\tau\tau} = \mathcal{L}\sigma_{\tau\tau} = \sum_{\text{runs}}(\int \mathcal{L}\ dt)_{\text{run}} \frac{(86.86\ nb)}{E^2_{\text{CM-run}}}(1+\delta)\ , \tag{6.2}$$

---

[*] The $\cos\alpha$ requirement used to select events suitable for the reconstruction of the pseudo rest frame spectrum is ignored here.

[†] The Michel parameter analysis uses a Monte Carlo sample that is twice the size of the generic tau Monte Carlo sample used for the branching ratio calculations. The additional 50% events comes from the Monte Carlo generation of the signal modes only.

where $\mathcal{L}$ is the integrated luminosity, $\sigma_{\tau\tau} = 86.856$ nb-GeV^2/s is the luminosity-weighted, radiatively-corrected cross section for $e^+e^- \to \tau^+\tau^-$, and $(1+\delta)$ is the radiative correction factor.

The KORALB Monte Carlo simulation package calculates the required continuum cross section, including mass and spin effects, Z° propagator effects, and the radiative corrections to order α^3. The radiative correction to the point cross section is $(1+\delta) = 1.173$, approximately constant in the 10.5 - 10.6 GeV center of mass energy range utilized, with a 1% theoretical error due to the uncertainty in the $\mathcal{O}(\alpha^4)$ corrections.

The data used here were obtained with the CLEO II detector in running periods covering the energies below, and at the $\Upsilon(4S)$ resonance (10.52-10.58 GeV). Since tau events created via the $e^+e^- \to \Upsilon(4S) \to \tau^+\tau^- X$ process are expected to have many tracks in the event, and tau events resulting from the decay of the $B\overline{B}$ in $e^+e^- \to \Upsilon(4S) \to B\overline{B}$ can be neglected as a result of the small $B \to \tau\bar{\nu}_\tau$ branching fraction, it is assumed that all the $\tau\tau$ events come from the continuum, and none from the decay of the Υ_{4S}. The cross section $\sigma(e^+e^- \to \Upsilon(4S) \to \tau^+\tau^-)$ is expected to be approximately 0.01 pb.

The integrated luminosity for each data set used here has been measured using wide angle Bhabha scattering events, $e^+e^- \to \gamma\gamma$ events, and μ-pairs separately with errors of 1.3%, 1.1% and 2.0% respectively. The three methods used all give consistent results, although the QED cross section computations are different, and different trigger lines are important. The results for the three processes are averaged, and the overall systematic error on the luminosity determination is estimated to be 1.0% [74, 75, 76, 77].

Considering the muon sample, the nominal cuts give $N_{\tau\tau} = (2705 \pm 40) \times 10^3$, $\sum_i(\mathcal{B}_i \times \epsilon_i) = (196.49 \pm 1.38) \times 10^{-4}$ (the sum over all modes contributing to the tag mode as shown in Table 5.1), $N_S = 18652$, and $(1 - f_B) = 0.989 \pm 0.001$. Using Equation 6.1, we get:

$$\mathcal{B}(\tau^- \to \mu^-\overline{\nu}_\mu\nu_\tau\ ) \quad = \quad 17.35 \pm 0.13(a) \pm 0.08(b) \pm 0.11(c) \pm 0.25(d)\ , \qquad (6.3)$$

where the errors come from (a) 0.7% from event statistics; (b) 0.5% from Monte Carlo statistics; (c) 0.6% from tag side branching ratios; (d) 1.4% from the error on the luminosity measurement. The background subtraction procedure used to remove the hadron-punch through contamination does not significantly contribute to the error on the branching ratio. The error is dominated by the error on the luminosity measurement.

For the electron sample, $N_{\tau\tau}$ is the same as above, $\sum_i(\mathcal{B}_i \times \epsilon_i) = (275.90 \pm 1.77) \times 10^{-4}$ (Table 5.1), $N_S = 26815$ and $(1 - f_B) = 0.9982 \pm 0.0001$ leading to:

$$\mathcal{B}(\tau^- \rightarrow e^-\overline{\nu}_e\nu_\tau\,) \;=\; 17.93 \pm 0.11(a) \pm 0.06(b) \pm 0.11(c) \pm 0.25(d) \qquad (6.4)$$

where the errors come from (a) 0.6% from event statistics; (b) 0.3% from Monte Carlo statistics; (c) 0.6% from tag mode branching fractions; (d) 1.4% from $N_{\tau\tau}$. Once again, the error is dominated by the luminosity measurement. The efficiency is significantly higher than the muon mode as one now includes electrons down to 500 MeV/c momentum (instead of the 1.5 GeV/c momentum cut-off in the muon mode).

These ratio of these branching ratio measurements $\mathcal{B}_e/\mathcal{B}_\mu$ can be used to obtain a measurement of the low energy spectral shape parameter η using Equation 2.63 [‡]. Using the $\pi \rightarrow \ell\nu_\ell$ decays to calculate $g_\mu/g_e = 1.0012 \pm 0.0016$, $f(x_\mu) = 0.9726$, and the BES tau mass measurement $m_\tau = (1777.0 \pm 0.26)$ MeV/c^2, we obtain $\eta = 0.02 \pm 0.06$. The current world average results $\mathcal{B}_\mu = (17.33 \pm 0.09)\%$, and $\mathcal{B}_e = (17.79 \pm 0.09)\%$ can be used to calculate $\eta = 0.007 \pm 0.029$. These errors obtained on using the world average measurements are comparable to the errors obtained from measurements in the muon sector.

[‡] The largest systematic error contribution from the luminosity cancels in the ratio of branching ratios.

Figure 6.1 shows both the electronic and muonic branching ratios obtained in this analysis, along with the corresponding world average values indicated by the hatched regions. The result obtained for $\mathcal{B}_e$ and $\mathcal{B}_\mu$ are consistent with the corresponding world average results. No attempt has been made to minimize the errors shown in this figure.

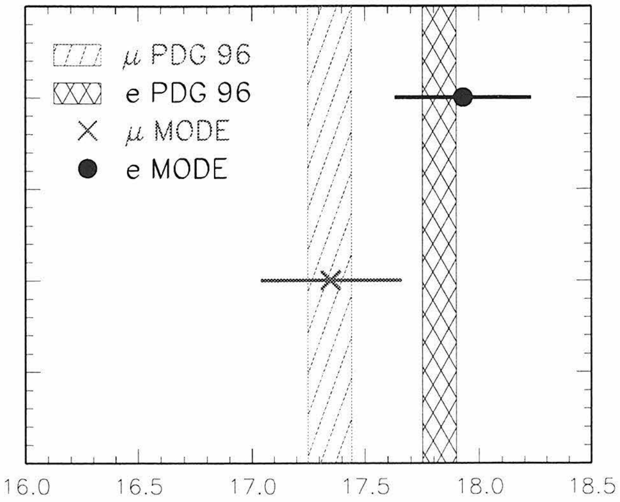

Figure 6.1: The electronic and muonic branching ratios.

Chapter 7 Experimental Technique

In this chapter, we describe the experimental technique employed to measure the Michel parameters ρ and η simultaneously, using the energy spectrum of the charged daughter leptons in leptonic tau decays. The energy spectrum of the charged daughter lepton in the tau rest frame is ideal to measure both these parameters. Figure 7.1 plots this energy spectrum in the tau rest frame scaled by the maximum kinematically allowed energy in that frame of reference, $E_{max} = (m_\tau^2 + m_\ell^2)/2m_\tau$, for three different values of the parameter ρ. The other Michel parameters are fixed to their Standard Model expectations, and we note that the three distributions shown here are clearly distinct over the entire range plotted.

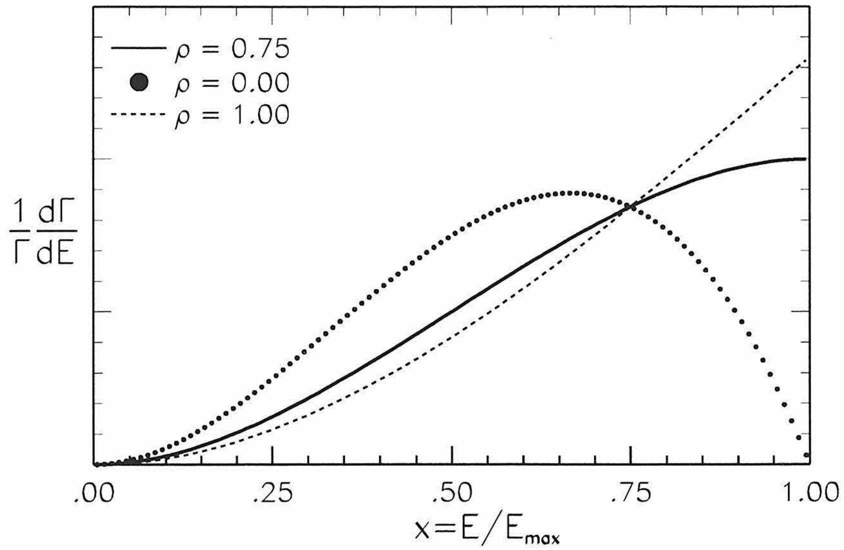

Figure 7.1: The $x = E_\ell/E_{max}$ distributions in the tau rest frame for different values of the ρ parameter. Each distribution has been normalized to have unit area.

When both the tau lepton and the daughter charged lepton (electron or muon) couple to the intermediate $W_L^\pm$ boson as $V - A$, one gets the Standard Model prediction, $\rho = 3/4$, indicated by the solid line. If both leptons couple as $V + A$ to the $W_L^\pm$ boson, we expect the same ρ value. If only the tau lepton couples as $V + A$, and the light lepton couples as $V - A$, we obtain $\rho = 0$, and the daughter lepton energy distribution in the tau rest frame has to go to zero at $x = 1$, as indicated by the dotted line. Since the daughter lepton interaction is known to be $V - A$ to good precision (Table 2.6), in this analysis, we utilize this experimental fact to infer information on the tau coupling to the W boson.

The energy spectrum of the daughter lepton in the tau rest frame is also sensitive to the η parameter. As seen in Chapter 2, any deviations from the Standard Model expectation $\eta = 0$, would imply the existence of a scalar coupling which couples with the right-handed tau and the right-handed daughter lepton ℓ. Interference between the amplitudes of this new scalar boson which mediates this coupling, and the Standard Model $W_L^{\pm}$ boson would alter the energy spectrum of the daughter lepton. Figure 7.2 shows the expected change in the scaled muon energy distribution in the tau rest frame when the η parameter is changed by ±1.0 (ρ=3/4 fixed). We note that the three distributions shown are clearly distinct. Since this effect is helicity suppressed in the electron spectrum (it corresponds to a flipping of the lepton's spin) and it scales with the lepton mass (equation 2.58), it cannot be observed in the electron spectrum.

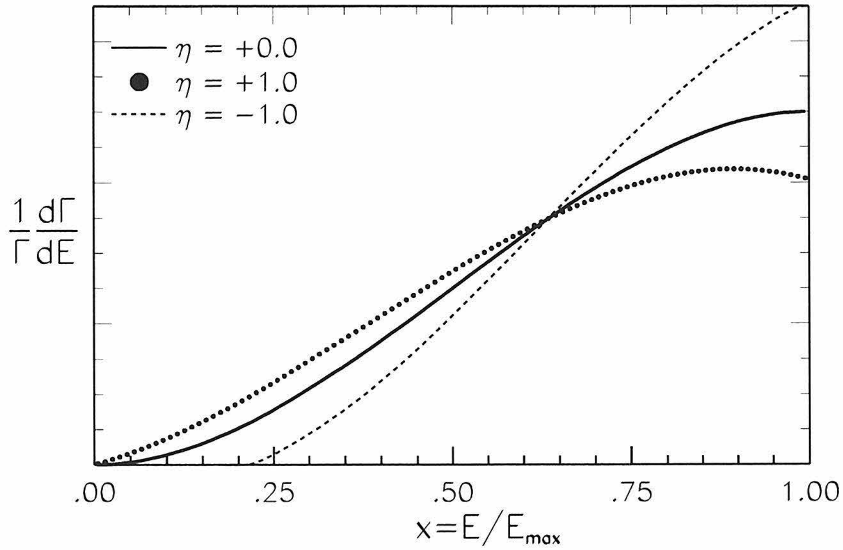

Figure 7.2: The $x = E_\mu/E_{max}$ distributions in the tau rest frame for different values of the η parameter. Each distribution has been normalized to have unit area.

The distributions in Figures 7.1 and 7.2 imply that the lepton rest frame energy spectrum is very sensitive to both the Michel parameters studied in this thesis. Unfortunately, the two neutrinos in the decay $\tau^- \to \ell^- \overline{\nu}_\ell \nu_\tau$ are not detected by the CLEO II detector, making it impossible to reconstruct the tau lepton four-momentum, and thus precluding the explicit reconstruction of the rest frame spectrum of the daughter charged lepton ℓ.

The observed lepton momentum distribution in the laboratory frame of reference is very different from its rest frame counterpart. This distortion is a result of the Lorentz boost at the $\Upsilon(4S)$: $\gamma \simeq 5.29/1.777$. Figure 7.3 illustrates the muon laboratory momentum spectrum for the Standard Model $V - A$ $[\rho = 3/4, \eta = 0]$, the $V + A$ $[\rho = 0, \eta = 0]$, the $\eta = 1$ $[\rho = 3/4, \eta = 1]$ Monte Carlo samples.

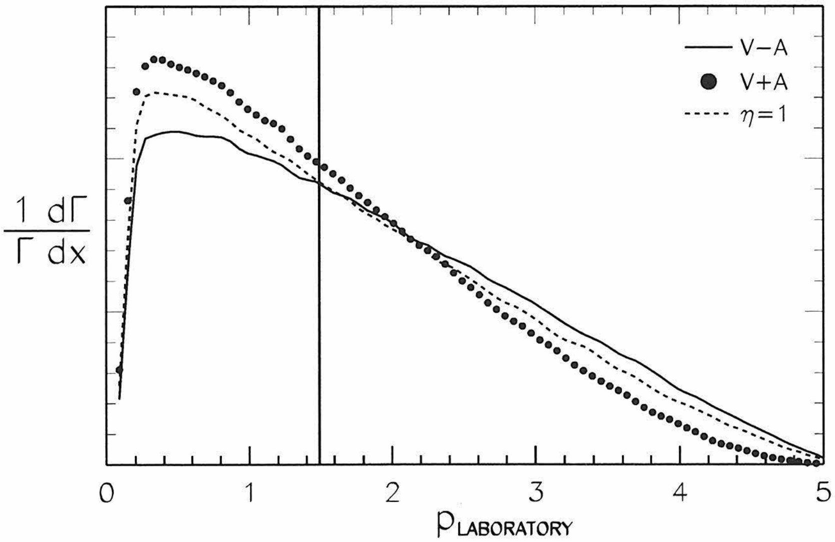

Figure 7.3: The direct laboratory momentum spectrum for the three different Monte Carlo samples, $V \pm A$, and $\eta = 1$. Each distribution has been normalized to have unit area. The solid line indicates the 1.5 GeV/c minimum momentum cut-off imposed by the muon identification system.

We note that maximum sensitivity to the η parameter lies in the low momentum end of the spectrum; the high momentum region of the spectrum has much lower statistics since the spectrum falls off sharply at higher momentum. Good muon identification requires a 1.5 GeV/c minimum momentum cut-off *, indicated by the solid line in the figure. Thus, most of the sensitivity to the η parameter is lost, and the direct laboratory frame spectrum is not very useful in measuring this parameter.

7.1 Reconstruction of the Pseudo Rest Frame

As shown earlier in this chapter, the charged lepton energy spectrum in the tau rest frame is ideal to measure the Michel parameters. CESR operates far above tau production threshold, where the observed laboratory momenta of the daughter leptons depends on both the rest frame momenta and the emission angle due to the Lorentz transformation. In order to perform a Lorentz boost into the tau rest frame, the tau four-momentum must be known. The energy of the tau can be determined by the beam energy up to initial and final state radiations. On the other hand, the direction of the tau cannot be exactly reconstructed because there are neutrinos amongst the daughter particles, and CLEO II, like most e^+e^- detectors, does not detect neutrinos.

In this section, we describe a technique first exploited by ARGUS [9]: the direction of the tau lepton is inferred from the direction of the system of charged hadrons (h) originating from the decay of the other tau lepton in the event. This other tau lepton (defined as the "tag" tau in Chapter 4) was required, by ARGUS, to decay into $(3h)^\pm$ or $(3h)^\pm\pi^0$. Due to its relatively high mass, these hadronic systems both give a good approximation to the flight direction of its parent tau and, consequently, of the tau under study, since both tau leptons are flying back-to-back. The rest system determined with this approximation defines the pseudo rest frame. Using fits to Monte Carlo samples, ARGUS found that the accuracy of the ρ measurement was higher in the tau pseudo rest frame by a factor of 1.5, and that the precision on the η measurement improved by a factor of 2.

In the analysis presented in this thesis, the tau pair events are tagged by the decay mode $\tau^+ \to h^+\pi^0\overline{\nu}_\tau$, to take advantage of its much larger branching ratio,

---

* CLEO II muon identification can be extended down to 1.0 GeV/c momentum, but the muon identification efficiencies in the low momentum region are not known well enough for the precision required in this analysis.

thus leading to a higher statistics sample. Further, the background contamination is lower when one uses this tag mode instead of the $3h^{\pm}(\pi^0)$ modes used by ARGUS. The $h^{\pm}\pi^0$ system has a lower mass and thus does not give as good an approximation to the flight direction of its parent mode. We thus apply the $\cos\alpha$ requirement, as explained below, to select events in which the τ flight direction is estimated well, and reconstruct the pseudo rest frame for this subset of the entire data sample. Events which fail the $\cos\alpha$ constraint are analyzed in the laboratory frame of reference.

The electron-positron interactions result in tau pairs which are produced back-to-back as shown in Figure 7.4. The two tau leptons decay in opposite hemispheres of the detector and the tag decay mode is used to identify the tau events, as well as to estimate the flight direction of its parent tau. α is the angle between the tau direction in the laboratory frame and the $h^+\pi^0$ (A) system in the laboratory frame.

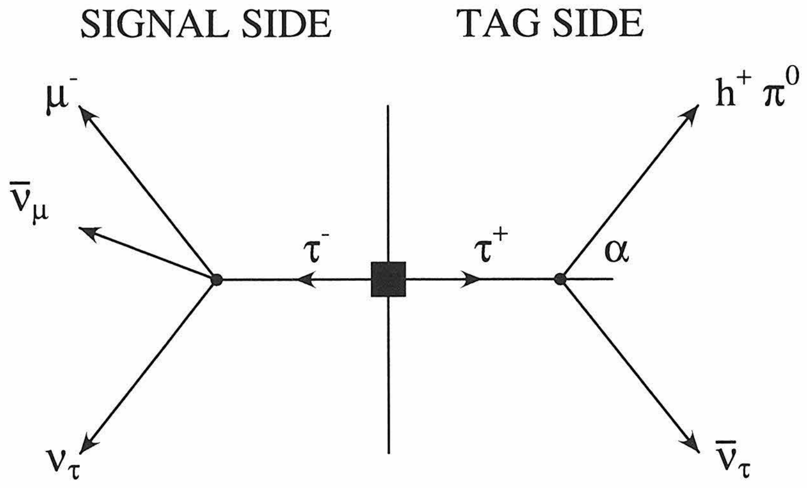

Figure 7.4: Event topology.

To reconstruct the pseudo rest frame we exploit the kinematics of the tag $\tau^+ \to A^+\bar{\nu}_\tau$ decay, where A^+ is some hadronic system. This decay can now be treated like a two-body system, and the conservation of the four-momentum in the decay,

$$(P_\tau - P_A)^2 = P_\nu^2 , \tag{7.1}$$

leads to the kinematic equation:

$$m_\tau^2 + m_A^2 - 2E_\tau E_A + 2p_\tau p_A \cos\alpha \quad = \quad m_\nu^2 \, . \tag{7.2}$$

Here, E_A, p_A and $m_A = \sqrt{E_A^2 - p_A^2}$ are all measured quantities, and α is the angle of the τ direction with respect to the measured hadronic A ($h^+\pi^0$, in this analysis) system in the laboratory frame of reference. Now, $E_\tau = E_{beam}$, $p_\tau = \sqrt{E_{beam}^2 - m_\tau^2}$, and assuming that $m_\nu = 0$, one can calculate $\cos\alpha$, an indicator of how well the true tau direction has been estimated in the event under consideration.

Requiring $\cos\alpha$ close to unity ($\cos\alpha \geq 0.970$) selects events in which the tau flight direction is well approximated, thus providing a sufficiently accurate approximation to the true rest frame conditions. Since one now knows both the tau energy, and its flight direction for these selected events, the lepton from the decay of the other tau in the event can be boosted into its parent's frame of reference resulting in the reconstructed pseudo rest frame spectrum. The $\cos\alpha$ requirement has been optimized to achieve maximum sensitivity to the η parameter; this optimization is discussed in detail in Section 9.8.

Figure 7.5 shows a logarithmic plot of this variable in the electron sample. The corresponding plot in the muon sample is nearly identical to this one. We note that the Monte Carlo simulation program simulates this variable very well. This figure also plots the distribution from background multi-π^0 tag modes, $\tau \rightarrow \pi^- n\pi^0 \nu_\tau$, $n > 1$, where one or more of the π^0's in the event are not reconstructed. This background has a different distribution and could result in a bias in the reconstructed pseudo rest frame spectrum. Fortunately, it can be minimized using veto cuts on extra unused showers in the event, after which it is small as shown here. There are events in both the data and the Monte Carlo distributions with $\cos\alpha > 1$, an unphysical region. These events are few and result from measurement errors. They are not used in the pseudo rest frame analysis.

The pseudo rest frame spectra obtained for the three different Monte Carlo samples, $V \pm A$, and $\eta = 1$ are shown in Figure 7.6. Here, one plots the energy of the

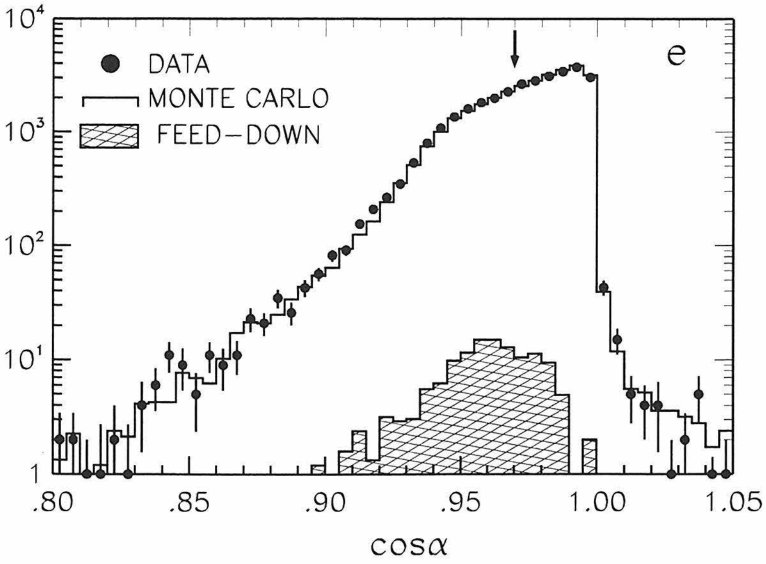

Figure 7.5: The distribution for the $\cos\alpha$ variable for the data (dots) as well as the generic tau Monte Carlo simulation (solid histogram). Backgrounds from multi-π^0 modes are included in the Monte Carlo distribution in the appropriate proportions (hatched region). The arrow indicates the nominal requirement: $\cos\alpha \geq 0.970$.

muon in the pseudo rest frame, calculated using the hadronic system to estimate the τ flight direction, scaled by the maximum kinematically possible energy in the τ rest frame $E_{MAX} = (m_\mu^2 + m_\tau^2)/2m_\tau$. We note that the three spectra are distinct over the entire scaled energy range, thus leading to the improved sensitivity over the laboratory frame analysis. We further note that the $V - A$ spectrum does not completely resemble the corresponding Monte Carlo true tau rest frame spectrum shown in Figure 7.1; in particular, all the events above $x = 1$ are unphysical in the true rest frame. The difference is primarily a result of the fact that the hadronic system is not a perfect estimator of the tau flight direction, with contributions from radiative effects and mismeasurement. Tightening the $\cos\alpha$ requirement to select "better" estimators of the tau flight direction ($\cos\alpha \geq 0.995$, for example) would result in fewer entries in the unphysical region, $x > 1$, and the spectra would better resemble their true tau rest frame counterparts. This tighter requirement results in an unaffordable loss in statistics and is thus not employed.

The $\cos\alpha \geq 0.970$ requirement is approximately 60% efficient, as can be seen

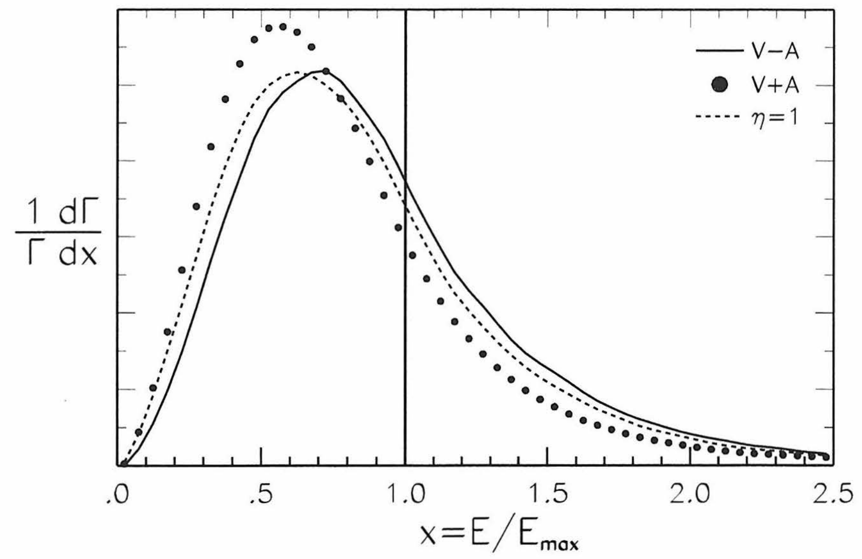

Figure 7.6: The reconstructed lepton energy in the pseudo rest frame scaled to the maximum kinematically allowed energy in the τ rest frame for the three Monte Carlo distributions, $V \pm A$, and $\eta = 1$. Each spectrum has been normalized to have a unit area, and has been reconstructed using events which survive the $\cos\alpha \geq 0.970$ requirement.

in Figure 7.5. If one utilized the $\tau^+ \rightarrow \pi^+\pi^-\pi^+\bar{\nu}_\tau$ decay mode instead, as done by the ARGUS experiment, the $\cos\alpha$ requirement would be approximately 100% efficient, since the 3π system is a better estimator of the tau flight direction. However, the probability for a tau lepton to decay into the 3π mode is significantly lower; $\mathcal{B}(\tau^+ \rightarrow \pi^+\pi^-\pi^+\bar{\nu}_\tau) \simeq 13\%$. Further, there is negligible QED background associated with the $h^+\pi^0$ mode, and the full reconstruction of the entire event helps suppress backgrounds from hadronic, two-photon events and cosmic rays. The 3π mode has larger $q\bar{q}$ background.

7.2 Low Momentum Muons

The factor of 2 improvement seen by ARGUS in the η measurements using the pseudo rest frame of the τ lepton was not entirely due to the improved sensitivity resulting from the clear distinctions in the shapes of the spectra observed in Figure 7.6. A significant improvement resulted from the addition of low momentum muons ($p_\mu <$ 1.5 GeV/c), identified without the use of conventional muon identification techniques. At CLEO II, the muon detectors can be used to identify muons down to a laboratory momentum of 1.0 GeV/c , but the muon identification efficiency in the low momentum region is not flat and is not known to the precision required for the measurements presented in this dissertation.

Charged particles with a laboratory momentum between 0.5 and 1.5 GeV/c can be kinematically identified as muons in the pseudo rest frame after elimination of all other possible decay hypotheses: $e\nu\bar{\nu}$, $\pi\nu$, $K\nu$, and $hn\pi^0\nu$. Figure 7.7 shows a plot of the pseudo rest frame energy for such tracks, scaled to the maximum possible energy in the tau rest frame, $X = E_\mu/E_{MAX}$ where $E_{MAX} = (m_\mu^2 + m_\tau^2)/2m_\tau$. The dominant background modes are also shown in this figure.

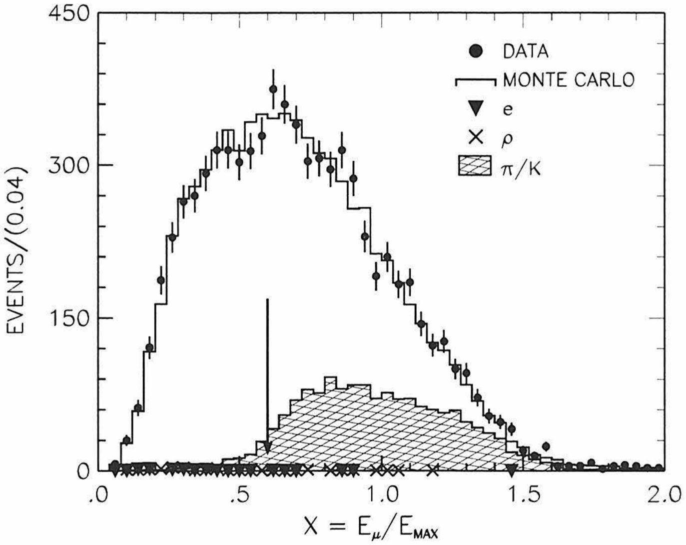

Figure 7.7: The scaled pseudo rest frame muon energy spectrum in the data (dots), the $V-A$ Monte Carlo simulation (solid histogram), for μ's identified kinematically. The Monte Carlo spectra for the background modes are also illustrated; their contributions are small for $E_\mu/E_{\rm MAX} < 0.6$, indicated by the arrow. Each Monte Carlo histogram has been normalized to the data.

For the two-body modes $\pi\nu$ and $K\nu$, we have $X_{\pi(K)} = 0.89(0.95)$ in the true rest frame. This is broadened to the distribution shown as the hatched histogram in Figure 7.7. A cut at $X \leq 0.6$ reduces the π/K contamination to $(2.63 \pm 0.21)\%$. The electron identification efficiency ($E/p \leq 0.85$ and SGELDI$\geq$ 0.3) for electrons with $p_e \geq 0.5$ GeV/c laboratory momentum is well known, and is close to 100%. Electron identification is used to veto electron-like tracks and to reduce the electron contamination down to $(0.64 \pm 0.11)\%$. No extra unmatched showers above 60 MeV are allowed, either in the barrel or the endcap region, to minimize backgrounds from $h\pi^0\,\nu$ and other multi-pizero modes; this contamination is estimated to be $(0.78 \pm 0.12)\%$. All the background estimates presented here are calculated with the Monte Carlo simulation, and subtracted from the data. Thus, we recover a significant fraction of muons lying below the momentum cut-off of the muon identification system. This sample is $\simeq$ 96% pure. Almost 35% of the background results from the electron and $h\pi^0$ contamination. Both these backgrounds are distributed uniformly across the pseudo rest frame scaled energy spectrum, as can be seen in the figure, and do not have a significant impact in this analysis.

The results obtained on analyzing the electron and muon spectrum using the pseudo rest frame spectra, as well as the direct laboratory frame spectra, are described in detail in the following chapter, and a discussion of the various sources of systematic errors is detailed in Chapter 9.

Chapter 8 Fitting and Results

8.1 Fit Functions

The decay spectrum of the charged daughter lepton (using Equation 2.58), after integration over the two undetected neutrino momenta, and averaged over the tau spin direction is:

$$\frac{1}{\Gamma}\frac{d\Gamma}{dx}(\rho,\eta) = \frac{x^2}{1+4\eta(m_\ell/m_\tau)}\left[12(1-x)+\frac{4\rho}{3}(8x-6)+24\eta\frac{m_\ell}{m_\tau}\frac{(1-x)}{x}\right], \quad (8.1)$$

where ℓ denotes the observed charged daughter lepton, $x = E_\ell/E_{max}$ and $E_{max} = (m_\tau^2 + m_\ell^2)/2m_\tau$. The radiative corrections do not depend on the Michel parameters and are neglected in this equation. The spectral shape Michel parameters studied in this analysis are ρ and η. These parameters are not measured using the convention maximum likelihood estimator method. Instead of a semi-analytic approach, we extract these parameter values from a simple χ^2 fit to a function of three binned Monte Carlo spectra:

1. the standard $V-A$ spectrum with $\rho = 3/4$ and $\eta = 0$;
2. the $V+A$ spectrum with $\rho = 0$ and $\eta = 0$;
3. the $\eta = 1$ spectrum with $\rho = 3/4$ and $\eta = 1$.

All effects associated with the boost, acceptance and resolution of the detector, efficiency of all cuts, as well as radiative corrections, are included in the full Monte Carlo simulations of these three spectra. Tau-pairs are generated and decayed with the KoralB(v2.2)/Tauola(v2.4)/Photos(v1.06) package, followed by the detector simulation package CLEOG using Geant 3.15.

The true number of events generated by the accelerator $N_T = \sum_i N_{Ti}$, where

$$N_{Ti} = \mathcal{L}\ \sigma\ \mathcal{B}_{h\pi^0}\ \mathcal{B}_\ell \frac{1}{\mathcal{B}_\ell}\frac{d\mathcal{B}_\ell}{dx_i}\ , \tag{8.2}$$

is the number of events generated in bin i, $\mathcal{L}$ and σ denote the integrated luminosity and the cross section for $e^+e^- \to \tau^+\tau^-$ respectively, and $\mathcal{B}_\ell$ and $\mathcal{B}_{h\pi^0}$ denote the tau branching fractions to the $\ell\nu\bar{\nu}$ and $h\pi^0\,\nu$ decay modes. We now use the Monte Carlo simulation to model:

$$\frac{1}{\mathcal{B}_\ell}\frac{d\mathcal{B}_\ell}{dx_i} = \sum_\alpha C_\alpha f_{\alpha i}\ , \tag{8.3}$$

where $f_{\alpha i}$ is the fraction of events in bin i for the three Monte Carlo models listed above ($V-A$, $V+A$, and $\eta = 1$), normalized so that $\sum_i f_{\alpha i} = 1$ for $\alpha = 1, 2, 3$, and the three coefficients:

$$C_1 = C_{V-A} = \frac{4\rho/3 - \eta}{1 + 4\eta(m_\mu/m_\tau)}, \qquad C_2 = C_{V+A} = \frac{1 - 4\rho/3}{1 + 4\eta(m_\mu/m_\tau)}$$

$$\text{and } C_3 = C_{\eta=1} \;=\; \frac{\eta[1 + 4(m_\mu/m_\tau)]}{1 + 4\eta(m_\mu/m_\tau)}. \tag{8.4}$$

We note that $\sum_\alpha C_\alpha = 1$, independent of the parameter values ρ and η. The parent distribution associated with the observed lepton spectrum may now be expressed as a function of the three Monte Carlo model distributions:

$$\frac{dN_{obs}}{dx}(\rho,\eta) \;=\; C_{V-A}\,\frac{dN}{dx}(3/4,0) + C_{V+A}\,\frac{dN}{dx}(0,0) + C_{\eta=1}\,\frac{dN}{dx}(3/4,1), \tag{8.5}$$

when one assumes that the the efficiency $\varepsilon_\alpha = \int P(x|\alpha)\epsilon_\alpha(x)dx$ is independent of the model α. The detection efficiency $\epsilon_\alpha(x)$ is in fact model independent, but the probability distribution function $P(x|\alpha)$ does depend on the choice of the model considered, largely as a result of the minimum momentum cut-offs dictated by lepton identification criteria. Thus $\varepsilon_{V-A} \neq \varepsilon_{V+A} \neq \varepsilon_{\eta=1}$, and to account for this efficiency dependence we require an additional correction factor.

Now, the number of observed events in each Monte Carlo sample can be written as:

$$N_\alpha = \sum_i N_{\alpha i} = \sum_i N_{g\alpha} \, f_{\alpha i} \, \varepsilon_{\alpha i} = N_{g\alpha} \, \varepsilon_\alpha \, , \tag{8.6}$$

where $N_{g\alpha}$ is the number of events generated for the model α, $f_{\alpha i}$ is the fraction of events in bin i of the model α distribution, and $\varepsilon_\alpha = N_\alpha / N_{g\alpha}$ is the efficiency for that model. The number of observed events in bin i can also be written as:

$$N_{oi} = N_{Ti} \, \varepsilon_i = \mathcal{L} \, \sigma \, \mathcal{B}_\ell \, \mathcal{B}_{h\pi^0} \sum_\alpha C_\alpha \, f_{\alpha i} \, \varepsilon_i \tag{8.7}$$

using Equation 8.3, and thus the total number of observed events:

$$N_o = \sum_i N_{oi} = \mathcal{L} \, \sigma \, \mathcal{B}_\ell \, \mathcal{B}_{h\pi^0} \sum_\alpha C_\alpha \varepsilon_\alpha \, , \tag{8.8}$$

implying that

$$\mathcal{L} \, \sigma \, \mathcal{B}_\ell \, \mathcal{B}_{h\pi^0} = \frac{N_o}{\sum\limits_\beta C_\beta \varepsilon_\beta} \, . \tag{8.9}$$

Substituting the result obtained in Equation 8.9 into Equation 8.7, the number of observed events in bin i can now be written as:

$$\begin{aligned} N_{oi} &= \frac{N_o}{\sum\limits_\beta C_\beta \varepsilon_\beta} \sum_\alpha C_\alpha \, f_{\alpha i} \, \varepsilon_\alpha = \frac{N_o}{\sum\limits_\beta C_\beta \varepsilon_\beta} \sum_\alpha C_\alpha \frac{N_{\alpha i}}{N_{g\alpha}} \\ &= \frac{N_o}{\sum_\beta C_\beta \varepsilon_\beta} \sum_\alpha C_\alpha \frac{N_{\alpha i}}{N_\alpha} \varepsilon_\alpha \\ &= \sum_\alpha \left(\frac{C_\alpha \varepsilon_\alpha}{\sum\limits_\beta C_\beta \varepsilon_\beta} \right) \left(\frac{N_o}{N_\alpha} N_{\alpha i} \right) , \end{aligned} \tag{8.10}$$

where the term enclosed in the first set of parentheses depends only on the efficiency ε and the Michel parameters ρ and η, while the term enclosed in the second set of parentheses is the Monte Carlo spectra normalized to the number of observed events in the data N_o.

Thus, the function used to fit the lepton spectrum can now be written as:

$$\begin{aligned} \frac{dN_{obs}}{dx}(\rho,\eta) &= C'_{V-A}\,\frac{dN}{dx}(3/4,0) + C'_{V+A}\,\frac{dN}{dx}(0,0) + C'_{\eta=1}\,\frac{dN}{dx}(3/4,1), \\ \text{with } C'_\alpha(\rho,\eta) &= \frac{C_\alpha \varepsilon_\alpha}{\sum\limits_\beta C_\beta \varepsilon_\beta} \quad \text{and } \sum_\alpha C'_\alpha = 1 \ , \end{aligned} \tag{8.11}$$

and with each Monte Carlo distribution individually normalized to the integral over the observed data momentum spectrum. The coefficients C_α are the same as shown in Equation 8.4, and since they appear in both the numerator and the denominator, we note that the $(1+4\,\eta\ m_\ell/m_\tau)^{-1}$ term cancels. We now use the simplified coefficients:

$$C_{V-A} = \frac{4\rho}{3} - \eta \ , \quad C_{V+A} = 1 - \frac{4\rho}{3} \ , \quad \text{and} \quad C_{\eta=1} = \eta(1 + 4\frac{m_\ell}{m_\tau}) \ . \tag{8.12}$$

The background subtracted muon data spectrum is now fit to the function of the three binned Monte Carlo spectra, generated with the different values of the parameters, to measure simultaneously the Michel parameters ρ and η. This two parameter fit is simple since the spectra considered are one-dimensional distributions. We nominally use 100 MeV bins; effects associated with the choice of bin size are discussed in Section 9.13.

As seen in Equation 8.1, in the electronic decay mode, all sensitivity to the η parameter is lost as a result of the negligible mass of the electron relative to the tau mass. Thus Equation 8.11 simplifies to:

$$\begin{aligned} \frac{dN_{obs}}{dx}(\rho) &= C'_{V-A}\,\frac{dN}{dx}(3/4) + C'_{V+A}\,\frac{dN}{dx}(0) \ , \\ \text{with} \quad C_{V-A} &= \frac{4\rho}{3} \ , \quad \text{and} \quad C_{V+A} = 1 - \frac{4\rho}{3} \ , \end{aligned} \tag{8.13}$$

and a simple one parameter fit is now used to extract the Michel parameter ρ.

Events which survive the $\cos\alpha \geq 0.970$ requirement are analyzed using the pseudo rest frame spectrum; the remainder are analyzed using the laboratory frame spectrum.

The Monte Carlo spectra generated with the different parameter values for the three different Monte Carlo models, utilized in this fit procedure, are shown in Figure 7.3 (laboratory frame) and Figure 7.6 (pseudo rest frame). The optimization of the p_e, p_μ, and $\cos\alpha$ cuts, along with a detailed evaluation of systematic errors are described in Chapter 9. Since the results obtained in the two frames of reference are statistically independent, the final results are obtained by combining them in a simple weighted average. Correlations between the parameters, as well as data and Monte Carlo statistics, are taken into account when the results are combined.

8.2 Electron Mode Results

Approximately 60% of the electron sample survives the $\cos\alpha \geq 0.970$ requirement. These 18587 events are analyzed in the pseudo rest frame. Figure 8.1 shows the electron energy pseudo rest frame spectrum scaled by the maximum kinematical allowed energy, $E_{max} = (m_e^2 + m_\tau^2)/2m_\tau$.

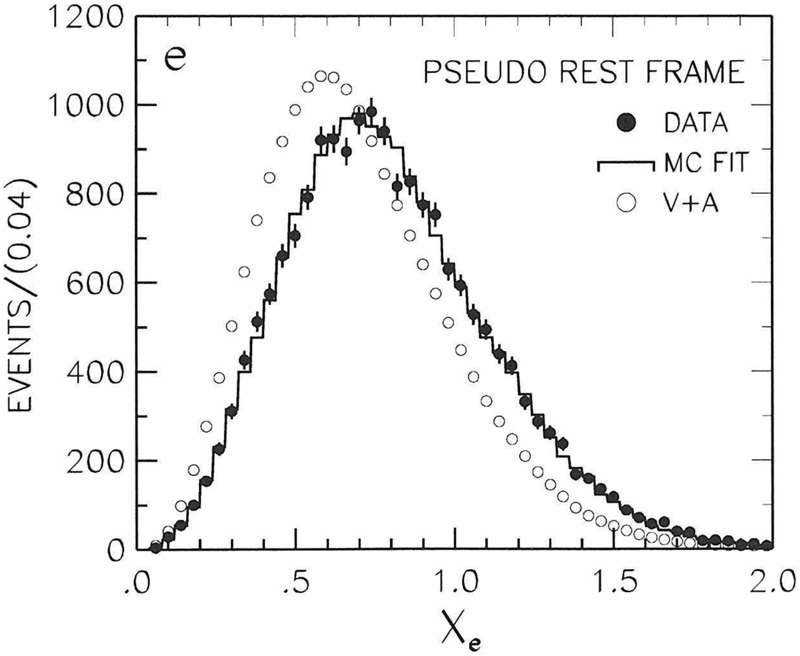

Figure 8.1: The electron scaled pseudo rest frame data energy spectrum fit to a linear combination of fully simulated Monte Carlo $V-A$ and $V+A$ spectra. The pseudo rest frame energy is scaled by $E_{\mathrm{max}} = (m_e^2 + m_\tau^2)/2m_\tau$.

We perform a χ^2 fit of the data spectrum to the function of binned Monte Carlo $V-A$ and $V+A$ spectra shown in Equation 8.13. The coefficients of the fit function are used to extract the Michel parameter ρ_e. We measure:

$$\rho_e = 0.733 \pm 0.017 \pm 0.007 \ , \tag{8.14}$$

with a χ^2 of 51.5 for 46 degrees of freedom. The first error accounts for the data statistics and the second accounts for the Monte Carlo statistics. We observe that the data and the fit to a combination of $V-A$ and $V+A$ Monte Carlo spectra in Figure 8.1 agree extremely well. We further note that the $V+A$ Monte Carlo spectra is distinct from the data over the entire energy range shown.

The 12981 electron events that fail the $\cos\alpha$ constraint are analyzed in the laboratory frame of reference. The direct momentum spectrum as measured in the laboratory frame is shown in Figure 8.2.

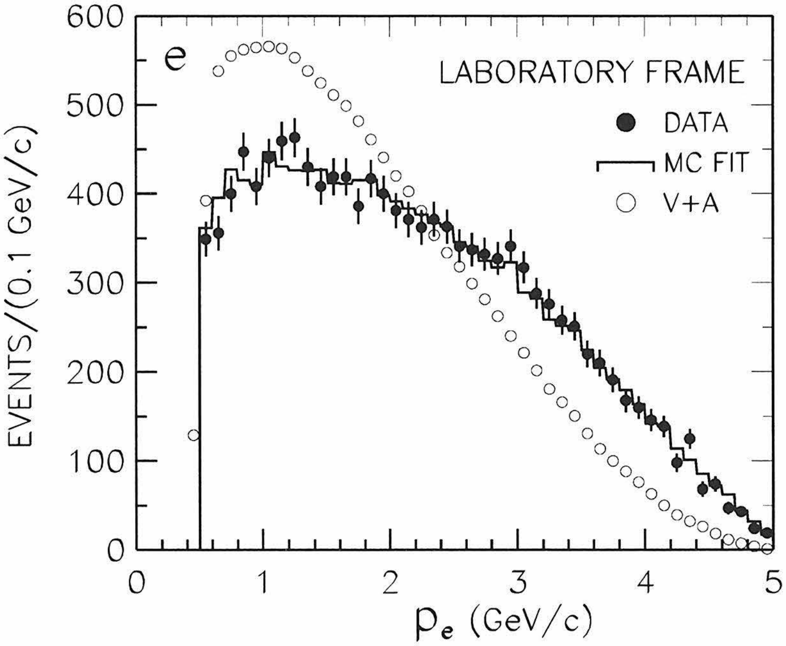

Figure 8.2: The electron laboratory frame data momentum spectrum fit to a combination of fully simulated Monte Carlo $V-A$ and $V+A$ spectra.

Once again, the data and the Monte Carlo fit function agree well, and are well differentiated from the $V + A$ Monte Carlo spectrum over the entire momentum range studied. The cut-off at 0.5 GeV/c is a result of the minimum momentum requirement for good electron identification. As before, the coefficients of the fit function in Equation 8.13 are used to measure:

$$\rho_e = 0.730 \pm 0.023 \pm 0.008 \ , \tag{8.15}$$

with a χ^2 of 36.2 for 44 degrees of freedom. Again, the first error accounts for the data statistics and the second accounts for the Monte Carlo statistics.

The results obtained in the two frames of reference considered are statistically independent. They are also consistent with each other and with Standard Model expectations. The statistical error obtained in the laboratory frame of reference is larger than the corresponding error obtained in the pseudo rest frame. Further, it is larger than that expected based on the relative sizes of the two samples. This is an indication of the reduced sensitivity to the Michel parameter in the laboratory frame relative to the pseudo rest frame.

We now form a simple weighted average of the two independent results in Equations 8.14 and 8.15, to obtain:

$$\rho_e = 0.732 \pm 0.014 \pm 0.005, \tag{8.16}$$

where the first error results from data statistics, and the second arises due to the Monte Carlo statistics. Both these errors are used in calculating the weighted average. They are also the largest sources of error. Since the other sources of systematic errors are independent of the choice of reference frame, and are significantly smaller, they are not used in the calculation of the weighted average result shown in Equation 8.16.

8.3 Muon Mode Results

In this decay mode, the two parameters ρ_μ and η_μ are strongly correlated and are measured simultaneously. Since the muon mass is not negligible relative to the tau mass, we are now sensitive to the η parameter, although most of this sensitivity lies in the low momentum region of the spectrum which is hard to reconstruct using the CLEO II muon identification system. As explained in Section 7.2, one can recover some fraction of the lost low momentum muons without using the muon identification counters. Including these additional 2931 muons results in the discontinuity observed at $X = 0.6$ in Figure 8.3, where the scaled pseudo rest frame energy spectrum (12580 + 2931 muons) is plotted for $\cos\alpha \geq 0.970$. The energy in the pseudo rest frame is scaled by the maximum kinematically allowed energy, $E_{\rm max} = (m_\mu^2 + m_\tau^2)/2m_\tau$. This figure also plots the Monte Carlo $\eta = 1$ spectrum that has been normalized to the data. We observe that it resembles the data over much of the energy range studied.

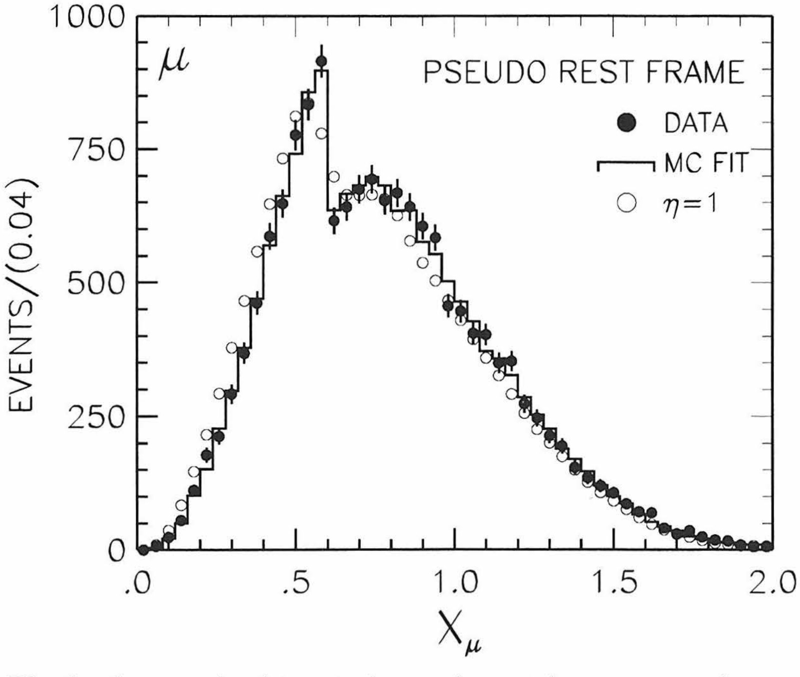

Figure 8.3: The background subtracted pseudo rest frame muon data energy spectrum fit to a combination of fully simulated Monte Carlo $V - A$, $V + A$ and $\eta = 1$ spectra. The pseudo rest frame energy is scaled by $E_{\rm max} = (m_\mu^2 + m_\tau^2)/2m_\tau$. The $\eta = 1$ Monte Carlo spectrum shown by the open circles resembles the data spectrum. The discontinuity observed at $X = 0.6$, in the pseudo rest frame spectrum, is a result of the addition of muons below the laboratory momentum of 1.5 GeV/c.

The coefficients of the fit function in Equation 8.11 are used to extract the Michel parameters ρ_μ and η_μ simultaneously. We measure:

$$\begin{aligned} \rho_\mu &= 0.780 \pm 0.055 \pm 0.025 \\ \text{and} \quad \eta_\mu &= 0.140 \pm 0.181 \pm 0.088 \ , \end{aligned} \tag{8.17}$$

with a χ^2 of 26.9 for 34 degrees of freedom, and a correlation coefficient, $C_{\rho\eta}$ of 0.943. The 1 σ error ellipse in $\eta - \rho$ parameter space is shown as the dashed contour in Figure 8.5. These errors are much larger than the corresponding pseudo rest frame electron mode result. This is due to the fact that we now perform a two parameter simultaneous fit, coupled with the lower statistics resulting from a higher momentum cut-off. Another important factor is the fact that the $\eta = 1$ Monte Carlo spectrum closely resembles the Standard Model $V - A$ spectrum.

Since the two parameters are strongly correlated, fixing one of them to its Standard Model expectation improves the sensitivity on the other tremendously. We now measure:

$$\begin{aligned} \rho_\mu &= 0.740 \pm 0.018 \pm 0.007 \text{ with } \eta_\mu \text{ fixed at } 0, \\ \text{and } \eta_\mu &= 0.047 \pm 0.062 \pm 0.022 \text{ with } \rho_\mu \text{ fixed at } 3/4. \end{aligned} \tag{8.18}$$

The error on the ρ_μ parameter is still significantly larger than the corresponding error on ρ_e measured using the electron pseudo rest frame energy spectrum. This reduced sensitivity is entirely a result of the higher 1.5 GeV/c momentum cut-off required for good momentum identification. In the pseudo rest frame analysis, one does recover a small fraction of the low momentum muons lost as a result of the momentum cut-off. However, it is only a small fraction of all the muons below the laboratory momentum of 1.5 GeV/c that are recovered.

Muon events (9186) in which the pseudo rest frame cannot be reconstructed, $\cos\alpha < 0.970$, are analyzed using their direct laboratory frame momentum spectrum shown in Figure 8.4. Once again, the $\eta = 1$ Monte Carlo spectrum resembles the data over much of the momentum range shown.

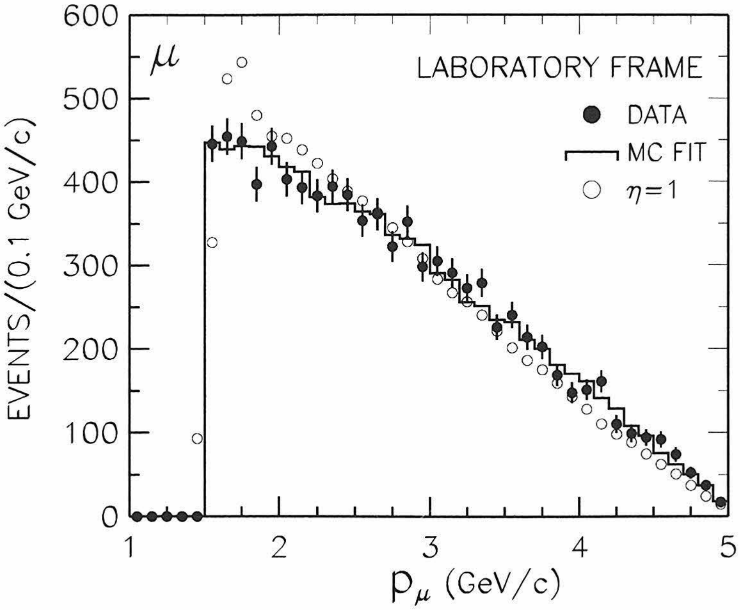

Figure 8.4: The background subtracted muon laboratory frame data momentum spectrum fit to a combination of fully simulated Monte Carlo $V-A$, $V+A$ and $\eta = 1$ spectra.

We now simultaneously measure:

$$\begin{aligned} \rho_\mu &= 0.607 \pm 0.111 \pm 0.088 \\ \text{and } \eta_\mu &= -0.431 \pm 0.309 \pm 0.259 \, , \end{aligned} \tag{8.19}$$

with a χ^2 of 28.1 for 33 degrees of freedom, and a correlation coefficient, $C_{\rho\eta}$ of 0.972. The solid contour in Figure 8.5 represents the 1 σ error ellipse in the $\eta - \rho$ parameter space. These errors are twice as large as the corresponding muon mode pseudo rest frame errors. One clearly observes the increase in sensitivity obtained by analyzing the data in the pseudo rest frame.

Once again, the two parameters are strongly correlated and one can better measure each parameter by fixing the other to its Standard Model expectation. We find that:

$$\begin{aligned} \rho_\mu &= 0.754 \pm 0.032 \pm 0.013 \text{ with } \eta_\mu \text{ fixed at } 0, \\ \text{and } \eta_\mu &= -0.034 \pm 0.089 \pm 0.041 \text{ with } \rho_\mu \text{ fixed at } 3/4. \end{aligned} \tag{8.20}$$

All the results obtained in the laboratory frame analysis are consistent with the corresponding results obtained in the pseudo rest frame analysis. They are also consistent with Standard Model expectations. Since the two analyses are statistically independent, we combine the results in Equations 8.17 and 8.19 to obtain:

$$\begin{aligned} \rho_\mu &= 0.747 \pm 0.048 \pm 0.026 \\ \text{and } \eta_\mu &= 0.010 \pm 0.149 \pm 0.089 \,, \end{aligned} \tag{8.21}$$

where the error contributions from both data and Monte Carlo statistics is used to combine the results measured in the two independent frames. We also account for the correlation between the two parameters when calculating this combined frame result.

The 1 σ error ellipse in the $\eta - \rho$ plane for this combined result along with the results obtained in the two individual frames is shown in Figure 8.5.

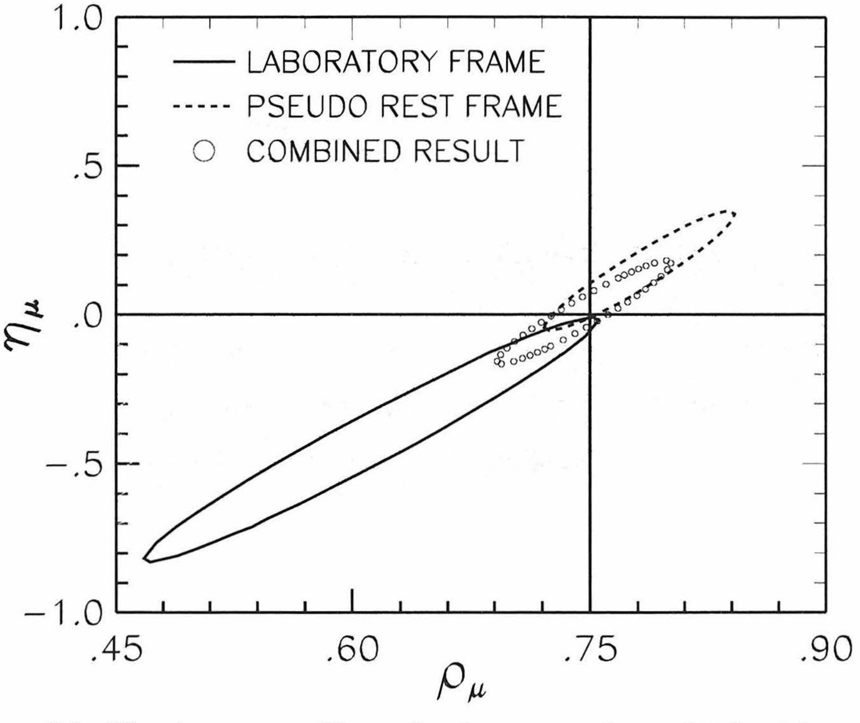

Figure 8.5: The 1 σ error ellipses in the $\eta - \rho$ plane obtained by analyzing the data in the pseudo rest frame, the laboratory frame and the two frames together. The hatched region encloses the allowed region in $\eta - \rho$ parameter space.

All contours lie well within the kinematically allowed region in $\eta - \rho$ space, as defined by the hatched region. There are strong correlations between the parameters in all three results and we observe that each result is consistent with the Standard Model expectation indicated by the point of intersection of the two solid lines in the figure. These errors indicate the contributions from data and Monte Carlo statistics only; the systematics errors are addressed in the next chapter.

One can also combine the measurement results for the two parameters obtained with one parameter fixed to its Standard Model expectation. Combining the results obtained in Equations 8.18 and 8.20, we obtain:

$$\begin{aligned} \rho_\mu &= 0.743 \pm 0.016 \pm 0.006 \quad \text{with } \eta_\mu \text{ fixed at } 0, \\ \text{and } \eta_\mu &= 0.022 \pm 0.051 \pm 0.020 \quad \text{with } \rho_\mu \text{ fixed at } 3/4. \end{aligned} \tag{8.22}$$

Once again, these results are consistent with the Standard Model expectations. A large number of experiments (MAC [78], ARGUS [79] and CLEO [80]) have measured ρ_μ ignoring the η parameter correlations. This result compares well with these experiments and is much more precise.

8.4 Invoking Lepton Universality

The results presented in the previous two sections, which measure the Michel parameters using electron and muon events, are consistent with each other. We now invoke lepton universality in the vector-like couplings which requires that $\rho_e = \rho_\mu$. The two parameters can now be extracted from simultaneous fits to both the lepton spectra used in the electron and muon analyses. Such a procedure takes advantage of the fact that the electron sample is insensitive to the η parameter as a result of the m_e/m_τ suppression (see Equation 8.1). The precise measurement of ρ_e helps constrain $\rho_{e\mu}$ thus reducing the correlation between the two parameters, and results in a precise measurement of $\eta_{e\mu}$. It is clear that in the leading model for scalar exchange contributions to η, that of a charged Higgs, lepton universality cannot be used, since the Higgs coupling strength is proportional to the lepton mass (see Equation 2.71).

Thus, we cannot assume $\eta_e = \eta_\mu$. However, in such models, the $V - A$ structure is not changed, and $\rho_e = \rho_\mu$ to high precision. We denote our result for η_μ using the constraint $\rho_e = \rho_\mu$ by $\eta_{e\mu}$, although we stress that we are **not** assuming $\eta_e = \eta_\mu$, or that scalar couplings are universal, only that V and A couplings are universal. Furthermore, we do not measure η_e and are insensitive to it.

We first consider the events that are analyzed using the scaled pseudo rest frame energy spectrum. A combined fit to both the electron and muon events results in a simultaneous measurement of the two parameters:

$$\begin{aligned} \rho_{e\mu} &= 0.739 \pm 0.016 \pm 0.006 \\ \text{and } \eta_{e\mu} &= 0.025 \pm 0.074 \pm 0.030 \ , \end{aligned} \tag{8.23}$$

with a correlation coefficient, $C_{\rho\eta}$ of 0.638, and a χ^2 of 69.5 for 75 degrees of freedom. Again, the first error denotes the statistical error while the second denotes the contribution from Monte Carlo statistics.

Next, we consider the events in both modes that cannot be used to reconstruct the pseudo rest frame spectrum, by virtue of the fact that they fail the $\cos\alpha$ requirement. These events are simultaneously analyzed using their direct laboratory frame momentum spectrum to yield:

$$\begin{aligned} \rho_{e\mu} &= 0.727 \pm 0.022 \pm 0.009 \\ \text{and } \eta_{e\mu} &= -0.104 \pm 0.106 \pm 0.053 \ , \end{aligned} \tag{8.24}$$

with a χ^2 of 62.7 for 78 degrees of freedom. Once again the correlation coefficient is reduced and $C_{\rho\eta} = 0.558$.

The results obtained by simultaneously analyzing the two lepton modes in both frames of reference (Equations 8.23 and 8.24) are consistent with each other. Since they are statistically independent, they are now combined using a simple weighted average (accounting for the correlations between the two parameters) to obtain:

$$\begin{aligned} \rho_{e\mu} &= 0.735 \pm 0.013 \pm 0.005 \\ \text{and } \eta_{e\mu} &= -0.015 \pm 0.061 \pm 0.026 \;, \end{aligned} \tag{8.25}$$

with a correlation coefficient of 0.614. These results are the most precise to-date measurements for these parameters. The errors on both parameters are significantly lower that the corresponding errors obtained on analyzing the individual modes. The 1 σ error ellipse in the $\eta - \rho$ parameter space obtained for this final result, along with the results obtained for the two different tau decay modes, is shown in Figure 8.6.

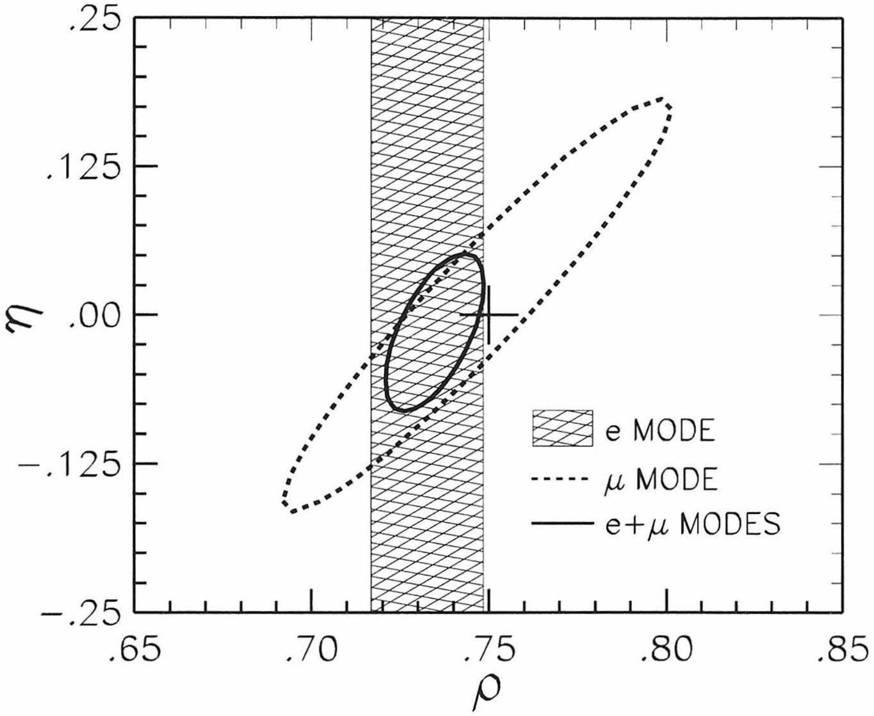

Figure 8.6: The 1 σ error ellipses in the $\eta - \rho$ plane obtained by analyzing the electron and muon modes individually along with the combined result. The error includes both data and Monte Carlo statistics. The Standard Model expectation is indicated by the cross in the center of the figure.

Chapter 9 Determining Systematic Errors

9.1 Sources of Error

The results presented in the previous chapter were obtained by comparing the observed charged daughter lepton's momentum spectrum with combinations of distributions predicted from Monte Carlo simulations. It is thus important to know not only the absolute efficiency to good precision, but also the momentum dependence of this efficiency. Most of the cuts utilized to select signal events as well as those aimed at rejecting the backgrounds were designed to avoid any bias in the lepton momentum spectrum studied. The CLEO II Monte Carlo simulation is used to determine the momentum dependence of the efficiencies for all cuts; the data are used to tune the simulation package wherever possible.

Systematic biases in this analysis could arise from the following list of sources:

- shifts caused because of an imperfect fitting procedure;
- imperfect modeling of the physics processes and detector response in the Monte Carlo simulation;
- imperfect simulation of the background sources and uncertainties in the normalization of the backgrounds relative to the signal;
- imperfect simulation of the correlations between the decay of the two tau leptons in the event arising as a result of radiation, spin correlations and/or global cuts imposed to select events;
- bin migration and resolution;
- other possible anomalous effects in the data.

In this chapter we explore these potential sources of systematic error in some detail to estimate conservative upper limits to their contribution to the errors.

9.2 How Well Does the Fit Technique Work?

Generator level (perfect detector) tests were performed to test the response of the fitting procedure. The first test was designed to study if this technique tracked the two parameters in their allowed physical space. Several Monte Carlo samples were generated at various points in parameter space, and Figure 9.1 shows the measured parameters as a function of their generated values. The $V \pm A$, and the $\eta = 1$ Monte Carlo samples used in the fit procedure were generated with very high statistics and are the same for each of the fits performed. The simulated "data" samples, generated at different points in parameter space, all have approximately the same number of events as the true data sample. Although the errors obtained on the different measured results depend on the parameters, we note that there does not appear to be any systematic bias associated with the fitting technique. This test confirms that the fit technique will measure the parameter of interest irrespective of its true value. This exercise was carried out for each parameter individually, with the other parameter assumed to be fixed at its Standard Model expectation.

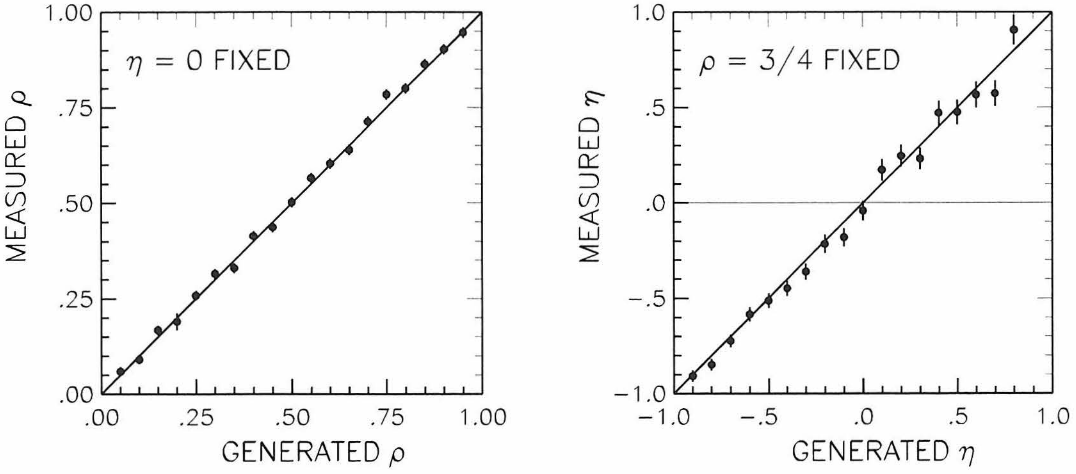

Figure 9.1: Tracking the two parameters over their allowed parameter space.

The next test was to track the parameters using two-dimensional simultaneous fits. We find that 60% of the time the fit reproduces the generated parameters at the

1 σ level, and 85% of the time, at the 2 σ level. These numbers are consistent with what one expects from pure statistics. No systematic error is assigned associated with an imperfect fit procedure.

Before the efficiency corrections in Equations 8.13 and 8.11 were applied, the fit procedure did appear to have some systematic problems. As explained earlier in Section 8.1, the detector efficiency is independent of the Monte Carlo sample considered. However, the probability distribution function does depend on the model considered, and since the spectra used in this study were obtained after all cuts applied in the data (including the momentum requirement), the efficiency corrections cannot be neglected in this study.

9.3 Trigger

In the data sets considered in this analysis, seven primary trigger lines along with some loose prescaled lines were active. We require at least one of the seven trigger lines to be satisfied. The Monte Carlo simulation predicts a trigger efficiency of $(99.58 \pm 0.01)\%$ for the $e\ vs.h\pi^0$ sample, and $(98.30 \pm 0.04)\%$ for the $\mu\ vs.h\pi^0$ sample after all cuts. Almost all triggered events pass the KIL2/LVL3 software filter. We selected the tau decay mode $\tau^+ \rightarrow h^+\pi^0\overline{\nu}_\tau$ to tag $\tau\tau$ events in this analysis partially because of the high trigger efficiency for this mode.

Although the Monte Carlo trigger simulation package (MCTR) is quite thorough, its inadequacies are addressed using real data. Figure 9.2 compares the distribution of the seven trigger lines in the 4S2 data set. The distributions are normalized to the number of events in the plot. There is quantitatively good agreement between the data and the Monte Carlo simulation for both the electron and muon samples. We observe similar agreements for the other data sets. Given the level at which the trigger is modeled, the fact that the trigger efficiency predicted by the Monte Carlo simulation is close to 100% suggests that it cannot be too far off. Further, approximately 95% of all events pass 2 or more trigger lines, and the trigger redundancy helps.

Since the Michel parameters are extracted from the lepton momentum spectra, the

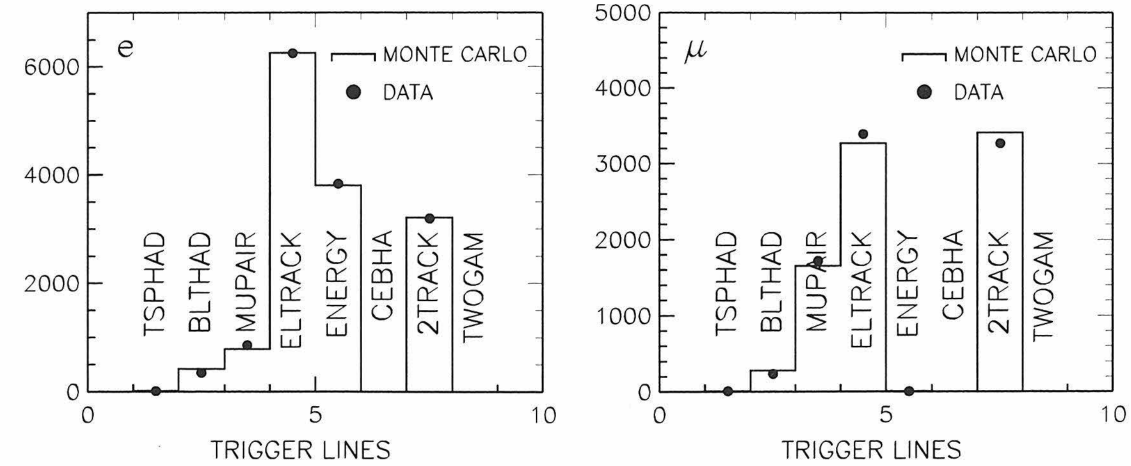

Figure 9.2: Distribution of the trigger lines in the 4S2 data and Monte Carlo simulation.

momentum dependence of the trigger efficiency is vital. The solid dots in Figure 9.3 indicate this momentum dependence for both samples considered.

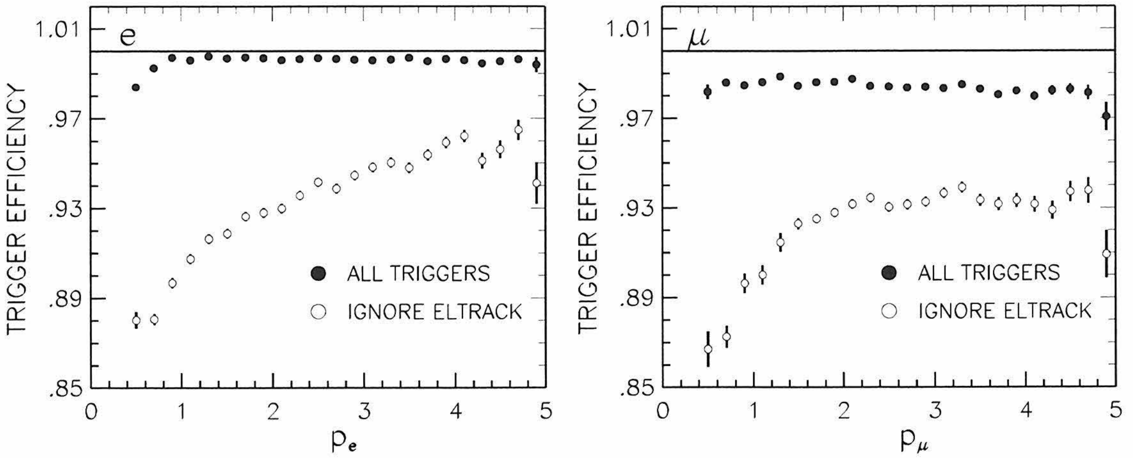

Figure 9.3: The momentum dependence of the overall trigger efficiency (solid dots) for the electron (left) and muon (right) samples. The momentum dependence of all the trigger lines ignoring the ELTRACK line (open dots) is also shown.

We observe that the overall trigger efficiency is independent of momentum over most of the range considered. Also shown in this figure is the trigger efficiency for all triggers excluding the ELTRACK trigger line (open dots). When this one trigger line is ignored, the trigger efficiency falls significantly. It also develops a marked momentum dependence.

Since the overall trigger efficiency is dominated by the ELTRACK trigger line's efficiency and over 90% of all events in this data sample pass this line, we estimate the trigger systematic error by estimating the systematic error resulting from the inaccurate modeling of the ELTRACK line in the Monte Carlo trigger simulation. This line utilizes both the tracking and neutral components of the trigger. We estimate the systematic error arising from both these components using the data. The trigger requirements for the ELTRACK line is shown in Table 9.1.

	Tracking	Time of Flight	Calorimeter	Data Set
L1:	2TIGHT	2TFBAR	1CBH	4S2
	2LOOSE	2TFBAR	1CBH	4S3
	1TRACK	2TFBAR	1CBH	4S4+
L2:	1PD			4S2-4S8
	PASS			4S9-4SA

Table 9.1: ELTRACK (Line 4) trigger line definition.

The tracking component of the trigger line can be studied using the subsample of events that survive the requirements of the ENERGY trigger line. This line contains no tracking requirements and a significant subsample of the electron mode events satisfy this line. Figure 9.4 shows the momentum dependence of the tracking component of the ELTRACK line as measured in both the data and the Monte Carlo electron samples. We find that the efficiency is high and slightly overestimated in the Monte Carlo simulation.

The neutral component of the ELTRACK line can be studied using the subsample of events that survive the requirements of the 2TRACK line. Figure 9.5 shows the momentum dependence of the HIGH BIT neutral component of the ELTRACK line in the electron sample. Once again, we find that the trigger efficiency is high over most of the momentum range studied. Further, the Monte Carlo simulation does an excellent job of modeling this efficiency over the entire momentum range.

The difference in the measured data and Monte Carlo simulation efficiencies in

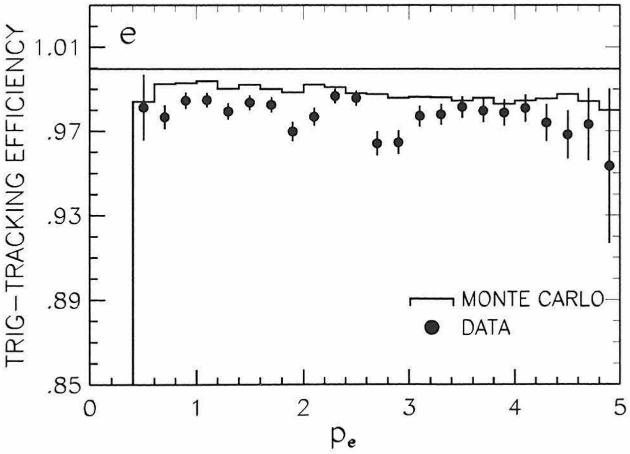

Figure 9.4: The momentum dependence of the tracking component of the ELTRACK trigger line in the data and the Monte Carlo simulation (e *vs.* ρ events).

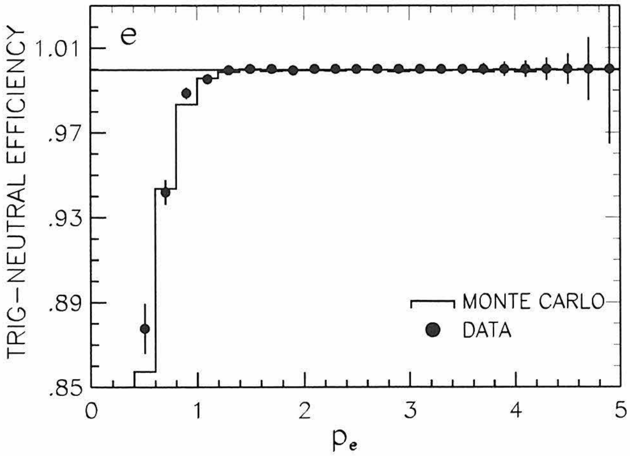

Figure 9.5: The momentum dependence of the neutral (calorimeter) component of the ELTRACK trigger line in the data and the Monte Carlo simulation (e *vs.* ρ events).

Figure 9.4 and Figure 9.5 are used to estimate the trigger systematic error arising from the imperfect simulation of this trigger line. We use 3σ variations in this difference to reweight the Monte Carlo electron spectrum. The Michel parameters are remeasured using the reweighted distributions, and the largest change observed in the parameters is used as an estimate of the systematic error. The errors resulting from the imperfect simulation of the third component of the ELTRACK trigger line, the Time-of-Flight component, is expected to be small relative to this estimate, and is ignored.

Muons do not satisfy the ENERGY line and thus it is not possible to estimate the trigger systematic using the above technique. However, there is no reason to expect that the momentum dependence of the ELTRACK line be any different in the muon sample. Thus we calculate the trigger systematic errors using the same differences utilized above to obtain the $3\ \sigma$ reweighted Monte Carlo muon distribution, and remeasure the Michel parameters. Once again, the largest shifts in the parameters is used as an estimate of the systematic error.

The KIL2/LVL3 efficiency is easy to calculate, since 1 in 7 events that fail the LVL3 criteria is saved. Events that fail are signified by a "garbage" bit in the event header word. Both Monte Carlo and data events identified by this bit are discarded.

The overall trigger contributions to the systematic error on all parameters measured are listed in Table 9.2. These errors are calculated for the results obtained after one combines the pseudo rest frame and laboratory frame analyses.

	ρ_e	ρ_μ	η_μ	$\rho_{e\mu}$	$\eta_{e\mu}$
Trigger	0.002	0.006	0.019	0.002	0.005
Statistics	0.014	0.048	0.149	0.013	0.061

Table 9.2: Trigger systematic error contributions to each of the Michel parameters measured.

This table also lists the statistical errors on the parameters for comparison. We find that the contributions from imperfect trigger simulations in the Monte Carlo package are small relative to the statistical errors.

9.4 Electron Identification

The electrons utilized in this analysis were identified with the SEID package described in Section 4.1.5. This package was designed for low multiplicity event topologies, and for analyses in which precise knowledge of the efficiency is needed, but optimal background rejection is not. The systematic errors resulting from fake electrons are discussed in a later section; here we consider the electron identification efficiencies. The nominal cuts imposed by the SEID subroutine are as follows:

$$\begin{gathered} |PQCD| > 0.5\ , \qquad |CZCD| > 0.707\ , \\ E/P > 0.85 \quad \text{and} \quad SGELDI > -2\ , \end{gathered} \tag{9.1}$$

where $PQCD$ is the signed track momentum, $CZCD$ is the angle the track makes with the beam axis, E/P is the ratio of the energy measured in the calorimeter and the momentum of the charged track as recorded by the tracking chambers, and $SGELDI$ is the difference between the measured dE/dx and the dE/dx expected for an electron divided by the resolution.

Since the original CLEO II Monte Carlo simulation did not reproduce the efficiency perfectly, SEID has hard-wired efficiencies extracted from a pure sample of radiative Bhabha events in the data. These efficiencies, shown in Table 9.3, are measured as a function of both the electron momentum and the angle in the detector. The SEID efficiency is approximately constant at 97.5%, to within ±1%. The errors include both statistical and systematic uncertainties associated with the data sample used.

There is a mild run dependence that is also handled automatically by SEID. The efficiency correction factors that are applied as a function of the data set are shown in Table 9.4.

Momentum Range	SEID Efficiency (%)		
(GeV/c)	$0.7 > \|\cos\theta\| > 0.6$	$0.6 > \|\cos\theta\| > 0.3$	$\|\cos\theta\| < 0.3$
0.50 - 0.75	0.9549 ± 0.0015	0.9758 ± 0.0008	0.9764 ± 0.0013
0.75 - 1.00	0.9776 ± 0.0012	0.9816 ± 0.0009	0.9775 ± 0.0014
1.00 - 1.25	0.9819 ± 0.0014	0.9833 ± 0.0011	0.9783 ± 0.0016
1.25 - 1.50	0.9851 ± 0.0016	0.9812 ± 0.0014	0.9803 ± 0.0017
1.50 - 1.75	0.9811 ± 0.0022	0.9787 ± 0.0017	0.9774 ± 0.0020
1.75 - 2.00	0.9832 ± 0.0023	0.9764 ± 0.0018	0.9784 ± 0.0019
2.00 - 2.25	0.9807 ± 0.0025	0.9774 ± 0.0018	0.9777 ± 0.0020
2.25 - 2.50	0.9814 ± 0.0024	0.9778 ± 0.0017	0.9735 ± 0.0020
2.50 - 2.75	0.9805 ± 0.0022	0.9808 ± 0.0013	0.9740 ± 0.0017
2.75 - 3.00	0.9803 ± 0.0015	0.9775 ± 0.0009	0.9751 ± 0.0010
3.00 - 3.25	0.9794 ± 0.0012	0.9773 ± 0.0008	0.9735 ± 0.0010
3.25 - 3.50	0.9829 ± 0.0010	0.9782 ± 0.0008	0.9746 ± 0.0014
3.50 - 3.75	0.9797 ± 0.0010	0.9793 ± 0.0008	0.9765 ± 0.0016
3.75 - 4.00	0.9805 ± 0.0009	0.9803 ± 0.0010	0.9759 ± 0.0015
4.00 - 4.25	0.9770 ± 0.0013	0.9768 ± 0.0012	0.9749 ± 0.0014
4.25 - 4.50	0.9828 ± 0.0015	0.9783 ± 0.0010	0.9733 ± 0.0013
4.50 - 4.75	0.9797 ± 0.0014	0.9775 ± 0.0009	0.9716 ± 0.0011
4.75 - 6.50	0.9793 ± 0.0011	0.9774 ± 0.0008	0.9745 ± 0.0012

Table 9.3: SEID efficiency as a function of the momentum and $\cos\theta$.

Data Set	Correction Factor	Data Set	Correction factor
4S1	-	4S5	0.9702
4S2A	0.9794	4S6	0.9774
4S2B	0.9769	4S7	0.9788
4S3A	0.9885	4S8	0.9788
4S3B	0.9839	4S9	0.9759
4S4	0.9748	4SA	0.9729

Table 9.4: SEID efficiency run dependent correction factors as a function of the data set considered.

Figure 9.6 shows the momentum dependence of the electron identification efficiency with both the angular and run dependence integrated out. The angular distribution of electrons from the signal Monte Carlo simulation is used to integrate out the angular dependence (see Table 9.5).

Position	Percentage of final electron sample
$0.0 < \lvert\cos\theta\rvert < 0.3$	49.04
$0.3 < \lvert\cos\theta\rvert < 0.6$	40.85
$0.6 < \lvert\cos\theta\rvert < 0.7$	10.12

Table 9.5: Angular distribution of the electrons in the signal Monte Carlo sample.

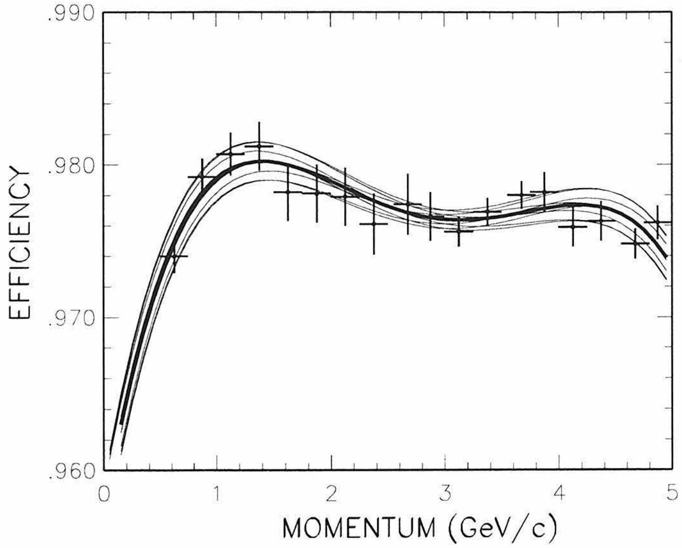

Figure 9.6: SEID electron efficiency (crosses) from radiative Bhabha events and $ee(ee)$ events after the $\cos\theta$ dependence has been integrated out. Both statistical and systematic errors are shown. The bold line indicates the best fit and the solid lines indicate $3\,\sigma$ variations of the fit as described in the text.

The bold line in Figure 9.6 is a 4th order fit to the measured efficiency after the angular dependence has been integrated out. We now fix this polynomial fit function to its best value and add a linear uncertainty of the form:

$$f(p_e) = \alpha(p_e - C)\ , \tag{9.2}$$

to the fit function. The data are re-fit, and we measure the free parameter α for different values of the inflexion point C. The errors obtained for α are the following:

$$\begin{array}{ll} \Delta\alpha = \pm 0.00015 \text{ for } C = 1.5\text{GeV}/c & \Delta\alpha = \pm 0.00021 \text{ for } C = 2.5\text{GeV}/c \\ \Delta\alpha = \pm 0.00021 \text{ for } C = 3.5\text{GeV}/c & \Delta\alpha = \pm 0.00015 \text{ for } C = 4.5\text{GeV}/c \end{array} \quad (9.3)$$

The solid lines in the figure show the modified fit function for 3 σ variations of α. This leads to the following weights:

$$\begin{array}{ll} w_1 = 1 \pm (p_e - 1.5\text{GeV}/c)\dfrac{0.0004}{\text{GeV}/c} & w_2 = 1 \pm (p_e - 2.5\text{GeV}/c)\dfrac{0.0006}{\text{GeV}/c} \\ w_3 = 1 \pm (p_e - 3.5\text{GeV}/c)\dfrac{0.0004}{\text{GeV}/c} & w_4 = 1 \pm (p_e - 4.5\text{GeV}/c)\dfrac{0.0006}{\text{GeV}/c} \end{array} \quad (9.4)$$

Reweighting the measured electron momentum spectrum by the factor w_2 leads to the largest changes in the Michel parameters measured in the electron mode analysis, as well as the combined electron and muon mode analysis. The observed change in the parameters is used as an estimate of the electron identification systematic error on the parameter measured. These errors are shown in Table 9.6 and are small relative to the corresponding statistical errors on the parameters.

Source	$\Delta\rho_e$	$\Delta\rho_{e\mu}$	$\Delta\eta_{e\mu}$
Electron Identification	< 0.001	< 0.001	± 0.001
Statistics	0.014	0.013	0.061

Table 9.6: Electron identification systematic errors.

9.5 Muon Identification

Muons, utilized in this analysis, are identified with the SMID package described in Section 4.1.5. This package identifies muons above 1.5 GeV/c, and it uses efficiencies and fake rates measured using the data, to identify muons in the Monte Carlo simulation. The momentum dependence of the muon identification efficiencies has been measured using $\mu\mu\gamma$ [81] events for five different $\cos\theta$ bins, and is shown in Figure 9.7.

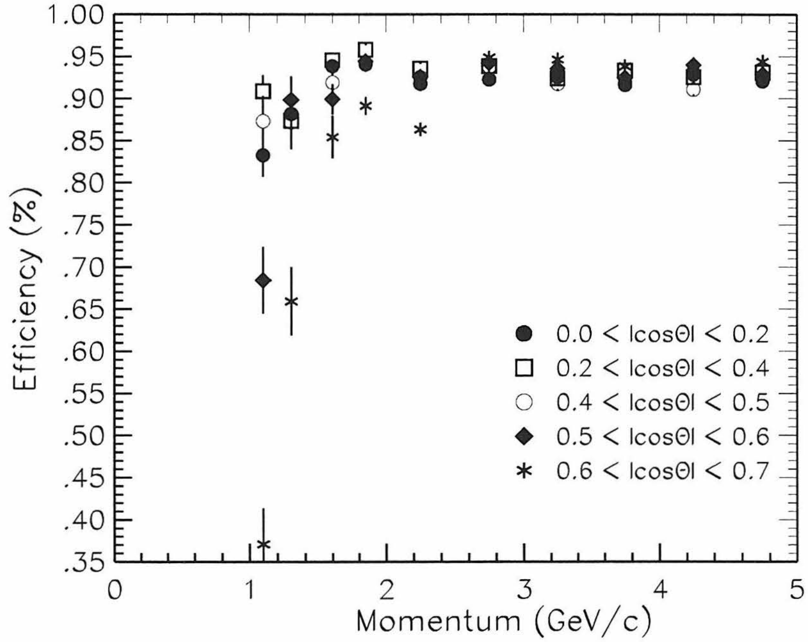

Figure 9.7: Muon identification efficiencies measured using radiative muon pair events in the data as a function of momentum and polar angle.

We note that the CLEO II detector can identify muons in the 1.0-1.5 GeV/c momentum range. The η parameter is very sensitive to the low momentum muons, and including this low momentum region could significantly improve the results obtained. However, the fact that the muon identification efficiency falls rapidly in this low momentum region and thus requires a finer binning, coupled with the limited data statistics in the $\mu\mu\gamma$ low momentum sample, results in large errors on the efficiency measurements in this region. These larger errors translate into larger systematic errors on the η measurements. Thus, the large improvement in precision that could be obtained by including these low momentum muons is nullified by the equivalent increase in the systematic error. We choose not to include these low momentum muons in this analysis [*].

The procedure used to evaluate the systematic error associated with the electron identification efficiency is applied here to estimate the muon identification systematic error. We first integrate out the angular dependence of the muon identification efficiency using the distribution of muons seen in the Monte Carlo simulation of the signal $\tau^- \to \mu^- \overline{\nu}_\mu \nu_\tau$ decay mode (Table 9.7).

Position	Percentage of final muon sample
$0.0 < \lvert\cos\theta\rvert < 0.2$	26.77
$0.2 < \lvert\cos\theta\rvert < 0.4$	24.40
$0.4 < \lvert\cos\theta\rvert < 0.5$	20.59
$0.5 < \lvert\cos\theta\rvert < 0.6$	16.47
$0.6 < \lvert\cos\theta\rvert < 0.7$	11.77

Table 9.7: Angular distribution of the muons in the signal Monte Carlo sample.

The resulting measured efficiency is now fit to a fifth order polynomial, and the fit function is fixed to its best value. We now add a linear uncertainty of the form:

$$f(p_\mu) = \alpha(p_\mu - C)\ , \tag{9.5}$$

and fitting this linear uncertainty to the measured efficiency yields the following measurements for the free parameter α:

$$\begin{aligned} \Delta\alpha &= \pm 0.0004 \text{ for } C = 2.0 \text{ GeV}/c\ , \quad \Delta\alpha = \pm 0.0007 \text{ for } C = 3.0 \text{ GeV}/c \\ \text{and } \Delta\alpha &= \pm 0.0008 \text{ for } C = 4.0 \text{ GeV}/c\ . \end{aligned} \tag{9.6}$$

---

[*] Some low momentum muons are recovered in the pseudo rest frame analysis without using muon identification to select them as described in Section 7.2.

Using 3 σ variations of this parameter leads to the weights:

$$
\begin{aligned}
w_1 &= 1 \pm (p_\mu - 2.0\mathrm{GeV}/c\,)\frac{0.0012}{\mathrm{GeV}/c}\,, \quad w_2 = 1 \pm (p_\mu - 3.0\mathrm{GeV}/c\,)\frac{0.0021}{\mathrm{GeV}/c} \\
\text{and } w_3 &= 1 \pm (p_\mu - 4.0\mathrm{GeV}/c\,)\frac{0.0024}{\mathrm{GeV}/c}\,. \qquad (9.7)
\end{aligned}
$$

These weights are used to reweight the Monte Carlo muon spectrum, and the Michel parameters are remeasured for each of the reweighted spectra. Using the weight w_3 results in the largest changes in the Michel parameters, in both the stand-alone muon analysis, as well as the the combined electron and muon mode analysis. These changes are now used as estimates of the systematic error, and are listed in Table 9.8. This table also lists the statistical error on each of the parameters measured.

Source	$\Delta\rho_\mu$	$\Delta\eta_\mu$	$\Delta\rho_{e\mu}$	$\Delta\eta_{e\mu}$
Muon Identification	±0.004	±0.018	±0.001	±0.024
Statistics	±0.014	±0.149	±0.013	±0.061

Table 9.8: Muon identification systematic errors.

We note that although the errors listed are not negligible, they are significantly smaller than the corresponding statistical errors. This would not be true if one relaxed the momentum requirement down to 1.0 GeV/c; the statistical errors would reduce by approximately 16% while the systematic error would increase by over 100% in the combined electron and muon mode analysis.

9.6 Backgrounds

The background contaminations from all potential sources and their estimation were described in detail in Chapter 5. The negligible background sources were ignored, while a background subtraction was performed for each of the substantial sources. In this section, we describe the systematic error estimates associated with the more significant background sources: misidentified leptons, and the feed-down from multi π^0 modes into the tag $\tau^+ \rightarrow h^+\pi^0\overline{\nu}_\tau$ decay mode. The contributions from each of the non tau background modes is negligible, and thus there is no systematic error associated with these modes.

Hadrons fake both electrons and muons. This background source is the largest source of contamination in the data sample, and is potentially the most dangerous since the fake lepton spectrum is momentum dependent. The spectral shape Michel parameters ρ and η are directly measured using the lepton momentum spectrum, and to achieve the level of precision desired, one is required to understand absolutely both the normalization as well as the shape of this background source using the data.

9.6.1 Fake Muons

Both the source of the fake muon contamination and the fake rates are momentum dependent. Muons with $p_\mu \geq 1.5$ GeV/c are identified using SMID and the contamination in this momentum range is solely due to pions and kaons faking the muon signal. SMID selects muon events in the data by looking at the signals in the CLEO II muon identification chambers. The muons with $p_\mu < 1.5$ GeV/c are not identified using these signals in the muon chambers. Instead, one applies cuts to veto all possible τ decay modes resulting in a sample of muons as described in detail in Section 7.2. In addition to the hadron contamination, one now observes a non-negligible electron contamination.

Fake muons with $p_\mu > 1.5$ GeV/c:

The probability that a hadron will fake a muon, and the momentum dependence of this probability are determined using the very clean hadron sample obtained from the decay of the tag tau in these data events $\tau^+ \rightarrow h^+\pi^0\overline{\nu}_\tau$, as described in Appendix B. These fake rates, coupled with the parent hadron distribution, also obtained using this data sample, as detailed in Section 5.1.1, results in an excellent estimate of the fake muon momentum spectrum normalized to the data muon spectrum. The background estimation procedure does not in any way rely on the Monte Carlo simulation †. We perform a bin by bin background subtraction to remove statistically this background source before the data are utilized to measure the parameters of interest.

The solid contours shown on the left (right) in Figure 9.8 depict the 1 σ and 2 σ error ellipses obtained in the $\eta - \rho$ plane for the measurements performed using the laboratory (pseudo rest) frame momentum (energy) spectrum. The dotted contours depict the corresponding measurements when the fake muon background spectrum was not subtracted from the data.

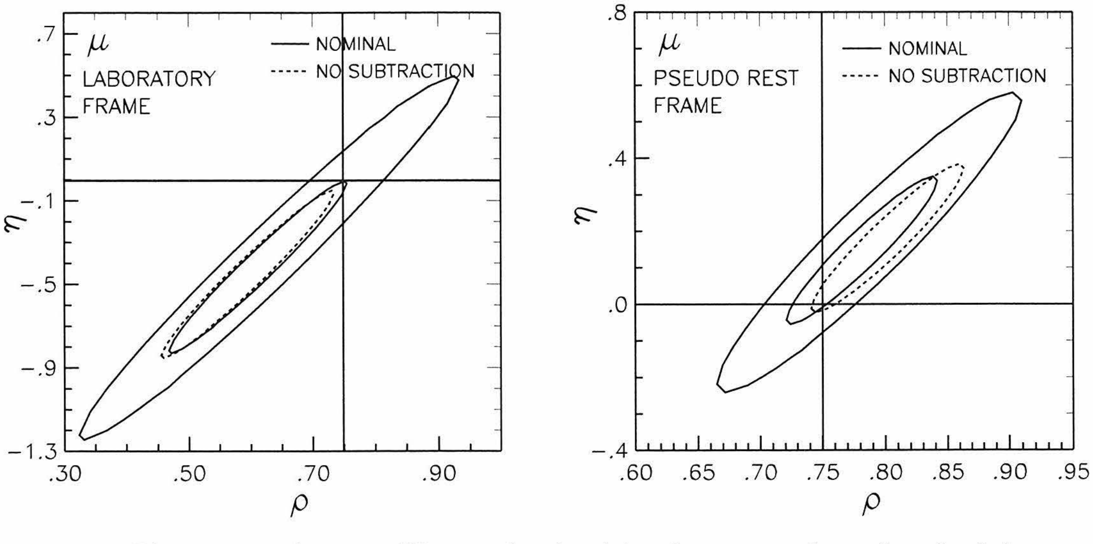

Figure 9.8: The nominal error ellipses obtained in the $\eta - \rho$ plane for the laboratory (pseudo rest) frame muon analysis are depicted by the solid contours on the left (right). The dotted contours are obtained when this background source is ignored.

---

† The old version of the CLEO II Monte Carlo simulation program underestimated the fake rates, and the newer version, which invokes NUCRIN to simulate the hadronic interactions, overestimates them.

Although the background subtraction is $\simeq 1\%$, we note that the change is fairly significant for both parameters in the pseudo rest frame analysis.

In Figure 9.9, we illustrate the corresponding results obtained when the two leptonic modes are simultaneously analyzed. Once again, we observe a more significant change in the pseudo rest frame analysis. We also note that the central value of the parameter ρ does not change significantly in both these plots. This results from the fact that ρ is nailed down by the precise electron mode analysis measurement.

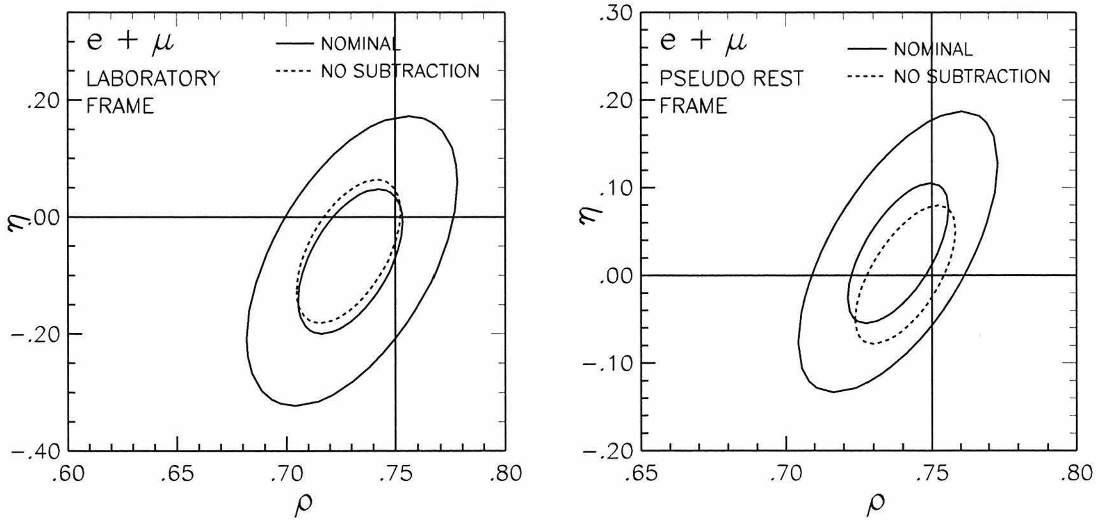

Figure 9.9: The nominal error ellipses obtained in the $\eta - \rho$ plane for the laboratory (pseudo rest) frame analysis are depicted by the solid contours on the left (right). These contours are obtained by analyzing both the electron and muon modes simultaneously. The dotted contours are obtained when this background source is ignored.

To evaluate the systematic error associated with the estimation of this background source we vary both the shape and the normalization of the background spectrum obtained from the data by 1 σ, where σ is the error obtained in the data estimate of the quantity being varied. This error estimate includes a 15% systematic error on the fake rate determination. The parameters are remeasured and the largest changes observed are used as estimates for the systematic error associated with this background subtraction procedure. These are listed in Table 9.9. We note that these error estimates are not negligible.

Fake muons with $p_\mu < 1.5$ GeV/c:

As mentioned earlier, fake muons in this low momentum region result from both hadrons as well as electrons. Hadrons result from the direct $\tau^- \to \pi^-/K^-\nu_\tau$ decay mode as well as from the decay of intermediate resonances such as the ρ, K^*, a_1, etc. These low momentum muon fake background only affects the data analyzed in the pseudo rest frame, since they can only be identified in that frame of reference.

In Figure 9.10, we illustrate the nominal 1 σ and 2 σ results obtained in the muon (left) analysis and the combined lepton (right) analysis. Also shown here are the corresponding 1 σ error ellipse obtained when one ignores the low momentum fake muons. In the muon mode, both measured parameters change significantly, while in the combined mode the ρ parameter is unchanged as a result of its precise determination using the electron mode events.

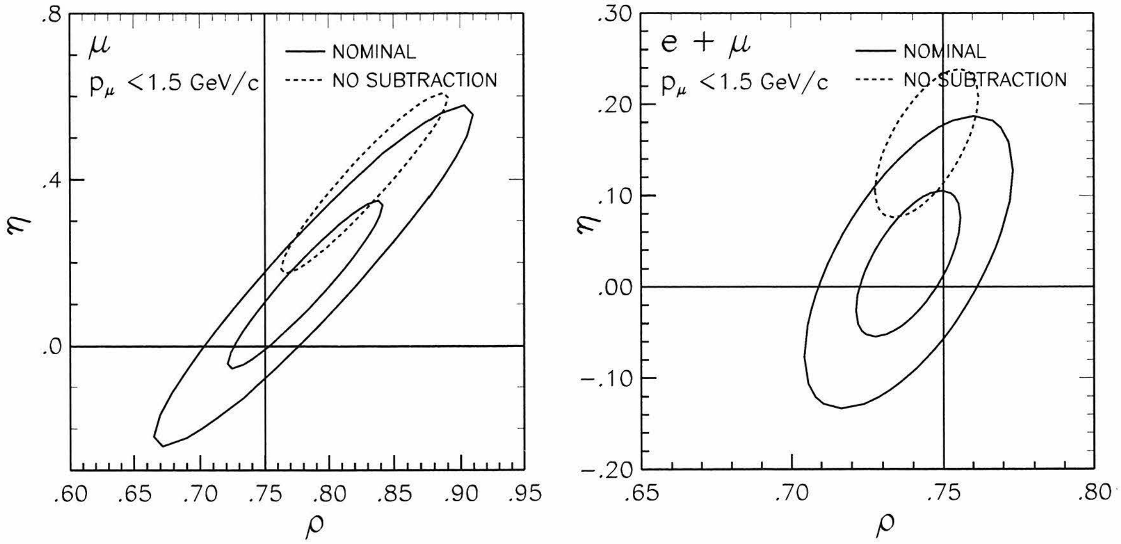

Figure 9.10: The $\eta - \rho$ error ellipses for the nominal results obtained in the muon (combined mode) pseudo rest frame analysis are shown on the left (right). Ignoring the low momentum fake muons would result in a big shift in the result, as depicted by the dotted contours.

We note that neglecting these backgrounds would result in very different result. Both the shape and the absolute normalization ($\simeq 4\%$) of all these backgrounds are estimated using the generic τ Monte Carlo simulation events. The different input branching ratios in this simulation are listed in Table 3.1. The fake spectrum obtained in the Monte Carlo sample is normalized to the data, and is subtracted from it before the parameters are measured. Each mode is individually normalized using the Particle Data Group (PDG) 1996 branching ratios. To evaluate the systematic error associated with this background, we vary the normalizations of the individual τ background decay modes by $3\,\sigma$, where σ is the error on the PDG world average results. The systematic error estimates thus obtained, along with the estimates obtained for the higher momentum region are shown in Table 9.9. Although neglecting the low momentum fake muons results in substantial shifts in the results obtained, the background procedure is well defined and the systematic error estimates are smaller than the corresponding estimates for the higher momentum muons. The high momentum estimate is dominated by the errors on the fake rate measurements made using the data. An increased data set would result in smaller errors on those measurements, thus resulting in a smaller error estimate here. In this analysis, the systematic errors obtained here are one of the more dominant ones.

Source	$\Delta\rho_\mu$	$\Delta\eta_\mu$	$\Delta\rho_{e\mu}$	$\Delta\eta_{e\mu}$
$p_\mu \geq 1.5\text{GeV}/c$	±0.024	±0.101	±0.002	±0.022
$p_\mu < 1.5\text{GeV}/c$	±0.006	±0.033	< 0.001	±0.011
Fake Muons	±0.025	±0.106	±0.002	±0.025
Statistics	±0.014	±0.149	±0.013	±0.061

Table 9.9: Fake muon systematic errors. The error estimates for the two different momentum regions are added in quadrature to obtain the final error estimate for this source.

9.6.2 Fake Electrons

The hadron background to the electron sample is small and comprises only 0.135% of the electron sample in the data. In the nominal analysis, no background subtraction is performed. To evaluate the systematic error associated with this small background, we estimate both the fake electron rate and the absolute normalization using the data, following the procedure applied for the fake muons. The shift in the nominal result obtained on applying this background subtraction procedure is used as an estimate of the systematic error. This is an overestimate of the error, but since it is small relative to other sources of error, more work need not be done to evaluate it. The error estimates for fake electrons in this analysis are shown in Table 9.10.

Source	$\Delta\rho_e$	$\Delta\rho_{e\mu}$	$\Delta\eta_{e\mu}$
Fake Electrons	0.004	0.004	0.015
Statistics	0.009	0.013	0.061

Table 9.10: Fake electron systematic error estimates.

As shown in Chapter 5 the background contamination from Bhabha events is negligible. Thus, no systematic error is assigned associated with this background source. Figure 9.11 shows on a logarithmic scale the tail end of the electron spectrum (before the $\cos\alpha$ requirement), used to measure the Michel parameter ρ . In this figure, the E/P requirement on the tag side of the event has been removed to allow any existing Bhabha background to sneak into the sample. Still, after the π^0 sideband subtraction, there is absolutely no indication of any background from this source.

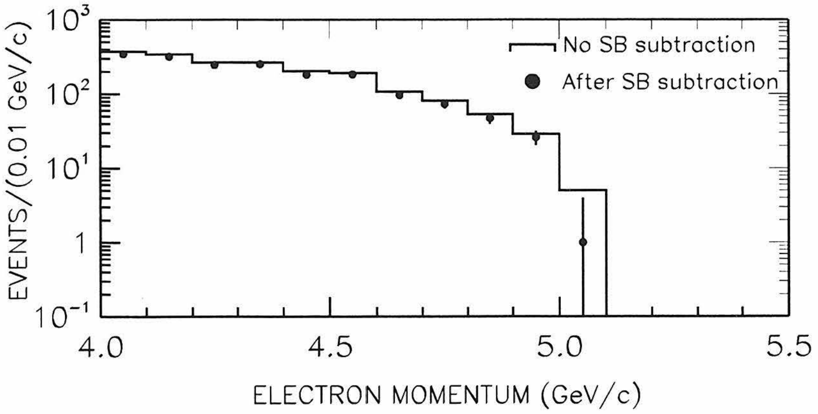

Figure 9.11: The tail end of the electron data spectrum (solid histogram) on a logarithmic scale. The dots indicate the spectrum after the nominal π^0 sideband subtraction procedure.

9.6.3 Feed-down into Tag Mode

Tau feed-down into the tag $\tau^+ \to h^+\pi^0\overline{\nu}_\tau$ mode is minimized by the application of veto cuts on any unused showers in the detector. In principle, feed-down events on the tag side should not affect the results obtained in the laboratory frame analysis. The laboratory lepton momentum spectrum obtained for the decay of the other τ in the event should essentially be independent of the tag decay mode, except for spin correlations and initial state radiation, which are both modeled by the Monte Carlo generator KORALB, and are addressed in a following section.

Feed-down events become very important in the pseudo rest frame analysis, where the flight direction of the parent τ is estimated by the $h\pi^0$ system, and is directly used to calculate the boost, and to reconstruct the energy spectrum in the pseudo rest frame. An improper knowledge of the normalization, or a poor simulation of these feed-down events would potentially result in a badly reconstructed energy spectrum. Changing the nominal veto requirements to let in more feed-down events into the sample analyzed does not significantly change the results obtained. This stability in the results seen when the feed-down background is increased by more than a factor of 5-10 indicates that the feed-down modes are included in approximately accurate proportions, and that this feed-down and the spin correlations are well modeled in the Monte Carlo simulation.

The ratio of tau decays into the feed-down modes to the tag mode decay is well known. To evaluate a systematic error, we artificially change this ratio in the Monte Carlo distributions by 3 σ, where σ is the PDG 96 [72] error on this ratio, and remeasure the Michel parameters. The largest shifts observed are used as systematic error estimates, and are listed in Table 9.11 along with the statistical errors obtained for each of the measured parameters. We note that this systematic error estimate is small relative to the corresponding statistical errors.

Source	$\Delta\rho_e$	$\Delta\rho_{mu}$	$\Delta\eta_\mu$	$\Delta\rho_{e\mu}$	$\Delta\eta_{e\mu}$
Feed-down	0.001	0.002	0.007	0.002	0.008
Statistics	0.014	0.048	0.149	0.013	0.061

Table 9.11: Systematic error estimates arizing from the imperfect modeling of feed-down modes in the Monte Carlo simulation.

9.7 Beam Energy Corrections

The data used here were collected at two different beam energies; approximately 2/3 of the data is collected at beam energies of 5.29 GeV , and the remainder are collected at beam energies of 5.26 GeV . These running conditions are such that the center of mass energy lies near the peak of $\Upsilon(4S)$ resonance, and just below it, respectively. The $V-A$ Monte Carlo sample has been generated at the two different beam energies in approximately the same ratio as in the data sample. The non-standard Monte Carlo samples have all been generated at a beam energy of 5.29 GeV . The contributions of the non-standard Model Monte Carlo samples to the fit are small, and thus one does not expect any bias as a result of the single beam energy sample.

The solid contours in Figure 9.12 shows the 1 and 2 σ error ellipses in the $\eta-\rho$ plane obtained in the nominal electron and muon mode combined analysis. Ignoring the fact that two different beam energies were utilized during the data collection results in the dotted ellipses in this figure. We note that the change is small relative to the overall statistical errors. This change is entirely due to the muon data; the electron mode result is unchanged if these corrections are ignored.

The pseudo rest frame analysis is not affected by the different beam energies used, since the correct beam energy is used to calculate the pseudo rest frame energy spectrum. Thus the difference in the two 1 σ ellipses in Figure 9.12 is entirely due to the events analyzed in the laboratory frame of reference. Since we know the exact ratio of the two different beam energy samples in the data, the Monte Carlo sample is generated in approximately the same ratio, and since the two different beam energies used are close enough to each other to result in a non-significant change in

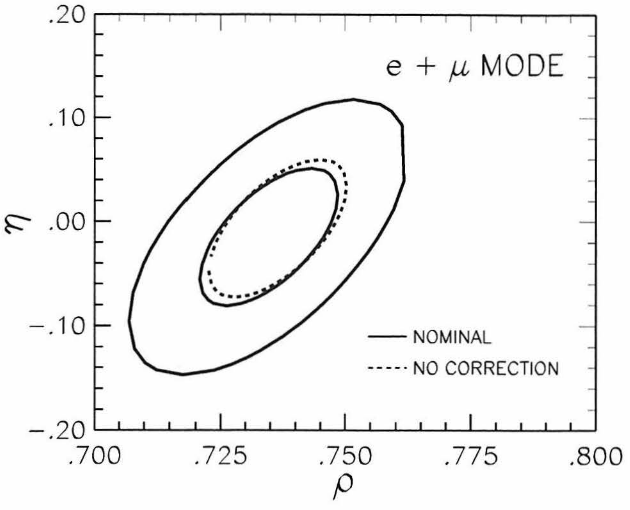

Figure 9.12: The 1 σ, 2 σ $\eta - \rho$ error ellipses for the nominal results obtained in the combined electron and muon mode analysis are depicted by the solid contours. The dotted contour shows the result obtained in the absence of any beam energy corrections.

the parameters measured, no systematic errors are assigned here.

9.8 Tau Flight Direction Estimation in Pseudo Rest Frame Analysis

Approximately 60% of the events in both the leptonic modes considered are analyzed using the scaled pseudo rest frame energy spectrum. One can reconstruct the pseudo rest frame spectrum for these events since the tag $h^{\pm}\pi^{0}$ system is a good estimator of its parent τ flight direction. We require that $\cos\alpha \geq 0.970$ for the events utilized, where α is the angle between the direction of the tag system and its parent τ flight direction in the laboratory frame of reference. The Monte Carlo simulation does an excellent job in simulating this angle as shown in Figure 7.5. Feed-down modes such as the $\tau \rightarrow \pi 2\pi^{0} \nu_{\tau}$ decay would distort this distribution. The excellent agreement between the data and the Monte Carlo distributions indicates that the feed-down modes are included in the Monte Carlo simulation in the appropriate amounts and with the correct dynamics.

To understand the systematics associated with the choice of the $\cos\alpha$ cut, we divide the data and Monte Carlo distributions into ten different $\cos\alpha$ bins and measure the parameters in each bin. The figure on the left (right) in Figure 9.13 plots the results obtained for the ρ parameter using the electron (muon) mode events. In the muon analysis, the η parameter is fixed to its Standard Model expectation, since one does not have sufficient statistics to measure the parameters simultaneously in each $\cos\alpha$ bin. Further, the bin sizes selected are not uniform, since the events with $\cos\alpha$ close to unity are more sensitive to the parameters.

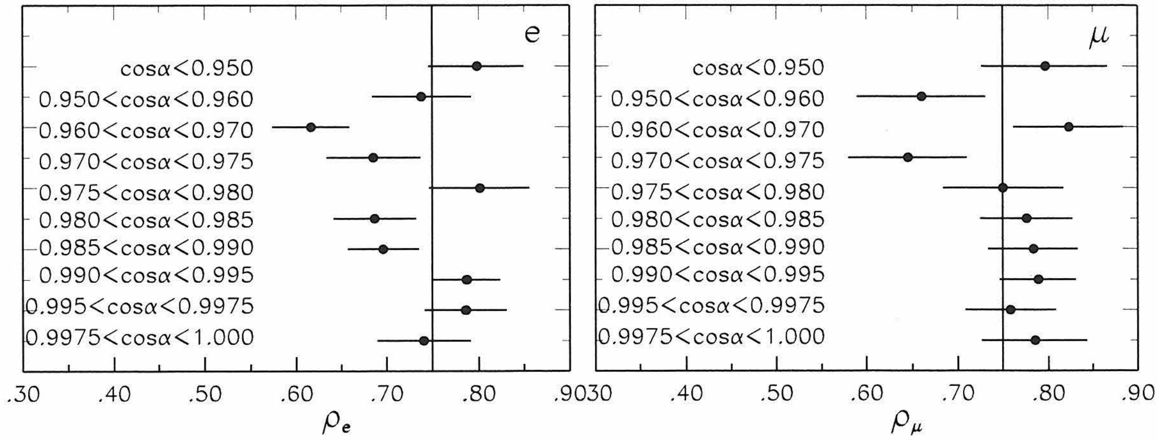

Figure 9.13: The Michel parameters ρ_e and ρ_μ for different slices in $\cos\alpha$.

We find that the Michel parameters measured are independent of the choice of the $\cos\alpha$ bin. Thus, there is no systematic error associated with the choice of the $\cos\alpha$ requirement, and we select events with $\cos\alpha \geq 0.970$ and analyze them using the pseudo rest frame spectrum; the remainder are analyzed using the laboratory spectrum. This choice of $\cos\alpha$ is optimal since it maximizes the sensitivity to the two parameters, and thus minimizes the final error obtained. In Figure. 9.14, we plot Δ_η, the error on the η parameter, obtained in a combined electron and muon mode Monte Carlo generator level analysis, as a function of the $\cos\alpha$ requirement. The arrow indicates the nominal choice for $\cos\alpha$.

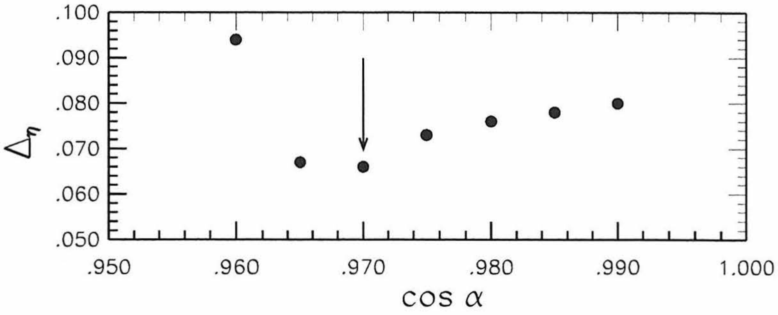

Figure 9.14: The error on the η parameter as a function of the $\cos\alpha$ requirement in a Monte Carlo generator level study using the combined electron and muon modes.

9.9 Radiative Processes

Radiation shifts the lepton energy spectrum to lower energies. As a result, a $V-A$ momentum spectrum resembles the $V+A$ or $\eta = 1$ momentum spectrum. This shift in the spectrum can bias the Michel parameter measurements. Since this analysis is designed to search for small deviations from the Standard Model expectations, it is important that radiative effects are appropriately accounted for in the Monte Carlo simulation.

Radiative photons arise as a result of three different processes:

1. initial and final state radiation;
2. external bremsstrahlung in the CLEO material;
3. internal bremsstrahlung or decay radiation. Electrons radiate $\simeq 10$ times as much as muons, and this effect is thus more pronounced in the electron channel.

The $V-A$ Monte Carlo samples were generated using KORALB for the generation of the $\tau^+\tau^-$ pairs with initial and final state radiation. TAUOLA is used for the decay radiation to order $\mathcal{O}(\alpha)$ in $e\nu\bar{\nu}$ and $\mu\nu\bar{\nu}$ events, while the PHOTOS package is used to simulate the decay radiation in non-leptonic decays of the tau. The simulation of bremsstrahlung in the CLEO II detector is performed by the GEANT-based CLEOG package. The non-Standard Model Monte Carlo samples were also generated using the above mentioned packages with a small modification to enable the generation of $\tau^{\pm} \rightarrow \ell^{\pm}\nu\nu_{\tau}$ decays with arbitrary values of the parameters ρ and η.

To lowest order, photons from all possible sources are simulated in the Monte Carlo samples. Table 9.12 lists the percentages of the different types of radiative photons present in the Monte Carlo samples utilized.

Mode	No γ	ISR/FSR	Decay	Bremsstrahlung
e *vs.* ρ	1.4%	58.2%	16.1%	96.0%
μ *vs.* ρ	16.8%	58.4%	4.0%	50.8%

Table 9.12: Radiation photons in the Monte Carlo samples.

Initial and final state radiation has a large rate, and thus a great potential to distort the lepton's momentum spectrum. The KORALB package includes single photon radiation, correct to $\mathcal{O}(\alpha)$, and the $\mathcal{O}(\alpha^2)$ corrections are not expected to be any larger than 2-3% relative to the $\mathcal{O}(\alpha)$ calculations. To evaluate any systematic error that might arise due to the imperfect modeling of these radiative effects in KORALB, the relative normalization of the events with these radiative photons in the Monte Carlo is changed by ±10%. This upper limit on the change in the relative normalization is obtained from data and Monte Carlo comparisons of the unused (not used to form the π^0 in the event) shower energy spectrum lying in the same hemisphere as the lepton in the event. Final state radiation in $e^+e^- \rightarrow \tau^+\tau^-(\gamma)$, as well as internal and external bremsstrahlung from the lepton are expected to lie close in angle to the lepton, and showers in the other hemisphere might be hadronic split-offs. Figure 9.15 plots the energy spectrum of all unused showers above 60 MeV in the lepton hemisphere. We note that the Monte Carlo simulation approximately reproduces the data over the entire energy range. Increasing the radiation by more than 10% in the Monte Carlo simulation would make the data and Monte Carlo shower energy spectra inconsistent with each other. In fact, this 10% change is allowed only as a result of the low statistics in the data sample.

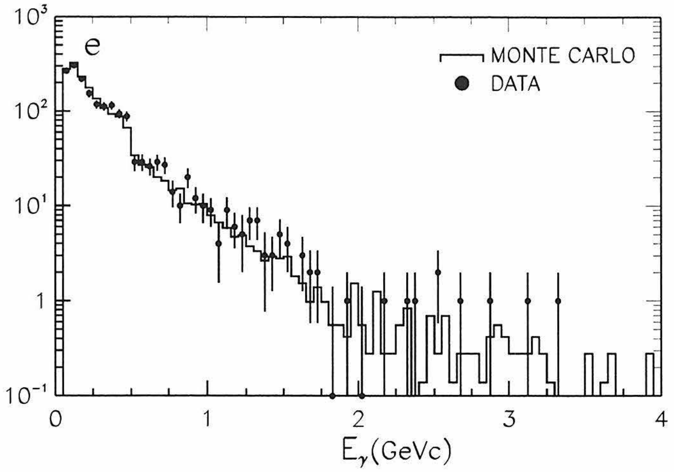

Figure 9.15: The energy spectrum for all unused showers lying in the lepton hemisphere in the event.

Figure 9.16 shows the change in the Michel parameters ρ_e and η_μ as the normalization of the radiation weighted events in the Monte Carlo $V-A$ spectrum are changed. A change of -100% corresponds to a Monte Carlo sample with no radiation, and we note that such a negligence would result in a significant change in the measured value of the parameters. The arrows indicate the $\pm 10\%$ change used to estimate the systematic error resulting from the imperfect modeling of radiative effects in the Monte Carlo simulation.

Decay radiation is a small effect and turning it off in the Monte Carlo simulation produces a negligible change in the parameters measured. The material in the CLEO II detector Monte Carlo simulation is known to 5-10%; one can thus vary the bremsstrahlung tagged spectrum by this amount to evaluate the systematic error resulting from the imperfect knowledge of the material. Once again, we observe a negligible change in the Michel parameters.

The overall systematic error resulting from imperfect radiative effects in the Monte Carlo simulation are listed in Table 9.13 for each of the parameters measured. These errors are obtained by adding the contributions from the three different sources in quadrature. We note that the systematic error is not negligible, but is small relative

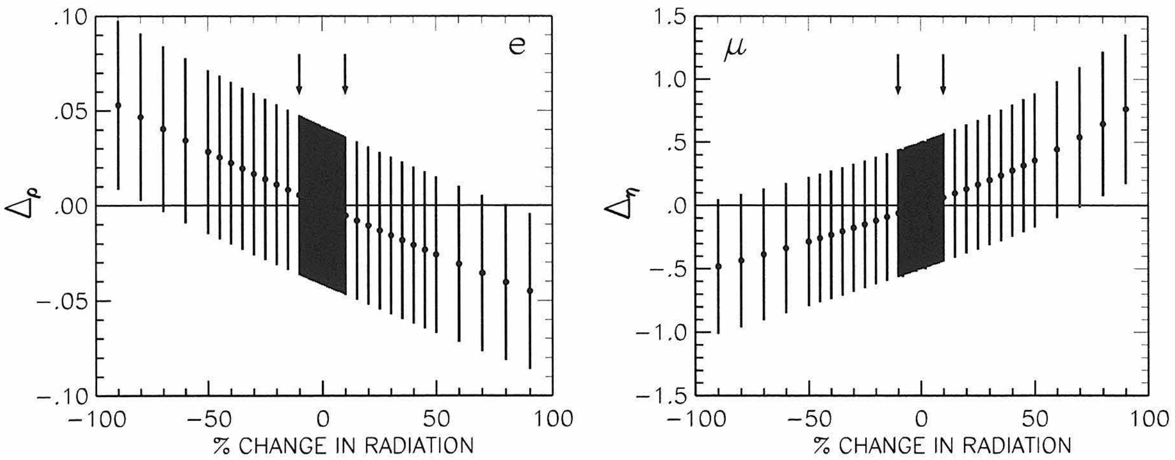

Figure 9.16: The dependence of the Michel parameter ρ (left) and η (right) on the normalization of the radiation weighted spectrum in the Monte Carlo simulation; $\Delta_\rho(\text{measured}) = \rho(\pm x\%) - \rho(\text{nominal})$, and $\Delta_\eta = \eta(\pm x\%) - \eta(\text{nominal})$.

to the statistical error estimate for the corresponding parameter.

	ρ_e	ρ_μ	η_μ	$\rho_{e\mu}$	$\eta_{e\mu}$
Radiation	0.005	0.003	0.050	0.001	0.004
Statistics	0.014	0.048	0.149	0.013	0.061

Table 9.13: Radiation systematic error contributions to each of the Michel parameters measured.

9.10 Spin Correlations

In this analysis, we consider e^+e^- annihilations at $\sqrt{s} \simeq 10$ GeV . Since the beams are unpolarized and photon exchange dominates the interaction, the average τ polarization is zero. However, spin-spin correlations exist between the two τ leptons in $e^+e^- \rightarrow \tau^+\tau^-$, leading to correlations between the kinematical quantities of the decay products. These correlations are not directly utilized in this analysis, but an imperfect modeling of them in the Monte Carlo simulation would result in biases in the measurements of the Michel parameters. In this section, we try and evaluate how well these correlations are incorporated in the Monte Carlo simulation and we estimate a systematic error to cover their imperfect modeling.

The polarimeter variable or the spin analyzer ω, as defined in Appendix C, can be utilized to separate statistically the left-handed τ^- from the right-handed τ^- [‡]. The Michel parameter measurements for the samples with different spin contents should ideally yield identical results if the spin correlations are correctly modeled in the simulation.

Figure 9.17 shows the ω distributions obtained for the events used in the electron mode analyses. The corresponding figures for the muon events are identical. The figure on the left includes all the events that are used in the pseudo rest frame analysis, while the figure on the right includes the events analyzed in the laboratory frame of reference. We note that the two ω distributions are remarkably distinct, indicating that the spin contents of the events analyzed in the two different frames of reference are very different. The fact that the results obtained in the two different frames of reference are consistent with each other indicates that both the spin dependence and the spin population are well modeled in the Monte Carlo. We also note that since the Monte Carlo samples were generated with the Standard Model values for the spin-dependent parameters ξ and δ, not only are spin correlations under control, but also the assumption that these two parameters are given by the Standard Model is good enough that the associated systematic error is small.

[‡] In the Standard Model (to the extent of CP invariance) the left-handed τ^- is equivalent to the right-handed τ^+ and the right-handed τ^- is equivalent to the left-handed τ^+.

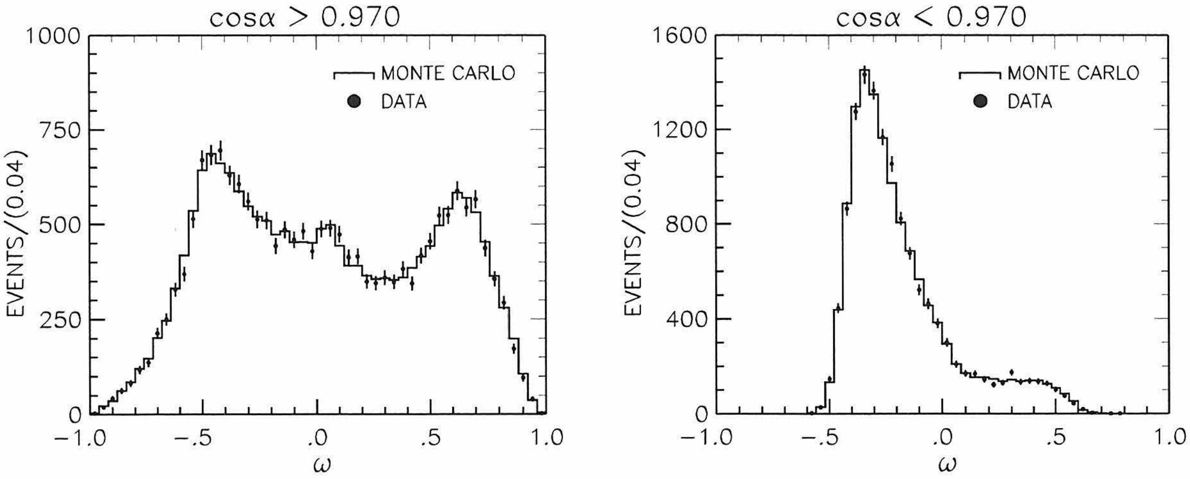

Figure 9.17: The polarimetric variable ω for the electron mode events used in both the pseudo rest frame and laboratory frame analyses is shown here.

The above two figures indicate that the Monte Carlo simulation of the spin analyzer distribution reproduces the corresponding distributions in the data. Figure 9.18 shows the ratio of the data and Monte Carlo distributions normalized to the Monte Carlo distribution. The solid lines indicate 3 σ variations in this difference and are used to reweight the Monte Carlo ω distribution. This ratio of the data spectrum to the Monte Carlo spectrum is fit to a linear uncertainty of the form:

$$f(\omega) = \alpha\,(\omega - C) \tag{9.8}$$

We now fit for α as a free parameter for different values of C ranging from -1 to 1. The fit with the larges error is used to determine the weight used in the reweighting procedure, and using 3 σ variations of α we obtain the following weights:

$$\begin{aligned}
w_\omega &= 1 \pm (\omega)\frac{0.05}{\mathrm{GeV}/c} && e \text{ mode, pseudo rest frame} \\
w_\omega &= 1 \pm (\omega + 0.25\mathrm{GeV}/c)\frac{0.12}{\mathrm{GeV}/c} && e \text{ mode, laboratory frame} \\
w_\omega &= 1 \pm (\omega + 0.25\mathrm{GeV}/c)\frac{0.25}{\mathrm{GeV}/c} && \mu \text{ mode, pseudo rest frame; } p_\mu \leq 1.5
\end{aligned}$$

$$w_\omega = 1 \pm (\omega)\frac{0.06}{\mathrm{GeV}/c} \qquad \mu \text{ mode, pseudo rest frame; } p_\mu > 1.5$$
$$w_\omega = 1 \pm (\omega + 0.25\mathrm{GeV}/c\,)\frac{0.14}{\mathrm{GeV}/c} \qquad \mu \text{ mode, laboratory frame.} \tag{9.9}$$

The Michel parameters are recalculated with the reweighted spectrum, and the shifts from the nominal parameter values are used as an estimate of the systematic error resulting from imperfect simulation of the spin analyzer variable.

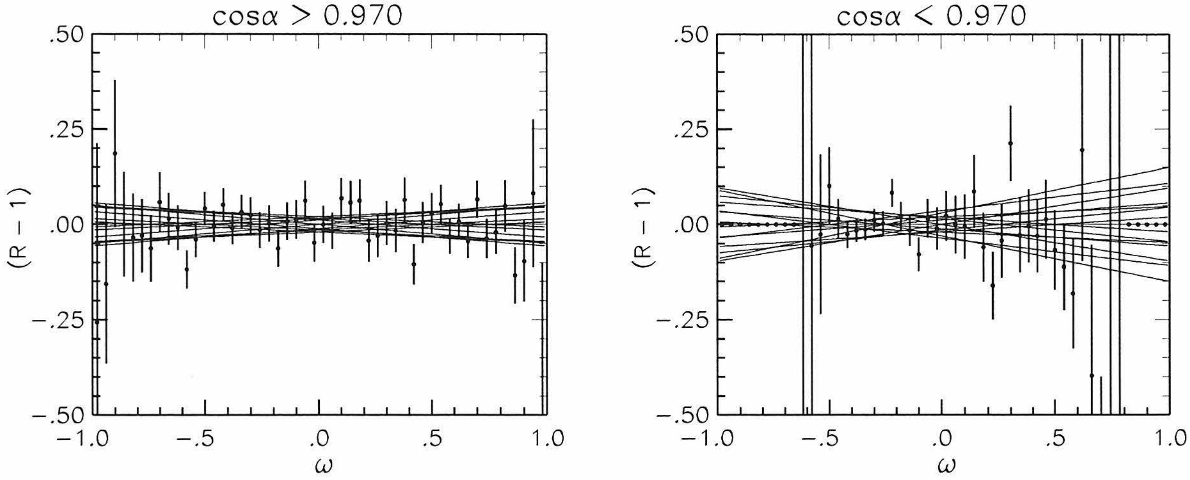

Figure 9.18: The distribution of the ratio (data divided by the Monte Carlo simulation) for the polarimetric variable ω normalized to the Monte Carlo simulation for electron mode events used in both the pseudo rest frame and laboratory frame analyses is shown here. The solid lines show the $3\,\sigma$ variations in this ratio, and are used to reweight the Monte Carlo spectra.

The spin analyzer is dependent on the following kinematic variables: the momentum/energy of the charged and neutral pions, and the angle between the two pions. The error estimate obtained using $3\,\sigma$ variations in the ω variable in the Monte Carlo distribution directly addresses the angle between the two pions (and somewhat the ρ energy as well). We now consider the momentum of the charged pion (see Figure 9.19) as well as the energy on the π^0 (see Figure 9.20) in the event.

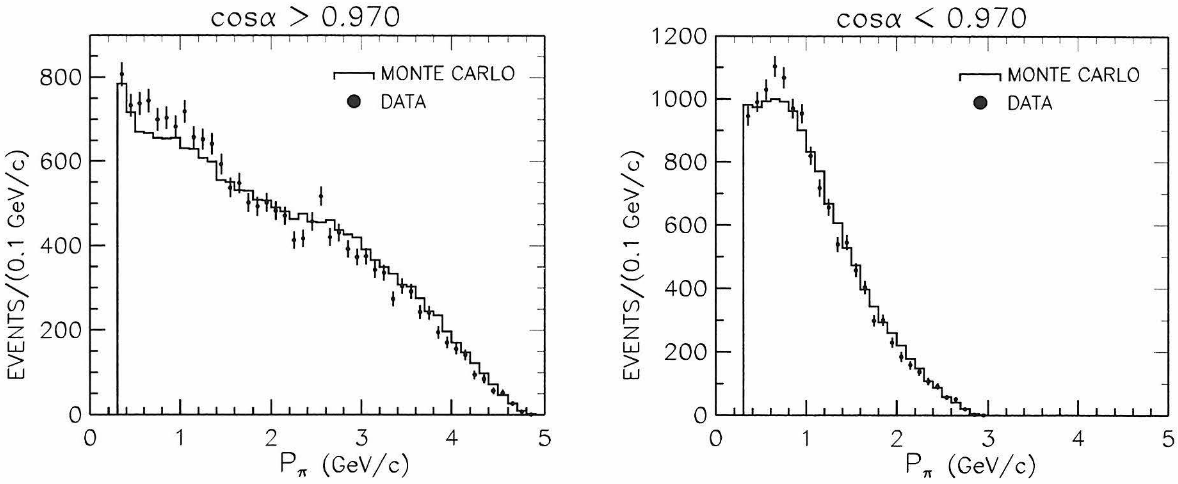

Figure 9.19: The charged pion momentum spectrum for events utilized in the electron pseudo rest frame (left) and laboratory frame (right) analyses.

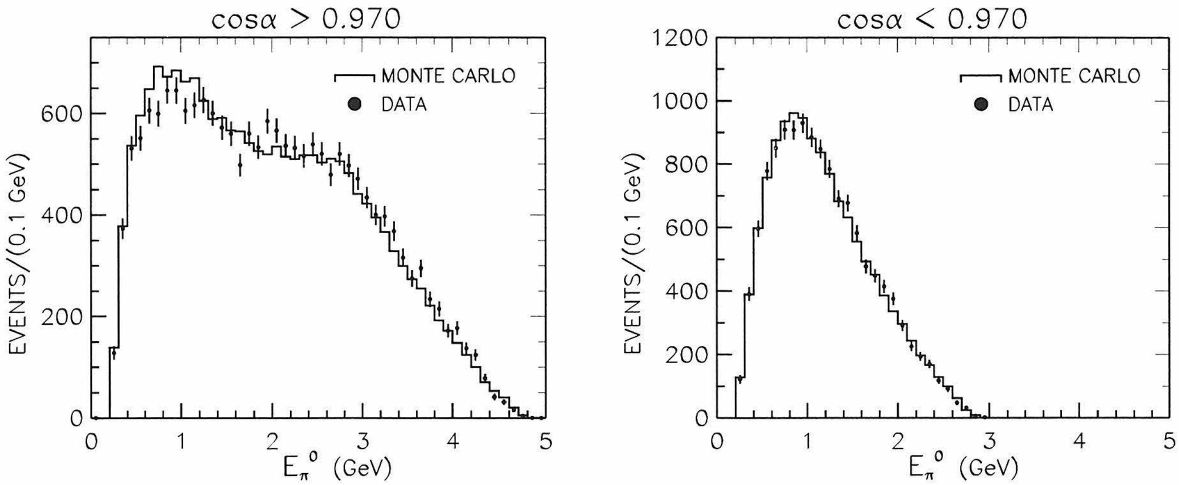

Figure 9.20: The π^0 energy spectrum for events utilized in the electron pseudo rest frame (left) and laboratory frame (right) analyses.

In each of these electron mode figures [§], we note that the Monte Carlo reproduces the data for most of the energy and momentum range; there are some significant discrepancies in the low energy and low momentum regions. An interesting feature observed in these figures is the marked differences between the spectrum used in the two different frames of reference analyzed. These differences are directly related to the $\cos\alpha$ cut designed to select events in which the pseudo rest frame spectrum can be reconstructed. Requiring that the tag $h^{\pm}\pi^0$ system be a good estimate of its parent τ flight direction selects events in which either the hadronic track or the π^0 have a large momentum. Thus the events in the laboratory frame analysis show depletions in the high momentum/energy regions.

We also note a minimum momentum and energy cut-offs in the plots shown. There is a $p_{\pi^\pm} \geq 300$ MeV/c requirement to ensure efficient trigger and tracking conditions. No nominal requirement has been made on the energy of the π^0; the requirement that the minimum photon energy used to form a π^0 does, however, translate into an indirect minimum energy requirement. These nominal cuts, along with other cuts, correlate the two sides of the event and could potentially result in a mismeasurement of the parameters if they are not adequately treated in the Monte Carlo simulation.

To estimate the systematic errors resulting as a result of these discrepancies, we once again reweight the Monte Carlo distributions as described before, and refit for the Michel parameters. We fit the ratio of the data to the Monte Carlo spectra to a linear uncertainty of the form:

$$f(p_{\pi^\pm}) = \alpha(p_{\pi^\pm} - C) \text{ or } f(E_{\pi^0}) = \alpha(E_{\pi^0} - C) \ , \tag{9.10}$$

depending on the distribution being considered. We then fit for α as a free parameter for different choices of C, and the fit with the largest error on α is used to determine the weight used in the reweighting procedure. Using $3\,\sigma$ variations on α, we obtain:

$$w_{\pi^\pm} = 1 \pm (p_{\pi^\pm} - 2.0\text{GeV}/c)\frac{0.026}{\text{GeV}/c} \tag{9.11}$$

[§] The corresponding muon mode figures are similar.

$$w_{\pi^0} = 1 \pm (p_{\pi^0} - 2.0\mathrm{GeV})\frac{0.023}{\mathrm{GeV}} , \qquad (9.12)$$

where C=2.0 GeV/c in Equation 9.11 and in Equation 9.12 results in the largest shifts in the parameters from their nominal values in both the electron and muon samples. These shifts are used as an estimate of the systematic error resulting from the imperfect modeling of the charged and neutral pions in the Monte Carlo simulation.

Table 9.14 lists the systematic error assignments calculated in this section. These errors are the quadratic sum of the largest changes observed in the measured parameters when the Monte Carlo sample is reweighted with weights calculated using the ω distributions, the distributions of the momentum of the charged pion and the energy distributions for the neutral pions. This table also lists the statistical errors obtained on each of the parameters. We note that the systematic error resulting from the imperfect modeling of spin correlations in the Monte Carlo simulation package is not negligible, but it is significantly smaller than the corresponding statistical errors.

	σ_{ρ_e}	σ_{ρ_μ}	σ_{η_μ}	$\sigma_{\rho_{e\mu}}$	$\sigma_{\eta_{e\mu}}$
Spin Correlations	0.003	0.012	0.050	0.003	0.035
Statistics	0.014	0.048	0.149	0.013	0.061

Table 9.14: Systematic errors resulting from the imperfect modeling of spin correlations, the momentum of the charged pion and the energy of the neutral pion in the Monte Carlo simulation.

9.11 Geometric Acceptance

The two charged tracks in the event are required to lie in the good barrel region of the detector, defined by $|\cos\theta| \leq 0.71$, where θ is the angle that the track under consideration makes with respect to the beam direction. Figure 9.21 shows the $\cos\theta$ distributions in the data and the Monte Carlo simulation for electron, muon and pion tracks. The two photons that are used to reconstruct the π^0 on the tag side of the event are also required to lie in the good barrel. These two requirements were selected to ensure efficient tracking and trigger conditions.

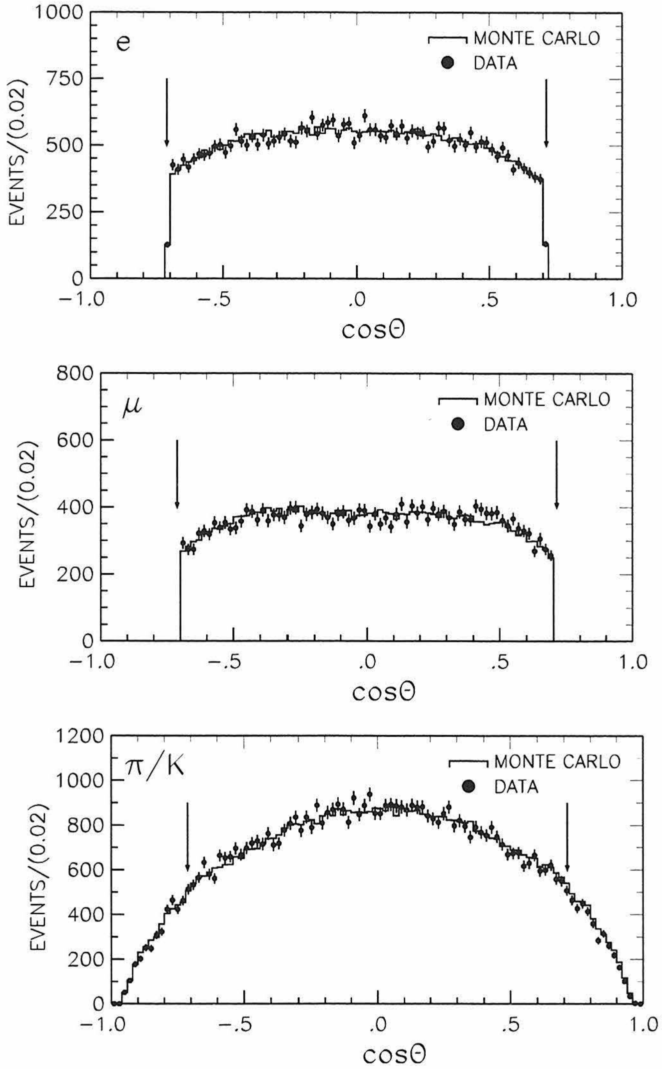

Figure 9.21: Cosine of the angle the electron, muon, and pion tracks make *w.r.t.* the beam direction. The arrows enclose the good barrel region of the detector; all tracks must lie in this region.

The Monte Carlo simulation reproduces the data in each of these distributions. The muon identification efficiency falls off rapidly as one extends beyond $|\cos\theta| > 0.71$, and this requirement does not significantly reduce the muon sample. On the other hand, it does reduce the pion and electron samples significantly.

To check if the above choice for the $\cos\theta$ requirement results in a systematic bias, we measure the parameters for different definitions of the good barrel region.

Figure 9.22 shows the changes seen in the parameters as a function of the choice of the $\cos\theta$ requirement. We note that there is a strong correlation between the points in each plot. Since no systematic effects are seen, we conclude that the geometric acceptance does not result in any significant systematic errors to this analysis.

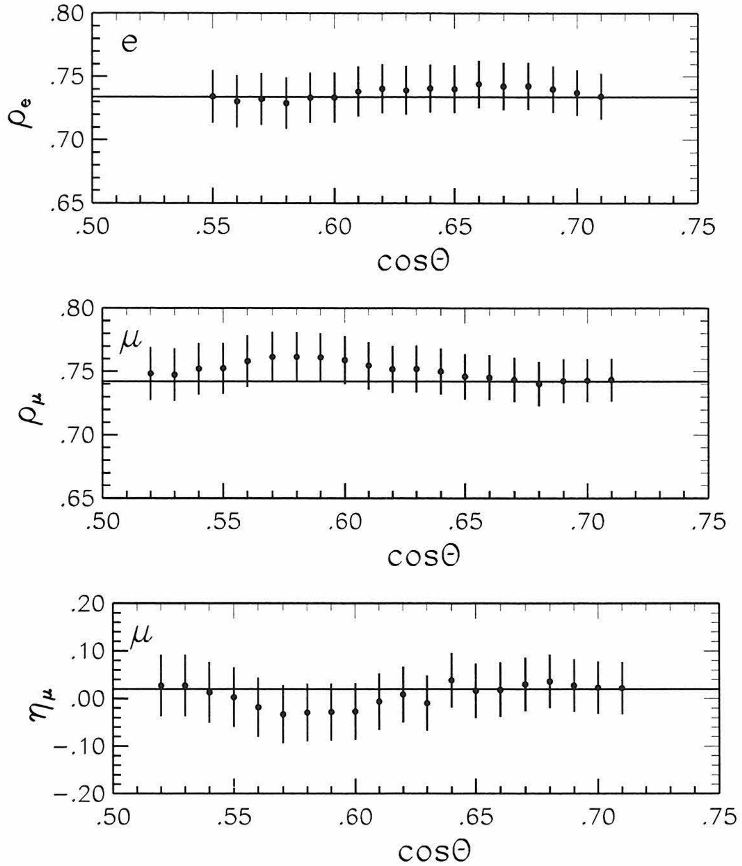

Figure 9.22: The Michel parameters ρ_e, ρ_μ, and η_μ as a function of the acceptance of the two charged tracks in the events.

9.12 Monte Carlo Statistics

In principle, the Monte Carlo samples can be infinitely large and thus would result in no errors. In reality, however, the five different Monte Carlo samples used in this analysis are all equivalent to approximately ten times the data in size. The systematic error arising as a result of the finite size of each of these samples, along with the total data and Monte Carlo statistical errors are shown in Table 9.15. The $V+A$ Monte Carlo samples do not contribute significantly to the fit, and as a result the error arising from their finite statistics is small. The $\eta = 1$ Monte Carlo sample resembles the $V-A$ Monte Carlo sample over most of the momentum range. As a result, its contribution to the systematic error is larger. We also note that the total systematic error on the η parameter due to limited Monte Carlo statistics is significant, but it is smaller than the corresponding error due to data statistics.

	σ_{ρ_e}	σ_{ρ_μ}	σ_{η_μ}	$\sigma_{\rho_{e\mu}}$	$\sigma_{\eta_{e\mu}}$
$(V-A)_e$	0.005	-	-	0.004	0.014
$(V+A)_e$	0.001	-	-	0.001	0.002
$(V-A)_\mu$	-	0.015	0.054	0.002	0.019
$(V+A)_\mu$	-	0.009	0.028	0.001	0.002
$(\eta=1)_\mu$	-	0.019	0.065	0.001	0.010
Monte Carlo	0.005	0.026	0.089	0.005	0.026
Data	0.014	0.048	0.149	0.013	0.061

Table 9.15: Systematic errors resulting from finite statistics in the different Monte Carlo samples.

9.13 Bin Migration and Resolution

Bin migration alters the observed lepton momentum and energy distributions. The Monte Carlo package simulates this effect to the lowest order, but the poorly simulated tails could potentially be important. Figure 9.23 plots the momentum dependence of the difference between the generated and measured laboratory momenta for muon tracks in the Monte Carlo simulation. We note that although the bin migration is significant, this difference does not exceed 100 MeV/c. High momentum tracks migrate more, but they are less significant statistically, since the laboratory momentum distribution falls sharply at high momentum.

All the fits utilized to extract the Michel parameters were performed using distri-

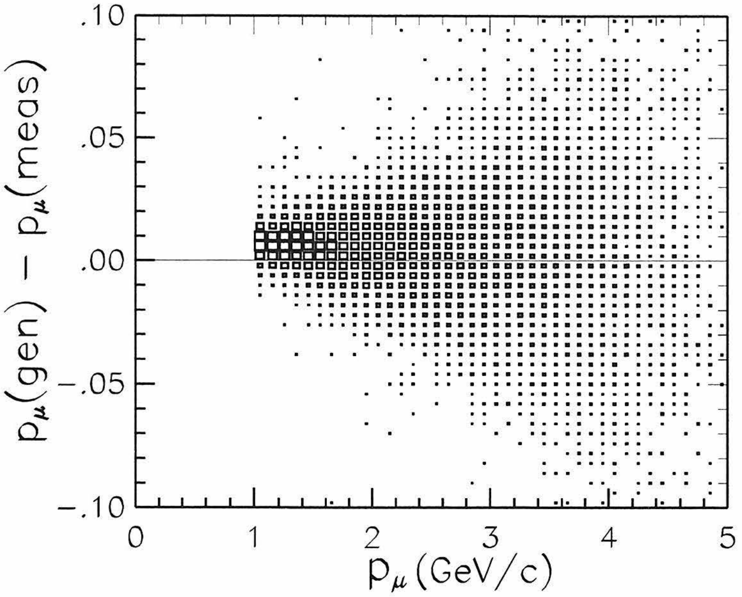

Figure 9.23: The momentum dependence of the difference between the generated and the reconstructed muon momentum in the Monte Carlo simulation.

butions with 100 MeV/c bins. Thus, one expects that the systematic error associated with the imperfect modeling in the Monte Carlo simulation is small. To evaluate this systematic error, we change the bin size by a large amount and remeasure the parameters. The largest changes in the results were observed on using 50 MeV/c bins instead of the nominal 100 MeV/c bins. These changes (shown in Table 9.16) in the central values of the parameters are used as estimates for the systematic error. Also shown here are the corresponding statistical errors for each of the parameters measured. Although the systematic error estimates on many of the parameters measured are significant, they are much smaller than the corresponding statistical errors.

	σ_{ρ_e}	σ_{ρ_μ}	σ_{η_μ}	$\sigma_{\rho_{e\mu}}$	$\sigma_{\eta_{e\mu}}$
Bin Migration	0.001	0.020	0.066	0.002	0.019
Statistics	0.014	0.048	0.149	0.013	0.061

Table 9.16: Systematic errors resulting from bin migration.

9.14 Are There Any Anomalous Effects in the Data?

There could be any number of anomalous effects in the data, and in this section we study the most obvious possible effects.

The results obtained for the different Michel parameters are not expected to depend on the data set studied. However, we know that detector and trigger conditions vary as a function of time and thus as a function of the data set considered. To ensure that these changes in the detector conditions do not bias the measurements, we consider the results obtained as a function of the different data sets used in the analysis. Figure 9.24 shows the results obtained in the combined electron and muon mode analysis for the 4S2-4S8 data sets. The non-$(V-A)$ Monte Carlo samples have not been generated for the 4S9 and 4SA data sets and thus the results for these two individual data sets are not shown here. We note that there is no obvious data set dependence in both $\rho_{e\mu}$ (left) and $\eta_{e\mu}$ (right), measured with the other parameter fixed at its Standard Model expectation. Further, the nominal result, indicated by the shaded band, is consistent with Standard Model expectations.

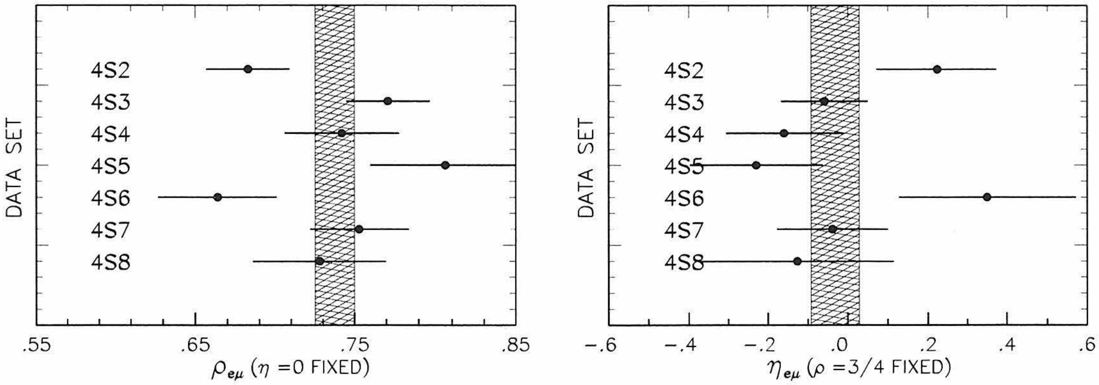

Figure 9.24: The Michel parameter $\rho_{e\mu}$ ($\eta_{e\mu}$) with $\eta_{e\mu} = 0$ ($\rho_{e\mu} = 3/4$) fixed to its Standard Model expectation is shown in the figure on the left (right) as a function of the different data sets used in this analysis. The results are obtained by combining the pseudo rest frame and laboratory frame results, and the errors represent the data and Monte Carlo statistics contribution. The nominal results obtained using the 4S2-4SA data sets is indicated by the hatched region.

The Michel parameters should be independent of the charge of the lepton analyzed. We now split the electron and muon samples into their respective positive and negative lepton samples and remeasure the parameters in the combined electron and muon mode analysis. Figure 9.25 shows the 1 σ error ellipses obtained in the $\eta - \rho$ plane for the positive lepton spectra (closed dots), and the negative lepton spectra (open dots). Also shown here are the 1 and 2 σ ellipses for the nominal result. We note that although the two charged samples are not identical, both are consistent with each other and with Standard Model expectations.

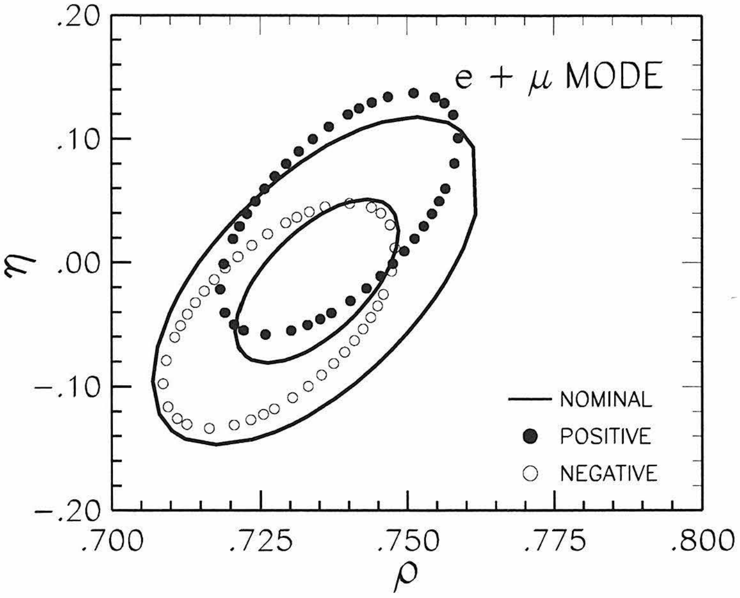

Figure 9.25: The 1σ error ellipses obtained on analyzing the positive (closed dots) and negative (open dots) lepton samples individually along with the 1 σ and 2 σ nominal result (solid lines).

The two halves of the detector ($\cos\theta > 0$ and $\cos\theta < 0$) are essentially identical and the parameters should be independent of the location of the lepton in the detector. Figure 9.26 shows the results obtained in the two different hemispheres of the detector when the two leptonic decay modes are simultaneously analyzed. The open (closed) circles illustrate the 1 σ error ellipse obtained when all leptons lying in the $\cos\theta < 0$ ($\cos\theta > 0$) hemisphere of the detector are utilized to measure the parameters. The figure also illustrates the nominal result. We note that although the two samples do not yield identical results, the results are consistent with each other and with Standard Model expectations.

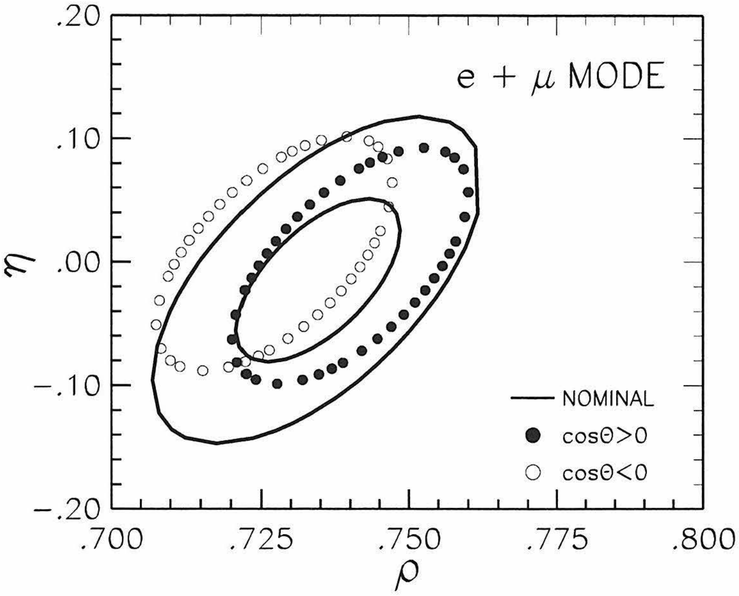

Figure 9.26: The error ellipses obtained as a function of the position of the two leptons in the detector. The solid circles illustrate the 1 σ error ellipse in the $\eta - \rho$ plane for leptons in the $\cos\theta > 0$ half of the detector, while the open circles illustrate the corresponding ellipse for leptons in the $\cos\theta < 0$ half of the detector. The solid lines indicate the 1 σ and 2 σ nominal result.

Since nothing unexpected was seen in this search for anomalous effects, there is no systematic error assigned here.

9.15 The Tau Neutrino

All Monte Carlo samples were generated assuming a massless tau neutrino. A massive tau neutrino would alter the charged lepton momentum spectrum in the laboratory frame of reference, and would bias the pseudo rest frame spectrum which is calculated assuming a massless tau neutrino. A Monte Carlo generator level study was performed to study the effects of massive neutrinos. We note that the neutrino must have a minimum lass of 70 MeV$/c^2$ before it can have any affect on the measured parameters. Since the current limit on the mass of the tau neutrino 24 MeV$/c^2$ is well below this mass, we do not assign any systematic error.

9.16 Total Systematic Errors

The systematic errors studied in the preceding sections are compiled in Table 9.17. We find that the total systematic error (all contributions added in quadrature) on the ρ measurements are smaller than the corresponding statistical errors. On the other hand, in the η measurements the systematic error estimates are slightly larger than the corresponding statistical error estimates.

	ρ_e	ρ_μ	η_μ	$\rho_{e\mu}$	$\eta_{e\mu}$
Electron ID	< 0.001	–	–	< 0.001	0.001
Muon ID	–	0.004	0.018	0.001	0.024
Fake Electron	0.004	–	–	0.004	0.015
Fake Muon	–	0.025	0.106	0.002	0.025
Feed-down	0.001	0.002	0.007	0.002	0.008
Trigger	0.002	0.006	0.019	0.002	0.005
Bin Migration	0.001	0.020	0.066	0.002	0.019
Correlations	0.003	0.012	0.050	0.003	0.035
Radiation	0.005	0.003	0.050	0.001	0.004
MC Statistics	0.005	0.026	0.089	0.005	0.026
Systematics	0.009	0.044	0.171	0.008	0.062
Data Statistics	0.014	0.048	0.149	0.013	0.061

Table 9.17: All significant sources of errors.

Chapter 10 Summary and Conclusions

In this chapter, we provide a brief recapitulation of the results presented and discuss the interpretation and significance of this work. We also briefly discuss future improvements to these results.

10.1 Results

In the preceding chapters, we have presented in detail the measurement of the spectral shape Michel parameters ρ and η, using data recorded by the CLEO II detector. These parameters are utilized to study the Lorentz structure of the charged weak interaction which manifests itself in the two tau decay modes: $\tau^- \to e^-\overline{\nu}_e\nu_\tau$ and $\tau^- \to \mu^-\overline{\nu}_\mu\nu_\tau$. Tau pairs are produced by the $e^+e^- \to \tau^+\tau^-$ process at CESR, running at center of mass energies around the $\Upsilon(4S)$ resonance (approximately 10.5 GeV). Both the leptonic tau decay modes are analyzed, and the results obtained are shown in Table 10.1; the first error is statistical and the second is systematic. The two parameters are strongly correlated, thus requiring their simultaneous measurement.

Parameter	This Thesis	World Average [37]	S.M.
ρ_e	$0.732 \pm 0.014 \pm 0.009$	0.736 ± 0.028	3/4
ρ_μ	$0.747 \pm 0.048 \pm 0.044$	0.74 ± 0.04	3/4
η_μ	$0.010 \pm 0.149 \pm 0.171$	-0.24 ± 0.29	0
$\rho_{e\mu}$	$0.735 \pm 0.013 \pm 0.008$	0.736 ± 0.028	3/4
$\eta_{e\mu}$	$-0.015 \pm 0.061 \pm 0.062$	-0.01 ± 0.14	0

Table 10.1: The results obtained for the Michel parameters measured in this thesis. The first error is statistical and the second is systematic. The subscript on the parameter indicates the decay mode utilized to measure the parameter. This table also shows the 1996 world average results and the corresponding Standard Model (S.M.) expectation values.

First, we note that all the results presented in this table are consistent with both the results presented in the 1996 Particle Data Group [37], and the Standard Model expectations. We further note that these results (with the exception of ρ_μ) are close to a factor of two better than the corresponding world average results. The PDG world average result for the ρ_μ parameter includes measurements that were performed with the η_μ parameter fixed at its Standard Model expectation, thus improving the precision of those measurements, and consequently the world average measurement.

The results obtained in this analysis are more precise than all previous measurements as shown in Figure 10.1. Further, they are more precise than the PDG 96 world average results indicated by the hatched region. As mentioned above, the ρ_μ world average band shown here is deceptive.

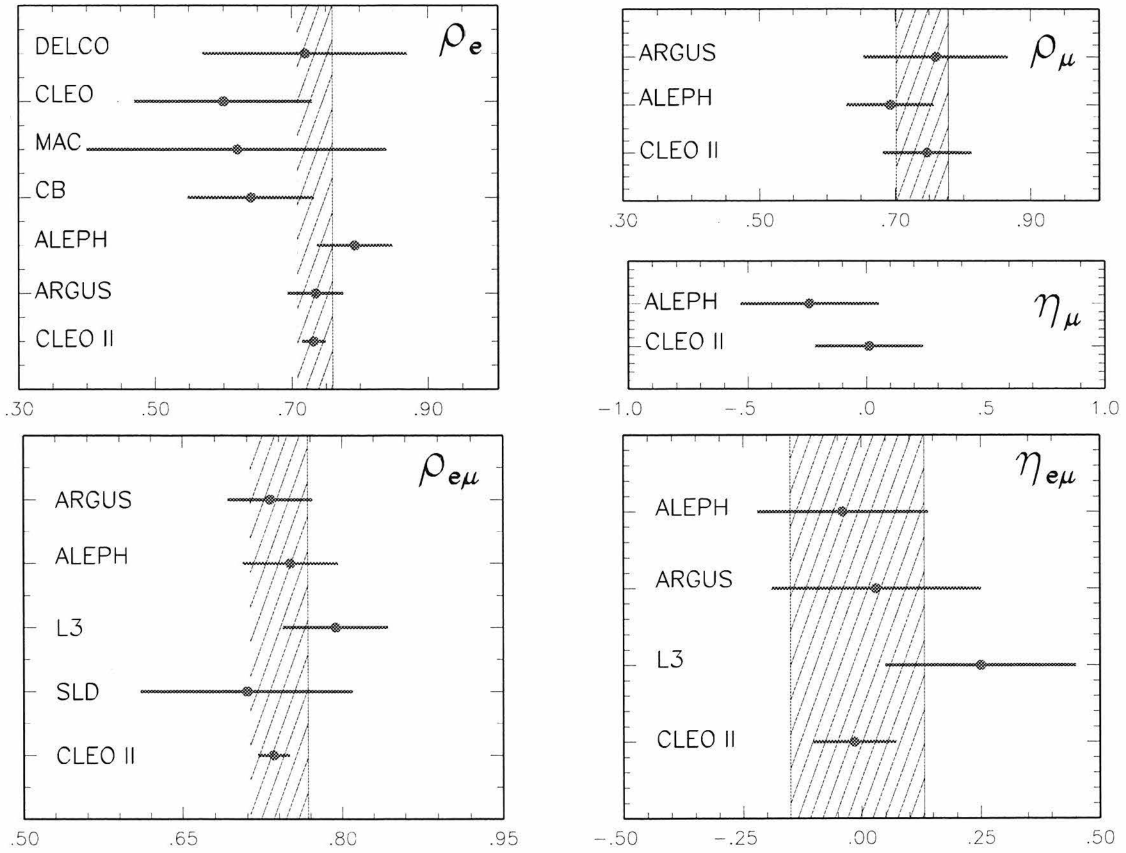

Figure 10.1: Comparing the results obtained for the five different parameters (labeled CLEO II) with other measurements. The hatched region indicates the PDG world average result.

10.2 Future Improvements

The data available at the CLEO experiment has significantly increased since this analysis. In fact, it is increasing every day, and in the future one might expect to further improve the precision on the results presented here.

It is important to note that at present the systematic error on the η parameter measurements is approximately on the order of the statistical error. However, as the statistical error decreases with increased statistics, most of these systematic errors are also expected to decrease, since one gains an improved knowledge of the detector with improved statistics. As can be seen in Table 9.17, several of the sources of systematic errors studied are detector related. Both the muon identification efficiency (determined using $e^+e^- \rightarrow \mu^+\mu^-$ data), and the fake muon or pion punch-through error (determined using the tag $\tau \rightarrow h\pi^0\nu_\tau$ decay mode in the data) are expected to decrease with improved statistics. Re-tuning the Monte Carlo simulation to further reduce the differences between data and Monte Carlo efficiencies in the tag mode would reduce the error resulting from correlations between the two sides. The Monte Carlo statistical error can also be reduced either by the generation of larger Monte Carlo samples, or by using improved techniques such as the "reverse" Monte Carlo technique employed in reference [44].

Future experiments such as the B factories, CLEO III, and Tau-Charm factories could have large tau samples which might result in improved measurements as well. We have learned, in this analysis, that the data are a factor of two more significant when analyzed in the "pseudo" rest frame of the tau. One would achieve maximum sensitivity in the true tau rest frame, and measurements made at a τ factory running close to threshold might be very interesting if one gathered sufficient statistics.

10.3 Interpretation of the Results

The measurements presented in this thesis, together with the recent measurements of the asymmetry parameters from the CLEO II Collaboration [44], have been used to determine new limits on the ten complex coupling constants $g^{\gamma}_{\epsilon\omega}$, where $\gamma = S$, V, T indicates a scalar, vector, or tensor interaction; and ϵ, $\omega = R, L$ indicate a right-handed or left-handed chirality of the daughter charged lepton and the parent lepton respectively.

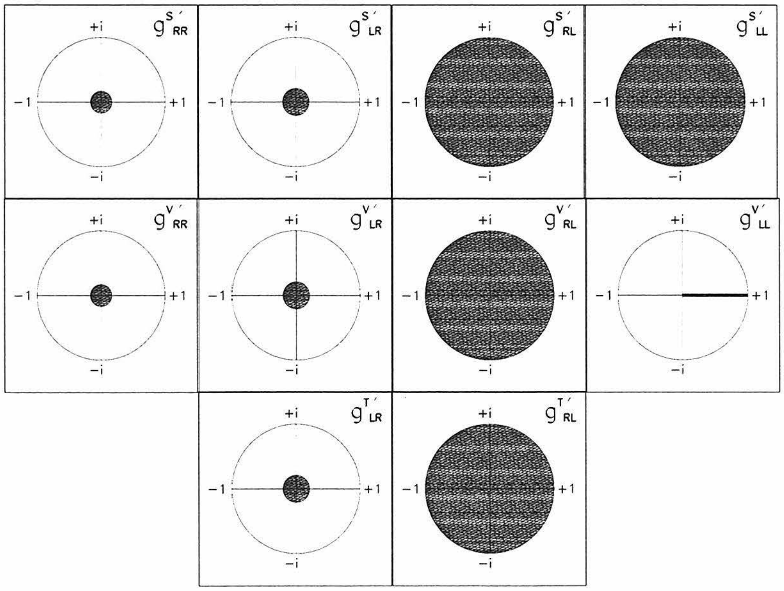

Figure 10.2: 90% confidence level experimental limits for the normalized τ-decay couplings $g^{n'}_{\epsilon\omega} \equiv g^{n}_{\epsilon\omega}/N^{n}$, where $N^{n} \equiv \max(|g^{n}_{\epsilon\omega}|) = 2,\ 1,\ 1/\sqrt{3}$ for $n = S, V, T$. The results presented in this analysis are included in the calculations.

These new limits are shown in Figure 10.2, and we note that these limits are significantly better that the corresponding limits obtained using the 1996 world average tau Michel parameters (see Figure 2.4). However, these new limits are still much weaker than the corresponding muon sector limits shown in Figure 2.3. Although consistent with Standard Model expectations, the limits on the couplings obtained in the tau sector do not prove $V - A$ in the same sense as has been done in muon decay.

Even if we assume infinite precision for the measurements of the Michel parameters, we do not improve the limits on the left-handed tau couplings. Thus, to significantly improve these limits, we require additional experiments such as the measurements of the daughter charged lepton polarization, or of the neutrino correlations, or of the cross section for the inverse decay $\nu_\tau \, \ell^- \rightarrow \tau^- \bar{\nu}_e$.

The limits on non-standard couplings presented here leave plenty of room for physics beyond the Standard Model. The measurement of the η parameter is particularly interesting, since a non-zero η measurement can be used to determine the mass of the charged scalar Higgs in the Two Higgs Doublet Model. We find that η is consistent with zero, and the measurement presented in this thesis can be used to set a limit on the mass m_H of the charged scalar Higgs as a function of $\tan\beta$, the ratio of vacuum expectation values of the two Higgs doublets. Using Equation 2.71, we obtain a lower mass limit:

$$\frac{m_H}{\tan\beta} > 0.97 \text{ GeV } (90\% \text{ C.L.}) \,. \tag{10.1}$$

This new limit on the mass of the charged Higgs becomes competitive with that from direct searches for a charged Higgs (> 43.5 GeV, 95% C.L. [82]) only in the region of large $\tan\beta$.

The measurement of the low energy η parameter is also important for the evaluation of the Fermi coupling constant given by:

$$G_F^2 = \frac{1}{\tau_\tau} \frac{192\pi^3}{m_\tau^5} \frac{1}{1 + 4\eta \, m_\ell / m_\tau} \,, \tag{10.2}$$

where ℓ is the daughter charged lepton and τ_τ is the lifetime of the tau meson. The measurement of the η_μ parameter is important for the muonic decay mode since m_μ/m_τ is not negligible. A non-zero η measurement would alter the universality of this coupling constant.

The ρ parameter measurement can be used to set a limit on anomalous dipole couplings described in Section 2.7, and we find that the anomalous dipole complex form factor $\kappa_\tau^W = -0.04 \pm 0.04$. This result is still not quite at the desired level of precision. However, it is clear that future experiments at CLEO or the B-factories with more than an order of magnitude increase in statistics should begin to probe κ values or order 0.01. The interesting range of $|\kappa_\tau^W|$ may not be much larger than about 0.01 - 0.001, since the corresponding κ_τ^Z couplings were found to be quite small.

Considering the left-right symmetric model for the electroweak interaction, where parity violation has its origin in the spontaneous symmetry breaking of the left-right symmetry, one can set limits on the mass of the pure right-handed W_R boson as shown is Section 2.7. When the mixing angle ζ, between the W_L and W_R bosons, is zero, W_R is identical to W_2 in Equation 2.72, and we find that:

$$m_{W_R} > 304 \text{ GeV}/c^2 \text{ at } 90\% \text{ C.L.}$$

The mass limit obtained for ζ free is:

$$m_{W_R} > 260 \text{ GeV}/c^2 \text{ at } 90\% \text{ C.L.},$$

where the results obtained in reference [44] are used in conjunction with the results obtained in this analysis to calculate these mass limits.

10.4 Conclusion

In conclusion, we have made the most precise to-date measurements of the spectral shape Michel parameters ρ and η, using the leptonic decays of the tau. We find no deviations from Standard Model expectations. The precision on these parameters is now beginning to get interesting, as we approach the precision levels required to set limits on physics beyond the Standard Model.

Appendix A Some Mathematics

A.1 Solving the Covariant Integral $I_{\alpha\beta}$

The differential decay rate for the decay, $\tau^-(p_\tau) \rightarrow \ell^-(p_\ell) + \bar{\nu}_\ell\,(p_1) + \nu_\tau\,(p_2)$, was found to be:

$$d\Gamma = \frac{2\,G_F^2}{(2\pi)^5}\,\frac{1}{m_\tau E_\ell}\,(p_\ell - m_\ell s_\ell)^\alpha (p_\tau - m_\tau s_\tau)^\beta d^3\mathbf{p}_\ell\; I_{\alpha\beta} \tag{A.1}$$

in Chapter 2. The covariant integral,

$$I_{\alpha\beta} = \int p_{2\alpha}\; p_{1\beta}\frac{d^3\mathbf{p}_1}{E_1}\frac{d^3\mathbf{p}_2}{E_2}\delta^4(p_1 + p_2 - \overline{p_\tau - p_\ell})\;, \tag{A.2}$$

must be of the form: $I_{\alpha\beta} = g_{\alpha\beta}A(q^2) + q_\alpha q_\beta B(q^2)$, where $q = p_\tau - p_\ell = p_1 + p_2$ is the only momentum vector remaining. Now,

$$\begin{aligned}
g^{\alpha\beta}I_{\alpha\beta} &= 4A(q^2) + q^2B(q^2)\\
&= \int (p_1\cdot p_2)\frac{d^3\mathbf{p}_1}{E_1}\frac{d^3\mathbf{p}_2}{E_2}\delta^4(p_1+p_2-q)\\
&= \frac{1}{2}\int (p_1+p_2)^2\frac{d^3\mathbf{p}_1}{E_1}\frac{d^3\mathbf{p}_2}{E_2}\delta^4(p_1+p_2-q)\\
&= \frac{q^2}{2}\int \frac{d^3\mathbf{p}_1}{E_1}\frac{d^3\mathbf{p}_2}{E_2}\delta^4(p_1+p_2-q) = \frac{q^2}{2}\,\mathcal{I}\;, &\text{(A.3)}\\
\text{and}\quad q^\alpha q^\beta I_{\alpha\beta} &= q^2A(q^2) + (q^2)^2B(q^2)\\
&= \int (q\cdot p_1)(q\cdot p_2)\frac{d^3\mathbf{p}_1}{E_1}\frac{d^3\mathbf{p}_2}{E_2}\delta^4(p_1+p_2-q)\\
&= \int (p_1\cdot p_2)^2\frac{d^3\mathbf{p}_1}{E_1}\frac{d^3\mathbf{p}_2}{E_2}\delta^4(p_1+p_2-q)\\
&= \left(\frac{q^2}{2}\right)^2\int \frac{d^3\mathbf{p}_1}{E_1}\frac{d^3\mathbf{p}_2}{E_2}\delta^4(p_1+p_2-q) = \frac{q^4}{4}\,\mathcal{I}\;. &\text{(A.4)}
\end{aligned}$$

To evaluate the Lorentz invariant integral $\mathcal{I}$, we choose a convenient frame of reference in which the two neutrinos have equal and opposite momenta. Now, $|\mathbf{p}_1| = |\mathbf{p}_2| = E_1 = E_2$, $\int \delta^3(\mathbf{p}_1 + \mathbf{p}_2 - \mathbf{q})d^3\mathbf{p}_2 = 1$, and

$$\begin{aligned}
\mathcal{I} &= \int \frac{d^3\mathbf{p}_1}{E_1}\frac{d^3\mathbf{p}_2}{E_2}\delta^4(p_1 + p_2 - q) \\
&= \int \frac{d^3\mathbf{p}_1}{E_1}\frac{d^3\mathbf{p}_2}{E_2}\delta^3(\mathbf{p}_1 + \mathbf{p}_2 - \mathbf{q})\delta(E_1 + E_2 - E) \\
&= \int \frac{d^3\mathbf{p}_1}{E_1^2}\delta(2E_1 - E) = 4\pi \int dE_1 \delta(E - 2E_1) = 2\pi \; . \qquad \text{(A.5)}
\end{aligned}$$

Thus,

$$\begin{aligned}
4A(q^2) + q^2 B(q^2) &= \pi q^2 \, , \\
q^2 A(q^2) + (q^2)^2 B(q^2) &= \frac{q^4\pi}{2} \, , \qquad \text{(A.6)}
\end{aligned}$$

and solving simultaneously for $A(p^q)$ and $B(q^2)$ leads to

$$I_{\alpha\beta} = \frac{q^2\pi}{6} g_{\alpha\beta} + \frac{\pi}{3} q_\alpha q_\beta \; . \qquad \text{(A.7)}$$

A.2 Calculating the Limits of Integration

The decay rate for the decay mode, $\tau^-(p_\tau) \to \ell^-(p_\ell) + \bar{\nu}_\ell(p_1) + \nu_\tau(p_2)$, in terms of the Dalitz plot variables was found to be:

$$\Gamma = \frac{G_F^2 m_\tau^5}{16\pi^3} \int_{min}^{max} d\varepsilon_\ell \int_{min}^{max} d\varepsilon_1 \varepsilon_1 (1 - \varepsilon_1) \qquad \text{(A.8)}$$

in Chapter 2. To calculate the limits of integration, we assume $m_1 = m_2 = m_\ell = 0$. Thus $0 \leq E_\ell \leq m_\tau/2$ and $0 \leq \varepsilon_\ell \leq 1$. In the tau rest frame, $p_\tau - p_1 = p_{\ell 2}$, leading to

$$E_1 = \frac{1}{2m_\tau}[m_\tau^2 + m_1^2 - m_{\ell 2}^2] \; . \qquad \text{(A.9)}$$

Since

$$m_{\ell 2}^2\left({}^{max}_{min}\right) = (E_\ell^* + E_2^*)^2 - (\mathbf{p}_\ell^* \mp \mathbf{p}_2^*)^2$$

$$E_1\binom{max}{min} = \frac{1}{2m_\tau}[m_\tau^2 + m_1^2 - (E_\ell^* + E_2^*)^2 + (\mathbf{p}_\ell^* \pm \mathbf{p}_2^*)^2] \, . \tag{A.10}$$

Thus $E_1^{max} = m_\tau/2$, $\varepsilon_1^{max} = 1$, and

$$E_1^{min} = \frac{1}{2m_\tau}[m_\tau^2 - 4E_\ell^* E_2^*] \, . \tag{A.11}$$

Using $p_\tau = p_\ell + p_{12}$, $p_{12} - p_2 = p_1$, and $p_\tau - p_\ell = p_{12}$, we find

$$\begin{aligned} E_\ell^* &= \frac{m_\tau^2 - m_\ell^2 - m_{12}^2}{2m_{12}} \, , \\ E_2^* &= \frac{m_{12}^2 + m_2^2 - m_1^2}{2m_{12}} \, , \\ \text{and } m_{12}^2 &= m_\tau^2 + m_\ell^2 - 2m_\tau E_\ell \end{aligned} \tag{A.12}$$

respectively. E_ℓ^* and E_2^* are the energies of the lepton ℓ and the anti-neutrino $\bar{\nu}_\ell$ in the m_{12} rest frame. Substituting in Equation A.11, and neglecting the neutrino masses and m_ℓ, we get

$$E_1^{min} = \frac{m_{12}^2}{2m_\tau} = \frac{1}{2}(m_\tau - 2E_\ell) = \frac{m_\tau}{2}(1 - \varepsilon_\ell) \, , \tag{A.13}$$

and $\varepsilon_1^{min} = 1 - \varepsilon_\ell$. Thus, using the limits of integration calculated above, the decay rate or transitional probability in Equation A.8 can be written as:

$$\Gamma = \frac{G_F^2 m_\tau^5}{16\pi^3} \int_0^1 d\varepsilon_\ell \int_{1-\varepsilon_\ell}^1 d\varepsilon_1 \varepsilon_1 (1 - \varepsilon_1) \, . \tag{A.14}$$

Appendix B Muon Fake Rates

The fake rate is defined as the fraction of hadrons that are misidentified as muons leading to a fake signal. There are four physical processes which contribute to the fake signals:

- hadrons reach the muon chambers without interacting with the hadron absorber;
- hadrons interact with the absorber and the product of the interaction results in a muon signal;
- hadrons decay in flight into muons and the daughter muons are detected;
- the random overlap of track projection with noise hits in the muon chamber.

In this appendix, we estimate the overall probability that a hadron is misidentified as a muon using the data; no attempt is made to isolate the different processes listed above. The charged hadron in the $\tau \rightarrow h\pi^0\nu$ decay mode is used to study the behavior of hadrons in the muon system. The other τ in the event is required to decay leptonically. All events must satisfy the selection criteria listed in Section 4 with the exception of the extra energy veto. This cut is relaxed to include the $\tau \rightarrow h2\pi^0\nu$ decay events where the second π^0 is not explicitly reconstructed, thus increasing the hadron sample without any contamination from non-hadrons. The explicit reconstruction of the π^0 in the event along with the sideband subtraction described in Section 4.1.6 helps minimize the contamination from cosmic rays and mu-pair events. These events are also suppressed by TAUSKM cuts (#2 and #6) described in Section 4.2.1 and by requiring that $(|\vec{p_1} + \vec{p_2}|)/(|\vec{p_1}| + |\vec{p_2}|) > 0.05$.

Most of the hadrons identified in this data sample are pions; there is 2% admixture of kaons due to the Cabbibo suppressed decay $\tau \rightarrow K^*\nu$ followed by the $K^* \rightarrow K\pi^0$.

Figure B.1 shows the DPTHMU versus momentum distributions for identified hadrons and muons in the data sample. Only a few percent of all hadrons studied populate the plot on the right; the remaining hadrons all have DPTHMU=0. On the other hand $\simeq 98\%$ of the muons studied appear in the plot on the left; muon identification inefficiency results in the small loss.

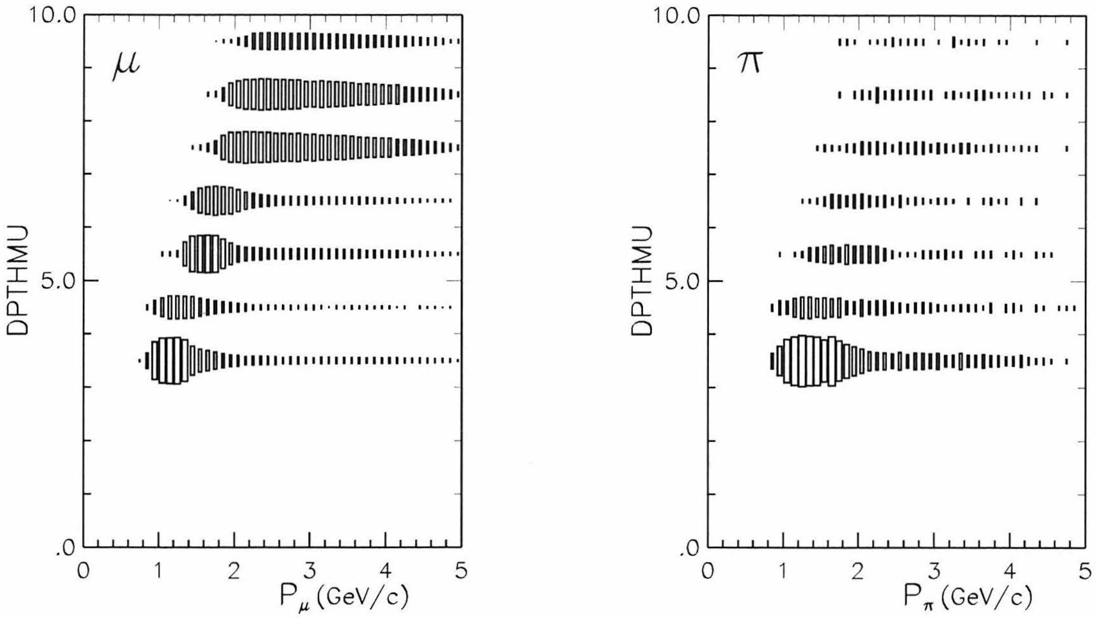

Figure B.1: DPTHMU versus the momentum of the charged track. The figure on the left (right) is for identified muons (pions) in the data sample. The number of entries in both plots have been normalized to unity.

Most of the hadron signal lies in the first set of muon counters and a DPTHMU>5 requirement would reduce the fake muon contamination considerably. This requirement would also reduce the statistics, but more importantly it would eliminate a large fraction of the muons in the $1.0 - 2.5\text{GeV}/c$ momentum region. These low momentum muons are essential in the measurement of the low energy η parameter. One is thus forced to allow DPTHMU>3 muons into the event sample and perform a statistical background subtraction instead to remove the hadron contamination.

In addition to the DPTHMU constraint, the muon identification code also requires that MUQUAL = 0 for identified muons. This variable is set to zero for all tracks where the penetrated absorption lengths (DPTHMU) is consistent with the expected depth calculated from the track's momentum in the drift chamber. Muon identification, in this analysis, also requires that the total shower energy deposited in the electromagnetic calorimeter, and matched to the muon track, does not exceed 600 MeV (see Figure 5.3).

The above three criteria, for a track to be identified as a muon, are now applied to the hadronic track in the sample to obtain the momentum dependent fake rates for the three different DPTHMU requirements shown in figure B.2. The Monte Carlo estimates are not identical to the data estimates and are not utilized in this analysis.

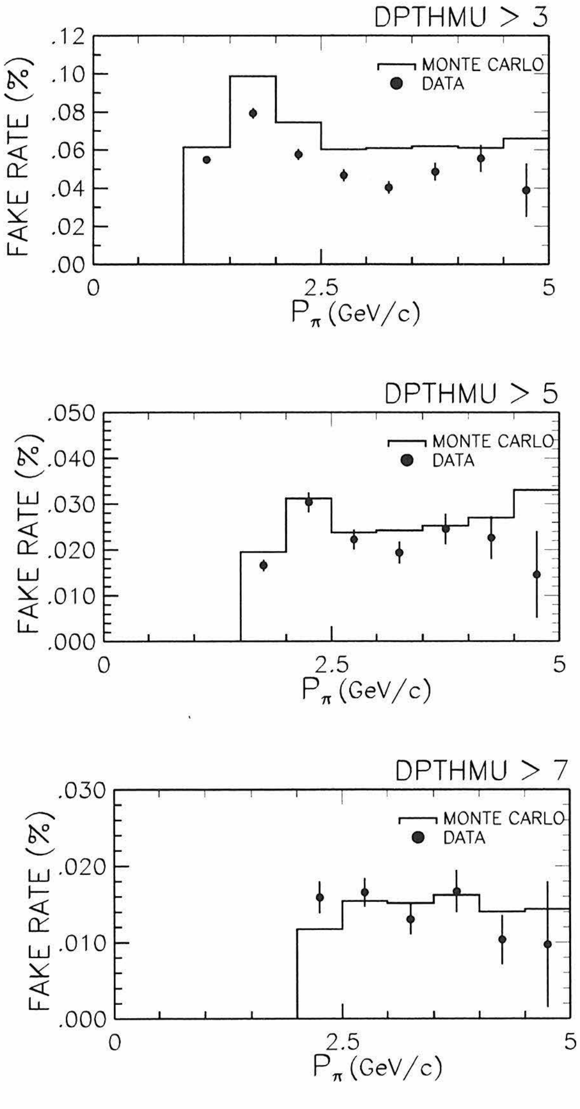

Figure B.2: Hadron fake rates and their momentum dependence measured for the three different DPTHMU variables. These fake rates are measured after the application of the maximum allowed shower energy sum associated with the pion track.

Appendix C The Spin Sensitive Variable ω

For the decay of a polarized tau, the differential partial width is given by:

$$d\Gamma = \frac{1}{2m_\tau}|\mathcal{M}|^2 dPS \ ; \ \text{where} \quad |\mathcal{M}|^2 = B + s_\mu H^\mu \tag{C.1}$$

is the matrix element assuming the standard $V - A$ interaction for a semi-hadronic τ decay. B denotes the spin independent part of the decay and the polarimetric vector; H^μ denotes the spin dependent part of the decay and contains all the spin analyzing information in the decay. The spin vector of the tau is denoted by s_μ, and s_0=0 and $\vec{s} = \pm\hat{p}_\tau$ in the tau rest frame. The unit vector, $\hat{p}_\tau$, is the spin quantization direction and is positive (negative) for right- (left-) handed tau spin polarizations. It is equivalent to the direction of the τ in the laboratory frame of reference.

Considering the $\tau^\pm \to W^\pm \to \pi^\pm\pi^0\,\nu_\tau$ decay mode,

$$\begin{aligned} B &= 2(\tau \cdot J)(\nu \cdot J) - J^2(\tau \cdot \nu) \ \text{ and} \\ H^\mu &= m_\tau(2(\nu \cdot J)J^\mu - J^2\nu^\mu) \ , \end{aligned} \tag{C.2}$$

where the hadronic current, J, can be written as:

$$J^\mu = F(q^2)\left(g^{\mu\nu} - \frac{P^\mu P^\nu}{P^2}\right)Q_\nu \simeq F(q^2)Q^\mu \ . \tag{C.3}$$

$P^\mu = (p_\pi + p_{\pi^0})^\mu$, $P^2 = {m_{\pi\pi^0}}^2 = q^2$, $Q^\mu = (p_\pi - p_{\pi^0})^\mu$ and $F(q^2)$ is the Briet Wigner for the ρ/ρ'. Now, the differential partial width can be rewritten as:

$$d\Gamma_\pm = \Gamma_0\left(1 + \frac{s_\pm \cdot H}{B}\right) = \Gamma_0\left(1 \pm \frac{\hat{p}_\tau \cdot \vec{H}}{B}\right) \ . \tag{C.4}$$

Defining

$$\omega \;=\; (\hat{p}_\tau \cdot \vec{H})/B \;=\; \frac{m_\tau\,(2(\nu \cdot Q)(\hat{p}_\tau \cdot Q) - Q^2(\hat{p}_\tau \cdot \nu))}{2(\tau.Q)(\nu \cdot Q) - Q^2(\tau \cdot \nu)}\;, \qquad \text{(C.5)}$$

we get:

$$d\Gamma_\pm \;=\; \Gamma_0(1 \pm \omega)\;. \qquad \text{(C.6)}$$

Thus, $\omega > 0$ preferentially selects right-handed τ^- (left-handed τ^+) and $\omega < 0$ preferentially selects left-handed τ^- (right-handed τ^+). As seen in Equation C.5, one needs to know the τ momentum to evaluate ω. Neglecting initial state radiation, the τ momentum lies on a cone around the flight direction of the daughter hadronic ($\pi\pi^0$) system. Using this approximation, the experimental observable ω is obtained by numerically integrating over the unknown azimuthal angle ϕ of the tau. This integration reduces the polarimetric power of ω, but is of no importance to the analysis.

Figure 9.17 shows plots of the ω variable for events analyzed in both the pseudo rest frame of the tau ($\cos\alpha \geq 0.970$) and the laboratory frame of reference ($\cos\alpha < 0.970$). The events analyzed in the pseudo rest frame have approximately the same mix of left-handed and right-handed taus, while the events analyzed in the laboratory frame have a much larger concentration of left-handed τ^- and right-handed τ^+.

Appendix D SVD Development

The CLEO II.5 detector has a new silicon microstrip vertex detector (SVD) installed as a major upgrade to the tracking system. This new detector component was physically installed between May and September of 1995. The detector surrounds a new 2.0 cm radius beam pipe, and replaced the precision straw-tube tracker described in Chapter 3. Schematic end view (top) and side view (lower) pictures of this new detector are shown in Figure D.1.

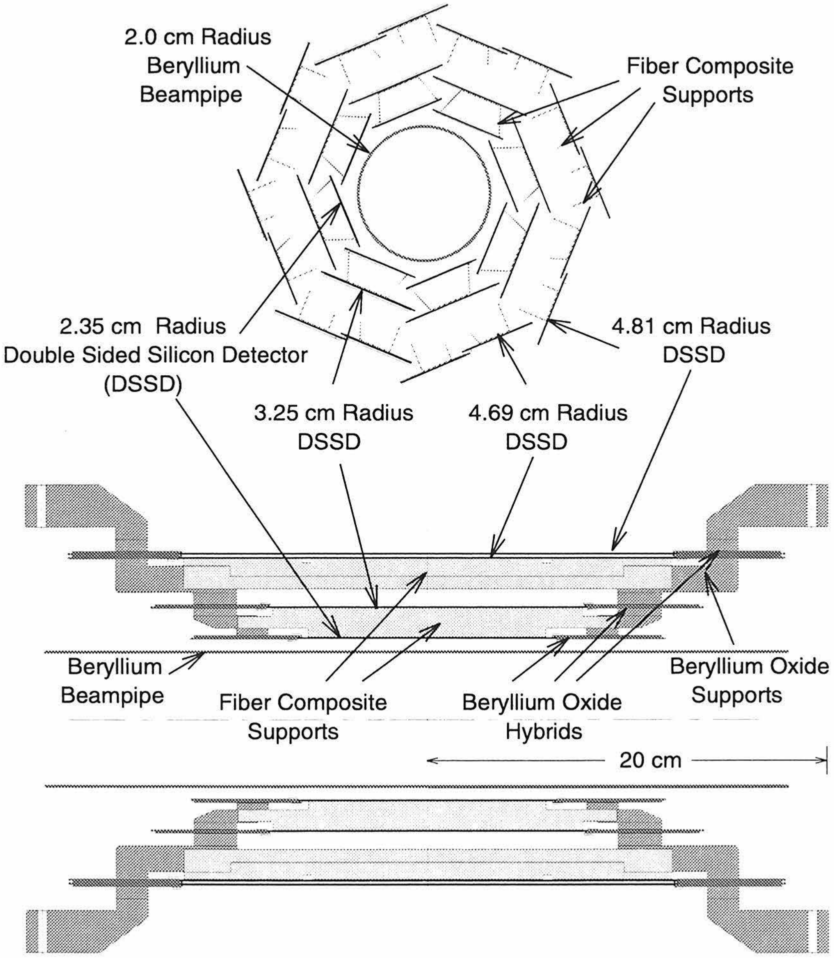

Figure D.1: Schematic end (top) and side (bottom) views of the CLEO II.5 Silicon Vertex Detector.

The thick black lines in the end view schematic indicate the locations of the Hamamatsu double-sided silicon strip detectors. There are a total of 64 silicon detectors in the assembly, and 96 silicon wafers. Pairs of silicon wafers are ganged together lengthwise in the third layer.

The sensitive strips on the detector sides that face away from the center run in and out of the paper, and are used to measure particle trajectories in the plane of the paper ($r - \phi$). The strips that face inward run in the plane of the paper, and measure trajectories in and out of the plane of the paper ($r - z$). For this side, an extra layer of metallization on the silicon is used to route the signals to the electronics at the ends of the detector. Both sides (r-ϕ and z coordinates) are read out at the ends of the wafers in order to reduce the amount of mass in the fiducial region of the detector where multiple scattering would otherwise dominate the resolution for soft tracks.

These strips form the active elements of the device and are arranged in eight octants of twelve wafers each. The detectors are supported by U-channels of carbon fiber composite. Hybrid circuits built on a substrate of beryllium oxide, that incorporate CAMEX and JAMEX integrated circuits, are used to read out the detectors. The entire structure is supported by a carbon fiber composite tube.

I have contributed to two different aspects of the design for this new vertex detector. First, in the summer of 1992, I worked on the new mechanical support structure for this detector. Over the following two years, I spent a significant fraction of my time, along with two post-doctoral fellows, designing, constructing, testing, and installing a data acquisition system to read out the new detector. Both these involvements are described in more detail in the following sections.

D.1 Silicon Vertex Detector Mechanical Assembly

The demands of the mechanical design are fairly rigorous: the structural integrity must be very good in order to position accurately the devices; the mass of the structure in the fiducial region must be low to minimize multiple scattering; the thermal properties must be such that adequate cooling is provided for the CAMEX chip and its line driver; and the thermal expansion coefficient of the materials used must sufficiently conform to that of the silicon.

For this detector, we opted to use a U-shaped channel of boron carbide foam sandwiched between the layers, and held in place by a beryllium oxide (BeO) support structure. The radiation length for tracks at normal incidence introduced by the foam represents only a 30% increase beyond that of the three silicon layer, for a total of 1.26%. Furthermore, both materials have thermal expansion coefficients similar to that of silicon, while the BeO also has a thermal conductivity similar to that of a good metal.

We constructed (with the help of machine shop personnel at Newman Laboratory, Cornell University) a full-scale model of the new interaction region (defined by the inner walls of the drift chamber) in order to carry out mechanical tests of the support system for the new silicon vertex detector. The new interaction region design called for a reduced beam-pipe radius (of 2 cm). Reduction in the radius results in an increased rate of backgrounds which are controlled by masking the beam-pipe. This masking increases the weight of the beam-pipe by about an order of magnitude. Water cooling, needed to handle the larger thermal loads expected at higher beam currents, further increases the weight of the beam-pipe. Since the silicon vertex detector is expected to achieve an order of magnitude improvement in position resolution, it requires a very stable support system.

The full size mock-up of the interaction region and the present support system was constructed using aluminium instead of steel, as in the original design, to ensure that stresses and strains would be enhanced and weak spots in the design would be easily identified. Once identified, the weak spots were redesigned and improved versions were constructed and tested.

The entire support system in the interaction region hangs off of the drift chamber endplates. These plates are very thick, heavy and stable, and it was assumed here that the addition of the SVD along with the new and heavier beam-pipe will not affect their stability. Various mechanical tests were performed to verify this assumption as well.

D.2 The CLEO II.5 SVD Data Acquisition

In this section, the work completed to devise and implement a readout scheme for the silicon vertex detector is described briefly. The read-out consists of 416 CAMEX/JAMEX chips, each with a single analog output that multiplexes 64 charge-integrated signals, for a total of 26,624 channels. Because of the large number of channels, it is necessary to sparsify the data; since the occupancy is low (a typical hadronic event hits less than a thousand microstrips), it is feasible to do so.

The design criteria, which are partly dictated by the present system and timing constraints, are as follows:

- The front-end electronics must digitize and store all channels in 1 ms. (CLEO-II's present front-end electronics digitizes the data in 2 ms, but there is a provision to reduce this by half).
- Within 10 ms the data must be sparsified, with the event fragment ready for the event builder process.
- The hardware and software must be compatible with the current data acquisition system.
- The ground for the readout electronics must float at the bias voltage of the detector.

The system consists of several components; a schematic of how all the pieces fit together to make the data acquisition system is shown in Figure D.2.

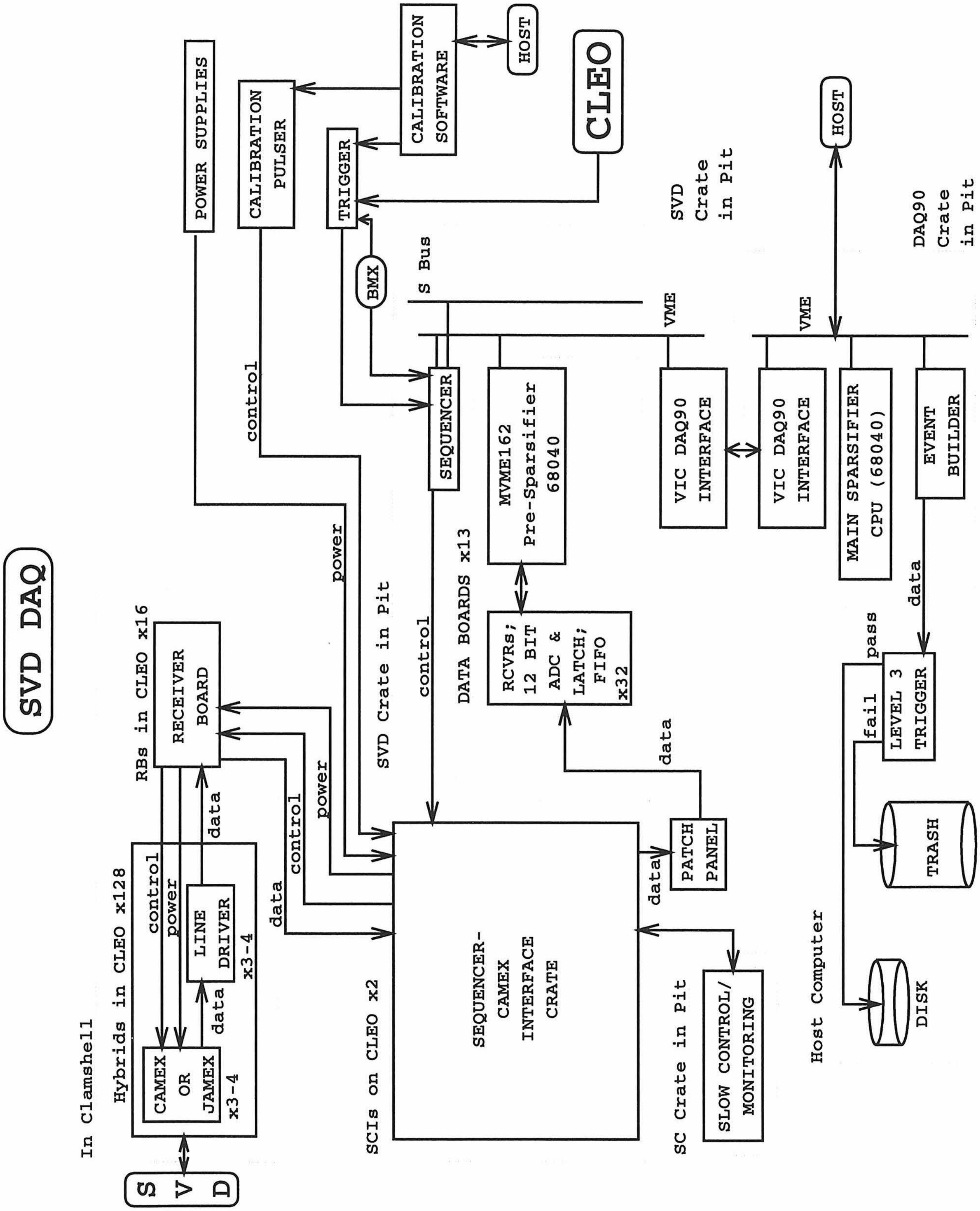

Figure D.2: A schematic of the silicon vertex detector data acquisition system, showing the on-board electronics, the Receiver Board, the Sequencer-CAMEX Interface (SCI) crate, the Slow Control crate, the data acquisition crate with its constituent boards, and the final event building hardware.

Databoards: There are 13 databoards in the SVD crate, each with an analog and a digital section. The analog section services 32 CAMEX analog outputs with a sample/hold circuit and an ADC (analog to digital converter) for each. The sample/hold allows one set of CAMEX channels to be digitized, while the next set are addressed. The digital section begins with a first-in-first-out memory (FIFO) into which ADC data is written. The FIFO can hold several events if necessary. Following the FIFO is a "pre-sparsifier," a standard Motorola MVME162 board (based on the 68040 CPU) that will sparsify the data by suppressing common-mode noise, tagging data above threshold, and generating an address for each. One MVME162 board resides on each databoard. From here, data are placed into the MVME162 memory which serves to buffer events at the front-end so that CLEO can be re-enabled as quickly as possible.

Sequencer board: A customized board that generates the appropriate sequence of clocks and channel addresses to the CAMEX chips and the databoards. A signal from the CLEO-II event trigger sets it into action.

Sequencer-CAMEX Interface (SCI) crates: These crates route the control signals and output signals to the appropriate places, maintain the floating grounds, handle test pulsing of the CAMEXes/JAMEXes, control grounding of the test pulse lines, and interface the detectors with the slow-control system for monitoring. Since I worked primarily on the design of these crates, they are discussed in more detail in the following section.

Main sparsifier: This is a 68040 CPU board identical to those in the existing DAQ90 system. In addition to supervising activity within the crate, it fetches the pre-sparsified data from the data board CPUs and notifies the main event builder in the DAQ90 system that the event fragment is ready to be incorporated into a formatted event.

VICbus VME crate link: Connects the SVD VME crate to the main DAQ90 VME system for data transfer and control messages.

D.2.1 SCI Crates

The Sequencer-CAMEX Interface (SCI) crates are the links between the silicon vertex detector and the outside world. They provide all the silicon vertex detectors with their required power, bias voltages and control signals. There are two identical SCI crates, one servicing each half of the detector. The final printed circuit boards for both the Controller and I/O boards, which populate these crates as shown in Figure D.3, were laid out using the design tool CADENCE.

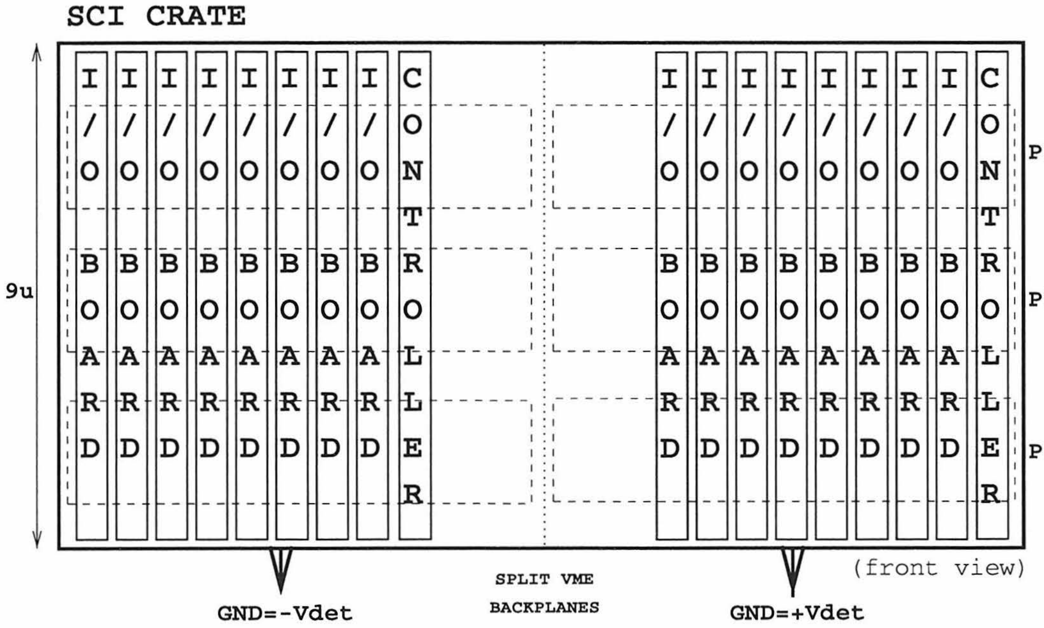

Figure D.3: The SCI crate.

Their main function of the SCI crates is to fan out all the relevant signals from several discrete sources to each of the 416 CAMEXes. These crates shape several of the higher-frequency sequencer signals in an effort to minimize the noise they broadcast to the signals of the nearby vertex detector (VD) and drift chamber (DR) subdetectors. They also provide many of the signals monitored by the slow control system. The analog data output signals are routed out through the SCI crates to a large patch panel which translates between the output signal multiplicity, dictated by the 26 CAMEXes per detector octant, and the input signal multiplicity of the 32 ADCs of each data board. All power lines coming from the power supply system pass through the SCI crates. Their voltage levels are monitored, and in certain cases, derived and adjusted. Finally, the SCI crates oversee the grounding and ungrounding of each CAMEX/JAMEX test pulse line during running and calibration respectively. Studies have shown that this grounding/ungrounding of the test pulse lines is critical to their proper operation.

Voltages and control signals enter the SCI crate through the controller board; a schematic for which is shown in Figure D.4. Some of these signals are changed from square to "trapezoidal" in shape and decreased in amplitude to reduce broadcast noise.

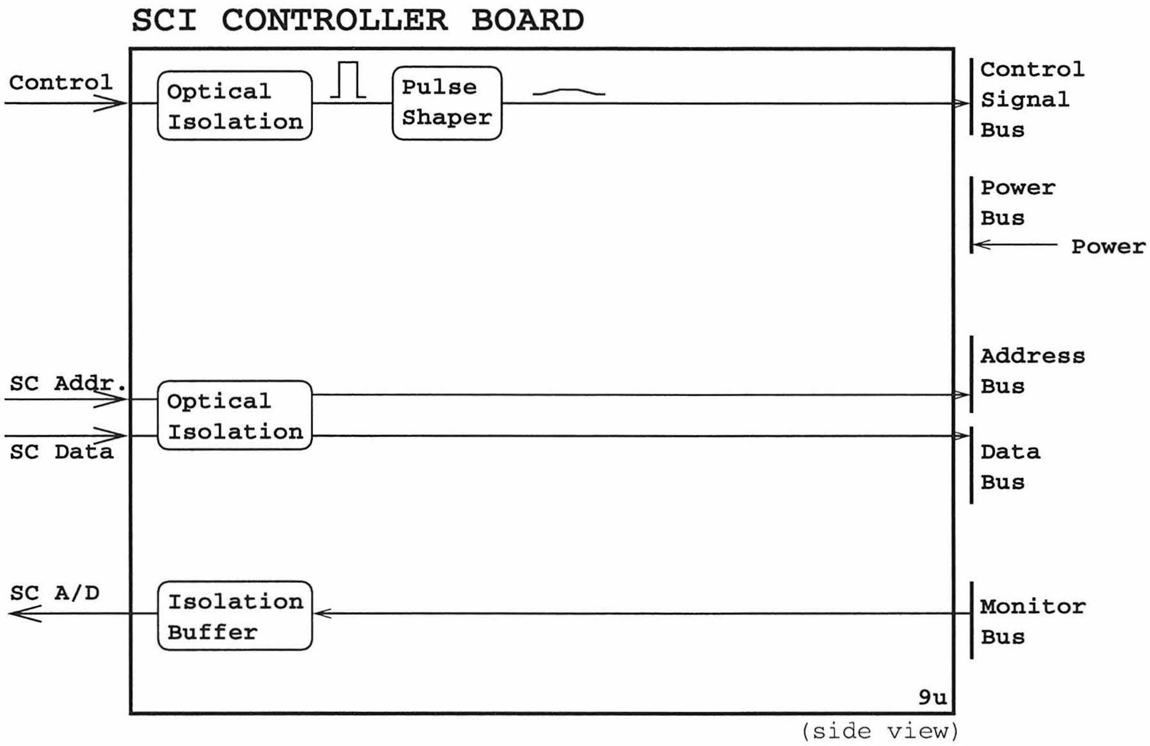

Figure D.4: The SCI Controller Board.

The voltages and control signals are placed on the backplane for distribution to the I/O boards; a schematic picture is shown in Figure D.5. Each I/O board provides voltages and control signals for half an octant (there are eight octants in each half of the SVD). In response to the appropriate address placed on the backplane through the controller board by slow control, the I/O board puts various monitored analog quantities on the backplane. These quantities are then sent out via the controller board to be digitized and placed in the data stream or used to generate alarms as appropriate. Each I/O board has individually fused voltage lines supplying the CAMEX/JAMEXes, in order to facilitate shutting down individual chips in the event one fails, or, for example, begins to draw an excessive amount of current. The analog output signals from the chips also pass through the I/O boards where they are bundled together and sent to the patch panel and the databoards to be digitized.

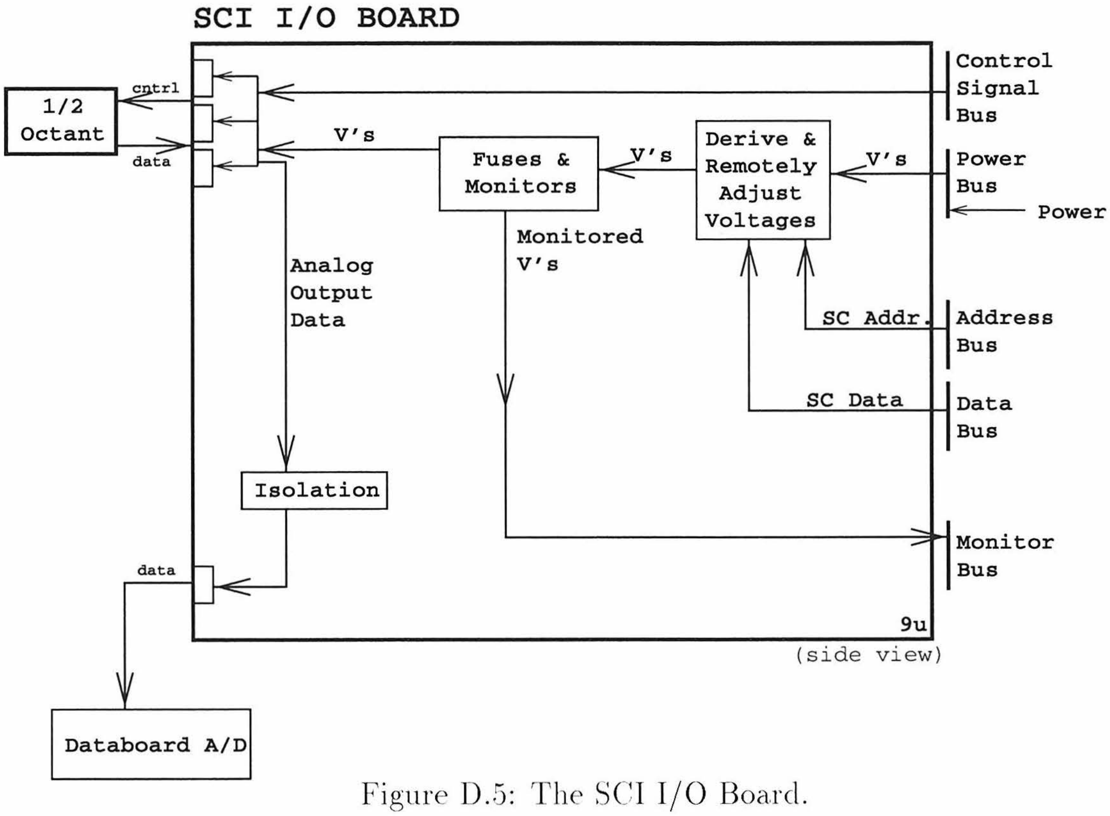

Figure D.5: The SCI I/O Board.

These SCI crates are also used to provide the "floating ground" for the detectors. There are two sets of strips that are used to readout the detector. The sense strips are the actual p or n material implanted into the bulk of the detector. The readout strips are separated from the sense strips by a thin layer of SiO_2, which acts as a capacitor. The electron-hole pairs generated by a passing track are collected on the sense strips, and the resulting signal is capacitively coupled onto the readout strips. In the original readout scheme, the p and n sense strips were to be kept at -50 V and $+50$ V respectively, so that the detector would be biased while the readout strips (which are attached to the input of the CAMEX pre-amplifier) would be kept at ground. Unfortunately, the thin layer of SiO_2 seemed to develop "pinholes" occasionally (on $\simeq 5\%$ of the strips), thus joining the 50 V bias voltage to ground through the preamplifier chips. A large ($\simeq$ MΩ) resistor limited the current draw, but this still caused the channel and many of its neighbors to function improperly. To combat this problem, it was decided that all of the readout electronics would have "floating grounds" that were at ± 50 V relative to earth ground. That way if a pinhole occurred, smaller currents would be drawn.

When it became clear that the pinhole rate was too high, Hamamatsu added an additional layer of silicon nitride. This reduced the pinhole rate to less than 1% on the later detector deliveries.

The floating ground readout scheme has been implemented. Opto-coupler chips are used to float the incoming TTL logic signals from earth ground to floating ground. Capacitors are used to bring the floating analog CAMEX output signals back down to earth ground. All of this translation is done at the SCI crate.

D.3 Schematics

Figure D.6 shows the detailed schematic layout of the SCI Controller board. Each rectangle on this sheet represents a specific part of this board; their specific functions are mentioned below.

The differential control signals from the receiver board enter through the sequencer connector shown on the top left-hand corner of this schematic. These differential signals are received by the electronics in the schematic box labeled **RECEIVER.SCH**, before they are level shifted from earth ground to the floating voltage by the optocouplers in **OPTOP.SCH**. The highest frequency pulse signals are converted to trapezoidal signals to reduce their risetimes, and thereby reduce the broadcast noise to neighboring detectors (for example, through the drift chamber preamplifiers). The risetime, and lower and upper limits of these pulses, are adjusted using three potentiometers on each Controller board. All this shaping electronics lies in the schematic box labeled **TRAPEZP.SCH**.

Next, the control signals and address lines are buffered in **BUFFER.SCH** before they are placed onto the J1 backplane for distribution to the I/O boards. **BACKPLANES.SCH** includes the schematics for the three backplane connectors on this board. The J1 connector collects the control signals from the buffers for distribution to the I/O boards. There are a total of 44 and 53 monitored quantities for P and N-side sections, and these are collected from the I/O boards through the J3 backplane. The J2 connector supplies the Controller board with all the required power, and is connected to the Pdist board of the power supply system. Voltage dividers in **VOLTAGE.SCH** are used to prepare appropriate voltage levels needed by other parts of the Controller board.

A Comparator in **SCENAB.SCH** is used to provide the slow control enable signal. The Slow Control system determines which of the 36 boards in the two SCI crates is to be monitored at any given time by sending a 6-bit address to the Controller boards. This address is placed on the J2 backplane and each board compares it to the unique hardwired geographical slot address. The 74ALS520 chip which performs this comparison can be strobed (output enabled) either by using the 7^{th} bit, or can be enabled at all times (selection is made via a jumper).

The schematic for the pulser, designed by Shun Chan and Chris O'Grady, a Caltech graduate student and post-doctoral fellow respectively, resides in the box labeled **PULSER.SCH**. Test pulse triggers enter the Controller board, and are used to place a test pulse of a certain length and amplitude onto the backplane for distribution to the I/O boards. A DAC is used to determine the height of the test pulse. Each of the three test pulse lines can be activated independently via Slow Control. The length of the test pulse line is determined via a one-shot, the output of which is controlled by a potentiometer. Since there is only one DAC, only one pulse size may be generated at any given time.

Various power supply voltages and many of the control and pulser signals are connected to front-panel LEDs. All signals to the LEDs are collected, and voltage dividers in **LEDCONN.SCH** are used to drop voltages to levels that are accepted by the LEDs. The front panel LEDs in **LEDS.SCH** provide a visual status display for the Controller board.

Optocouplers are used to float all the Slow Control signals to the floating voltage in **SCOPTOP.SCH**, and CMOS switches are used in **SWITCHES.SCH** to switch the Controller board voltages monitored by the Slow Control system. The "Slow Control Enabled" signal is generated by the comparator in **SCENAB.SCH**.

Floating currents (from the I/O boards via the J3 backplane) are level-shifted down to Earth ground in **DEFLTPI.SCH** before they are sent off to the slow control ADC to be digitized for monitoring purposes. Floating voltages are level-shifted down to Earth ground in **DEFLTPV1.SCH** and **DEFLTPV2.SCH**.

The edge connectors in **EDGECONN.SCH** are used to collect (and transfer) all the currents and voltages that are to be monitored by the Slow Control system.

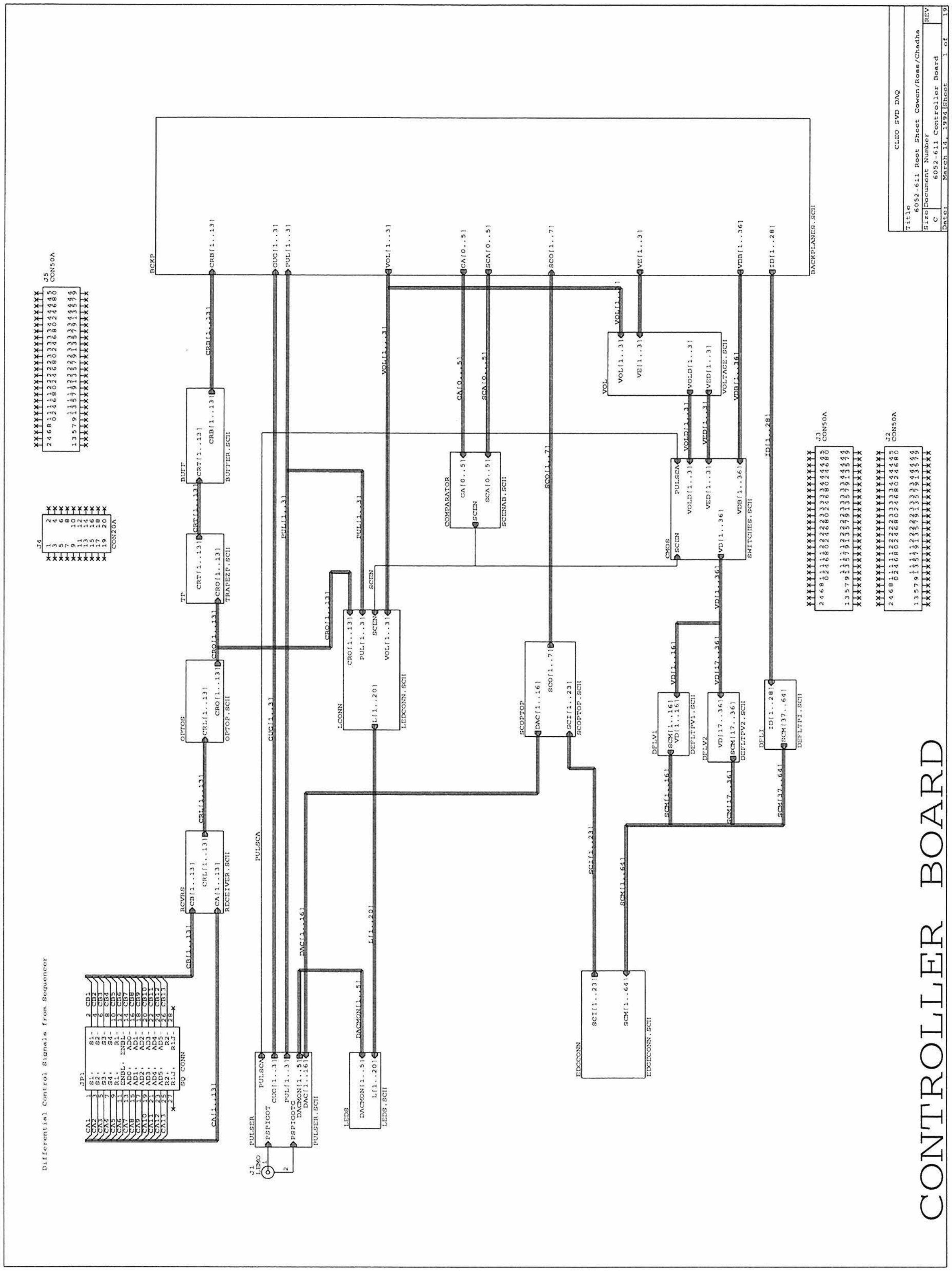

Figure D.6: The SCI Controller Board schematic drawing. Each rectangle on this sheet represents a specific part of this board.

The I/O boards take the control signals placed on the backplane by the Controller board, attenuates them by a factor of twenty, and differentializes and buffers them before sending them off to the Receiver boards which transfers them to the CAMEXes. The P -side I/O boards talks to both CAMEXes and JAMEXes, and thus, two sets of reference voltages are required on them. Figure D.7 shows a schematic drawing for the N-side I/O board.

The connections to the three backplane connectors on the I/O boards lie in the **BACKPLANES**. The Control signals are read via the J1 backplane, and all the hybrid and CAMEX (JAMEX) power supply voltages, provided by the power supply system, enter through the middle J2 backplane in the same manner as for the Controller board. Whenever an I/O board is Slow Control enabled, it closes its CMOS switches, thereby placing its monitored voltages onto the J3 backplane.

The chips used to differentialize the control signals from the J1 backplane are contained in **CSDIFF**. The attenuation and differentializing reduce the control signal's ability to broadcast noise to the components of neighboring subdetectors. Differentializing these signals also improves their immunity to external noise sources. The control signals are buffered in **CSDIFFBUFF** before they are sent off to the Receiver boards. The address lines and the output enable (OE) are buffered in **CSBUFF**.

Each of the hybrid and power supply voltages that enters via the J2 backplane is fused, monitored and routed to the appropriate output connector in **SWITCHYARD**. Certain voltages are derived from the power supply voltages so that they can only be present if power is present, and are adjusted using potentiometers on each I/O board. The detector bias voltages, or the offsets from floating ground, are derived independently on each I/O board for each detector wafer via four potentiometers. Many of these voltages can be measured by means of test points located just above the DataBoard connectors along the face of the I/O boards. All monitored voltaged are brought down to appropriate levels in **VOLTAGE MONITORS** using several voltage dividers.

A comparator in **IOCOMPARATOR** is used to determine if the particular board is being addressed at a given time. It is identical to the one on the Controller board.

The Slow Control CMOS switches occupy the rectangle labeled **SC CMOSSWITCHES**. When a board is selected via the Comparator, a "Slow Control Enable Signal" is sent out and the CMOS switches are closed. The monitored voltages are then placed onto the J3 backplane.

During calibration, each I/O board takes test pulses off the backplane, buffers them, and routes them to the appropriate output connectors in **TESTPULSE**. Whenever test pulsing is disabled, the test pulse lines can be grounded by means of a solid-state relay either directly to floating ground, or through a potentiometer-controlled resistance. The grounding mechanism is controlled by a jumper.

Some signals are monotored via front panel LEDs in **IOLEDMONITORS**. The signals are brought down to levels accepted by the LEDs on these boards in **LEDLEVELS**. As with the Controller board, the LEDs provide a visual status display for the I/O boards.

The output data from the CAMEXes is sent differentially to the I/O boards from the Receiver boards. The I/O boards receive these signals, buffer them, and level-shift them in **LEVEL SHIFTERS** by means of an AC-coupled differential op-amp (to eliminate any noise between floating ground and Earth ground). The AC-coupling is achieved by means of 1μF, 50 V capacitors. The gain of this defloating amplifier is controlled by means or resistors. This adjustability enables us to optimize the output signal with respect to the Databoard ADCs.

Finally, the **CONNECTORS** rectangle shows the connections to the hybrid connectors, and temperature sensors monitor the temperature of the I/O boards in **TEMPERATURE**.

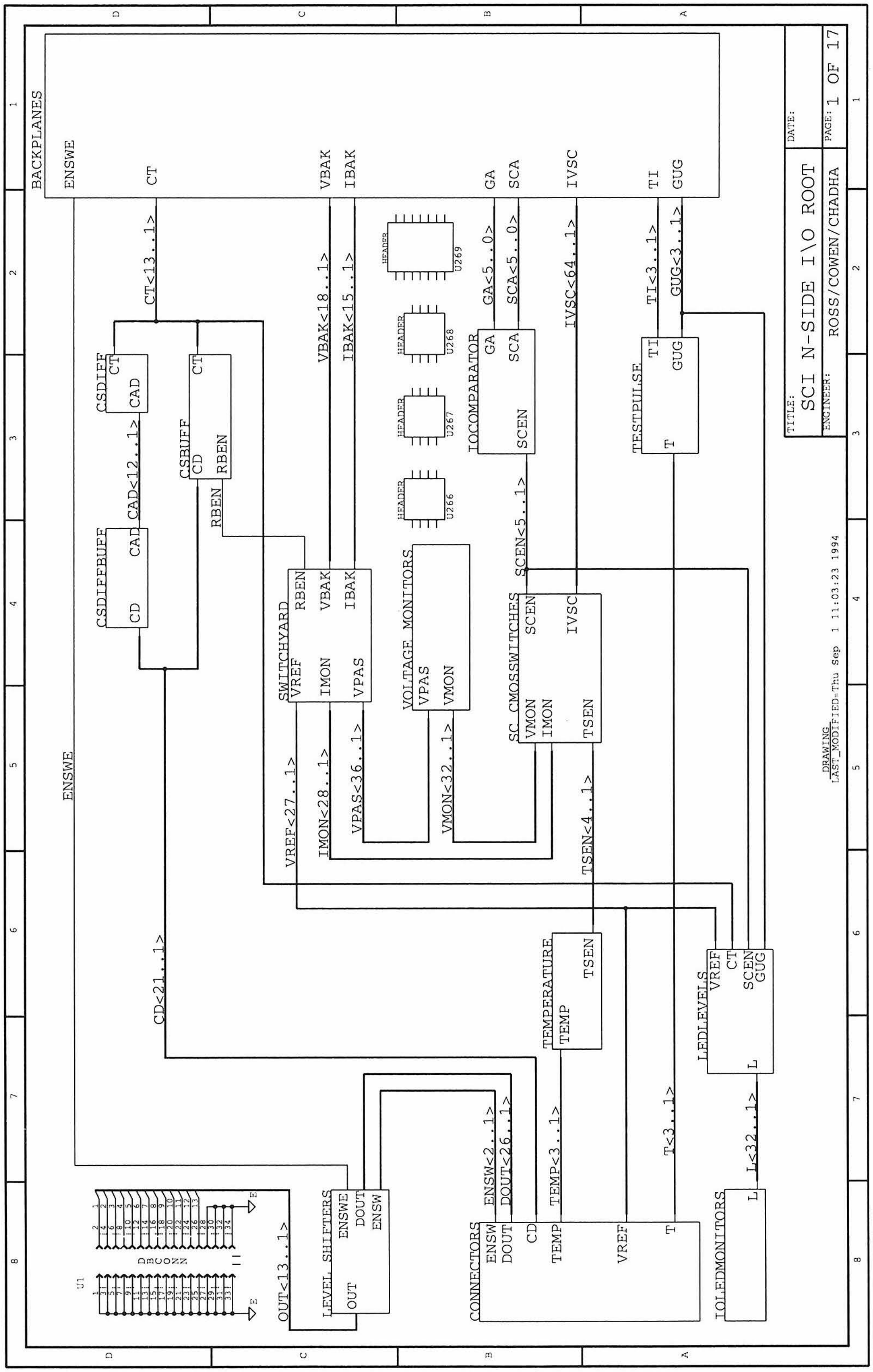

Figure D.7: The *N*-side SCI I/O Board schematic. Each rectangle on this sheet represents a specific part of this board designed to accomplish a specific task.

D.4 Printed Circuit Boards

For both the final SCI Controller and I/O printed circuit boards (PCB), we used 9U boards (366.7mm × 227.3mm). In addition to the top and bottom layers, that were utilized primarily for the routes connecting the various components, each board has eight embedded voltage and ground planes. These boards are highly populated with a total of 484 components for each Controller board, and a total of 575 components for each I/O board. Table D.1 shows the various components used on these boards.

Component	Quantity	
	Controller Board	I/O Board
Chips	160	120
Resistors	85	210
Capacitors	250	200
Fuses	6	36
Connectors	7	7
Jumpers	6	30
Limos	1	0
Transistors	12	3
Sips	11	30
Pots	3	13

Table D.1: The various components of the SCI Controller board and the SCI I/O board.

Both boards have approximately 2000 connections. They require approximately 2000 inches of etch length and 375 vias to complete these connections. The final printed circuit boards have both a solder mask and a silkscreen layer, and no gold plating was used in either board.

Bibliography

[1] G. t′ Hooft, *Scientific American,* 242 (1980).

[2] B. C. Barish et al., Caltech Collaboration, *Phys. Rev. Lett.* **34**: 538 (1975).

[3] F. J. Hasert et al., *Phys. Lett.* **B46**: 138 (1973).

[4] G. Arnison et al., UA1 Collaboration, *Phys. Lett.* **B122**: 103 (1983).

[5] G. Arnison et al., UA1 Collaboration, *Phys. Lett.* **126B**: 398 (1983).

[6] S. Abachi et al., D0 Collaboration, *Phys. Rev. Lett.* **74**: 2632 (1995).

[7] F. Abe et al., CDF Collaboration, *Phys. Rev. Lett.* **74**: 2626 (1995).

[8] A. Anastassov et al., CLEO Collaboration, *Phys.Rev.* **D55**: 2259 (1996).

[9] H. Albrecht et al., ARGUS Collaboration, *Phys.Lett.* **B341**: 441 (1995).

[10] D. P. Barber et al., Mark J Collaboration, *Phys. Reports 63* **No 7**: 337 (1980).

[11] A. J. Weinstein and R. Stroynowski, *Ann. Rev. Nucl. Part. Sci* **43**: 457 (1993).

[12] B. C. Barish and R. Stroynowski, *Phys Rep* **157**: 1 (1988).

[13] Y. S. Tsai, *Phys Rev.* **D4**: 2821 (1971); Erratum *ibid.* **D13**: 771 (1976).

[14] M. L. Perl et al., *Phys. Rev. Lett.* **35**: 1489 (1975).

[15] M. L. Perl et al., *Phys. Lett.* **63B**: 466 (1976).

[16] R. Brandelik et al., DASP Collaboration, *Phys. Lett.* **73B**: 109 (1978).

[17] Y. S. Tsai, *SLAC-PUB*-2356 (1979).

[18] C. Albajar et al., UA1 Collaboration, *Phys. Lett.* **185B**: 233 (1987).

[19] J. Alitti et al., UA2 Collaboration, *Z. Phys.* **C52**: 209 (1991).

[20] F. Abe et al., CDF Collaboration, *Phys. Rev. Lett.* **68**: 3398 (1992).

[21] A. Savoy-Navarro, Proc. Workshop on τ lepton physics. Editors: M. Davier and B. Jean-Marie (1991).

[22] F.del Aguila et al., *Phys. Lett.* **B271**: 256 (1991).

[23] C. Bottcher and M. R. Strayer, *J. Phys.* **G16**: 975 (1990).

[24] B. Pontecorvo, *Zh. Eksp. Teor. Fiz.* **53**: 1717 (1967); **34**: 247 (1958); **33**: 549 (1957).

[25] L. Michel, *Proc. Phys. Soc. (London)* **A63**: 514 (1950).

[26] T. D. Lee and C. N. Yang, *Phys. Rev.* **108**: 1611 (1957).

[27] T. Kinoshita and A. Sirlin, *Phys. Rev.* **113**: 1652 (1959).

[28] W. J. Marciano and A. Sirlin, *Phys. Rev. Lett.* **61**: 1815 (1988).

[29] Particle Data Group, R. M. Barnett et al., *Phys. Rev.* **D54** (1996).

[30] R. H. Dalitz, *Phil. Mag.* **44**: 1068 (1953).

[31] C. Bouchiat and L. Michel, *Phys. Rev.* **106**: 170 (1957).

[32] F. Scheck, *Phys. Rep.* **44** (1978).

[33] H. Albrecht et al., ARGUS Collaboration, *Phys. Lett.* **B349**: 576 (1995).

[34] D. Buskulic et al., ALEPH Collaboration, *Phys. Lett.* **B346**: 379 (1995); Erratum-ibid **B363**: 265 (1995).

[35] M. Acciarri et al., L3 Collaboration, *Phys. Lett.* **B377**: 313 (1996).

[36] K. Abe et al., SLD Collaboration, *Phys. Rev. Lett.* **78** 4691 (1997).

[37] R. M. Barnett et al., Particle Data Group, *Phys. Rev.* **D54**: 272 (1996).

[38] R. M. Barnett et al., Particle Data Group, *Phys. Rev.* **D54**: 254 (1996).

[39] W. Fetscher, H. J. Gerber and K. F. Johnson, *Phys. Lett.* **B173**: 102 (1986).

[40] S. R. Mishra et al., *Phys. Lett.* **B252**: 170 (1990).

[41] W. Fetscher, *Phys. Lett.* **140B**: 117 (1984).

[42] J. Missimer, F. Scheck and R. Tegan, *Nucl. Phys.* **B188**: 29 (1981).

[43] W. Fetscher, *Phys. Rev.* **D42**: 1544 (1990).

[44] J. P. Alexander et al., CLEO Collaboration, CLNS 97/1480, (submitted to PRD) (1997).

[45] W. Hollik and T. Sack, *Phys. Lett.* **B284**: 427 (1992).

[46] A. Stahl, *Phys. Lett.* **B324**: 121 (1994).

[47] M. A. B. Bég et al., *Phys.Rev. Lett.* **38**: 1252 (1977).

[48] T. G. Rizzo, *SLAC-PUB-7453* (1997); *to be published in Phys. Rev.* **D** (1997).

[49] T. M. Aliev et al., *Phys.Rev.* **D47**: 2879 (1993).

[50] Y. Kubota et al., *Nucl. Instrum. Methods* **A320**: 66 (1992).

[51] R. Talman, *Nucl. Instr. Methods* **159**: 189 (1979).

[52] S. Jadach and Z. Was, *Computer Physics Communications* **36**: 191 (1985).

[53] S. Jadach, J. H. Kuhn, and Z. Was, *Computer Physics Communications* **64**: 275 (1990).

[54] S. Jadach and Z. Was, *Computer Physics Communications* **76**: 361 (1993).

[55] E. Barberio and Z. Was, *Computer Physics Communications* **79**: 291 (1994).

[56] S. Jadach and Z. Was, *Computer Physics Communications* **64**: 267 (1990).

[57] M. Schmidtler, IEKP-KA/93-14 (1993).

[58] CLEO Internal note, CSN 89-282 (1989).

[59] R. Brun et al., Technical Report CERN-DD/EE/84-1, CERN (1987).

[60] D. G. Cassel and H. Kowalski, *Nucl. Instr. Methods.* **185**: 235 (1981).

[61] S. Roberts, M. Battle and E. Thorndike, internal CLEO report CBX 93-113 (1993).

[62] B. K. Heltsley, internal CLEO report CBX 88-39 (1988).

[63] E. Blucher et al., *Nucl. Instr. Methods.* **A249**: 201 (1986).

[64] B. K. Heltsley, Internal CLEO memo, CBX 92-108 (1992).

[65] T. Skwarnicki, Internal CLEO memo, CSN 90/301 (1990).

[66] T. Haupt, Internal CLEO memo, CBX 91-78 (1991).

[67] B. K. Heltsley, Internal CLEO memo, CSN 95-338 (1995).

[68] B. K. Heltsley, Internal CLEO memo, CBX 93-108 (1993).

[69] M. Chadha, Internal CLEO memo, CBX 91-88 (1991).

[70] M. Chadha, Internal CLEO memo, CBX 93-27 (1993).

[71] B. Heltsley, Internal CLEO memo, CBX 95-35 (1995).

[72] Particle Data Group, R. M. Barnett et al., *Phys. Rev.* **D54**: 256 (1996).

[73] B. K. Heltsley, Internal CLEO memo, CBX 92-49 (1992).

[74] B. K. Heltsley, Internal CLEO memo, CBX 91-90 (1991).

[75] B. K. Heltsley, Internal CLEO memo, CBX 92-106 (1992).

[76] B. K. Heltsley, Internal CLEO memo, CBX 93-95 (1993).

[77] B. K. Heltsley, Internal CLEO memo, CBX 96-40 (1996).

[78] W. T. Ford et al., MAC Collaboration, *Phys. Rev.* **D36**: 1971 (1987).

[79] H. Albrecht et al., ARGUS Collaboration, *Phys. Lett.* **B246**: 278 (1990).

[80] S. Behrends et al., CLEO Collaboration, *Phys. Rev.* **D32**: 2468 (1985).

[81] Skims provided by B. K. Heltsley.

[82] R. M. Barnett et al., Particle Data Group, *Phys. Rev.* **D54**: 230 (1996).

[83] R. Ammar et al., CLEO Collaboration *Phys.Rev. Lett.* **78**: 4686 (1997).